

Die approbierte Originalversion dieser
Dissertation ist in der Hauptbibliothek der
Technischen Universität Wien aufgestellt und
zugänglich.

<http://www.ub.tuwien.ac.at>



The approved original version of this thesis is
available at the main library of the Vienna
University of Technology.

<http://www.ub.tuwien.ac.at/eng>

Dissertation

Passive RFID for Automotive Sensor Applications

Submitted in part fulfilment of the requirements for the degree of
Doktor der technischen Wissenschaften
of the
Vienna University of Technology
Fakultät für Elektrotechnik und Informationstechnik

by

Gregor Lasser

advised by

Univ. Prof. Dr.-Ing. Christoph F. Mecklenbräuer
Vienna University of Technology
Institute of Telecommunications

Second Examiner

Zoya Popović, Ph.D.

Distinguished Professor, Hudson Moore Jr. Endowed Chair
University of Colorado at Boulder
Department of Electrical, Computer, and Energy Engineering

Vienna, October 2014

Abstract

Future vehicular sensors will further increase active and passive safety systems of cars and trucks. One particular promising objective is to gather tyre data as temperature, vibration, acceleration and tyre pressure by mounting sensors in the tyres. Since they are the actual elements which transfer the occurring acceleration and — more important — deceleration forces, any additional information about these essential load transmission components aids safety systems. Whereas the tyre pressure is already monitored in many vehicles using sensors mounted at the rim, the other mentioned parameters are only retrievable for a tyre-mounted sensor. The particular benefit about the knowledge of the acceleration forces lays in the possibility to compute the tyre's contact area, which is directly proportional to the maximum force that is transferable without wheelspin.

In this thesis, I evaluate the applicability of Ultra High Frequency (UHF) or microwave passive Radio Frequency IDentification (RFID) technology to communicate with tyre mounted sensor nodes to form an Advanced Tyre Monitoring System (ATMS). First, I focus on Onboard Unit (OU) antennas for this application. Vertically polarized dual-band antennas, which exploit the body floor pan beneficially, are presented and characterized. Further, a horizontally polarized Switched Beam Antenna (SBA) is developed, which is capable of steering a beam to one of the four tyres of a car. To shield this antenna from the deleterious metallic body floor pan, I propose, construct, and characterize two dual-band Frequency Selective Surface (FSS) structures based on the Artificial Magnetic Conductor (AMC) principle. Antenna measurements of the overall system are discussed.

Next, my thesis addresses broadband leakage cancellation. This topic is the key to RFID systems that are range-limited only by the tag sensitivity. Theoretical bounds for the isolation bandwidth are derived and confirmed in experiments. I present a comparison of leakage canceller adjustment algorithms, and derive the estimation noise and bias of a novel, fast algorithm. Again, this analysis is experimentally confirmed.

Finally, I report on dual-band channel measurements for RFID-based ATMS using previously characterized antennas. The analysis of these measurements demonstrates, that communication with UHF RFID-based sensors is feasible in 75% of all possible rotational angles, using state-of-the-art dual-antenna RFID tags and power combining.

Kurzfassung

Zukünftige Fahrzeugsensoren werden die aktiven und passiven Sicherheitssysteme von Autos und LKWs weiter verbessern. Ein besonders vielversprechender Ansatz ist das Erfassen von Reifendaten wie Temperatur, Vibrationen, Beschleunigungen und Reifendruck, indem Sensoren direkt in den Reifen montiert werden. Da sie jene Bauteile darstellen, welche die auftretenden Beschleunigungs-, und vor allem Bremskräfte übertragen, ist jede weitere Information über diese wichtigen Kraftübertragungselemente für Sicherheitssysteme hilfreich. Im Gegensatz zu der die in vielen Fahrzeugen bereits implementierten Reifendrucküberwachung mit in den Felgen montierten Sensoren, können die anderen erwähnten Parameter nur durch in den Reifen montierten Sensoren detektiert werden. Der besondere Vorteil von Beschleunigungsdaten aus den Reifen liegt in der Möglichkeit daraus direkt die Größe der Kontaktfläche der Reifen auf der Straße zu berechnen, die wiederum direkt proportional zu der maximalen Kraft ist die ohne Durchdrehen der Räder übertragen werden kann.

In dieser Arbeit untersuche ich die Anwendbarkeit von passiver Ultra High Frequency (UHF) oder Mikrowellen-Radio Frequency IDentification (RFID) Technologie um mit direkt in den Reifen montierten Sensorknoten zu kommunizieren, und so ein Advanced Tyre Monitoring System (ATMS) zu realisieren. Zuerst konzentriere ich mich auf Antennen für die Onboard Unit (OU). Ich stelle vertikal polarisierte Doppelband-Antennen vor, welche die Bodenplatte eines Fahrzeugs gewinnbringend nutzen. Weiters präsentiere ich eine Antenne mit umschaltbarer Hauptstrahlrichtung (Switched Beam Antenna (SBA)), die auf einen der vier Reifen eines Autos ausgerichtet werden kann. Um diese Antenne von der für sie schädlichen Bodenplatte des Fahrzeugs abzuschirmen, schlage ich eine frequenzselektive Struktur (FSS) vor, die nach dem Prinzip eines künstlichen magnetischen Reflektors (AMC) auf zwei Frequenzbändern arbeitet.

Als nächstes behandelt meine Dissertation die breitbandige Trägerunterdrückung. Dieses Thema ist der Schlüssel zu RFID-Systemen, die hinsichtlich der Lesereichweite nur durch die Transponder-Empfindlichkeit limitiert sind. Theoretische Grenzen für die Unterdrückungsbandbreite werden abgeleitet und in Experimenten verifiziert. Ich präsentiere einen Vergleich von Trägerunterdrückungsabweichalgorithmen und leite das Rausch- und Abweichungsverhalten eines neuen schnellen Algorithmus her. Diese Analyse wird ebenfalls mit Experimenten untermauert.

Schlussendlich berichte ich über doppelbandige Kanalmessungen für ein auf RFID Technologie basierendes ATMS, wobei die zuvor charakterisierten Antennen Verwendung finden. Die Analyse dieser Messungen demonstriert, dass die Kommunikation mit UHF RFID basierten Sensoren in 75 % aller Raddrehwinkel möglich ist, wenn aktuelle Tags mit zwei Antennen verwendet werden, und die Leistung an jenen Antennen summiert wird.

Acknowledgement

Research most of the time is real fulfilment, especially in a work environment as vital, socially active, and friendly as I was allowed to experience. This is especially true for the legendary 6th floor community, whom I all want to thank basically for sharing not just working time with me, but most importantly for being real friends: Arrate Alonso Gomez for cheering me up when I was not in perfect mood, Veronika Shivaldova for being a perfect travel companion and taking care of appointments and other things when I got too distraught. I thank Robert Dallinger for being the perfect \LaTeX and Matlab figure art guru often even overtaxing my nerd-level. Alex Paier was wisely managing the sixth floor during the first phase of my Ph.D and was a relaxed travel companion, too. Gerhard Schmid deserves thanks for sharing my technical curiosity and for endless discussions about almost every kind of engineering.

I deeply thank Robert Langwieser for being my mentor since my early days as a master student, not just scientifically but more important for organizational and practical matters. Lukas Mayer taught me the art of relaxed travelling, very important for conference trips, and I am grateful for his inspiration in the art of antenna measurement and design.

My two Telecommunist colleges Andreas Körner and Florian Xaver also deserve thanks. I share the time-consuming passion for teaching with them, and they became close friends during many years of indispensable fights about proper layout and notation of our created exams.

I thank David Löschenbrand for many inspiring discussions about near-field antenna measurements, and his alternative implementation of the near-field to far-field transform in Matlab.

Special thanks for proofreading this thesis appertain to Robert, Florian, and Carolina, whose valuable suggestions improved the readability of this thesis significantly. Carolina also deserves thanks for motivating me for sportive activities, especially biking to the University.

I want to thank my advisor Christoph for providing me almost unlimited freedom in choosing my research topic and supporting my education in all directions. His supporting faith in my abilities helped me to gain scientific self-assurance and enabled me to explore fields where I initially did not feel secure. I would like to express my gratitude to Zoya for her warm welcome in her group in Boulder, and for her valuable scientific support. I also thank Zoya for being my co-examiner and traveling to Vienna just for that purpose.

Finally, I am deeply grateful to my parents for wakening my curiosity and teaching me the value of ken as a small child. My sister Iris always supported me and is there whenever I need her, which is invaluable for me.

Contents

1	Introduction	1
1.1	RFID Link Budget Limitations	2
1.1.1	Forward Link Limit	2
1.1.2	Reverse Link Limit	2
1.2	RFID for Sensor Applications	4
1.3	Previous Art	4
1.4	Thesis organization	5
2	Reader Antennas for Sensor Applications	7
2.1	Vertically Polarized Antennas	7
2.1.1	Monopole Antenna	7
2.1.2	Low Profile Dual-band Loop	11
2.2	Steerable Horizontally Polarized Antennas	16
2.2.1	UHF Switched Beam Antenna	18
2.2.2	ISM Band Switched Beam Antenna	24
2.3	Frequency Selective Surface Shield	27
2.3.1	Frequency Selective Surface Design	28
2.3.2	SBA plus AMC Assembly Measurements	35
2.4	Summary	44
3	Leaking Carrier Cancellers	47
3.1	Hardware realization	47
3.2	Broadband Suppression Motivation	49
3.3	Single Tap Model	50
3.3.1	Measurement Setup	53
3.3.2	Suppression Performance	53
3.4	Multi Tap Model	55
3.4.1	Leakage Channel Measurement Setup	56
3.4.2	Broadband Leakage Canceller Evaluation	58
3.5	Cancellation Adjustment Techniques	60
3.5.1	LCC Adjustment principles	61
3.5.2	Noise Analysis	67
3.5.3	Measurements	73
3.5.4	Enhanced Procedures	80
3.6	Summary	82

4	Advanced Tyre Monitoring Systems	83
4.1	Channel Modelling	84
4.1.1	Uplink	85
4.1.2	Downlink	86
4.1.3	Fourier Series Truncation	87
4.1.4	Doppler Shift	87
4.2	Channel Simulations	88
4.2.1	Simulation Setup	88
4.2.2	Model without road surface	90
4.2.3	Model with road surface	92
4.3	Channel Measurements	93
4.3.1	Measurement Setup	94
4.3.2	Calibration and De-embedding	96
4.3.3	Measurement Results at the UHF Band	98
4.3.4	Measurement Results at the ISM Band	102
4.4	Link Budget Evaluation	103
4.4.1	Signal Combining Techniques	104
4.4.2	Statistical Analysis for Single Antenna Tags	105
4.4.3	Statistical Analysis for Dual Antenna Tags	108
4.4.4	Statistical Channel Description	109
4.5	Summary	110
5	Conclusion	113
A	Antenna Measurement System	115
A.1	Standard Measurement System	115
A.2	Cable-Less Measurement System	117
A.3	Used Coordinate Systems	117
A.4	Analysis of Measurement Impairments	118
A.4.1	Feed Cable Issues	120
A.4.2	Sphere Truncation	122
A.4.3	Orientation Comparison	124
A.5	MARS	127
A.6	Summary	129
B	Scale Drawings of the FSS Unit Cells	131
	Bibliography	135
	List of Abbreviations	144
	List of Figures	147
	List of Tables	152

Chapter 1

Introduction

Radio Frequency IDentification (RFID) is a technique to remotely identify and detect objects that carry a special transponder, called RFID tag [1]. RFID systems operate at several frequency bands, and use different methods to transfer data and energy between an RFID reader and the tags. Low-frequency systems that operate at 135 kHz, and high-frequency systems, which operate at 13.56 MHz, employ inductive coupling for communications between reader and tag. For this purpose both, the reader and the tag, carry an inductor. These inductors are coupled by the magnetic field and form a coreless transformer. Based on this operation principle, the range of inductively-coupled tags is low, typically a few tens of centimetres [2]. The situation is different for RFID systems operating at the Ultra High Frequency (UHF) (865 MHz to 915 MHz) or microwave Industrial, Scientific, Medical (ISM) 2.45 GHz bands: Here instead of inductive coupling electromagnetic waves are used for communication, and both, tag and reader carry an antenna [3]. Read ranges of several metres are obtained [2, 4].

In this work, I will focus on passive RFID systems operating at UHF or at 2.45 GHz, for which I will use the acronym ISM from now on. The word “passive” indicates that these RFID tags do not carry any power source. Instead, they are supplied by the electromagnetic field produced by the reader. This aids the construction of very inexpensive tags that only consist of a silicon Integrated Circuit (IC) and an antenna assembled on a support substrate, often made of paper or plastic. The communication link from the tag to the reader for passive tags is based on backscattering, a technique which relies on the fact that the amplitude and phase of the waves scattered from an antenna depend on its termination impedance. Thus, the tag chip sends data to the reader by modulating the impedance presented to the antenna terminals [5, 6]. While this backscattering technique enables remotely powered communication, it necessitates a constant Continuous Wave (CW) signal to be transmitted from the RFID reader during tag to reader data transfer [7, 2, 8]. This CW signal poses a challenge for RFID reader designs, since it interferes with the received backscattered tag-response and dominates the required dynamic range at the reader’s receiver. To reduce this dynamic range demand, Leaking Carrier Cancellers (LCCs) may be used. To cancel the interference, these devices inject a signal of opposite phase and equal amplitude at the receiver. Their influence on the receive Signal to Noise Ratio (SNR) is discussed in the next section.

1.1 RFID Link Budget Limitations

Passive RFID systems have two fundamental link limits corresponding to the required communication links: The forward link limitation describes the situation, when the received Radio Frequency (RF) power at the tag is too small to generate sufficient Direct Current (DC) power to supply the tag electronics. The reverse link limitation describes the effect when the received backscatter-modulated tag signal in comparison to the receiver noise is too weak to successfully decode the data [9, Chapter 2]. I will now formulate the two limits for a monostatic RFID system.

1.1.1 Forward Link Limit

The received RF power at the perfectly matched tag is given by

$$P_{\text{Tag}} = \frac{P_{\text{TX}} G_{\text{TRX}} G_{\text{Tag}}}{\text{FSPL}} = \frac{\text{EIRP} \cdot G_{\text{Tag}}}{\text{FSPL}}, \quad (1.1)$$

where P_{TX} is the reader transmit power, G_{TRX} is the gain of the reader antenna used for transmitting and receiving, G_{Tag} is the tag antenna gain, and the Free Space Loss (FSPL) describes the thinning of the transmit power due to the distance between reader and tag. Since the transmit Equivalent Isotropically Radiated Power (EIRP) is subject to legal limits¹, only the tag antenna gain is a means to increase the read range for a given tag with minimum received power. Quasi-omnidirectional tag antennas with low gains are usually used, since the orientation of tags is naturally unspecified, unpredictable, or changing. Therefore, the forward link limit for maximum read range or channel loss is solely defined by the technologically defined minimum required tag power $P_{\text{Tag}_{\text{min}}}$, which is called tag sensitivity.

1.1.2 Reverse Link Limit

The received power at the reader is given by:

$$P_{\text{RX}} = \frac{P_{\text{TX}} G_{\text{TRX}}^2}{\text{FSPL}^2} G_{\text{Tag}}^2 \eta_{\text{Mod}}, \quad (1.2)$$

where η_{Mod} is the modulation efficiency of the tag.

The minimum received power at the reader occurs for a tag operated at its sensitivity limit. In this case the maximum FSPL occurs:

$$\text{FSPL}_{\text{max}} = \frac{\text{EIRP}_{\text{TX}} G_{\text{Tag}}}{P_{\text{Tag}_{\text{min}}}}. \quad (1.3)$$

The received power for this case is computed by inserting (1.3) into (1.2) :

$$P_{\text{RX}_{\text{min}}} = \frac{G_{\text{TRX}}}{\text{EIRP}} P_{\text{Tag}_{\text{min}}}^2 \eta_{\text{Mod}}. \quad (1.4)$$

¹In Europe the maximum transmit Equivalent Radiated Power (ERP) of an RFID system is 2 W, which corresponds to an EIRP of 35.2 dB, using the gain of a half wave dipole $G_{\text{D}} \approx 2.2$ dBi.

We see that the minimum received signal power does not depend on the tag antenna, but depends quadratically on the tag sensitivity. It increases with decreasing reader EIRP, but this shifts the forward link limit towards shorter read distances. The modulation efficiency η_{Mod} does depend on the tag antenna matching [9, (2.14)] and the tag impedance shift which occurs during modulation.

The noise at the reader is composed of two parts. First, the thermal noise $N_{\text{th}} = kTB$, where k is the Boltzmann constant, enhanced by the receiver noise figure F , and the leaking transmit noise of the reader:

$$P_{\text{N}} = N_{\text{th}}F + \frac{P_{\text{TX}}}{\text{SNR}_{\text{TX}}IS \cdot G_{\text{I}}} = N_{\text{th}}F + \frac{\text{EIRP}_{\text{TX}}}{G_{\text{TRX}}\text{SNR}_{\text{TX}}IS \cdot G_{\text{I}}}, \quad (1.5)$$

where SNR_{TX} is the SNR of the transmitter, IS is the intrinsic Transmitter (TX)–Receiver (RX) isolation of the reader, and G_{I} is the isolation gain of an LCC optimized for broadband suppression, as will be discussed in Chapter 3. If no LCC is used $G_{\text{I}}=1$, if it is misadjusted or not optimized for broadband operation $G_{\text{I}}<1$.

The reverse link limit is defined by the necessary RX SNR at the reader, which is in turn defined by the selected symbol rate and coding scheme. This SNR is the quotient of (1.4) and (1.5). In (1.4) the only term which is neither technologically nor legally defined is the reader antenna gain. I therefore put much effort into designing directive reader antennas, which are adapted for the aimed application of an Advanced Tyre Monitoring System (ATMS). This work is presented in Chapter 2. Further, for a fixed EIRP, the second noise term of (1.5) is also decreased for increasing reader antenna gain.

In (1.5) leakage cancellation is of double importance: First, the receiver noise figure for any receiver incorporating an Automatic Gain Control (AGC) depends on the input power level. Since the leakage signal is usually the strongest received signal, the noise figure F depends on the LCC isolation gain. Second, the isolation gain directly enters the leaked transmit noise expressed in the second term. The physical limit set by thermal noise is reached for a perfectly adjusted LCC, so that the second term in (1.5) is negligible to the first one, which is then defined by the minimum noise figure of the reader since the AGC is at its maximum gain setting. That's why Chapter 3 is entirely devoted to LCCs and their efficient and fast adjustment.

Broadband leakage cancellation is necessary even for low-noise RFID readers to avoid reverse link limitation: To validate this claim, I present the following numerical example: When an European UHF RFID system operates at its legal power at $P_{\text{TX}} = 35.2$ dB using an omnidirectional (worst case) reader antenna and we assume the most sensitive RFID tag currently commercially available with a sensitivity of $P_{\text{Tag}_{\text{min}}} = -21.5$ dBm [10] connected to an omnidirectional antenna, using (1.3), we get a maximum allowed FSPL of 56.7 dB. Assuming a tag modulation efficiency $\eta_{\text{Mod}} = 10$ dB² we calculate the received power at the reader $P_{\text{RX}_{\text{min}}} = -88$ dBm. Using our RFID testbed frontend, the receiver noise figure is $F = 5$ dB [4, Table 2.1], and assuming a receiver bandwidth of 1 MHz the thermal noise is -109 dBm. Assuming a typical intrinsic TX–RX isolation of 20 dB, and

²the datasheet [10] of the picked tag chip does not specify any modulation efficiency, so I picked a typical value [9].

1 Introduction

no LCC, the transmit SNR needs to be 124.2 dB for the second term in (1.5) to be equal to the thermal noise level. This SNR value is practically inaccessible. If an LCC is used, a broadband isolation gain of 40 dB to 60 dB is achievable (see Section 3.3.2) lowering the demands on TX SNR to 84.2 dB to 64.2 dB which are achievable if a low noise transmit concept is used. Finally, assuming this equal noise contributions of the two terms in (1.5), we end up with a received SNR of $SNR_{RX} = -88 \text{ dBm} - -106 \text{ dBm} = 18 \text{ dB}$, which is sufficient to decode current RFID modulation formats with low symbol error probability. We see that in this example, without LCC the receiver noise is entirely dominated by the transmit SNR. The situation relaxes slightly if the reader antenna has gain larger than unity, but nevertheless broadband leakage cancellation and low-noise transmitter architectures are required to approach the physical noise limits at the reader. These purely theoretic analysis is validated by measurements presented in [11], which corroborates that the receiver SNR depends on the TX–RX isolation and LCC isolation gain.

1.2 RFID for Sensor Applications

Using RFID technology to create economical wireless sensor nodes is a promising idea [12, 13]. While there exist approaches to encode the sensor information using several unmodified tag chips and switches [14, 15], the most straightforward method is to use part of the memory bank of a modified tag to store the digitally encoded sensor information [16]. The sensor data is then retrieved by reading the data from the dedicated memory area using a standard RFID protocol, e.g. EPCglobal [17]. In this way, it is possible to retrieve the sensor data using any standard compliant RFID reader. This method of encoding additional information in the tag’s memory is already commercially available, e.g. the UCODE7 tags employ a memory area which contains information about the setting of a capacitor bank used to match the tag antenna impedance to the chip impedance [10].

While most parts of this thesis are relevant to any RFID-based sensors, Chapter 4 focuses on the automotive application ATMS. This system is an enhancement of state-of-the-art Tyre Pressure Monitoring System (TPMS). Additional sensor functionalities are enabled by placing the ATMS sensor directly at the tyre. This mounting position effectively bans batteries in the sensor nodes for mechanical reasons. The feasibility of a passive RFID-based ATMS is investigated in this thesis. I propose to use the tag memory area method to encode the sensor data which includes pressure, temperature and vibration. Additionally, the information stored in the standard RFID memory banks of the ATMS tags will provide valuable information about tyre manufacturer, type, speed index, and age of the tyre, which alone enable improvements of standard vehicular safety systems [18].

1.3 Previous Art

Naturally, I am not the first person to explore RFID-based vehicular sensor technology. Notable previous work includes my former college’s thesis [19], where she devotes a chapter

on tag antennas for ATMSs. Classical TPMSs are discussed in [20] which focuses on tyre classification and field simulations of 415 MHz TPMS. A master thesis, which aims on an RFID-based TPMS and focuses on a sensor node microcontroller implementation is presented in [21]. An excellent discussion about RFID tag-chip matching and a far-field measurement method for tag antennas is found in [9]. Important work on the ATMS principle of contact area detection based on vibration data is found in [22, 23]. Radiation measurements and evaluation of the electromagnetic properties of the steelbelt for an ATMS based on ISM band or ultra wide-band transmission were reported in [24, 25].

1.4 Thesis organization

My thesis is organized as follows: The second chapter following the introduction is devoted to reader antennas. First, vertically polarized antennas which utilize a ground-plane are presented, already aiming for an ATMS application. Then a horizontally polarized antenna system is presented, which is shielded from the body floor pan of a vehicle using an Frequency Selective Surface (FSS). The design and characterization of the FSS is also an important topic of Chapter 2. The antenna designs aim for both frequency bands, the UHF and the ISM band.

Chapter 3 treats the topic of leakage cancellation. A hardware realization is presented and single- and multi-tap models of leakage cancellation systems are derived and used to calculate the achievable suppression bandwidths. Finally, automatic adjustment routines of LCCs are discussed.

In Chapter 4, the automotive sensor application of ATMSs is analysed regarding channel characteristics and tag read probabilities. For these explorations, first a channel model is derived. Further, channel simulations and channel measurements at both frequency bands are compared. Finally, the channel measurement data is used to calculate read probabilities of RFID-based ATMS tags.

Chapter 5 presents concluding remarks and highlights the main achievements of this thesis.

In Appendix A, I describe the antenna measurement system used for the pattern measurements presented in chapters 2 and 4. I compare the results of different measurement methods of the Switched Beam Antenna (SBA) described in Section 2.2, to motivate the used Mathematical Absorber Reflection Suppression (MARS) method. This mathematical postprocessing of the measured Near-Field (NF) data is explained, which removes artefacts created in the chamber. Finally, Appendix B presents scale drawings of the developed FSS structures described in Chapter 3.

Chapter 2

Reader Antennas for Sensor Applications

In this chapter I address antennas specifically designed for Radio Frequency IDentification (RFID) reader applications. RFID systems in general are asymmetric regarding many technical aspects: Usually there are a few readers, mostly even just one, and many tags. Tags are cost optimized and therefore sophisticated antenna constructions are rarely seen. Readers, on the other hand, may use complex, intelligent, and maybe expensive antennas since they are not produced in extensive quantities.

This chapter targets compact dual-band antennas, referring to the European Ultra High Frequency (UHF) RFID band (865 MHz to 868 MHz) and the Industrial, Scientific, Medical (ISM) band at 2.45 GHz also used for RFID. The first section treats vertically polarized antennas, while the second one encompasses switched beam antennas. Special focus is given to the elevation angle and the compatibility with a mounting position on the body floor pan of a vehicle, because of the targeted Advanced Tyre Monitoring System (ATMS) application, which will be discussed in full detail in Chapter 4. Nevertheless, these antennas, especially the steerable kinds discussed in Section 2.2, are suitable for various applications outside ATMS for other sensor applications and standard RFID.

2.1 Vertically Polarized Antennas

Whenever an antenna is designed to operate close to a large metallic surface, those which use this surface as a reflector are a natural choice, e.g. a monopole antenna. This section describes the evolution from a simple monopole antenna to a dual-band monopole and finally to a very low profile dual-band antenna.

2.1.1 Monopole Antenna

In this section I present a modified monopole antenna which was designed for the dual-band channel measurements presented in Section 4.3, a picture of this antenna is found in Figure 4.13. The antenna design and the comparison with the low profile dual-band loop described in Section 2.1.2 were first published in [26].

The design goals of this antenna are high efficiency, low influence from a metallic mounting environment, simple construction and dual-band capabilities at both, the European

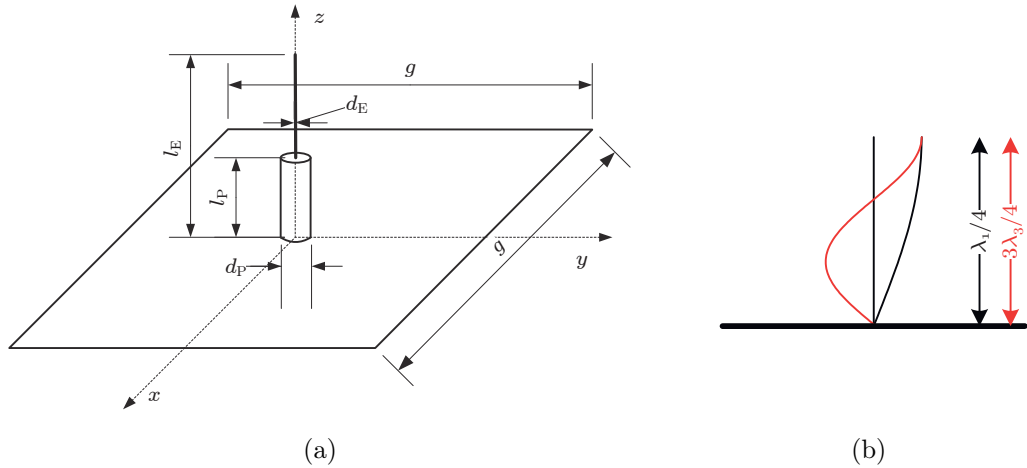


Figure 2.1: Illustration of the modified monopole: (a) Dimensional drawing; (b) Operational principle for dual-band operation. λ_1 is the wavelengths corresponding to the lower operational frequency, λ_3 is the wavelengths corresponding to the third harmonic.

UHF (865 MHz to 868 MHz) and the microwave RFID band (2.4 GHz to 2.5 GHz). Additionally, a low elevation angle is preferable for the targeted ATMS application, to beam the main lobe of the antenna towards the wheels.

Figure 2.1a displays a technical drawing of the monopole antenna, its mechanical parameters are summarized in Table 2.1. To reduce the effects of any uneven mounting structure, like a vehicular body floor pan, and ensure a low elevation angle, a rather large ground-plane with dimensions of 1.16 wavelengths λ manufactured from brass is used. The radiating element located in the centre of the ground-plane is comprised of a copper tube with an outer diameter of $d_E = 3$ mm. The radiating element is directly fed through a hole in the ground-plane with a semi-rigid coaxial cable of the RG-402 variety, which is terminated in a female SMA connector. The outer conductor of the coaxial feed cable is soldered to the backside of the ground-plane over the entire length to form an electrically and mechanically sound connection. This conventional monopole antenna was modified by placing a dielectric sleeve constructed from polymethylmethacrylate (PMMA) on the lower part of the radiating element. This dielectric loading electrically lengthens the radiating element, especially in regions bearing large electric fields. Due to the well known voltage distribution along a monopole [27], this dielectric loading close to the ground-plane does not severely affect the $\lambda_1/4$ -resonance of the monopole, as indicated in Figure 2.1b. However, the third harmonic is strongly affected due to the location of one voltage peak on the radiating element close to the ground-plane for $3\lambda_3/4$ -resonance. Based on this concept, the PMMA sleeve allows shifting of the natural third harmonic resonance at 2.6 GHz down to 2.45 GHz.

Table 2.1: Mechanical parameters of the modified monopole antenna.

Geometry Parameter	Variable	Value	Unit
Ground plane	g	40×40	cm
Element length	l_E	78	mm
Element diameter	d_E	3	mm
PMMA cylinder length	l_P	34	mm
PMMA cylinder diameter	d_P	10	mm

Simulation Results and Return Loss Measurements

Prior to actual implementation, the antenna was simulated in Ansoft's HFSS electromagnetic field simulator. The permittivity of the PMMA cylinder was set to $\epsilon_r = 2.6$ and its loss tangent was set to $\tan \delta = 0.008$, based on the results reported in [28], which were measured at 10 GHz. After fabrication of the antenna and measurement of the return loss with a Vector Network Analyser (VNA), the dielectric cylinder proved to be slightly too long, which was caused by underestimation of the permittivity of the PMMA at 2.45 GHz, and so it was shortened to the length stated in Table 2.1. The simulation was adapted by performing a parameter sweep of the dielectric constant of the PMMA cylinder using the actual antenna geometry parameters and picking the simulation value of $\epsilon_r = 3$ where simulated and measured return loss peaks of the $3\lambda/4$ -resonance coincide in frequency. A comparison between the resulting simulated and measured return losses is plotted in Figure 2.8. The antenna achieves a very good return loss. From 856 MHz to 885 MHz, it provides higher values than 14 dB. In the 2.4 GHz to 2.5 GHz range, the obtained 8 dB return loss is acceptable. The simulated radiation efficiency including material losses is found to be 99 % at the lower band and 100 % at 2.45 GHz. By including the matching losses the overall efficiency is calculated to be 93 % and 86 % at 2.45 GHz, respectively.

Anechoic Chamber Measurement Results

The antenna is placed in our anechoic chamber and a near field measurement is performed. For more information regarding the antenna measurement system, see Appendix A. The near field data is transformed to far-field data and probe correction for the used dual ridged horn is applied. A pseudo-colour plot of the gain pattern corresponding to E_θ is shown in Figure 2.2, using the coordinate system as drawn in Figure 2.1a. This plot, as well as all following pattern plots is normalized to the global peak of the antenna being $1 = 0$ dB. The antenna exhibits an almost omnidirectional pattern in azimuth, as expected for a monopole. However, due to the square shaped ground-plane, four lobes pointing in the direction of the edges of the ground-plane appear. These lobes are also identified in the azimuth radiation pattern in Figure 2.3a. If the antenna is mounted almost flush with the vehicle body floor pan as presented in Figure 4.13, we expect this effect to be minimized due to the additional extension of the ground-plane by the metallic environment. However, when mounting the antenna slightly lower, this

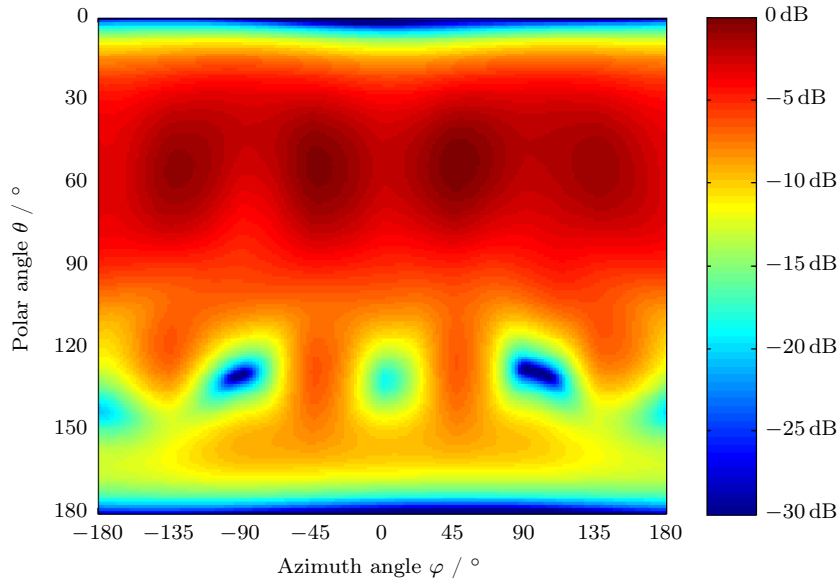


Figure 2.2: Logarithmically scaled pseudo-color plot of the gain pattern of the modified monopole antenna corresponding to E_θ at 866 MHz.

beam-effect may be utilized by shaping the ground-plane according to the tyre and reader antenna positions.

An additional noticeable effect is a slight concentration of the radiated energy towards small azimuth angles. This is caused by the coaxial feed cable which is protruding from the ground-plane on the x -axis, acting as a counterpoise for the radiating element similar as the corners of the ground-plane. Again, this effect will be minimized in mounting scenarios like the vehicle body floor pan shown in Figure 4.13.

The azimuth radiation pattern for $\theta = 90^\circ$ and the polar angle of the main lobe $\theta = 54^\circ$ is plotted in Figure 2.3a. The dependency on the polar angle is plotted in Figure 2.3b. For all azimuth angles the main beam elevation angle stays almost constant at 36° , but the beam is relatively broad in elevation so that for zero elevation ($\theta = 90^\circ$) the power is reduced by only 5 dB. The directivity calculated from the measurement results is found to be 4.3 dB.

At 2.45 GHz the elevation angle gets higher, but a sidelobe at a low elevation angle of 15° appears. This is observable in the pseudo-colour plot in Figure 2.4, and the polar plot in Figure 2.5. Due to the smaller wavelength, the ground-plane at this band is electrically approximately three times larger than in the lower band, and therefore the power concentration towards the ground-plane edges is negligible, see Figure 2.4. Compared to the lower frequency pattern, the radiated power is more concentrated in θ and the directivity at 2.45 GHz is 6.7 dB.

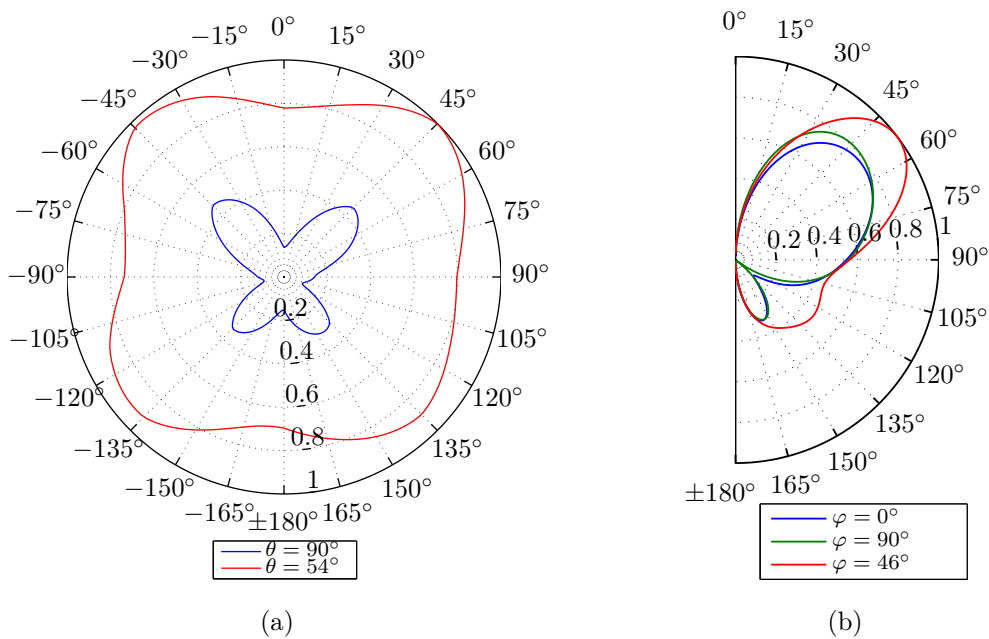


Figure 2.3: Radiation pattern of the modified monopole antenna at 866 MHz in (a) Azimuth and (b) polar angle, plotted for three φ -cuts.

2.1.2 Low Profile Dual-band Loop

While the modified monopole presented in Section 2.1.1 is an electrically perfect solution for an omnidirectional vehicular body floor pan antenna for ATMS, it is unsuitable for practical implementation due to its mechanical dimensions. A well known candidate for a vertical polarized omnidirectional antenna is the Directly Driven Resonant Radiator (DDRR) described in [29, 30]. The DDRR's antenna principle is based on a very short vertical radiator, which is top-loaded with a loop shaped transmission line to achieve impedance matching. While in both publications, the end of the transmission line terminates in a tuning capacitor, our approach is to omit this capacitor, similar to the design proposed in [31, Figure 2]. This is in principle nothing more than a curled up planar inverted F antenna, which was proposed by [32, 33, 34] and is very popular for cellular phones. In contrast to [29, 30, 31], the proposed Low-Profile Dual-band Loop (LPDL) is operational at two frequencies, where the second resonance frequency is achieved by a capacity coupled shortening structure in the loop centre.

The proposed LPDL antenna, as shown in Figure 2.6, has the same brass ground-plane dimensions as the modified monopole antenna, but its height is dramatically reduced to 6.5 mm. The vertical radiator is directly constructed from the centre conductor of the feeding coaxial cable, which is a silver plated steel wire. Since this short wire is the main source of radiation of the LPDL and this is a low impedance point of the antenna, a material with low surface resistance is required for high efficiency of the antenna. The silver coating of the used cable achieves this, as there is no significant current flow in the steel core due to the skin effect [35]. The resonant loop structure is manufactured as

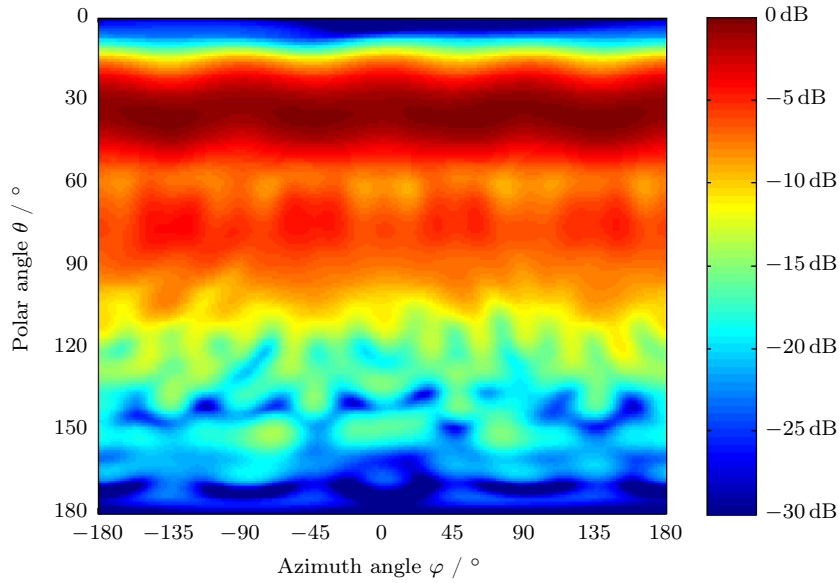


Figure 2.4: Logarithmically scaled pseudo-color plot of the gain pattern of the modified monopole antenna at 2.45 GHz for vertical polarisation.

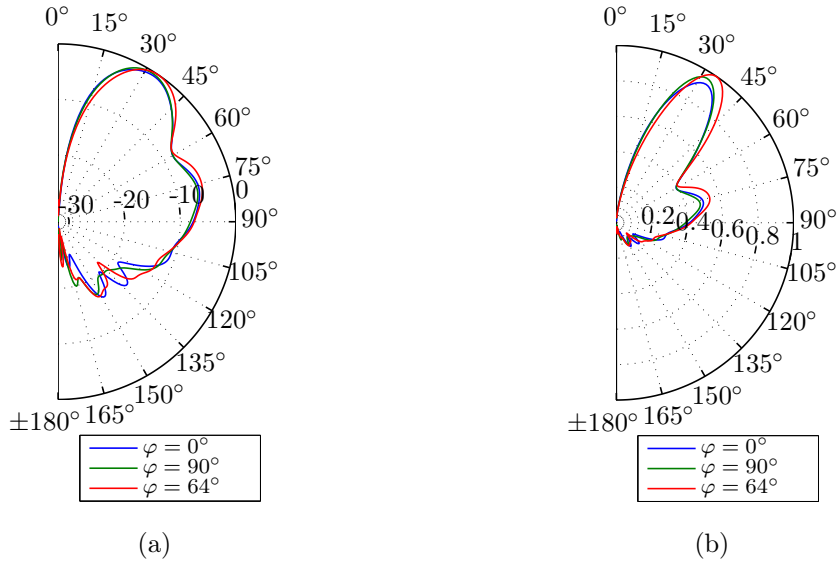


Figure 2.5: Radiation pattern of the modified monopole antenna in polar angle at 2.45 GHz, plotted logarithmically (a) and linear (b) for three φ -cuts.

copper trace on a single-sided FR-4 Printed Circuit Board (PCB). This PCB is mounted 5 mm above the ground-plane using four screws and spacers, both manufactured from Nylon. Adding the PCB thickness of 1.5 mm the loop is elevated 6.5 mm ($\approx 0.019 \lambda$) above the ground-plane. The vertical radiator is soldered to the copper trace on top of the PCB, as well as three silver plated copper wires which serve as ground connection for



Figure 2.6: Image showing the LPDL antenna (a), and close-ups of the vertical feed (b), and the PCB (c).

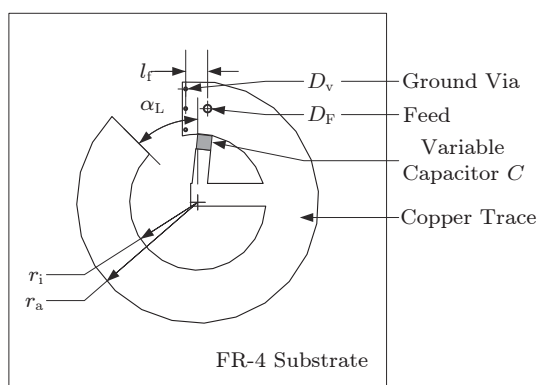


Figure 2.7: Dimensional drawing of the LPDL antenna PCB on a scale of 1:1.

the resonator. This feeding is similar to an inverted-F antenna, except that the stub of the inverted-F is coiled up in a loop. Details are given in Figure 2.7 and Table 2.2. To reach resonance at 2.45 GHz, an additional shortening structure inside the loop is used, which is coupled to the feed by means of a small variable capacitor C . This capacitor is adjustable between 0.55 pF and 1 pF and was tuned for best matching at 2.45 GHz by means of a VNA.

Simulation Results and Measured Return Loss

The LPDL antenna was again simulated in HFSS. This time, after some optimizations using the VNA, the actual geometry as described in Table 2.2 was entered into the simulation environment and a parameter sweep over the capacitance C was conducted. Best agreement at the 2.45 GHz resonance peak was found for $C = 0.6$ pF, this result is also depicted in Figure 2.8. The agreement at the lower frequency resonance is not perfect, which is most likely caused by the permittivity of the PCB material, which is not well defined for FR-4.

Both, measured and simulated antenna return losses of the LPDL presented in Figure 2.8 show the typical drawback of resonant compact antennas — their bandwidth

Table 2.2: Mechanical parameters of LPDL antenna.

Geometry Parameter	variable	Value	Unit
Ground plane	g	40×40	cm
FR-4 Substrate dimensions		$50 \times 50 \times 1.5$	mm
Substrate-ground-plane separation	h	5	mm
Feed distance	l_f	2.8	mm
Feed diameter	D_F	0.9	mm
Ground via diameter	D_v	0.5	mm
Inner loop radius	r_i	9	mm
Outer loop radius	r_a	16	mm
Loop opening angle	α_L	45°	

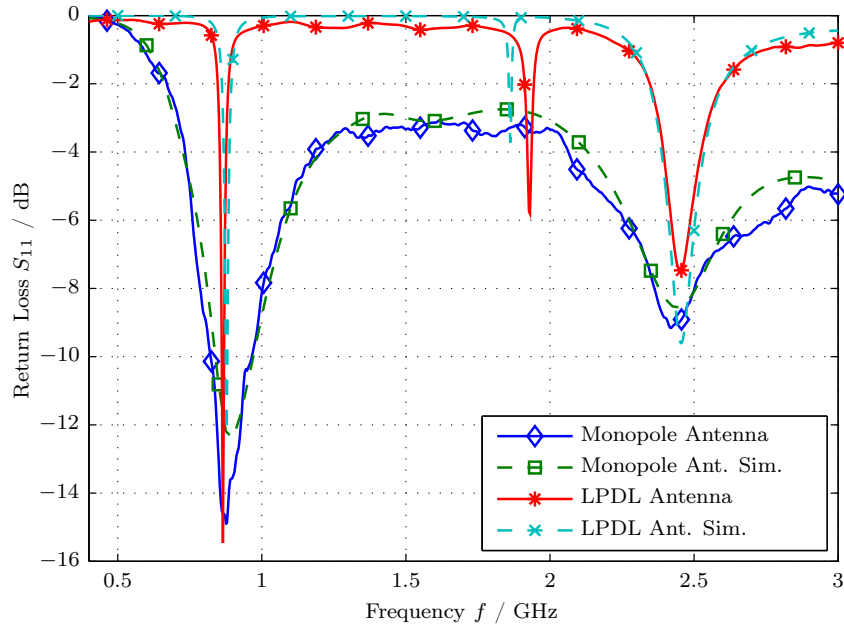


Figure 2.8: Comparison of antenna return losses of both antennas, both measured and simulated.

is small if the losses are not dominating. However, measurements of the return loss of the manufactured LPDL antenna show that the RFID band is still very well matched. In fact the 10 dB bandwidth ranges from 861 MHz to 869 MHz.¹

The measured matching at the upper band is slightly degraded when compared to the simulations. The measured 6 dB return loss bandwidth is ranging from 2.42 GHz to 2.49 GHz.

¹For actual vehicular implementation the antenna has to be covered in a radome to prevent detuning caused by accumulations of dirt. Especially, since this resonance is so narrow-banded.

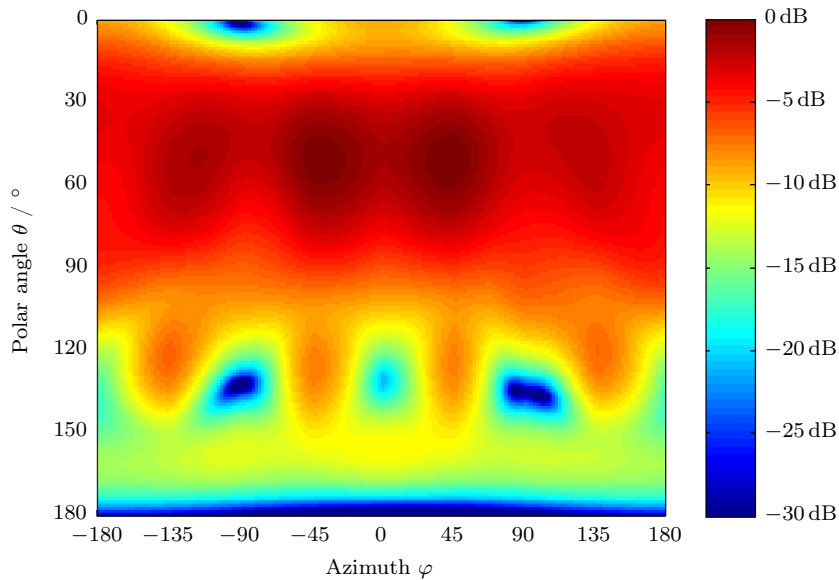


Figure 2.9: Logarithmically scaled pseudo-color plot of the gain pattern of the LPDL antenna at 866 MHz for vertical polarisation.

Anechoic Chamber Measurement Results

The LPDL antenna was measured in the same test range and directly after the modified monopole antenna to enable direct comparison and relative efficiency measurements. The overall relative efficiency of the LPDL antenna including matching losses, when compared to the modified monopole, was found to be 37 % in the UHF band and 68 % at the 2.45 GHz microwave band.

The radiation pattern at 866 MHz is shown in the pseudo-colour plot in Figure 2.9. Despite the dramatically shortened vertical radiator, the radiation pattern resembles the one of the resonant monopole depicted in Figure 2.2. The same is true for the dependency in the polar angle θ , when Figure 2.10a and Figure 2.3 are compared. Therefore, it is not surprising, that the measured directivity value of 4.6 dB is very alike for both, the LPDL and the monopole antennas. The elevation angle is slightly increased to 39°, but at $\theta = 90^\circ$ the radiation intensity is still 5 dB down.

At the upper band the antenna parameters change more significantly, because parts of the loop act as a horizontal radiator. Figure 2.10c and Figure 2.11 show a forked beam in θ , with one part being elevated 83° ($\theta = 7^\circ$) and a second one at $\theta = 48^\circ$ corresponding to an elevation of 42°. While the former lobe is not very beneficial for the proposed vehicular ATMS application, the later lobe has a lower elevation than the main lobe of the modified monopole, as depicted in Figure 2.5. According to Figure 2.10b the high elevated beam at $\theta = 7^\circ$ shows an almost dipole-like radiation pattern which is caused by the radiation of the inner shortening structure of the LPDL. While the weak beam at $\theta = 90^\circ$ is almost perfectly omnidirectional, the slightly elevated beam beneficial for the proposed ATMS application is slightly elliptically shaped. The directivity from the

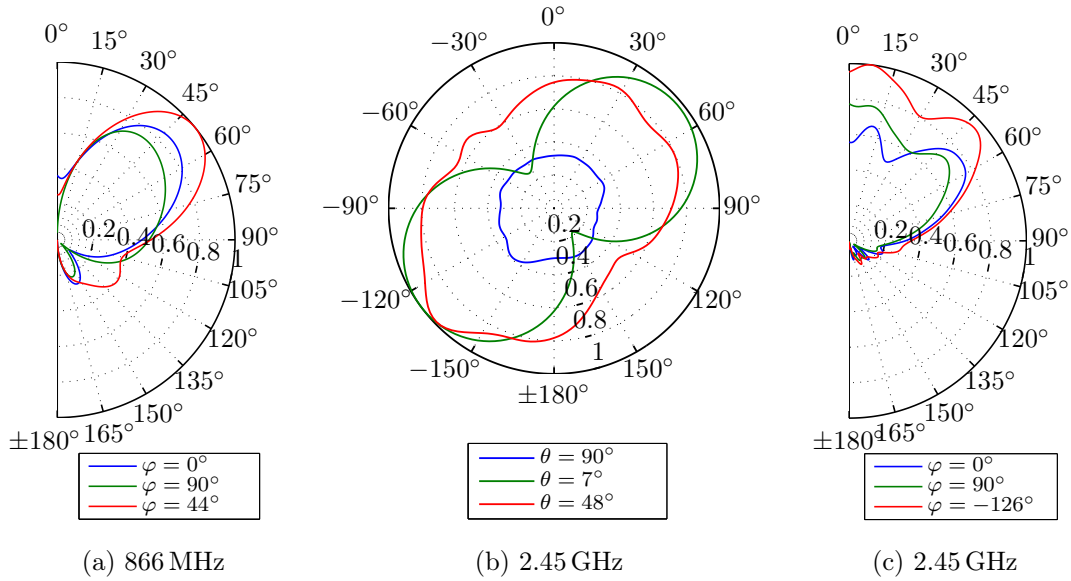


Figure 2.10: Radiation pattern of the LPDL antenna: (a) at 866 MHz, plotted for three φ -cuts; at 2.45 GHz: (b) plotted over azimuth φ , (c) and over polar angle θ for three cuts.

measurement results operating at this frequency was reckoned at 5.5 dB. This is slightly lower than that provided by the monopole, which does not show any forked beams.

2.2 Steerable Horizontally Polarized Antennas

In contrast to vertically polarized antennas, those horizontally polarized are not directly favoured by the environment of a close horizontal metallic object (like the body floor pan of a vehicle). The horizontal antenna elements are detuned due to the close conductor, and the overall efficiency and radiation pattern is degraded. Further details are provided in Section 2.3. Compact antennas with beam steering capabilities are realizable for horizontal polarization. Section 2.3 elaborates on how the negative effects of the close metallic object are handled by means of an Frequency Selective Surface (FSS).

In this section I will discuss two variants of a compact antenna which are able to produce four different beams under good matching conditions and six additional different beams with suboptimal matching. The antenna is useful for many applications where an RFID reader aims to detect only tags in a sector of the given measurement environment. Sectorizing a given volume containing RFID tags speeds up the read process based on less collisions, which need to be handled in the Medium Access Control (MAC) layer [36, 37]. Additionally, such an antenna provides a rough, simple localization function, when paired with a suitable low transmit power of the reader, such that only tags in the corresponding sectors are activated by the reader signal.

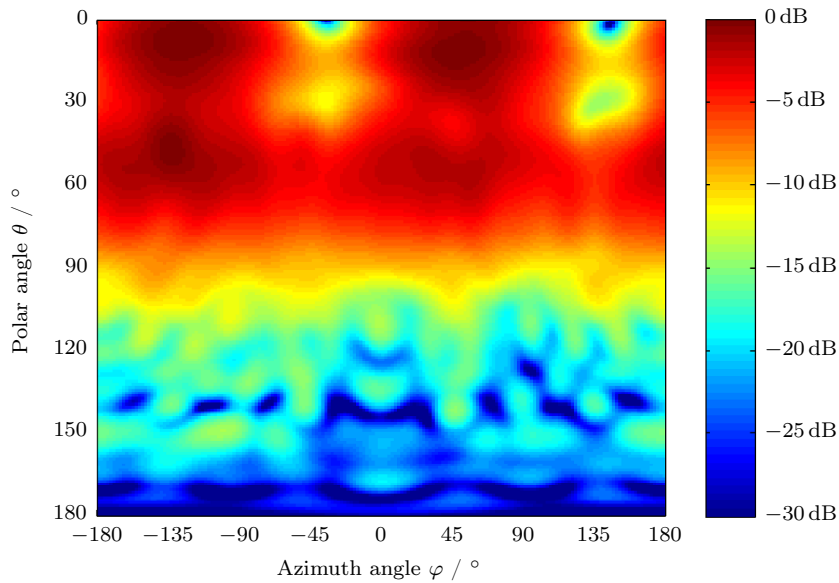


Figure 2.11: Logarithmically scaled pseudo-color plot of the gain pattern of the LPDL antenna at 2.45 GHz for vertical polarisation.

If we accept the prerequisite that an FSS compensates for the negative effects of the close body floor pan of a vehicle, both functionalities are also very fruitful for ATMS applications: When mounted below a car body floor pan the switched main beam of such an antenna points at one of the four wheels. This provides higher field strength at the wheel sensor which is selected for communication, while at the same time the field strengths at the other wheels is reduced. Due to the antenna directivity, a part of the large channel losses present in RFID Tyre Pressure Monitoring System (TPMS) systems is compensated for a selected wheel. Therefore, the sensitivity requirements of the RFID-based wheel sensor can be relaxed. When properly adjusted, the transmit signal will only be sufficient to power the sensor in the wheel that is currently selected by the antenna beam. This eliminates the need to identify the wheel sensor by an identification code, which has to be entered in the vehicular electronics memory manually in current systems. Therefore, when changing tyres, the vehicle automatically learns which sensor corresponds to which wheel. Many steerable antennas are found in literature, however most entries deal with phased arrays which are large antenna structures with respect to the wavelength, exceptions being [38, 39, 40, 41].

Both variants of the developed Switched Beam Antenna (SBA) are constructed on a PCB which carries four dipoles with balanced, centrally shorted lines on one side, and the feeding network on the other side, as displayed in Figure 2.12. In normal operation, only one dipole is driven by the feeding network, while the other three are deactivated by shortening their feed lines with PIN diodes. Since the transmission line between the central connection point to the coaxial connector and PIN diodes is a quarter wavelength long, the short circuits transform into an open at the central feed point. This means, that the active dipole element and its feed line alone contribute to the input impedance

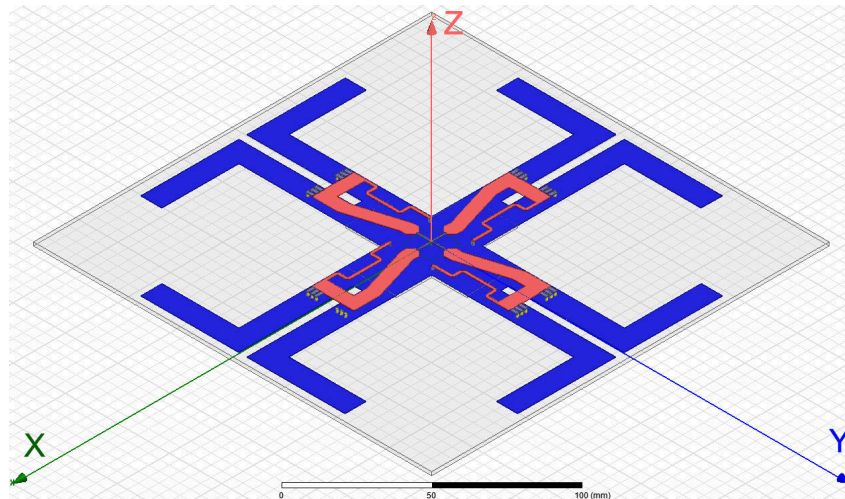


Figure 2.12: Antenna geometry of the UHF-SBA for simulation showing feeding side in red and dipole side in blue.

of the antenna. The directivity of the antenna is based on the fact that the balanced lines connecting the neighbouring deactivated dipoles act as a reflector for the driven element.

2.2.1 UHF Switched Beam Antenna

The version of the SBA designed for the UHF RFID band ranging from 865 MHz to 868 MHz was initially published in [42]. The proposed design is based on four dipoles arranged in a geometry similar to a Jerusalem cross², as shown in Figure 2.12. It is constructed on a PCB of FR-4 material with dimensions $190 \text{ mm} \times 190 \text{ mm}$ or $0.55 \lambda \times 0.55 \lambda$ and a thickness of 1.5 mm. The bottom side of the PCB contains the four dipoles which are each connected by a balanced line that leads to the antenna centre and terminates in a short circuit. These balanced lines form the plus shaped part of the Jerusalem cross.

When selecting a specific beam, only one dipole element is fed, and the neighbouring cross arms act as passive reflectors. The top side of the PCB incorporates the feeding network, consisting of two quarter-wavelength lines per element, which are shown in red in Figure 2.12. A detailed representation of the feeding network including discrete components is given in Figure 2.13. A low impedance microstrip line feeds each dipole. Blocking capacitors C1F-C4F and C1A-C4C disconnect the Direct Current (DC) paths used to control the beam-switching. A second line brings the control signal to the re-

²A more exact description for this widely used geometry in antenna and FSS design would be cross potent or crutch cross, since a Jerusalem cross classically also contains four additional small crosses. However, the name crutch cross bears a stigma similar to the swastika, since it was used in the time of Austrofascism between 1934–1938 and had been the icon of the “Vaterländische Front”, the fascist single political party lead by Engelbert Dollfuß [43]. I usually try to use the most suitable terms to describe technical details, but since the strictly speaking wrong term Jerusalem cross is already widely coined in literature [44, 45] and I do not want to give the wrong impression of having sympathy for the Austrofascism, I stick to the common term Jerusalem cross.

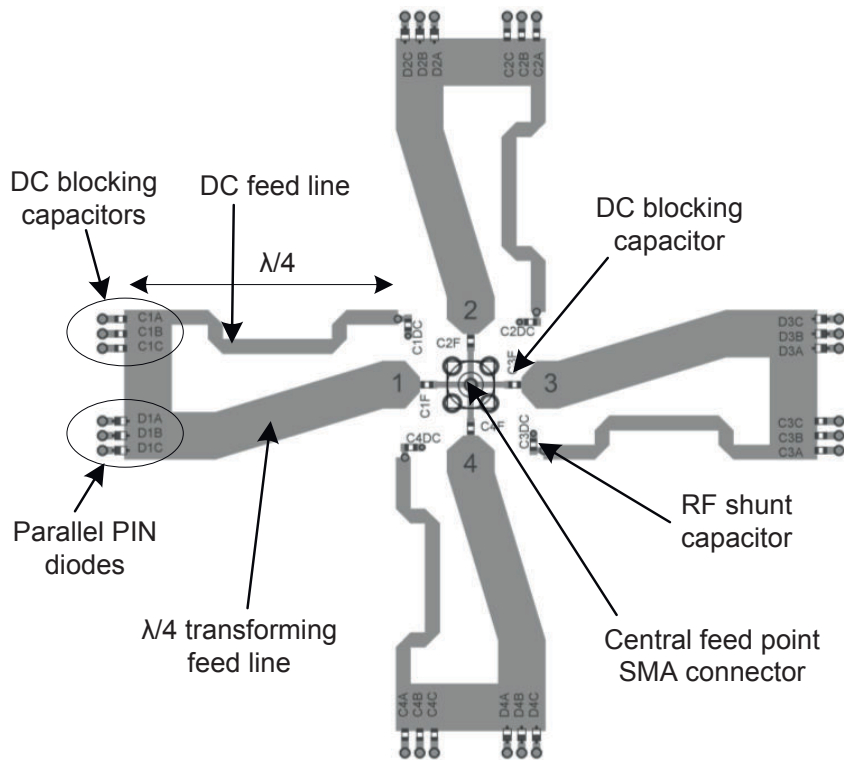


Figure 2.13: Feeding network of the UHF-SBA including discrete components.

spective switching diodes. These quarter-wavelength biasing lines are short-circuited for Radio Frequency (RF)-signals with the capacitors C1DC-C4DC.

Beam switching is done by means of PIN diodes D1A-D4C located at the end of the quarter-wavelength feed lines — The electrical lengths of the sum of the low impedance microstrip line and the short high impedance line connecting the DC blocking capacitor to the central feed point is a quarter wavelengths. Since the end of the $\lambda/4$ feed line is a low impedance point, three PIN diodes are put in parallel to create an appropriate low inductive short.

When selecting one beam the respective dipole element is activated by reverse biasing the corresponding PIN diodes. The three other elements are deactivated by conducting diodes. The quarter-wave feed lines of the deactivated arms thus present a high impedance point to the antenna centre where the coaxial cable is attached by an SMA connector. In contrast, the feed line of the active element transforms the impedance at the dipole feed point into 50Ω at the antenna centre. This provides that the power is directed only into the active dipole element. Additionally, the short circuited balanced line directly running to the dipole elements, and the quarter wavelength low impedance feed line act as a balun to ensure a symmetric feeding of the dipole elements. Note that the dipole elements are shorter than a half wavelengths, meaning that the shorted balanced line is likewise required to compensate for the dipole element's reactance.

Figure 2.14 presents simulation results in Ansoft's HFSS field simulator. The surface current density is plotted over the back side of the antenna, where currents induced by

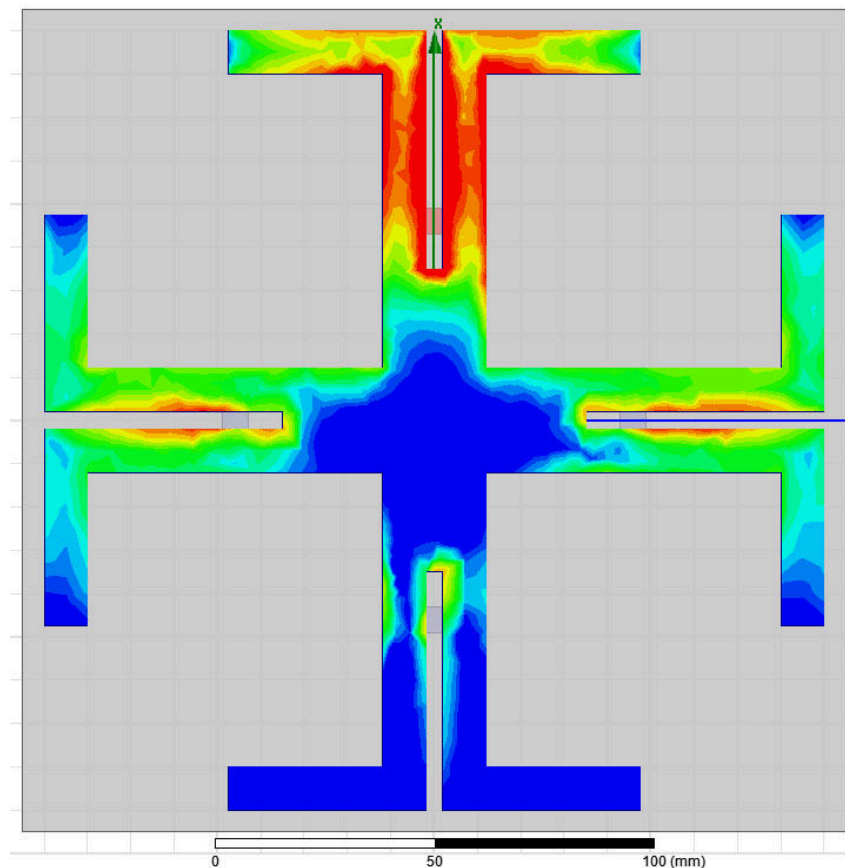


Figure 2.14: Simulated surface currents on bottom side of the dipole layer at 866 MHz for the UHF-SBA to illustrate the principle of directivity. Strong surface currents appear in red, weak currents in blue.

the feeding network do not appear. The top dipole element is radiating, while the other elements are short-circuited with their corresponding pin diodes. Red areas indicate high current densities, while blue areas indicate low densities. Besides the radiating dipole itself and its respective parallel balancing line, there are also noticeable currents on the balancing lines of the two dipoles which are oriented orthogonal to the radiating element. These lines and especially the slots of the unused orthogonal dipole balancing lines act as parasitic elements for the radiating dipole and contribute to the directivity of the antenna.

An additional cross shaped PCB in the centre of the antenna depicted in the image of the manufactured antenna in Figure 2.15. performs the level conversion from logic control signals to PIN-diode currents. Due to its position at the centre of the antenna where surface currents are low, this additional PCB does not affect the antenna parameters.

Measurement Results

After assembly of the antenna, the return loss was measured using a VNA. The current through a single PIN-diode was chosen to be 6.4 mA, in the non conducting state the

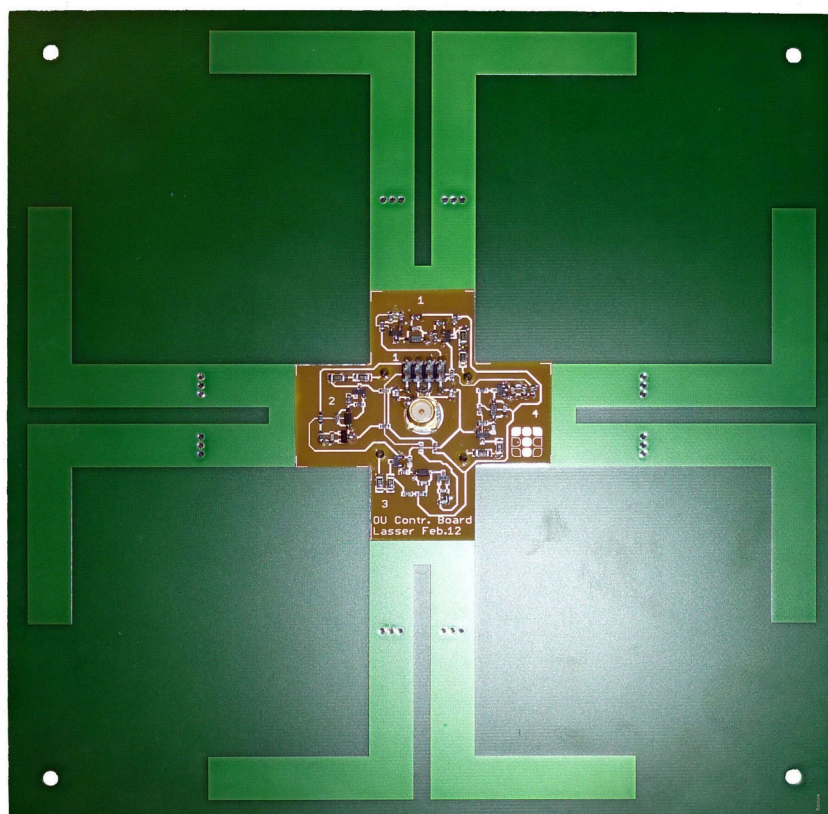


Figure 2.15: Picture of the manufactured UHF-SBA showing radiating elements and PIN-diode control circuitry.

diodes are reverse biased by 12 V. Figure 2.16 shows the results of the return loss of the antenna for various different beam settings and combinations. It is observable that the four beams behave very similar, which is of no surprise due to the symmetric design of the antenna. When no beam is selected, all diodes are forward biased and thus resemble short-circuits, which are transformed into a high impedance state at the central feed point by the quarter-wavelength transformers. Consequently, the return loss is low. The losses of the diodes and some parasitic radiation of the quarter-wave feed lines cause a return loss of some 4 dB. The 10 dB return loss frequency band of the antenna ranges from 824 MHz to 868 MHz, which is almost the same bandwidth but lower central frequency than the original design goals. This shift in frequency and slight reduction in bandwidth is most likely caused by the circuit board material (fiberglass reinforced substrate — FR-4), which happens to have a higher permittivity than that assumed in simulations. Additionally, the return loss for multi beam operation was measured, Figure 2.16 showing the example for beams I and II activated. Note that for this configuration the best return loss is decreased to 12 dB in the operating band. This is still higher than the theoretic return loss for two $50\ \Omega$ loads in parallel, which is 9.54 dB. The reason for this is the reactive coupling between the SBA dipole elements I and II, so the input impedance of the SBA switched to these two beams simultaneously is not just the simple parallel circuit

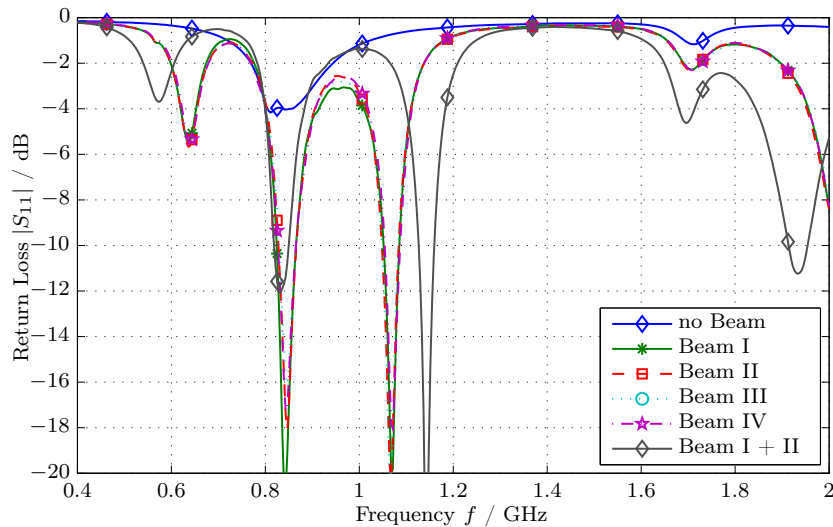


Figure 2.16: Measured SBA return loss for different beam settings.

of the input impedance of the individual antenna impedances when beams I and II are selected individually.

To evaluate the influence of possible non linear behaviour of the PIN-diodes on the return loss, a power sweep ranging from -7 dBm to 33 dBm is performed. The measured variation of the return loss is much smaller than the linearity of the measurement setup containing a VNA, specified for ± 0.1 dB linearity.

The antenna was placed in an anechoic chamber and near-field antenna measurements were performed for several beam settings. The directivity of the antenna for a single beam is measured to be $D_I = 4.7$ dB at 865 MHz³. The gain pattern of this antenna is plotted in Figure 2.17. It is based on the coordinate system shown in Figure 2.12, and beam I pointing in y direction was selected, creating a peak at $\varphi = 90^\circ$. Switching to different beams produces peaks at $\varphi = 0^\circ, 90^\circ, 180^\circ, 270^\circ$ without changing the gain pattern in the polar angle θ , as shown in the top three plots of Figure 2.18 and in the azimuth radiation pattern in Figure 2.19a. By activating two beam settings simultaneously, the lower three gain plots of Figure 2.18 were created. Note that the bidirectional setting for beam I + III creates a more directive pattern ($D_{I+III} = 4.8$ dB) with small sidelobes in the orthogonal direction. This is also very well indicated in the corresponding azimuth radiation pattern in Figure 2.19b. The activation of two neighbour beams also leads to a useful pattern, also seen in the mentioned plots. It has its peak between the peaks of the selected beams, so for example switching on beams I and II simultaneously leads to a peak at $\varphi = 45^\circ$. The pattern shows relatively strong radiation into the whole half sphere with a directivity of 4.0 dB but a better front to back ratio than the single standard beam.

Therefore, besides the steering capabilities into the four quadrants the antenna enables four additional beams which double the localization capabilities of the SBA, and two

³This result and the gain patterns presented in Figure 2.17 and Figure 2.18 was obtained using Mathematical Absorber Reflection Suppression (MARS) [46]. More information regarding the antenna measurement system is given in Appendix A.

2.2 Steerable Horizontally Polarized Antennas

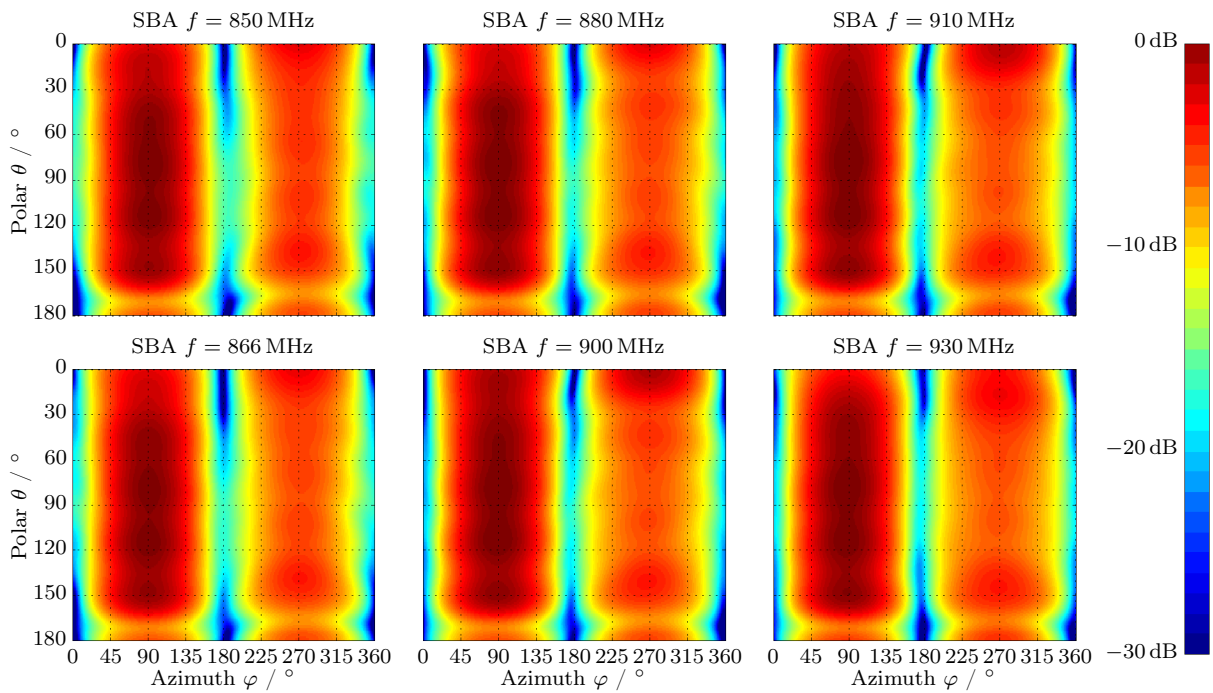


Figure 2.17: Comparison of normalized gainplots for the UHF-SBA in free space for different frequencies f ; plotted for beam I pointing in y -direction.

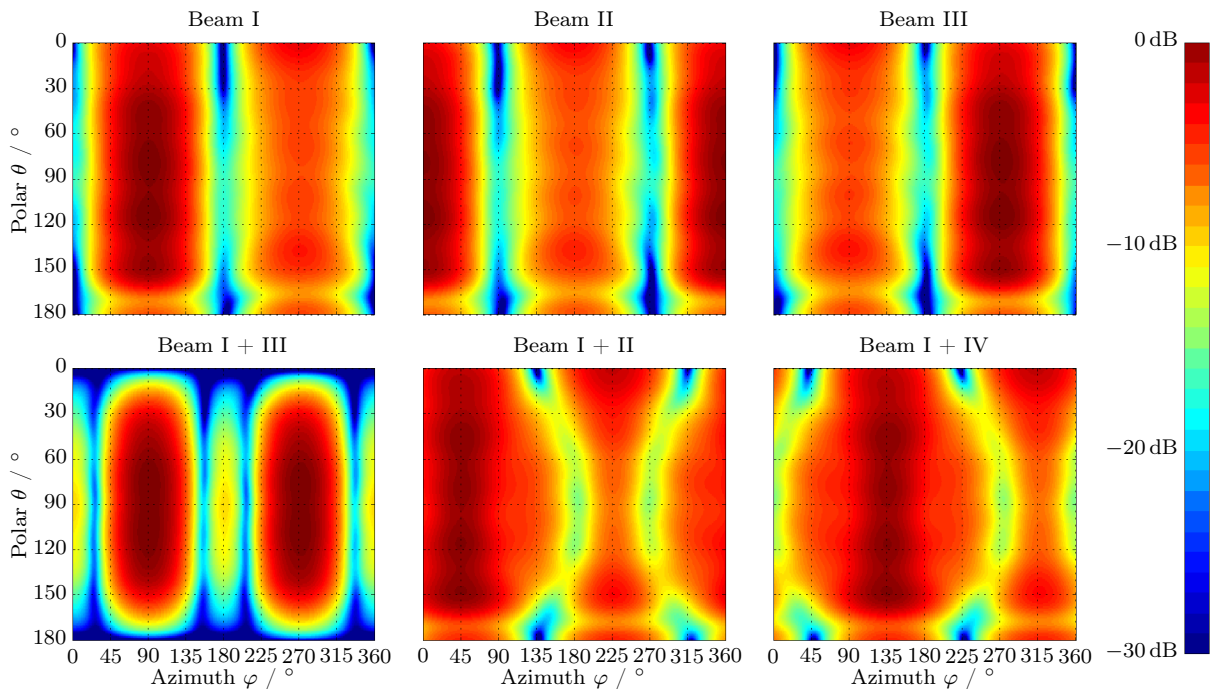


Figure 2.18: Comparison of normalized gainplots for the UHF-SBA at 866 MHz in free space for different activated beams.

additional beams which enable bidirectional operation. These features makes the SBA also a very interesting antenna for large warehouse scenarios, where it could be mounted in the centre and would enable faster inventory times while additionally providing rough localization.

The pattern variation of the SBA for different frequencies is low, as depicted in the gain plots in Figure 2.17 and the polar radiation pattern in Figure 2.20. The radiation pattern indicates that the peak is not exactly at $\theta = 90^\circ$ but rather at $\theta = 80^\circ$. In fact, this is just an effect seen on this particular measurement, others show more ripple in theta and the peak at different positions. The presented measurement is the cleanest one that is obtainable in this antenna orientation using the Near-Field (NF) antenna measurement facility of the Vienna University of Technology. Additionally, the sector $\theta > 160^\circ$ is not plotted here, since the Far-Field (FF) data is not correct due to truncation of the NF in this area. More details of the measurement system are given in Appendix A.

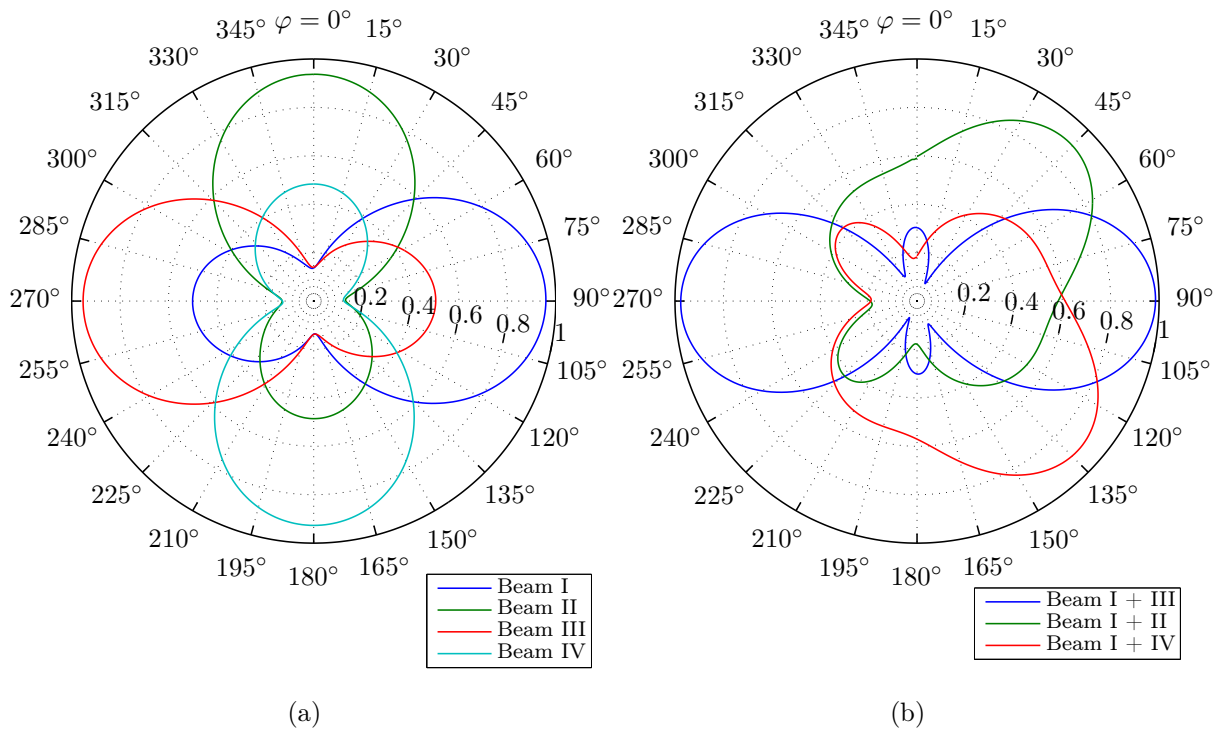


Figure 2.19: Azimuth radiation pattern of the UHF-SBA at $f = 865$ MHz, $\theta = 90^\circ$:
 (a) For normal operation switching through beams I – IV; (b) For beam combinations.

2.2.2 ISM Band Switched Beam Antenna

The principle of the antenna operation for the 2.45 GHz variant is the same, but the feeding network is different. Figure 2.21 shows the feedside of the antenna at a scale of 1:1, the dipole layer is seen through the FR-4 PCB with dimensions $70 \text{ mm} \times 70 \text{ mm} \times 0.8 \text{ mm}$.

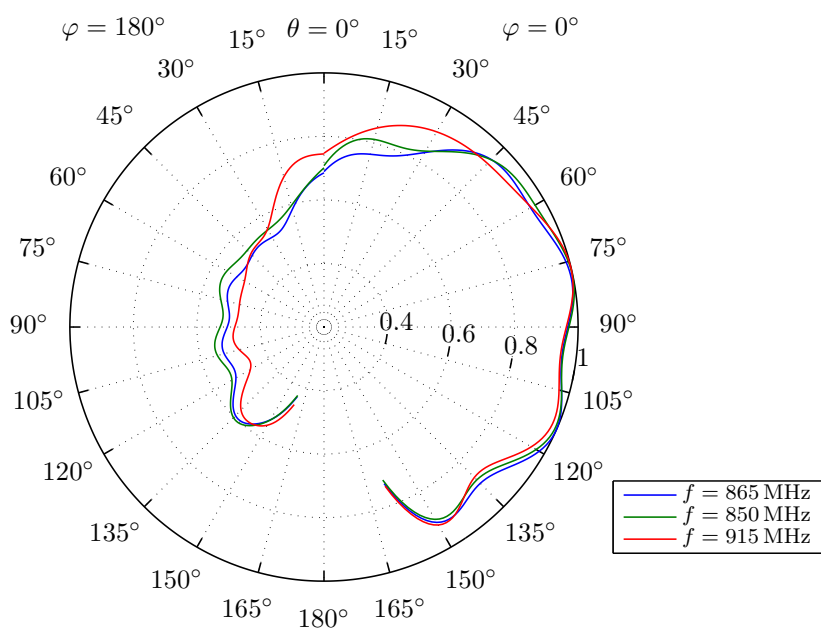


Figure 2.20: Polar radiation pattern for beam I at different frequencies f .

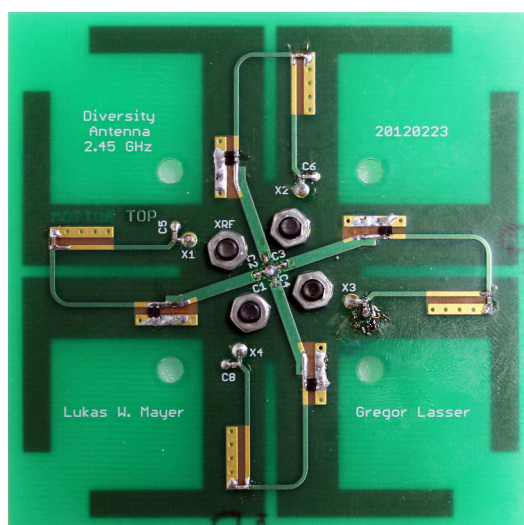


Figure 2.21: Picture of the manufactured ISM-SBA looking at the feed side printed up to scale. The dipole side can be seen through the semitransparent FR-4 printed surface board material. The four screws attach a standard SMA flange from the opposite side to the antenna PCB.

The first section of transmission line from the central feeding SMA connector to the PIN diodes is a $50\ \Omega$ line so no impedance transformation takes place here. Two parallel PIN diodes short three of the four arms for normal operation. From this point, a high impedance line, again $\lambda/4$ in length, runs to one arm of the dipole. Its high impedance matches the dipole feed point to the previous $50\ \Omega$ line. The balanced lines connected

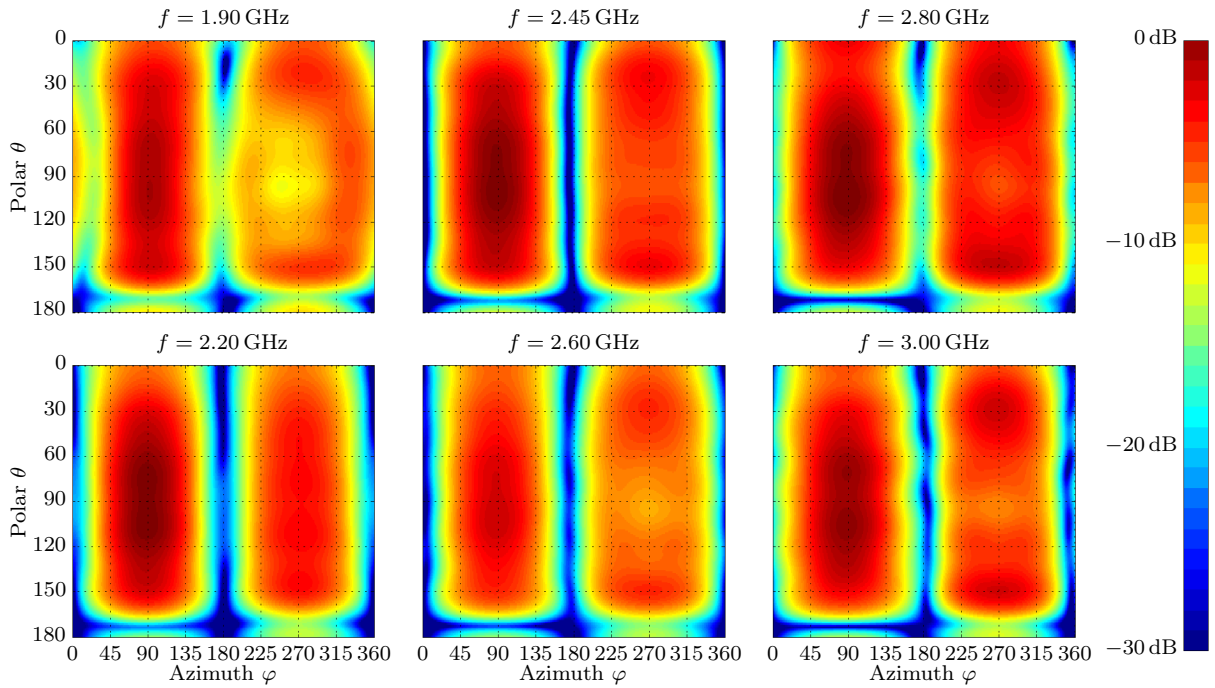


Figure 2.22: Comparison of normalized gain plots for the ISM-SBA in free space for different frequencies f ; plotted for beam I pointing in y -direction.

to the dipole elements are shorted at $\lambda/4$, thus in combination with the second high impedance part of the feed line they act as a balun. The DC bias for the diodes is again applied using a quarter wavelength line. Both, the DC blocking capacitor at the dipole feed point and the diodes are soldered on extended pads such that the exact position of these elements are fine-tuneable for production tolerances of the PCB material, to achieve optimum matching.

The gain plot for different frequencies is plotted in Figure 2.22. It is very similar to the UHF variant shown in Figure 2.17. The pattern does not vary significantly over a broad frequency range, at very low frequencies the symmetry of the feed gets lost due to the improper length of the feed lines, and the pattern gets asymmetrical as well. The directivity at 2.45 GHz is $D = 4.9$ dB.

2.3 Frequency Selective Surface Shield

Using the compact, horizontally polarized SBA from Section 2.2 close to a metal surface as the body floor pan of a car severely degrades the antenna in terms of efficiency, radiation pattern and matching. Therefore, I propose to use an FSS between the body floor pan of the vehicle and the antenna, to shield the antenna from the metal parts of the vehicle while maintaining a low overall antenna height. The requirement to the FSS to enable an efficient operation of a nearby parallel oriented dipole antenna is to have a surface reflection phase close to 0° . Such surfaces are called Artificial Magnetic Conductor (AMC) [47, 48], and their beneficial behaviour in proximity of antennas is illustrated in Figure 2.23. The left side illustrates the effect of a Perfect Electric Conductor (PEC) surface below a dipole antenna: The situation is represented by mirroring the dipole and its currents at the PEC surface, and inverting the current direction in the mirrored image. This explains why a dipole at a spacing of $\lambda/4$ to a large ground-plane resembles a directive antenna with good efficiency: The waves produced by the original dipole and the mirrored image dipole are in phase above the assembly. For closer spacing the efficiency is reduced, since the fields produced by the opposite currents in the real and fictitious dipole interfere destructively.

In contrast, an AMC behaves similar, but the mirrored currents in the fictitious dipole are in phase to the real dipole — corresponding to the zero reflection phase property mentioned before. This implies that for a small spacing the fields produced by both dipoles add constructively in the far-field. More spacing leads to a destructive interference, especially for $\lambda/4$ spacing.

The idea to combine a beam switching antenna with an FSS is not completely new. The configuration described in Deo et al. [41] is in some aspects similar to the configuration developed in [49] and described here. The antenna itself has comparable dimensions with respect to the wavelengths and it is operated close to an FSS. However, the SBA uses a single feeding point and is operational in free space, while the design of Deo et al. relies on a modified Sievenpiper structure. Since a classical Sievenpiper mushroom with square patches on the top layer is used in Deo et al, the patch elements have an edge length of approximately a quarter wavelengths and therefore cannot be considered electrically small. Moreover, the FSS will not behave as an homogenous surface. I will describe in Section 2.3.1 that I use techniques to reduce the size of a unit cell to 0.058λ at 868 MHz and 0.163λ at 2.45 GHz. Further, I investigate the case of identical unit cells, while Deo et al uses vias only at the outer cells of his FSS aiming a reduction in surface waves.

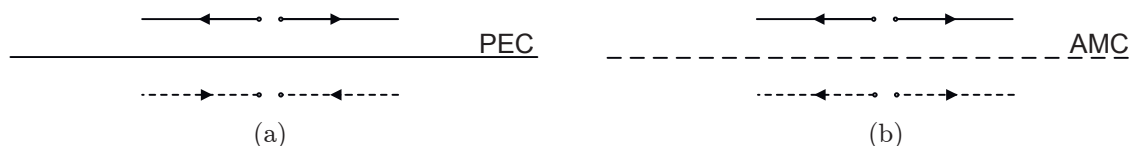


Figure 2.23: AMC principle.

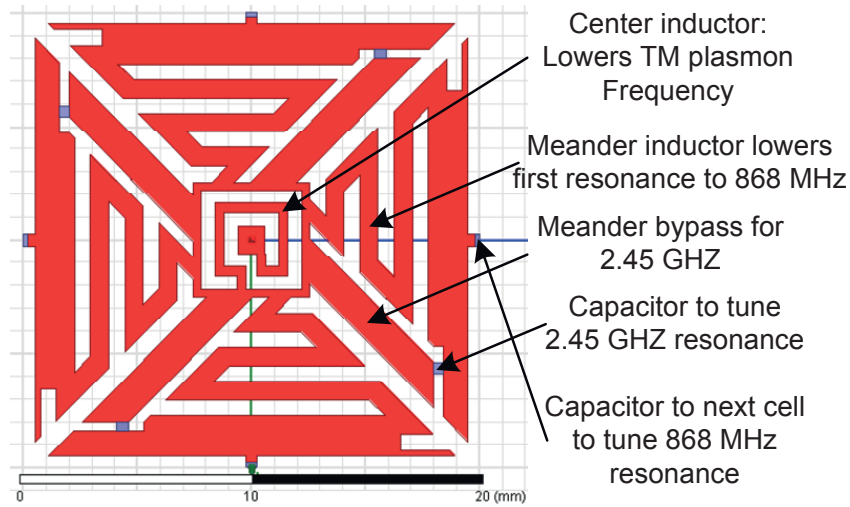


Figure 2.24: Unit cell geometry of the designed AMC FSS1. Red areas indicate top copper, capacitor positions shown in grey.

2.3.1 Frequency Selective Surface Design

The design goal for this FSS is to create a shield suitable for placing between an already designed antenna and a nearby large metallic object, the body floor pan of a vehicle. This shield should also be able to conserve key parameters like efficiency and a low elevation angle of the antenna system. Since the FSS for this application is required to have a phase response of 0° for incoming waves, the structure must resemble an AMC. Periodic structures allow the propagation of surface waves or spoof plasmons [50, 51, 52] which can degrade the antenna. I decided to base this design on mushroom shaped unit cells which are proven to feature a stop band and to suppress surface waves [47, 48]. Depending on the permittivity of the substrate and the ground-plane separation distance, the classical Sievenpiper mushroom unit cells extend up to almost a quarter wavelength. This makes the assumption of an homogenous media questionable. Interesting antenna designs as in Deo et al. [41] are using these rather large FSS patches, but here the antenna element acts more like a feed to the periodic patch resonator array. I used techniques similar to [53, 54] by implementing meanders in the unit cell design to reduce its size. To obtain two independent controllable resonances, lumped capacitors are employed, as suggested in [55].

The lumped components give further flexibility to the AMC design. Although this is not used here, different values of lumped components at different positions on the AMC panel create an inhomogeneous AMC structure with a phase gradient, which could be beneficial to antenna assemblies using this AMC. Further, instead of fixed capacitors or inductors, varactors are proposed to further enhance beam steering or effectively enhance the bandwidth of the system, as in [56].

I designed two variants of AMC structures which I denote FSS1 and FSS2 throughout. Both designs are manufactured from two single-sided PCBs made of FR-4 with dimensions of $300 \text{ mm} \times 300 \text{ mm} \times 1.5 \text{ mm}$. The copper layers from both PCBs face outside and nylon

spacers with a height of 8 mm are used to separate the PCBs. The overall dimensions of a single AMC panel are 300 mm \times 300 mm \times 11 mm. I discovered that less separation between the PCBs reduces the bandwidth of the AMC, so 8 mm separation distance was picked as a compromise between bandwidth and physical height. The lower PCB acts as a ground-plane, and the copper layer of the top PCB is structured to form the unit cells of the AMC.

The top layer of the unit cell of FSS1 is shown in Figure 2.24. In the centre of the unit cell, a via constructed from AWG 24 tinned copper wire connects to the ground-plane. The small planar inductor centred around the via does not lower the AMC resonance frequency, i.e., the frequency where the 0° phase reflection occurs. This contradicts the explanation of the simple LC circuit often used in literature to calculate the AMC resonance of the Sievenpiper mushrooms, first introduced by Sievenpiper himself [47, Fig. 5]. For a normally incident plane wave, there is no electric field component perpendicular to the AMC structure, and therefore there is no current flowing through the wires. This means that neither the wire forming the via, nor the centre inductor, is part of the inductance of the equivalent LC circuit. Rather, the centre ground path for the AMC is essential to suppress Transversal Magnetic (TM) surface waves. The introduced inductor therefore lowers the TM spoof plasmon frequency [50] or widens the band gap for TM waves. Transversal Electric (TE) waves are not altered by the central inductor or the via.

To reduce the size of the unit cell, its outer area is partitioned in four sectors, all identically constructed. Of course this technique could also be used to construct anisotropy by means of different geometries or loading capacitors for the individual sectors, while keeping the unit cells square. Identical meander inductors are employed in every sector to lower the first resonance frequency to the European RFID UHF band at 866 MHz. The coupling to the next cell by fringing fields is reduced by shrinking the outer dimension of the unit cell, so the dominant capacitance between cells is the discrete capacitor on every cell edge which connects to the next cell. This component also tunes the first resonance of the AMC structure. I used ceramic capacitors in 0402 package with $C_{\text{UHF}} = 0.4$ pF. For the resonance at the ISM band I bypass the meander by means of the diagonal line which runs from the centre ring to a coupling capacitor C_{ISM} , which couples to the cell edge bar. The width of this line and the capacitance of C_{ISM} sets the second resonance at 2.45 GHz. I use $C_{\text{ISM}} = 0.2$ pF capacitors. Both, C_{UHF} and C_{ISM} make the design of FSS1 relatively insensitive to the unreliable permittivity of the FR-4 substrate, since they dominate the relevant capacitances when compared to those of fringing fields between cells or stubs.

For FSS2 I substituted the discrete capacitors for structures in the copper layer of the top PCB. The coupling capacitor to the next cell C_{UHF} is simply substituted by reducing the gap between adjacent top cells to 1.1 mm. The second capacitor, which tunes the 2.45 GHz resonance, is replaced by a small single stub interdigital capacitor. To reach the same resonances with smaller capacitance values, the inductances of the meander inductor and the bypass stub are increased by lowering the width of these line elements. FSS2 is therefore more sensitive to substrate variations than FSS1. For a single AMC panel holding 15 \times 15 unit cells approximately 1300 precision capacitors are eliminated in this way. The unit cells for both AMC variants are drawn up to scale in Appendix B.

Discrete Components Model

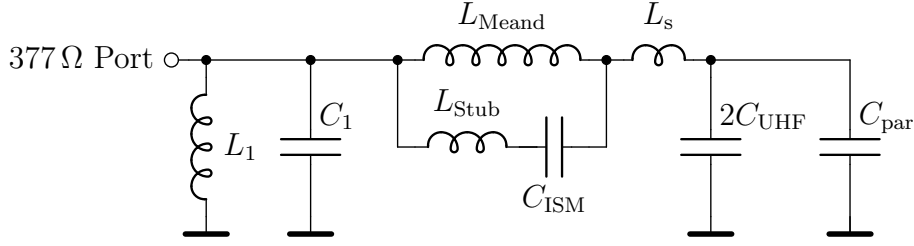


Figure 2.25: Equivalent circuit model for the developed AMC structures.

The design of the FSS structures was aided by Finite Element Method (FEM) simulations in HFSS, both using the eigen mode solver to create band structure diagrams and the modal solver to create the phase response for a plane wave at normal incident angle to the FSS. However, both techniques are rather slow, the eigen mode solver required two to four days for a complete simulation, and the modal solver took 15 min to 30 min for a single frequency point. To speed up the simulation process I developed the equivalent circuit model shown in Figure 2.25. This model is used to predict the phase response for a plane wave and normal incident in the interesting frequency range from DC to approximately 4 GHz very accurately. More interesting, most components are directly related to physical features of the FSS geometry, so new FEM simulations are now started with suitable values for fine tuning. The capacitors $2C_{\text{UHF}}$ and C_{ISM} directly relate to the discrete capacitors in FSS1, C_{ISM} is of the same value as the discrete capacitor that tunes the 2.45 GHz resonance, and the shunt capacitor to ground $2C_{\text{UHF}}$ is twice the value of the inter-element capacitor used to tune the UHF frequency. The factor two is clear, since the inter-element capacitors are substituted by single capacitors to ground, which are in series with respect to the neighbour elements, thus for the same effect they have to have the double capacitance. The inductances on the right also directly refer to physical properties: The inductance of the shortening stub for 2.45 GHz is L_{Stub} , the meander Inductance L_{Meand} , and L_s corresponds to the small series inductance of the last patch which connects the meander to the edge capacitor, and the inductance of the centre square surrounding the centre inductor. The parasitic capacitance between the neighbouring unit cells is modelled with C_{par} . The tank circuit $L_1 C_1$ corresponds to the interaction between the top layer of the FSS and the bottom ground-plane. It does change when the spacing between the layers is altered, but it does not change when the centre inductor of the FSS top layer or the via to ground is modified! The circuit is excited using a port with a source impedance of 377Ω corresponding to the free space wave impedance. All component values for the model for FSS1 except $2C_{\text{UHF}}$ and C_{ISM} were found by curve fitting the phase response curves for various simulated values of the discrete capacitors C_{UHF} and C_{ISM} . The model is most helpful to evaluate which meander lengths and capacitor values lead to which bandwidths of the corresponding resonance frequencies. Values for FSS1 are found in Table 2.3.

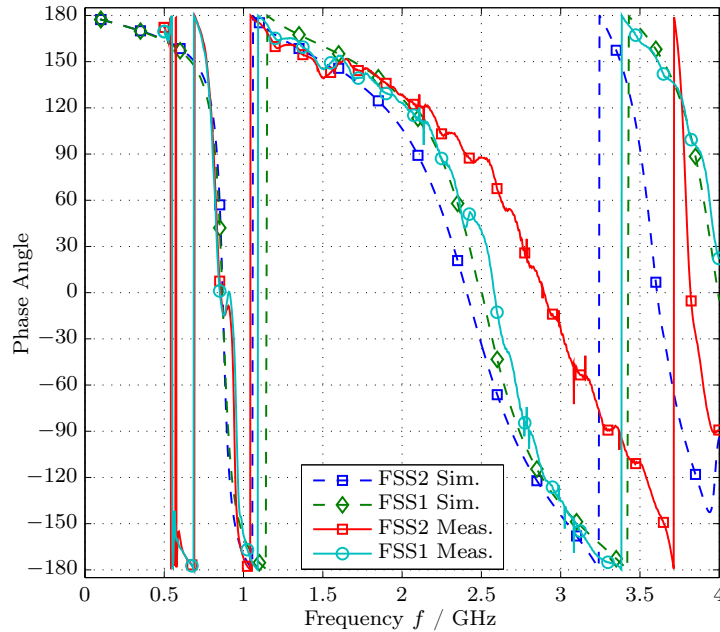
The model is also a valuable tool to evaluate the effects of relative permittivity changes of the substrate on the AMC resonances. Inductances L_{Stub} , L_{Meand} , and L_s depend

Table 2.3: Values of equivalent circuit model for FSS1.

	L_1	C_1	L_{Meand}	L_{Stub}	L_s	C_{par}	$2C_{\text{UHF}}$	C_{ISM}
Value in pf / nH	10.55	0.48	9.00	6.73	3.00	0.75	0.80	0.20



(a)



(b)

Figure 2.26: AMC phase response: (a) Measurement Setup using two identical horns in an anechoic chamber; (b) Reflected phase of the designed AMC surfaces, showing simulation and measurement.

on the relative permittivity following a square-root law, since they are based on short delay elements (lines) structured on the FR-4. The parasitic capacitance C_{par} needs to be modelled based on the copper thickness and the gap between unit cells. Here, the capacitance is not directly proportional to the substrate permittivity, since the ratio of the electric field in the material and the air gap also changes when the relative permittivity is altered.

Phase Response

A comparison of the phase response behaviour of both AMC structures is shown in Figure 2.26b. The dashed lines show the simulation results of a single unit cell using master slave boundaries in HFSS. The relative bandwidth of the second resonance is much larger than the first one. Specifically, it is 25% when compared to 7.5% for FSS2

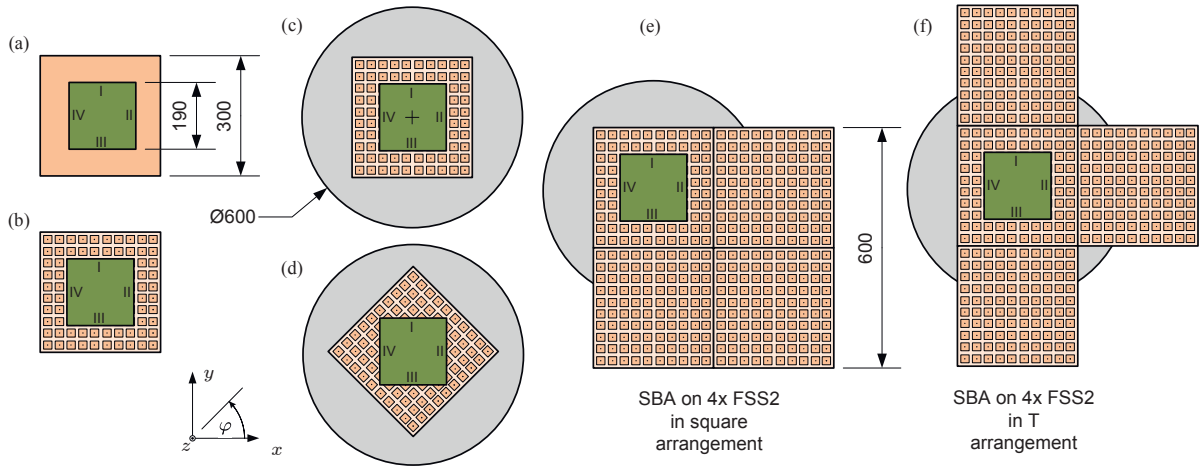


Figure 2.27: Schematic representation of the different performed measurement configurations, dimensions given in mm. The green square indicates the position of the SBA, the Latin numbers indicate the beam numbers of the SBA. Fig. (a) shows the SBA atop the reflector, (b) the SBA atop a FSS, (c) the SBA atop a FSS plus a ground-plane, (d) as (c) but with twisted FSS, (e) SBA mounted above 4 FSS2 panels in square arrangement, (f) on SBA mounted above 4 FSS2 panels in “T” arrangement.

and 20 % when compared to 9.8 % for FSS1. This is beneficial, since the second resonance is more affected by the permittivity value of the substrate. The measurements from Figure 2.26b were obtained in an anechoic chamber using the same methodology as in [47]. The AMC structure was placed on an absorber slab mounted on a wooden stand, see Figure 2.26a. Two identical ridged horn antennas (EMCO 3115) were placed side by side facing the AMC structure at 61 cm distance. A slab of foam absorber was placed between the horns to reduce direct coupling, especially at higher frequencies. The horn antennas were connected to a VNA and the transmission coefficient was measured.

For calibration, a metallic reflector of the same size as FSS1 and FSS2 is placed at the exact same position. The phase response is obtained by subtracting the phases of the two measurements, and adding the known phase response of 180° for the metallic reflector. We see that the results from FSS1, which relies on the discrete capacitors, is in close agreement with the simulation results. The response of FSS2 is slightly shifted towards higher frequencies for the second resonance. The measurement results for very low frequencies are not shown because the horn antennas are operated far outside their specified frequency range.

Surface Waves

To evaluate the possible guiding of surface waves I performed eigen mode simulations on a unit cell of the developed FSS. The periodic structure is studied analogous to classical crystals and Bloch theory, so it is best represented in a band diagram [57], as those created for FSS1 in Figure 2.28 , and for FSS2 in Figure 2.29. It is obtained from eigen mode

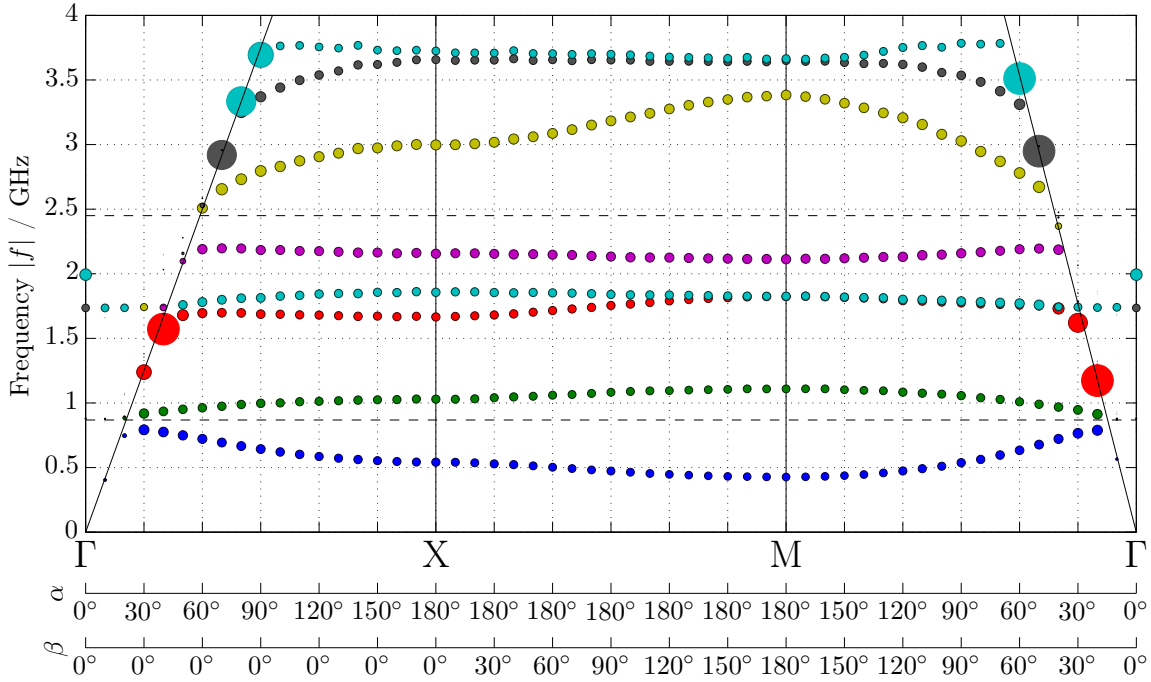


Figure 2.28: Simulated band structure diagram of FSS1. Different colours indicate different modes. The marker size is proportional to the Q of the corresponding mode. The slanted black lines correspond to the free space light lines.

simulations in HFSS, where the modelled unit cell is enclosed by master-slave boundaries on its opposite walls. The phase between the master-slave boundaries is controlled by phase angles α and β . They are swept in steps of 10° , and the complex eigen frequencies are calculated. Figure 2.29 shows the absolute values of the eigen frequencies plotted as coloured dots. The dot colour indicates specific modes, while its size is proportional to the Q factor of the corresponding mode. The Q factor is found by

$$Q = \frac{|f|}{2f_i}, \quad f = f_r + jf_i \quad (2.1)$$

where f_i is the imaginary part of the complex frequency f , and f_r is the real part [58]. The phase angles α and β relate to wave numbers by $k_x = \frac{\alpha}{a}$, $k_y = \frac{\beta}{a}$, where a is the unit cell width or periodicity constant, it is $a = 20$ mm in our case. The slanted solid lines indicate the free space light lines — thus the relation between f_L and k_i for a free space wave. It is given by

$$f_L = \frac{c_0}{2a\pi} \sqrt{\alpha^2 + \beta^2}. \quad (2.2)$$

Only eigen solutions below the light cone are guided on the FSS. By inspecting Figure 2.29 we see that several band gaps exist, not only at the design frequencies indicated by the dashed lines, but also between them. Note that at other band gaps, as the one at 1.7 GHz, the investigated FSS2 does not behave as an AMC. This is observable only in the phase response diagram Figure 2.26b. The Q -factor for the plotted eigen frequencies is relatively

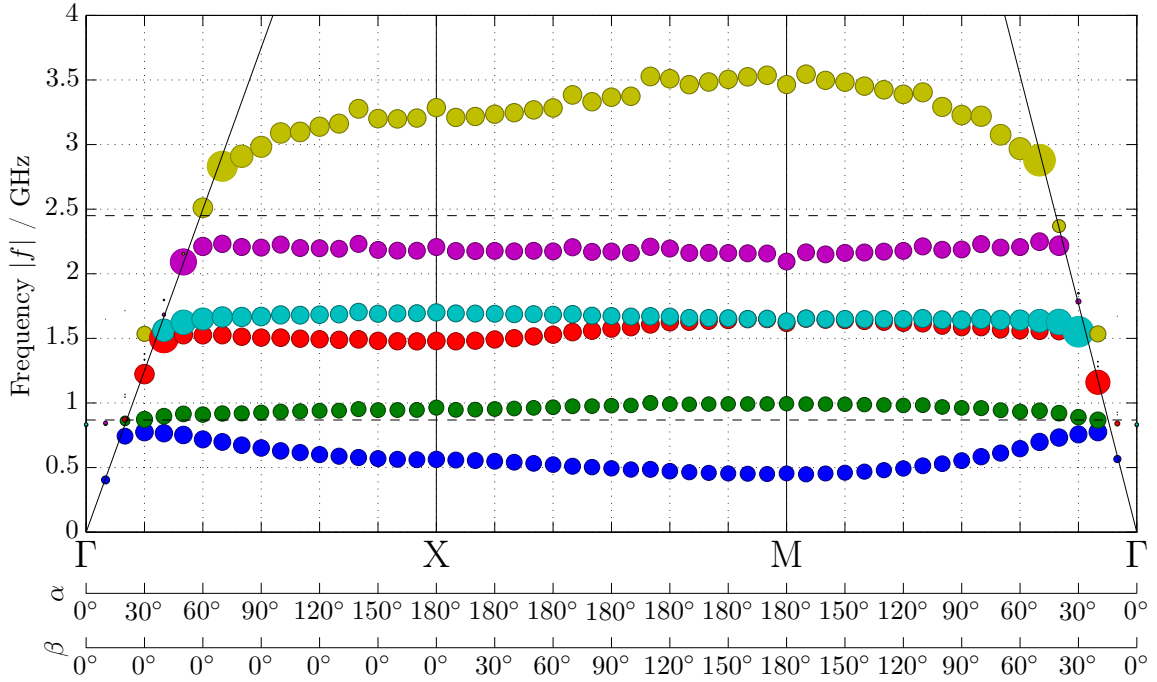


Figure 2.29: Simulated band structure diagram of FSS2. Different colours indicate different modes. The marker size is proportional to the Q of the corresponding mode. The slanted black lines correspond to the free space light lines.

constant in the area below the light line and in the order of 50, indicated by the size of the dots, which is more or less the same.

Experimentally, the wave guiding characteristics and band structure is obtained using a dielectric prism as described in [51]. Here, I follow the guidelines from [47] to obtain a frequency response of the transmission channel between two small probes placed close to the edges of a single AMC panel. The AMC panel and the field probes were placed onto a large foam absorber, to rule out wave guiding on the Ground-Plane (GP) side of the AMC panel. A picture of the measurement setup is shown in Figure 2.30a. TM waves are excited by an electric field probe orthogonal to the surface, while TE waves are excited by a field probe parallel to the surface. As a reference, the measurement was also performed on a GP of identical size. The resulting surface wave gain $G_{\text{SW}} = |S_{21_{\text{MM}}}|/|S_{21_{\text{GP}}}|$ is plotted in Figure 2.30b, both for TE and TM waves. It is interesting, that there are areas where TE waves are suppressed below 0 dB when compared to the GP— since a plane conducting plate is known to carry TM waves only. For the lower UHF design band, the suppression maxima of TE and TM bands are not identical. This is expected, since the two lowest modes in Figure 2.29 also belong to different modes. At 2.45 GHz the suppression band for TM waves is clearly identified, where there is only a small dip in the TE curve. Since the TM mode suppression for the intended application is what matters most, no further effort was done to analyse this TE mode behaviour.

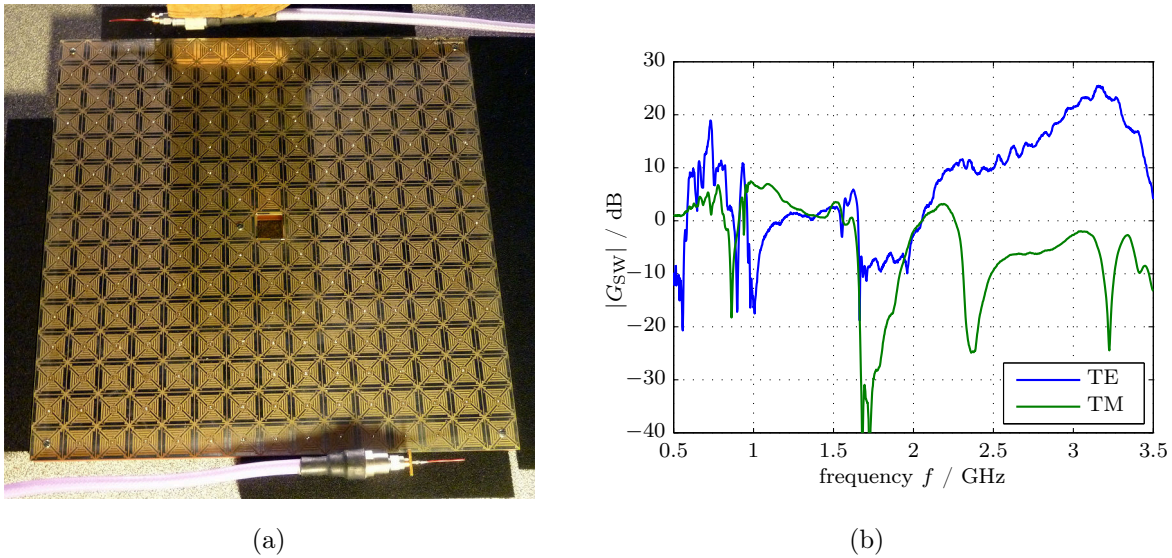


Figure 2.30: Surface Wave Measurement:(a) Picture of measurement setup for TE waves; (b) Measured surface wave gain G_{SW} of the FSS2 panel when compared to a GP of the same size.

2.3.2 SBA plus AMC Assembly Measurements

In this section I describe the pattern and efficiency measurements of an antenna system consisting of one variant of the SBA being mounted with foam spacers above FSS1 or FSS2. The analysed antenna system geometries and the used coordinate system are shown in Figure 2.27. The radiation patterns of the SBA in free space are compared to the ones obtained above either a reflector manufactured from copper, or one of the AMC structures. To mimic the effects of the body floor pan I use a circular ground-plane with 600 mm diameter, which is mounted directly below the FSS for particular measurements. At the UHF band, additional measurements are conducted on a larger FSS constructed by placing four panels of identical FSS2 structures beside each other, mounting them on the large circular ground-plane. Two configurations are measured, the square arrangement and the “T” arrangement. Since both are asymmetric with respect to the mounting of the SBA, the selected beam which is indicated by Latin numbers is important.

Return Loss Measurement Results

As the AMC surface for the complete antenna setup is placed in the reactive near field of the SBA, an influence on the return loss of the antenna is expected. The return loss of the UHF antenna is measured for different spacing values, either mounted atop FSS2, or above a metal ground-plane of identical size, corresponding to the setups 1 to 4 specified in Table 2.4. In Figure 2.31 the free space return loss of the UHF SBA is compared to two of these setup distances, setup 1 with 12 mm separation and setup 3 with 46 mm separation. The return loss degrades for both distances, if the SBA is mounted above

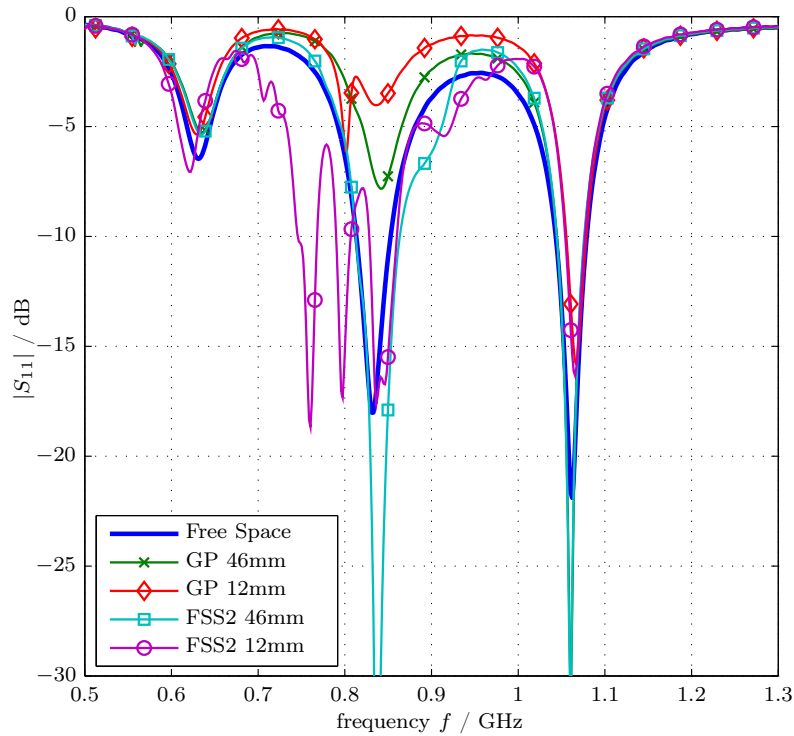


Figure 2.31: Return Loss of UHF-SBA mounted atop either a ground-plane or FSS2 in different heights. The thicker line without markers shows a free space measurement of the SBA. The design frequency band is 865 MHz to 868 MHz.

Table 2.4: Used measurement setups.

Setup:	1	2	3	4	5	6	7	8	9	10
Distance in mm	12	28	46	74	18	20	24	34	40	60
Distance in λ_{UHF}	0.03	0.08	0.13	0.21	0.05	0.06	0.07	0.10	0.12	0.17
Distance in λ_{ISM}	0.10	0.23	0.38	0.60	0.15	-	-	-	-	-

a ground-plane. For 46 mm of separation corresponding to 0.13λ the return loss in the operating band increases. For frequencies up to 925 MHz the return loss increases, too, most likely because here surface waves are excited on the AMC structure. The return loss for setup 2 is not shown here for clarity of the plot, but is similar to the just described one. For very close mounting of the FSS2 structure, corresponding to 12 mm separation or 0.03λ , the return loss again starts to degrade and two new resonances below the normal operation frequency appear. This is probably caused by detuned unit cells of the AMC structure. Namely, the close dipoles of the SBA cause different resonances for the adjacent unit cells. The return loss behaviour for FSS1 was found to be very similar to the one of FSS2 for all measured separation distances.

UHF Band Measurement Results

The following measurements of the UHF-SBA plus AMC structure assembly were taken in an anechoic chamber using a spherical near field scanning system. Since the intended application is the mounting of this assembly on the body floor pan of a car, I seek for an assembly with low overall height, while keeping the elevation angle of the main beam as low as possible and without too much efficiency degradation. Further, the size of the AMC structure should be small to keep the costs of the antenna system low. In Figure 2.32, the relative efficiency of the overall antenna system, that is, the quotient of the efficiency of the assembly over the efficiency of the SBA in free space, is plotted for different separations and configurations. As expected, the efficiency decreases for antenna mountings close to the ground-plane reflector. For the observed frequency range, the efficiency degradation is almost constant. For the FSS2 the efficiency is frequency dependent, which is clear due to the narrowband behaviour of FSS2 as discussed in Section 2.3.1. For setup 4 at 880 MHz there is even a small positive gain in efficiency, most likely caused due to better matching. For the other scenarios there are losses induced by FSS2, but for many frequencies the overall efficiency is better than the one using the metal reflector of the same size. When the measurements of the FSS2 setup 2 assembly using the large circular Ground Plane (GP) underneath the FSS2 structure are compared with the one without GP, only a minor degradation in efficiency which is 0.5 dB at maximum is observed. Therefore, the size of a single AMC panel with $0.87 \times 0.87 \lambda$ is sufficient to effectively shield the SBA from the GP with respect to overall antenna efficiency. For FSS1 the situation is very similar, except that the efficiency curves are shifted approximately 20 MHz towards higher frequencies.

For setup 2, which seems a reasonable compromise between assembly height and efficiency, the normalized gain patterns in Figure 2.33 and Figure 2.34 are plotted for three mounting scenarios of the SBA: First, above the GP reflector sized as the FSS2, second, mounted above FSS2, and third, mounted above the FSS2 plus large circular GP assembly. The gain plots are individually normalized and logarithmically show the gain corresponding to the electric field in φ direction, where φ is the azimuth angle measured in the x/y -plane and θ is the polar angle measured from the z -axis. As these plots show beam I, the desired main lobe is at $\varphi = 90^\circ$. For Figure 2.33 we see that adding a substructure to the SBA raises the elevation angle and reduces the front to back ratio of the antenna. When the three mounting scenarios are compared, the middle scenario using just the FSS2 as substructure creates the lowest elevation angle with considerable radiation between $\theta = 60^\circ$ and $\theta = 90^\circ$, but this effect is not usable in practice as adding the circular GP alters the gain pattern towards lower polar angles. A single AMC panel at UHF is large enough to shield from the GP with respect to efficiency, but not with respect to the radiation pattern. If the frequency is increased as in Figure 2.34, the SBA plus FSS2 assembly starts to behave as if the FSS2 structure would not be there, especially for 930 MHz. The radiation also occurs into the lower hemisphere and the peak of the main beam is close to $\theta = 90^\circ$. Of course, this effect vanishes if the circular GP is added, but the front to back ratio remains very good, exceeding the values of the pure SBA. In this frequency band the FSS supports leaking TE surface waves and I assume that they

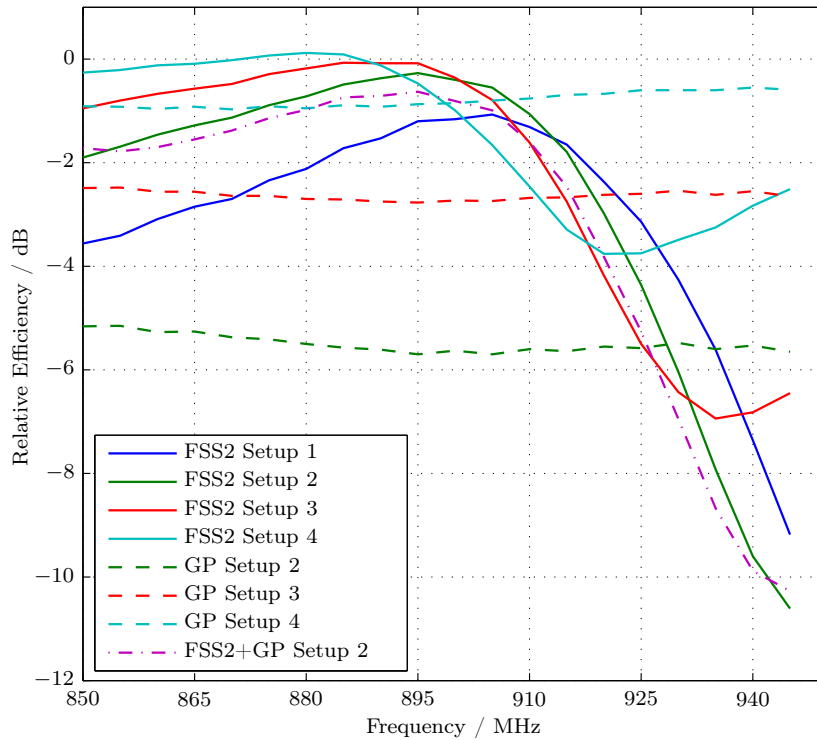


Figure 2.32: Relative efficiency of the SBA mounted atop different substrates in four different heights when compared to the SBA in free space. The different setups correspond to different SBA–FSS-spacings according to Table 2.4 and GP denotes a ground-plane.

influence the front to back ratio and elevation angle in positive sense.

Results for FSS1 are similar to the results discussed for FSS2 with respect to the gain pattern. However, since the efficiency is shifted towards higher frequencies, it is possible to create a pattern behaviour similar to the lower middle diagram of Figure 2.34 with an efficiency penalty of just 1 dB compared to the pure SBA. Further, at 910 MHz the pattern of the SBA using FSS1 as a substructure is also similar to the one using FSS2 shown in Figure 2.34, where even an efficiency improvement of 0.5 dB to the pure SBA is found.

The elevation angle of the different assemblies is further studied in Figure 2.35. The plot shows the polar peak position θ_P conditioned that the peak is in the forward direction direction, i.e. $\varphi = 90^\circ$. Interestingly, bigger FSS2–SBA separation distances lead to lower elevation angles. This behaviour would be expected for a regular GP or PEC, but not for an AMC. Notice that this holds for the whole observed frequency range, but higher frequency values lead to higher polar peak positions θ_P corresponding to lower elevation angles. When the frequency is further increased the reverse beam becomes stronger as the forward beam, and the plot is cropped. Again, I assume that the beneficial low elevation angles are not caused by the AMC behaviour but rather by leaking TE surface waves guided on the finite FSS, and radiation of the FSS surface.

2.3 Frequency Selective Surface Shield

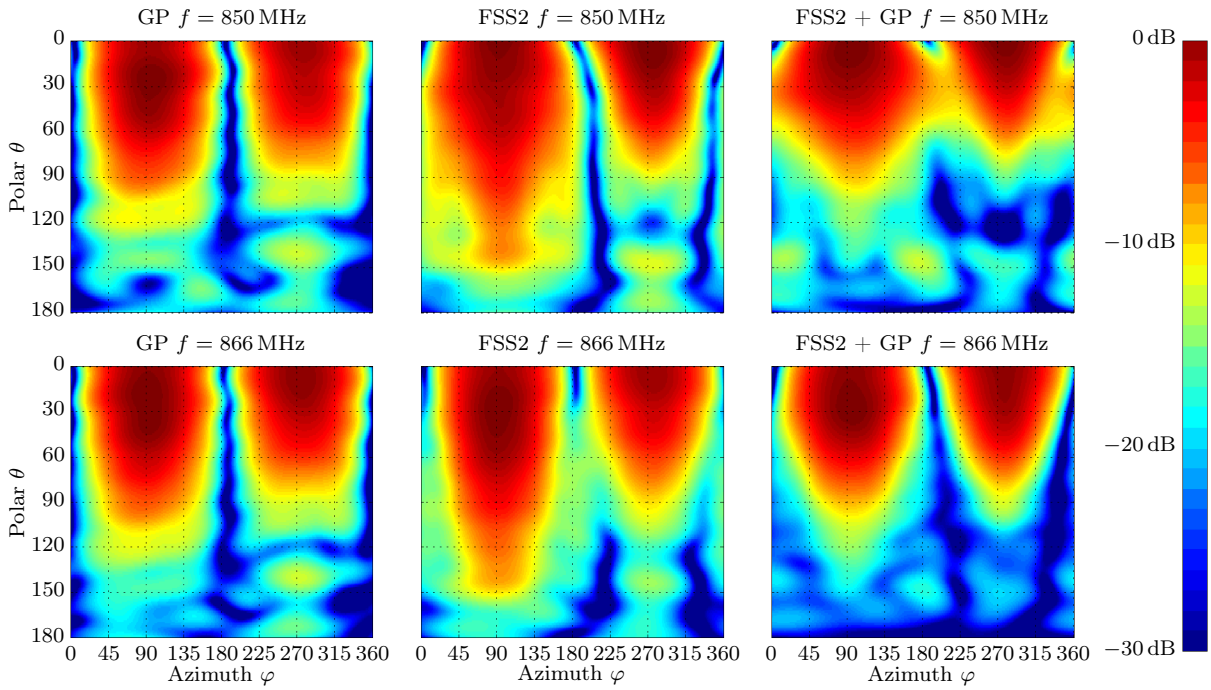


Figure 2.33: Comparison of normalized gain plots in setup 2 (28 mm separation): ground-plane, FSS2, and FSS2 plus large ground-plane at 850 MHz and 866 MHz.

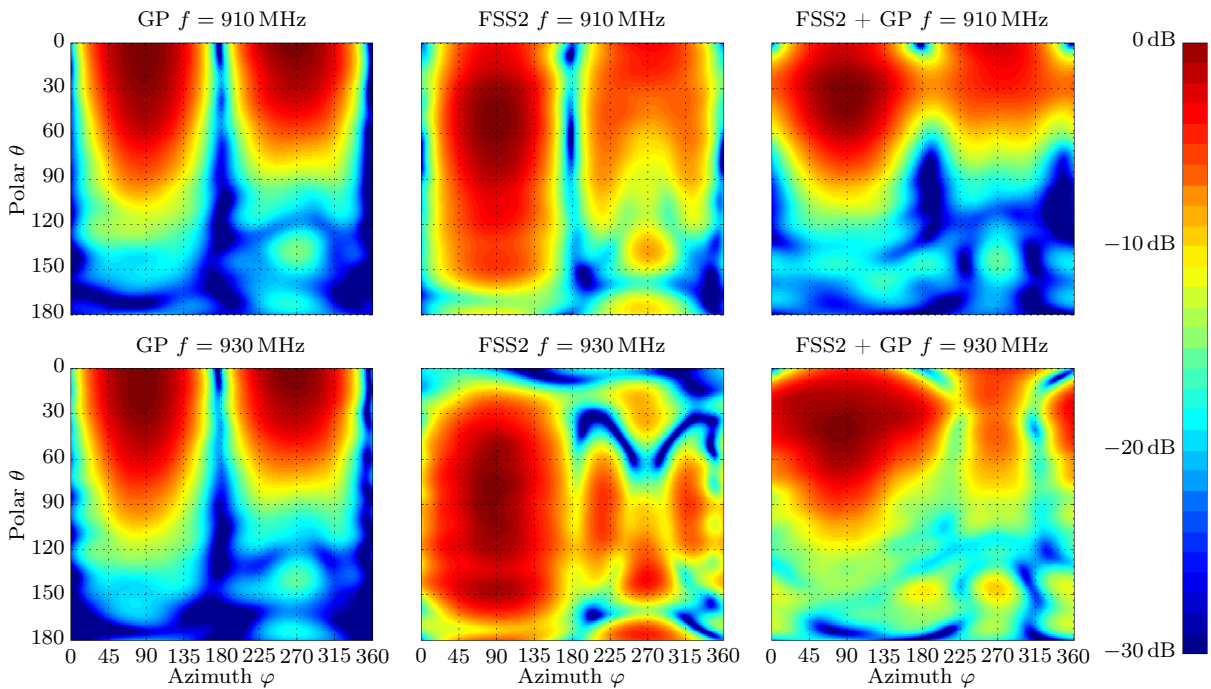


Figure 2.34: Comparison of normalized gain plots in setup 2 (28 mm separation): ground-plane, FSS2, and FSS2 plus large ground-plane at 910 MHz and 930 MHz.

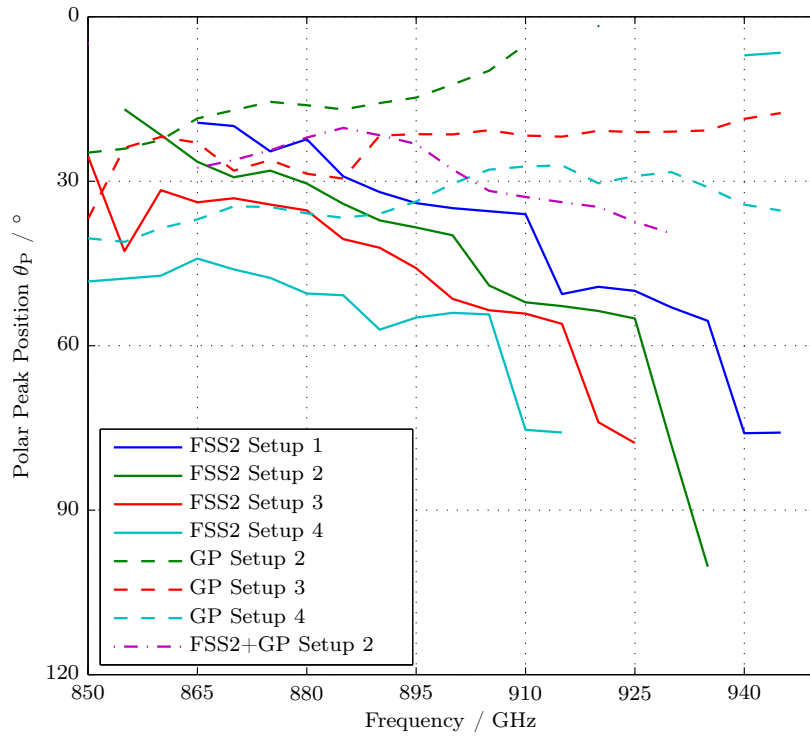


Figure 2.35: Polar peak position of the SBA mounted atop different substrates in four different heights when compared to the SBA in free space. The different setups correspond to different SBA–FSS-spacings according to Table 2.4 and GP denotes a ground-plane.

I conducted further measurements to see if a larger substructure improves the radiation pattern at UHF. A pattern comparison for various assemblies, especially including the variants (d-f) of Figure 2.27 is shown in Figure 2.36 and Figure 2.37. In Figure 2.36 the polar antenna pattern at design frequency of the SBA is shown. Angles between $-150^\circ > \theta > 150^\circ$ are not drawn since here our spherical measurement system does not produce satisfactory results due to its limited θ arm swing range. Here it becomes evident how much the circular GP degrades the performance of the SBA plus FSS2 assembly. For $\theta > 45^\circ$ the resulting pattern shows even less radiation than in the case where just a reflector sized as FSS2 is considered. Relatively good results are produced by the twisted application of FSS2 on the circular GP, corresponding to Figure 2.27 (d). Here, the front to back ratio is good, and though the main radiation peak is at $\theta_P = 25^\circ$ there is also significant radiation at 60° to 75° . When checking the efficiency in this mode a penalty of only 0.84 dB to the pure SBA is found. Lower main peak angles are achieved with a bigger AMC structure as the three last curves show. Remarkably, for the main peak an additional FSS2 panel in opposite of the selected beam direction does not improve the elevation angle, but enhances the front to back ratio when beams I and II of the “T” configuration are compared.

Figure 2.37 reveals that the relatively good radiation pattern produced by the FSS2 plus

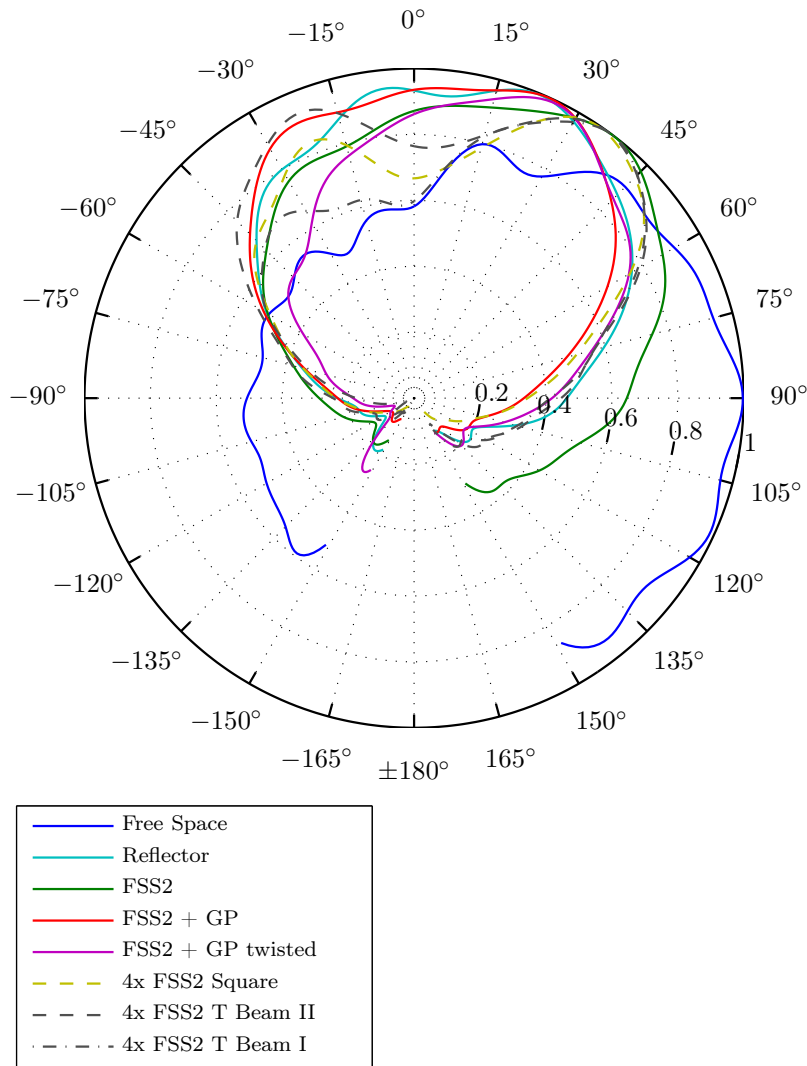


Figure 2.36: Thetacut for SBA at 865 MHz over different substrates in setup 2 (28 mm separation) and beam II except where noted otherwise.

GP configuration at 930 MHz is not a pure wave guiding effect on the FSS, but rather an induced radiation of the finite size FSS array and its edges, measuring approximately $\lambda \times \lambda$ at this frequency. This becomes evident when observing the bigger FSSs constructed by using four FSS2 panels: Their radiation pattern shows a relatively directive lobe straight up towards $\theta = 0^\circ$, which would not be the case if a surface wave is the main source of radiation at that frequency and the effective lengths of the FSS is doubled or tripled when compared to the FSS2 plus GP case.

ISM Band Measurement Results

At the ISM band centred at 2.45 GHz the AMC panels of FSS1 and FSS2 are relatively large structures with $2.45 \times 2.45 \lambda$ and therefore little effects of the large circular GP

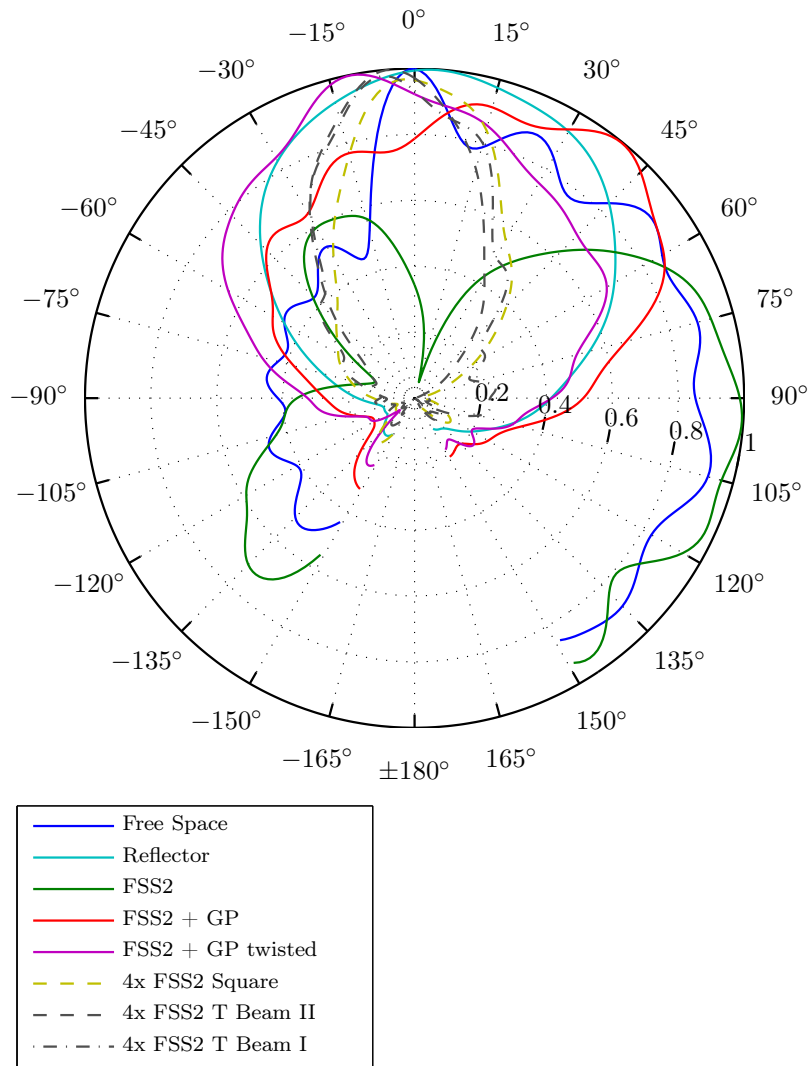


Figure 2.37: Thetacut for SBA at 930 MHz over different substrates in setup 2 (28 mm separation) and beam II except where noted otherwise.

are expected. This is verified by measurements, indeed the results for the setups corresponding to Figure 2.27(b) and Figure 2.27(c) are very similar, so I will graphically only present the ones using the GP. The corresponding gain plots for various frequencies are shown in Figure 2.38 and Figure 2.39, both for a spacing of 28 mm or 0.23λ . Surprisingly, these results for almost a quarter wavelengths separation are beneficial to the ones in setup 1 (0.1λ), both in efficiency and in elevation angle. This shows that the simple prediction of the behaviour of the ISM-SBA plus the FSS according to the AMC model and the measured 0° phase response for a plane wave incident (Figure 2.26b) does not accurately describe the radiation mechanisms of the antenna plus FSS assembly. Although the phase response of the FSS alone is not a perfect way to describe the AMCs behaviour, we picked figures Figure 2.38 and Figure 2.39 for comparison, since they correspond to FSS1 and FSS2 which have the same physical size but in production a slightly different

2.3 Frequency Selective Surface Shield

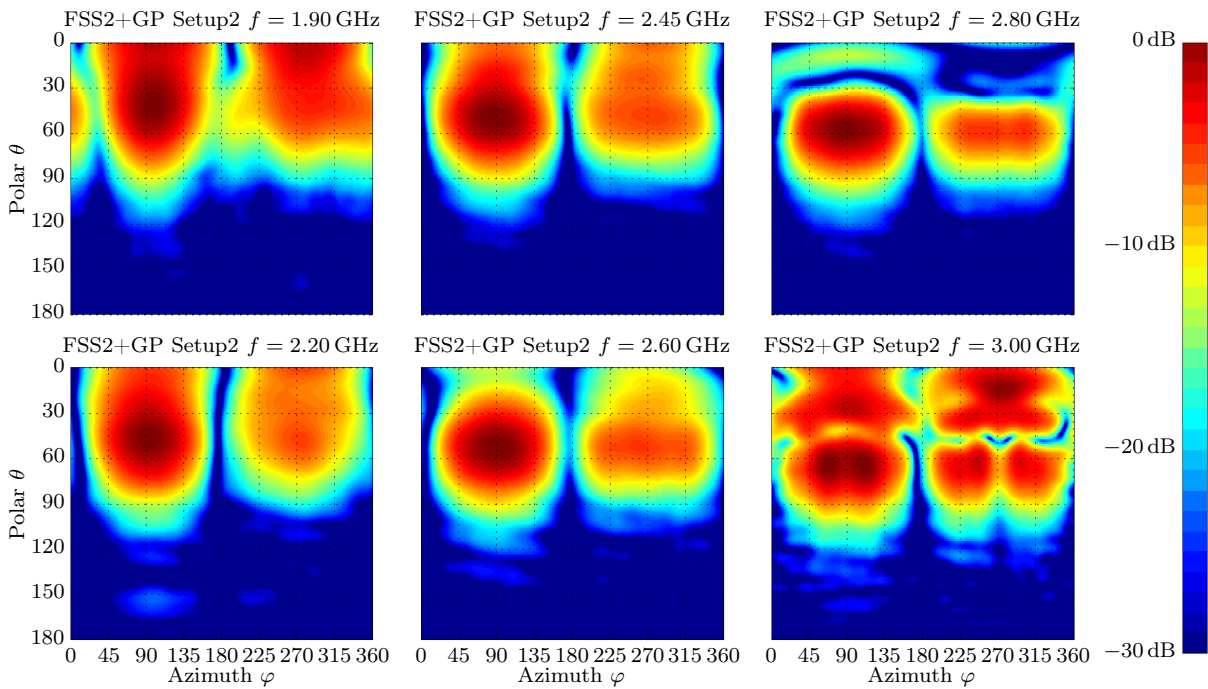


Figure 2.38: Comparison of normalized gain plots in setup 2 (28 mm separation) for the ISM-SBA assembly over FSS2 plus large ground-plane for different frequencies f .

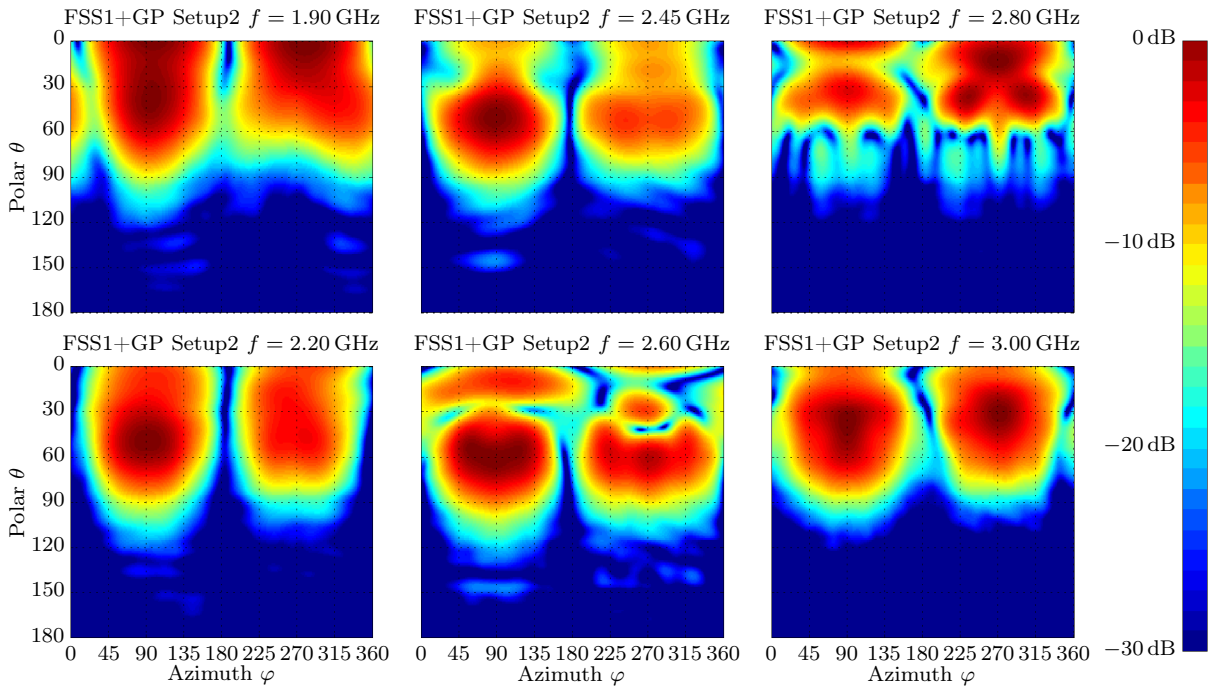


Figure 2.39: Comparison of normalized gain plots in setup 2 (28 mm separation) for the ISM-SBA assembly over FSS1 plus large ground-plane for different frequencies f .

phase response, see Figure 2.26b.

At the design frequency, both assemblies show a quite directive beams with directivity values of 10.2 dB and 10.1 dB, for FSS1 and FSS2, respectively. The peak of the main beam is at $\theta_P = 50^\circ$. At 2.8 GHz FSS2 is operated at the measured AMC resonance frequency and the radiation pattern becomes slightly more confined in θ . FSS1 at the same frequency is already operated outside the AMC bandwidth and the pattern shows a reverse beam pointing towards low θ values.

2.4 Summary

In this chapter three different dual-band antenna solutions suitable for mounting close to a metallic sheet were presented. The first two solutions, namely the monopole and the LPDL are vertically polarized and employ a GP, meaning that an additional metallic sheet potentially enhances the antenna performance. Both antennas are dual-band, and have similar radiation patterns, especially at UHF, but the LPDL is much shorter than the monopole. Despite its size of 8.3% of the monopole antenna, the LPDL antenna shows overall relative efficiencies of 37% (−4.3 dB) in the UHF band and 68% (−1.7 dB) at the 2.45 GHz microwave band when compared to the resonant monopole.

The SBA is a totally different antenna design, being optimized for beam switching in free space. It is a compact antenna (0.55 by 0.55 wavelengths), employs horizontal polarization, and provides eight directional beams and two additional bidirectional beams in azimuth. To enable operation of this antenna close to a metallic object, an AMC shield constructed of two PCBs made of FR-4 was presented. With this shield, the beam switching properties of the SBA remain intact and the antenna efficiency is preserved with a 0.8 dB penalty at a distance of only 0.08 wavelengths. Table 2.5 summarizes the data of these antenna solutions. For the monopole and LPDL antennas the columns UHF and ISM correspond to the two bands of the same antenna. For the SBA these columns correspond to the two antenna variants. The last two columns correspond to the assembly of the large circular GP mounted to FSS2, separated from the actual SBA by a spacer of 28 mm (Setup 2). For the UHF case two variants are given, the left one providing a directivity of 5.7 dB and a theta peak value of $\theta_P = 27^\circ$ corresponds to the slanted orientation of the SBA atop of a single FSS2 panel. The values in the right column correspond to the square arrangement of four panels, values given for beam I.

The relative efficiencies given in this table are with respect to the monopole antenna for the LPDL, and the SBA in free space for the SBA+FSS2+GP assembly. For the ISM band operation of the LPDL antenna the polarization is neither a pure horizontal nor a pure vertical one, so “mixed” is written here to indicate this. Since the LPDL radiates in this two modes, I included the second peak at 48° which corresponds to the vertical operation mode in Table 2.5.

When all three solutions are compared, aiming towards an ATMS application, it becomes clear that the monopole has beneficial radiation properties but is simply too long to be mounted below a vehicle. The LPDL conserves similar radiation properties at a very small height, but this is paid by an efficiency penalty, especially at UHF. The assembly

Table 2.5: Data summary of the designed antennas.

	Monopole		LPDL		SBA		SBA+FSS2+GP	
	UHF	ISM	UHF	ISM	UHF	ISM	UHF	ISM
Polarization	vert.	vert.	vert.	mix.	hor.	hor.	hor.	hor.
Direct. / dB	4.3	6.7	4.6	5.5	4.7	4.9	5.7 / 6.8	10.2
θ_P	54°	35°	51°	7° / 48°	90°	90°	27° / 38°	50°
Rel. Eff. / dB	—	—	4.3	1.7	—	—	0.8 / 1.8	0.5
Dim. xy / mm	400 × 400		400 × 400		190 × 190	70 × 70	300 × 300	
Dim. z / mm	78		6.5		1.5	0.8	28 + 11 = 39	

of SBA and FSS2 is a compromise in terms of overall height and efficiency. Setup 2, used for the data in Table 2.5, is exactly half the length of the monopole. The efficiency penalty is much smaller when compared to the LPDL. But more relevant, the antenna assembly features the beam switching capabilities of the SBA, which enables identification of the individual Wheel Unit (WU) sensors. Though the peak positions in azimuth are not optimal, the relatively wide beam still ensures good coverage at low elevation angles.

Chapter 3

Leaking Carrier Cancellers

RFID tags communicate with readers using backscatter communications. This technique relies on the principle that the amplitude and phase scattered back from any antenna depends on the impedance imposed to the antenna terminals [59, 4]. Passive tags, additionally require the reader's transmit signal to power their circuitry. Therefore, the RFID reader has to transmit a carrier signal, while it simultaneously receives a weak backscattered signal from the tag. To separate transmit and receive paths, readers either use single antennas and circulators or directional couplers, or separate transmit and receive antennas. In analogy to radar systems the first case is called monostatic, while the second one is called bistatic, corresponding to (a) and (b) of Figure 3.1. Still, both system concepts struggle with low transmitter to receiver isolations [60]. This demands for receivers with very large dynamic ranges, which enhance costs, both on the analogue frontend as well as on the analogue to digital converters. To reduce these demands, many authors [61, 8, 62, 63, 64, 65, 66, 67, 68, 69, 70] as well as commercial monolithic RFID reader chip manufacturers [71, 72] propose or use active leakage cancellation techniques. These techniques, which originate in radar [73, 74], extract a part of the transmit signal, adjust it in amplitude and phase and inject it at the receiver. When the amplitude is adjusted to be equal, and the phase to be opposite of the leakage signal, the deliberately added signal and the leakage signal cancel. In Figure 3.1, this is indicated by routing the received signal through the Leaking Carrier Canceller (LCC) block. Note the arrow going from the transmitter module to the LCC module, here the required sample of the transmit signal is extracted for the LCC module.

In the first part of this section I will treat cancellation hardware aspects, and models to derive the bandwidth of a classical LCC. Further, an enhanced broadband canceller will be presented based on a multi tap leakage channel model. The last section will treat adjustment techniques for LCCs, which are a critical aspect of any cancellation scheme.

3.1 Hardware realization

The hardware presented in this section has initially been developed to enhance the capabilities of the RFID testbed frontend designed at our institute [75] and is further explained in [66, 4]. In this testbed, both, the transmit module as well as the receive module carry directional couplers to extract or inject the cancellation signal. The remaining parts of the LCC, a vector modulator and an amplifier, were implemented as a separate assembly

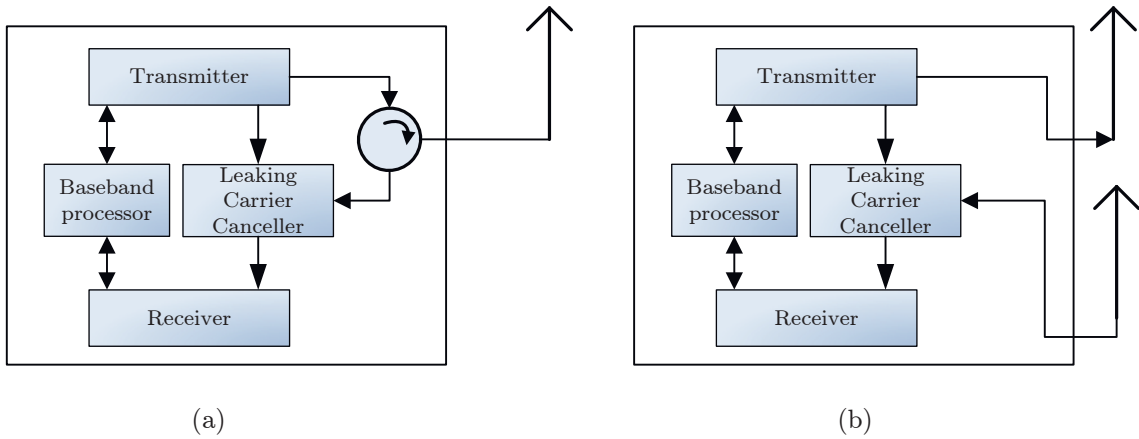


Figure 3.1: Block diagram of an RFID reader using an LCC: (a) monostatic; (b) bistatic scenario.

called Carrier Compensation Unit (CCU). A picture of the CCU is printed in Figure 3.2. CCU modules were used for the experiments presented later in this chapter.

The CCU's vector modulator functionality is provided by an IC from Analog Devices, the AD8340. This Integrated Circuit (IC) splits up the input signal in an inphase and a quadrature component with an integrated polyphase network. Further, this device contains separate balanced variable attenuators for the I and Q channel. These internal balanced attenuators allow to change the corresponding channel's polarity, so that a true 360° phase shift range can be obtained. The supported amplitude range is 30 dB. To compensate the coupler losses (at the transmitter as well as at the receiver) and enable cancellation of strong leaking carrier signals, the vector modulator is followed by an amplifier.

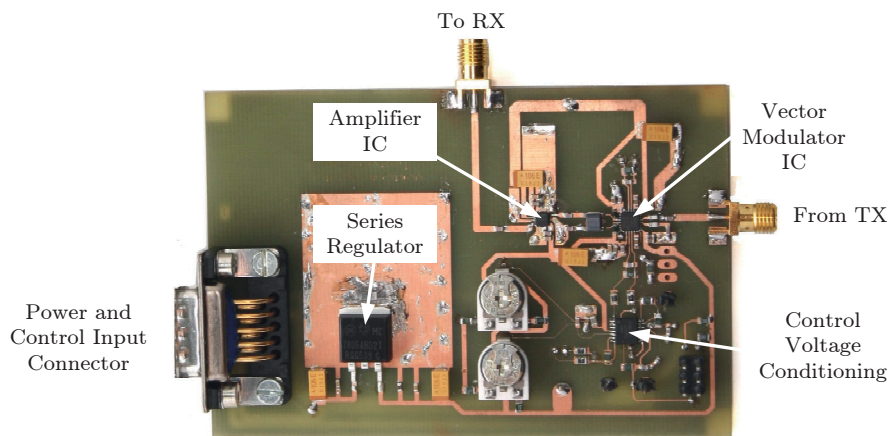


Figure 3.2: Picture of the CCU module.

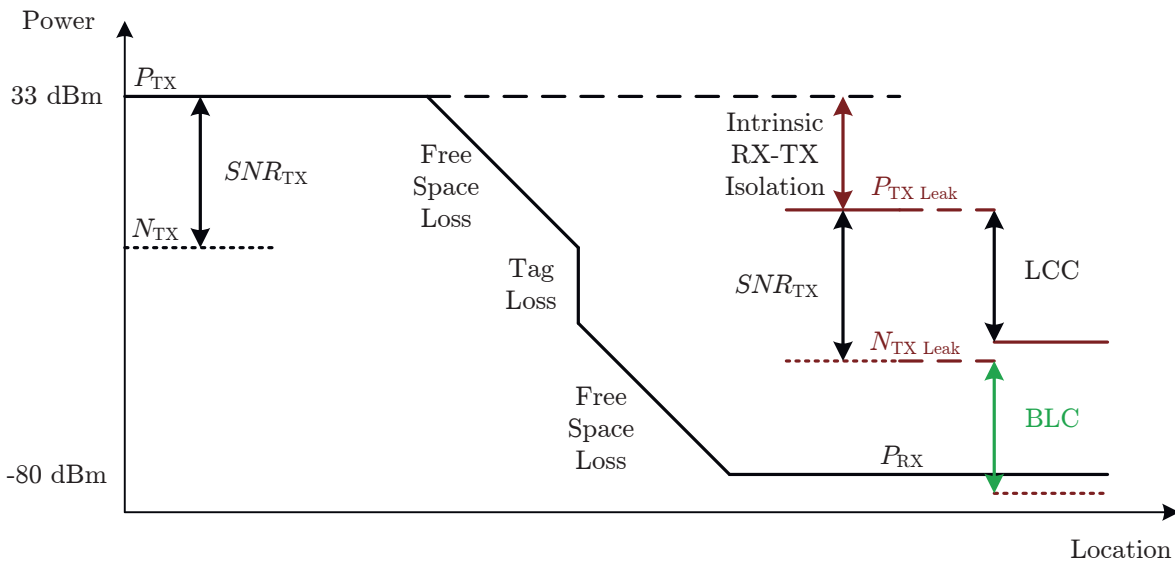


Figure 3.3: RFID link budget chart focusing on carrier cancellation and transmit noise.

3.2 Broadband Suppression Motivation

The usual approach to characterize LCCs in RFID systems is to measure the attenuation realized at the reader's carrier frequency only. But this approach is insufficient in many cases. For conventional passive RFID systems which only transmit a Continuous Wave (CW) signal during tag to reader communications, a narrowband canceller is adequate to suppress this sine wave. But since the power levels in RFID are extremely diverse, the transmit noise becomes an issue, too. This is illustrated in Figure 3.3, which shows a schematic link budget for RFID: On the left side a typical transmit power of 33 dBm¹ is plotted. Going from left to right, the free space loss, tag (modulation and matching) loss and second free space loss in the reverse direction reduce the power at the receiver to $P_{RX} = -80$ dBm. This is a realistic value for long distance reader to tag communications [4] using state of the art tags which have a sensitivity of 5 μ W [61]. Additionally, the transmit Signal to Noise Ratio (SNR) is plotted on the left side and the transmitted noise power N_{TX} is shown. On the right side, the intrinsic Transmitter (TX) to Receiver (RX) isolation is recorded. Without any leakage cancellation, the dynamic range of the reader RX needs to be at least $P_{TX Leak}/P_{RX}$, which possibly is in the order of 93 dB [4]. To reduce these RX demands, the LCC suppresses the leakage signal, as indicated by the corresponding arrow on the far right side. But the broadband TX noise component is not suppressed, and so the receive SNR is dominated by the leaking TX noise power $N_{TX Leak}$, being negative in the example plotted in Figure 3.3. A Broadband Leakage Canceller (BLC) on the other hand does also suppress the noise component, so while the necessary dynamic range remains unchanged when compared to the LCC, the received

¹For UHF RFID applications 2W Equivalent Radiated Power (ERP) is the maximum allowed transmission power in most European states.

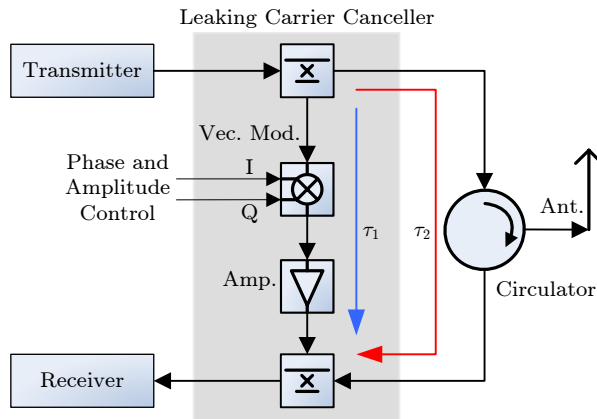


Figure 3.4: Monostatic RFID system with LCC illustrating the single tap model.

SNR is improved. In fact, a very narrow band LCC even enhances the noise level, since the leaking signal and the cancellation signal will interfere constructively at some frequencies.

Novel RFID technologies, such as chipless RFID [76] or localisation [77] necessitate RFID readers which operate at larger bandwidths. Either the transmit signal is composed of a broad band pseudorandom signal [78], or beside the main carrier additional carriers are used for ranging [79]. Consequently, those RFID systems require LCCs with increased bandwidth, too.

3.3 Single Tap Model

To model the frequency behaviour of active leaking carrier cancellers I first analyse the simple case when just a single point of reflection is present, either in the RFID reader itself, or, for perfectly matched antennas, in the space in front of the antennas by means of a single reflecting point object. More generally speaking, the leakage channel H_L is a complex constant and the corresponding impulse response $h_L(t)$ consists of a weighted single dirac distribution.

Following the example given in [66], this could be, for instance, an imperfect circulator (see Figure 3.4). All other components like cables or the antenna are perfectly matched and therefore do not produce reflections which end up in the receiver. We also assume that the unwanted reflection in the circulator does not introduce any phase shifts in the frequency band of interest. The directional coupler that is used to combine the receiving path with the compensation path is modelled as an ideal summation device.

With these assumptions the impulse response $h(t)$ of the overall system between the transmitter output port and the receiver input can be derived:

$$h(t) = A \cdot \delta(t - \tau_2) + B \cdot \delta(t - \tau_1) * p(t) \quad (3.1)$$

Here $\delta(t)$ is the Dirac delta distribution and $p(t)$ is the impulse response of the vector modulator. The first term describes the unwanted signal component with amplitude A and the second one the component produced by the canceller, scaled by B . With reference

to the transmitter, τ_2 and τ_1 are the delays of those components at the receiver. It is obvious that total suppression requires the amplitudes of both terms to be equal, so we set $A = -B = 1$ and $|p(t)| = 1$. For convenience we introduce $\Delta\tau = \tau_1 - \tau_2$ and substitute τ_1 . Without loss of generality, τ_2 can be set to zero, so that τ_1 becomes $\Delta\tau$.

The vector modulator's impulse response $p(t)$ can be expressed as

$$p(t) = \cos(\alpha)\delta(t) + \sin(\alpha)\frac{1}{\pi t} \quad (3.2)$$

so that $\cos(\alpha)$ represents the amplitude of the inphase component and $\sin(\alpha)$ the quadrature component's amplitude which vectorially sum up to 1. The phase shift introduced by the vector modulator is represented by the angle α . The quadrature component is generated by the term $\frac{1}{\pi t}$, the impulse response which corresponds to a Hilbert transform.

Insertion of (3.2) into (3.1) and adopting the described simplifications leads to the system's over-all impulse response:

$$h(t) = \delta(t) - \left(\cos(\alpha)\delta(t - \Delta\tau) + \sin(\alpha)\delta(t - \Delta\tau) * \frac{1}{\pi t} \right) \quad (3.3)$$

The system's transfer function $H(j\omega)$ is found by Fourier transformation:

$$H(j\omega) = \mathcal{F}\{h(t)\} = 1 - (\cos(\alpha)e^{-j\omega\Delta\tau} + \sin(\alpha)e^{-j\omega\Delta\tau}(-j \cdot \text{sign}(\omega))) \quad (3.4)$$

I now calculate the absolute value to find the magnitude of carrier suppression:

$$|H(j\omega)|^2 = 2(1 - \cos(\omega\Delta\tau + \alpha \cdot \text{sign}(\omega))). \quad (3.5)$$

For nonnegative values of ω the signum function in (3.5) can be omitted:

$$|H(j\omega)|^2 = 2(1 - \cos(\omega\Delta\tau + \alpha)) \quad | \quad \omega \geq 0 \quad (3.6)$$

The absolute value of the transfer function (3.6) is a periodic function in ω . Figure 3.5 depicts a plot of (3.6) with $\Delta\tau = 1.06$ ns and $\alpha = 29.02^\circ$. As indicated in Figure 3.5 we define an attenuation bandwidth $B = f_u - f_l$ where the level of suppression is above the targeted isolation gain G_I . With increasing delay offset $\Delta\tau$ of the interference and the compensation paths, the period of $|H(j\omega)|^2$ shortens and reduces the bandwidth B for a specified suppression value.

To calculate the maximum allowed delay offset $\Delta\tau$ for specific values of B and G_I we set $\omega = 2\pi f_u$:

$$G_I = 2(1 - \cos(2\pi f_u \Delta\tau + \alpha)) \quad (3.7)$$

To achieve maximum extinction at the frequency f_0 we find the constraint

$$2\pi f_0 \Delta\tau + \alpha = 2\pi n, \quad n \in \mathbb{Z}. \quad (3.8)$$

When we use (3.8) to express α and insert this expression in (3.7) we get

$$\Delta\tau = \frac{\arccos(1 - \frac{G_I}{2})}{\pi B} \quad (3.9)$$

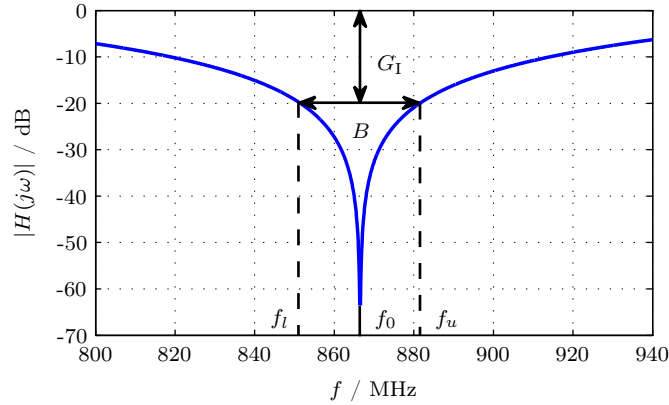


Figure 3.5: Transfer function of the modelled suppression system with $\Delta\tau = 1.06$ ns and $\alpha = 29.02^\circ$, creating 40 dB of suppression in the European RFID band.

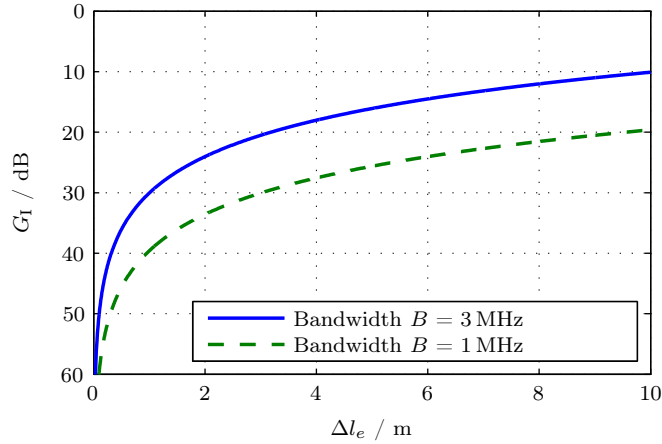


Figure 3.6: Isolation gain G_1 plotted over the electrical offset length Δl_e for two fixed bandwidth values.

where $f_u - f_0 = B/2$ was used. It is quite intuitive that the allowed delay for a given isolation gain is indirectly proportional to the targeted suppression bandwidth. For further interpretation it might be more intuitive to convert the delay offset $\Delta\tau$ into an electrical offset length $\Delta l_e = \Delta\tau \cdot c_0$. In Figure 3.6 the achieved attenuation is plotted over Δl_e for two different attenuation bandwidth values. The maximum allowed electrical length difference for 40 dB attenuation over the full European RFID band, being 3 MHz wide, is $\Delta l_e = 318$ mm, corresponding to the delay $\Delta\tau = 1.06$ ns picked for Figure 3.5.

When the leaking carrier canceller is used to compensate for an imperfect circulator in a single antenna scenario, the 318 mm boundary is easily achievable. The broadband suppression of reflections caused by badly matched antennas is more challenging. Especially, for non-handheld RFID readers where the antenna is attached with a cable of arbitrary length, the suppression bandwidth or rather the broadband attenuation can be severely degraded when the compensation path length is not adjusted accordingly.

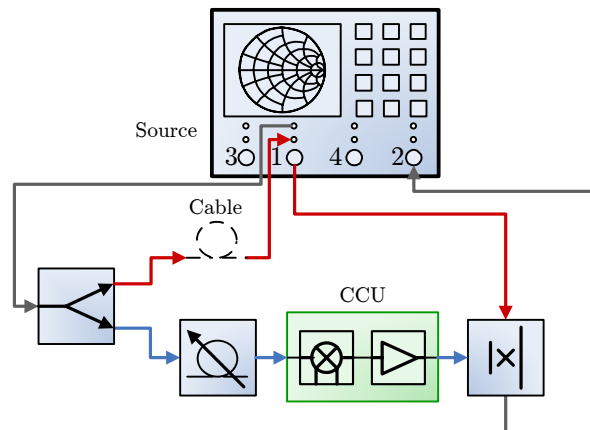


Figure 3.7: Measurement setup for broadband suppression properties of the CCU as leaking carrier canceller

3.3.1 Measurement Setup

To measure the realizable suppression ratio the test setup presented in Figure 3.7 is used. Our VNA provides direct access to the source ports of the internal measurement coupler. This access is used to insert a resistive 6 dB-power splitter to provide a reference signal for the CCU input port. Losses of the network analyser’s test set are compensated in the source path. Ports one and two of the network analyser are connected to the main path of a directional coupler, which is used to insert the output of the CCU module. A variable delay line is placed in the compensation path between power splitter and CCU to enable path length adaption. During the measurements different cables of fixed length were inserted in the reference path to generate defined path length offsets.

The VNA is calibrated using a regular Short Open Load Thru (SOLT) method, but using the directional coupler as “Thru”, while terminating the port which is later connected to the CCU. With this calibration, the VNA directly produces $|S_{21}|$ measurements corresponding to the overall transfer function $H(f)$ as calculated in (3.4)

3.3.2 Suppression Performance

In a first step the electrical path lengths of the main and compensation path were matched. This is done by continuous adjustments of the CCU’s vector modulator control input voltages and changing the setting of the variable delay line until no further enhancement of the attenuation bandwidth is achieved. For this adjustment a target suppression gain G_1 of 40 dB is chosen. Figure 3.8a presents the measurement results of the magnitude response of the resulting complete channel $H(j\omega)$ at this setting. A 40 dB suppression bandwidth B of 82 MHz is achieved. The dispersion of CCU, cables and directional coupler prohibit further enhancement of this value. This first measurement serves as a delay reference for the following measurements, especially because for frequencies close to 866.5 MHz the offset delay $\Delta\tau$ can be assumed to be zero. For the next step the adjustment of the variable delay line is not touched any more.

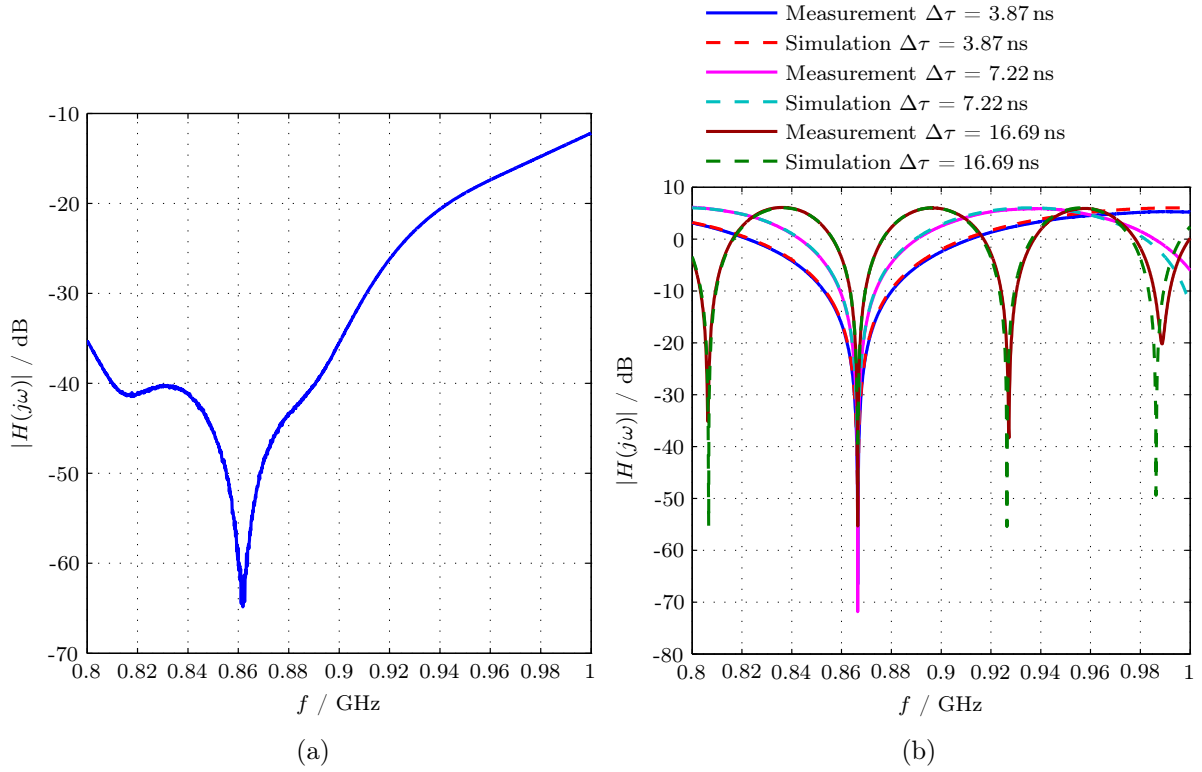


Figure 3.8: Magnitude response of the LCC measurement test setup: (a): with optimized reference path delay; (b) introducing extra path delay offsets.

In a second step fixed delays are introduced in the reference path by means of coaxial cables. These cables are characterized for their electrical length in a separate measurement with a conventionally calibrated VNA. Cables with electrical lengths of 3.87 ns, 7.22 ns and 16.69 ns were used. In our case this corresponds to mechanical lengths of 82 cm, 152 cm and 353 cm. For every measurement the phase controls of the CCU are adjusted for maximum attenuation at 866.5 MHz. The measured magnitude response is plotted in Figure 3.8b. At the centre frequency an attenuation values range between 55 dB and 70 dB.

The dashed lines correspond to simulations according to (3.6), where the measured values of the electrical length of the three test cables is used as $\Delta\tau$. Measured and simulated curves show strong conformity; at frequencies above 980 MHz a slight deviation is noticeable. This proves that the single tap model is suitable also in a practical hardware implementation to describe the behaviour of an LCC when it compensates a single tap leakage channel.

3.4 Multi Tap Model

I now extend the model to the more general case where the leakage channel is arbitrary. Again, the overall impulse response of the channel between TX and RX can be written as the sum of the leakage impulse response $h_L(t)$ and the canceller's impulse response $h_{\text{Can}}(t)$

$$h(t) = h_L(t) + h_{\text{Can}}(t). \quad (3.10)$$

In the previous Section 3.3 we treated a classical LCC, thus in this case the impulse response $h_{\text{Can}} = h_{\text{LCC}}$ is given by

$$h_{\text{LCC}}(t) = B \left(\cos(\alpha)\delta(t - \tau_1) + \sin(\alpha)\frac{1}{\pi(t - \tau_1)} \right), \quad (3.11)$$

where the amplitude B and phase angle α is controlled by the vector modulator in the LCC. The delay τ_1 is considered fixed, and controlled by the physical layout of the RFID reader only. I showed in (3.9), that the difference between this fixed delay τ_1 and the delay of the single reflecting point is indirectly proportional to the suppression bandwidth of the overall system. In the frequency domain, (3.11) corresponds to a frequency-flat canceller transfer function, which for optimum cancellation at frequency ω_0 is set to

$$H_{\text{LCC}}(j\omega) = \tilde{B}e^{-j\omega\tau_1} = -H_L(j\omega_0), \quad (3.12)$$

where \tilde{B} denotes the complex amplitude of the LCC including the phase rotation α . Note that in this equation, the right side is a single complex value not depending on frequency. The narrowband LCC is adjusted at ω_0 by picking the proper complex amplitude value given the fixed delay τ_1 . The corresponding impulse response is

$$h_{\text{LCC}}(t) = \tilde{B}\delta(t - \tau_1) = -H_L(f_0) \cdot \delta(t). \quad (3.13)$$

To be able to cancel arbitrary leakage channels, I introduce the BLC first published in [80] with the impulse response

$$h_{\text{BLC}}(t) = \sum_{i=1}^M B_i \left(\cos(\alpha_i)\delta(t - \tau_i) + \sin(\alpha_i)\frac{1}{\pi(t - \tau_i)} \right), \quad (3.14)$$

which is nothing but an M tap Finite Impulse Response (FIR) filter, with tap delays τ_i , amplitudes B_i , and phase angles α_i .

For optimum cancellation, the leakage channel must be inverted by the cancellation channel, so

$$h_{\text{BLC}}(t) = -h_L(t). \quad (3.15)$$

As long as the leakage channel can be approximated by a FIR filter, it is effectively cancelled by the BLC. In practise the use of FIR filters for channel equalization is widespread and known as the Rake receiver, and used in communication systems like UMTS [81, p. 376].

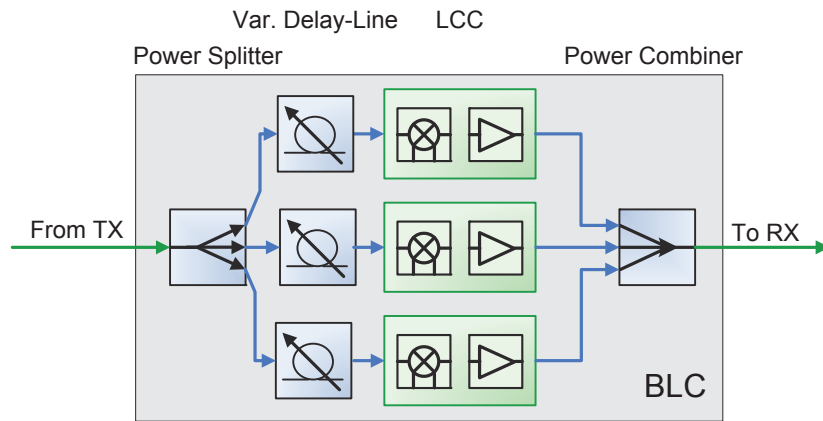
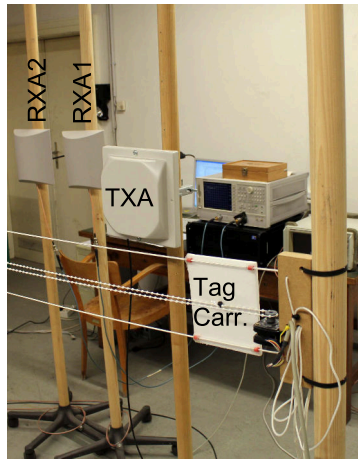
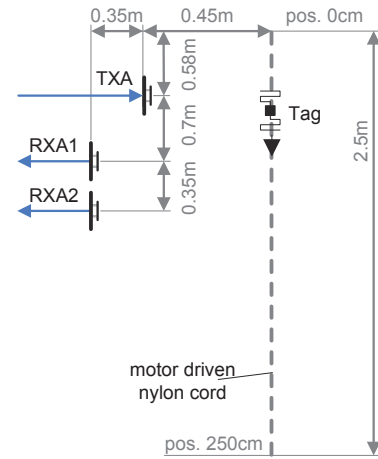


Figure 3.9: Block diagram of the proposed three tap BLC.



(a)



(b)

Figure 3.10: Photo (a) and principal drawing (b) of the measurement setup.

Figure 3.9 shows the block diagram of a practical realization of the BLC with $M = 3$ taps. The input signal is split in three equal parts using a power splitter. Every branch consists of a variable delay line and an LCC module which employs a vector modulator and an amplifier. Finally, the three branches are merged in a power combiner to form the output of the BLC which is injected into the receive path at the receiver. A practical implementation of a single branch of a BLC consisting of a variable delay line and a passive vector modulator is documented in [82]

3.4.1 Leakage Channel Measurement Setup

In this section I describe measurements carried out in the basement of the institute in the room where most of our RFID measurements are performed. The goal of this measurements initially reported in [80] is to capture the leakage channel of the RFID

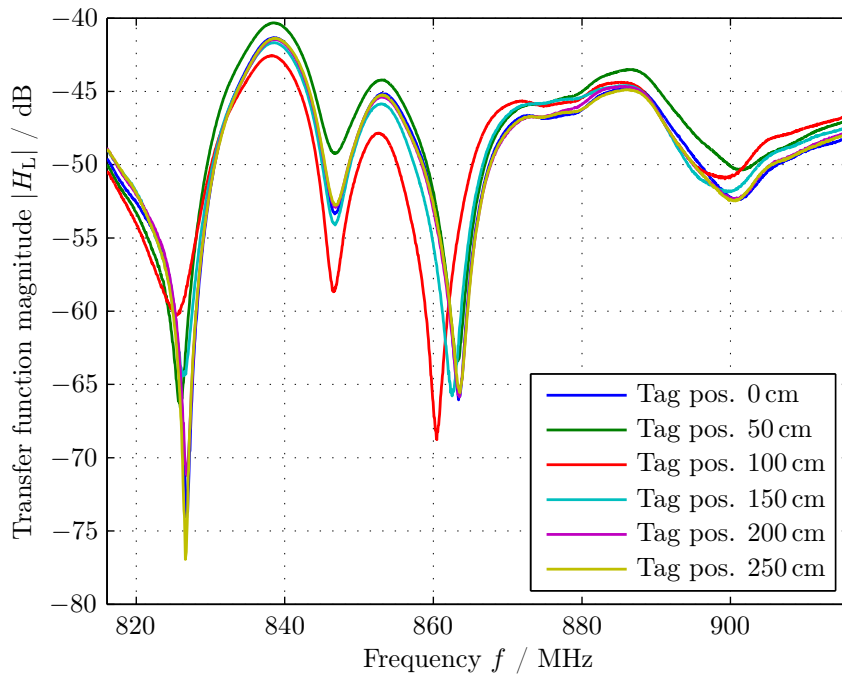


Figure 3.11: Leakage transfer function magnitude $|H_L|$ for different tag positions.

setup we are actually using for other experiments and show the feasibility of a three tap BLC.

The measurement setup consists of three commercial circular polarized patch antennas mounted on wooden supports, set up in a semi-industrial room, as shown in Figure 3.10a. Two identical antennas RXA1 and RXA2 with a nominal gain of 8 dBi are placed side by side. To increase the native isolation, a third antenna TXA with a nominal gain of 9 dBi is placed 35 cm offset to the two receive antennas RXA1 and RXA2, as depicted in Figure 3.10b. Additionally, a commercial RFID tag (UPM Raflatac DogBone) is mounted on a dielectric foam carrier, which can be moved on a track parallel to the receive antenna plane by means of a dielectric cord driven by a stepper motor. For the bistatic measurement considered here the tag track is mounted 45 cm in front of the transmit antenna TXA, and RXA1 is used as receive antenna. Both, TXA and RXA1 are connected to a VNA and 1601 samples between 816 MHz and 916 MHz are measured. We denote the transfer function between the two antennas, which is the leakage channel, by $H_L(f)$. In Figure 3.11, its magnitude $|H_L(f)|$ is plotted for several different tag positions. Note that here, the RFID tag acts as a passive unmodulated reflector, since it is not addressed by a query command. For our observed scenario, the frequency response of the leakage channel is not flat, not even for the small bandwidth of the European RFID band, so any narrowband LCC will fail to compensate this.

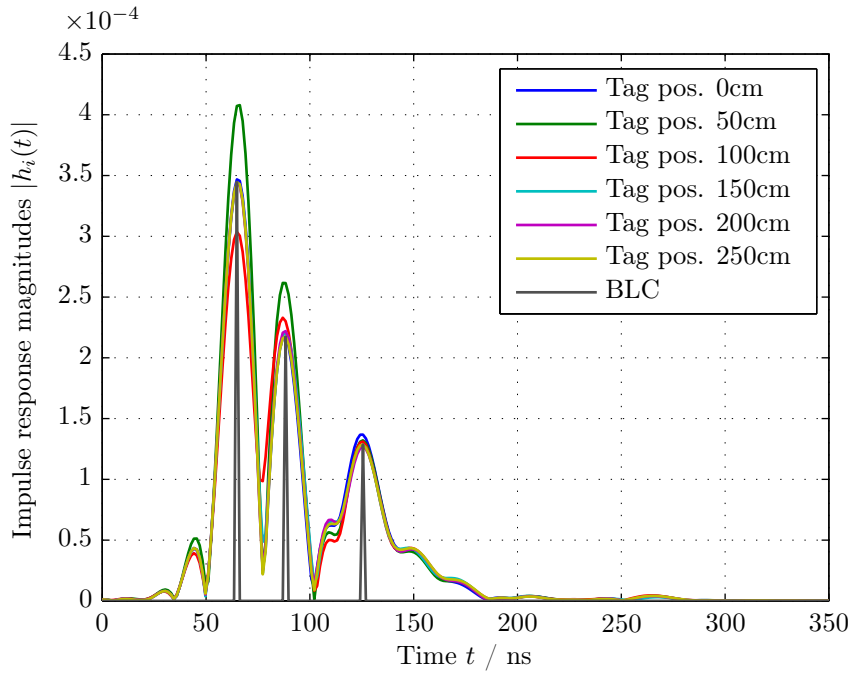


Figure 3.12: Impulse responses h_L and h_{BLC} for the leakage and BLC channel.

3.4.2 Broadband Leakage Canceller Evaluation

Figure 3.12 presents the impulse response calculated from the transfer function. First, a Tukey window [83] is applied in frequency domain with coefficient $\alpha = 0.65$ (i.e. 35% of the transfer function remains unchanged). This is done to reduce the artifacts that are generated if the frequency data, which is by nature hard windowed by the selected frequency range of the measurement, is converted to an impulse response by means of an inverse Fourier transform. Next, the windowed data are zero padded to achieve an interpolation in time. Finally the inverse discrete Fourier transform is carried out. The resulting impulse response $h_L(t)$ primarily consists of three peaks at delays 64.9 ns, 88.3 ns, and 125.6 ns, where most of the delay of the first peak is due to the cables connecting the antennas to the VNA, which were kept as usually used with our standard RFID reader testbed.

The three distinct pulses in the impulse response $h_L(t)$ motivate the use of a BLC with three taps, as shown in Figure 3.9. The impulse response $h_{BLC}(t)$ of this canceller is plotted in Figure 3.12. It is obtained by isolating the three most dominant samples (i.e., the samples with highest magnitude) in each of the three major peaks of $-h(t)$, which resulted from the measurements with the tag positioned at 250 cm. This tag position is chosen, since in this case, the influence of the tag to the measurements is negligible. Note that the negative sign in $-h(t)$ is introduced since the BLC is targeted to cancel out the leakage signal.

When converted to the frequency domain, $H_{BLC}(f)$ follows the leakage channel $H_L(f)$, as indicated in Figure 3.13. This figure compares the original transfer function $H_L(f)$, the windowed version which was used to calculate $h_L(t)$, the transfer function of the

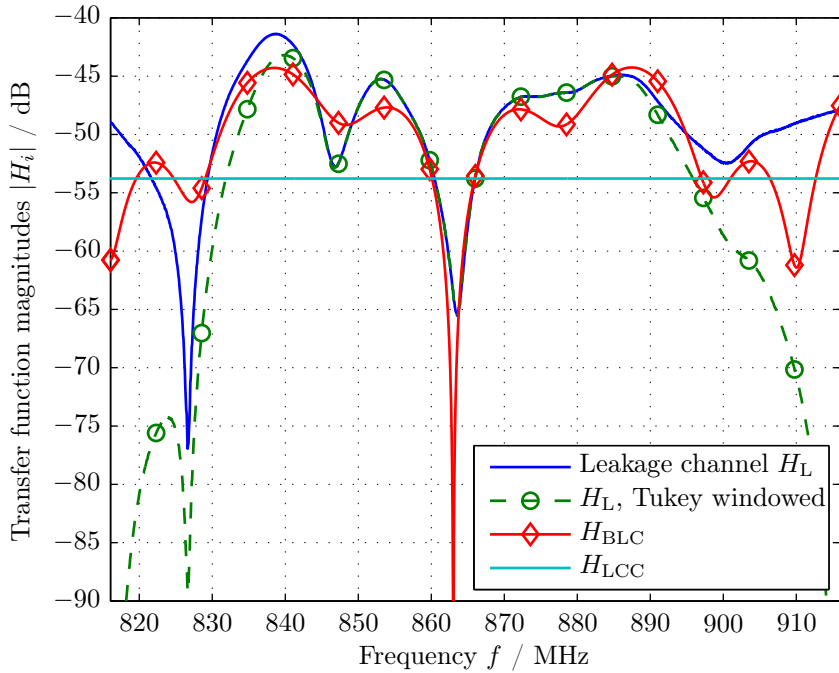


Figure 3.13: Magnitudes of the transfer functions of the leakage channel H_L , the Tukey windowed H_L , and the channels of the cancellers H_{BLC} , and H_{LCC} .

proposed BLC, and finally, $H_{LCC}(f)$ the transfer function for a conventional narrowband LCC adjusted at $f_0 = 866$ MHz. The improvement from the LCC to the BLC is evident, which is paid by tripling the hardware complexity of the canceller. Other scenarios, especially monostatic configurations lead to impulse responses with a higher number of significant peaks, but still a BLC with only three taps, adapted to the three highest peaks, follows the ideal transfer function more closely than a conventional LCC.

To quantify the results we define the isolation gain

$$G_I(f) = \frac{|H_L(f)|}{|H(f)|}, \quad (3.16)$$

where $H(f) = H_L(f) + H_{BLC}(f)$ is the resulting leakage path from transmitter to receiver after applying the BLC. A comparison of the isolation gains for BLC and LCC are plotted in Figure 3.14. Here, both cancellers are adjusted at the tag position 250 cm, and then remain constant for the other tag positions to investigate the performance of a static adjustment². It is observed from Figure 3.12 that for other tag positions a dynamic adaption of the BLC will only require changes of the phase and amplitude components, since the peak delays stay constant.

²The LCC is adjusted for zero delay τ_1 in (3.12). This was compared to setting τ_1 equal to the delay of the first tap of the BLC. The results are very similar to the LCC setting analysed here, except for slightly different isolation gains at frequency offsets larger than 3 MHz, being slightly larger at higher frequencies and lower at lower frequencies — which is a coincidence depending on the specific leakage channel.

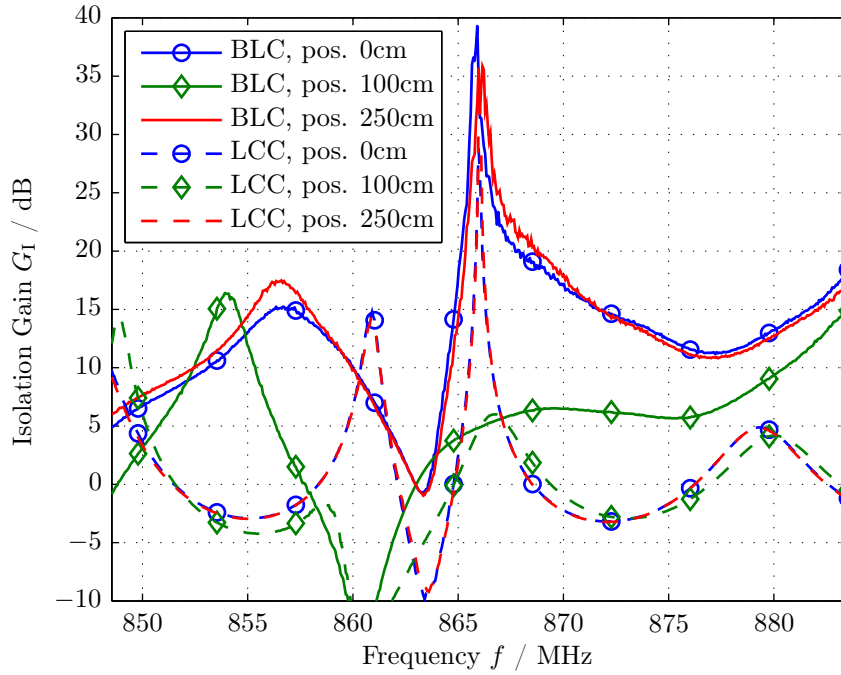


Figure 3.14: Isolation gain $G_I = \frac{|H_L(f)|}{|H(f)|}$ for BLC and LCC.

For the adjustment tag position at 250 cm the isolation gains at the centre frequency $f_0 = 866$ MHz are extremely large for both cancellers. However, while the LCC shows an isolation gain higher than 15 dB only on a 600 kHz wide frequency band, the isolation gain of the BLC remains above 15 dB over a 6.7 MHz wide frequency range. For larger bandwidths the gain of the LCC becomes negative, so it actually degrades the original leakage transfer function in these regimes. In the whole observed frequency band ranging from 848.5 MHz to 883.5 MHz, which is equal to the range of $H(f)$ untouched by windowing, the gain of the BLC stays positive, with the exception of a -1 dB dent at 863.4 MHz. At this frequency, H has a strong intrinsic minimum (-66 dB) which is difficult to capture with the BLC. Keeping this in mind, a slight degradation of this very high isolation point can be accepted. For the worst case tag position 100 cm shown in Figure 3.14, the isolation gain is still positive, except for a region of very good intrinsic isolation between 857 MHz to 863 MHz, which is flattened out by the misadjusted BLC. To conclude, the BLC concept is proved based on realistic leakage channel measurements. The broad bandwidth properties of the BLC also remain under slight misalignment situations caused by a moved tag, here the BLC is robust and still performs better than an LCC.

3.5 Cancellation Adjustment Techniques

In the previous sections of this chapter I reported on bandwidth and implementation aspects of LCCs and showed measurement results of realized suppression gains. In this section I now treat the topic of LCC adjustment techniques, based on [84, 85]. Adjustment

of an LCC is tricky because the purpose of the LCC is to lower the demands on the RX architecture — but so this simpler receiver cannot be used to adjust the LCC, because it is overloaded from the leaking TX signal. While there exist many publications on hardware implementations of LCCs, few exist on adjustment algorithms to adapt them. However, adaption is critical [86, 80], because typical RFID scenarios like warehouses and conveyor belts change permanently and therefore cannot be adjusted statically.

In this section I will:

- present a comparison of four adjustment algorithms, regarding their demands on hardware linearity, detector type and LCC calibration, and their setting speed,
- present a new “fast algorithm”, which is analytically and numerically analysed regarding noise performance and bias,
- practically compare the fast algorithm with the gradient search algorithm using our RFID testbed,
- present an enhancement to the fast algorithm, which both gives better results under nonlinear detector conditions, as well as a better noise performance,
- report on observed step number reductions by using the result of the fast algorithm for initialising the gradient algorithm: 72% reduction on average in our experiment, which directly relates to the speed of the algorithm.

The following discussion of adjustment methods applies to classical LCCs. For broadband suppression, sophisticated adjustment techniques require a vectorial detection over a broad frequency range. Thus, for most situations adjustments of BLCs will require two steps, where first only a single path of the BLC is adjusted to bring the receiver in a linear operational range, and second, the now operational receiver will be used to further adjust the BLC. For the first step the same methods apply which I discuss now for LCCs.

3.5.1 LCC Adjustment principles

In this section the principal possibilities of active leakage cancellation adjustment techniques with focus on hardware challenges are discussed. In the beginning I present a generic RFID reader hardware concept to illustrate the different detection points used for LCC adjustment. Figure 3.15 illustrates the simplified block diagram of this bistatic RFID reader. The upper part of the figure shows the transmitter, which is composed of a signal generator, a modulator to send data to the tag, a Power Amplifier (PA) to create the necessary output power, and a directional coupler. This coupler is used to extract a small part of the transmit signal and feed it into the LCC. Most of the transmit power is fed to the transmit antenna, where it is radiated. The lower part of Figure 3.15 illustrates the reader’s receiver part. The receiver antenna picks up the tag’s response and an unwelcome leakage signal from the transmitter. Both signals pass a Band Pass Filter (BPF) and directional couplers (CPLRs). The first coupler enables injection of the cancellation signal from the LCC. The second coupler feeds Detector (Det.) A. The coupler is followed by a Low Noise Amplifier (LNA) and a mixer stage. The received signal is filtered and amplified by a Variable Gain Amplifier (VGA). Here, again a directional coupler is present to feed Det. B. The coupler is followed by an Analogue to Digital

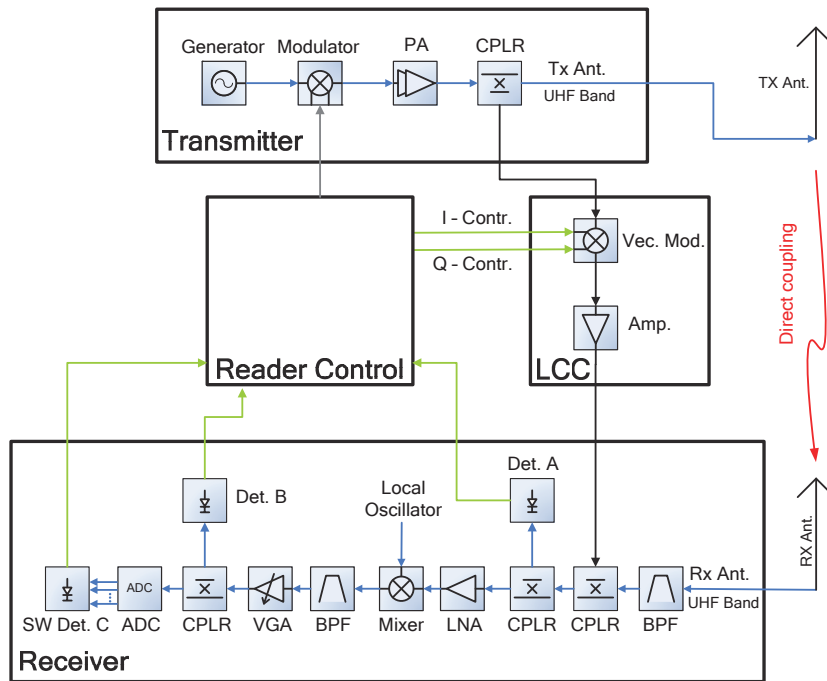


Figure 3.15: Block diagram of a simplified RFID reader showing possible detector positions for LCC adjustment routines.

Converter (ADC), which converts the received signal into a data stream. Detector C is implemented in the digital domain.

The LCC consists of a vector modulator and an amplifier. The vector modulator is controlled by the reader control block and enables to adjust the amplitude and phase of the transmit signal sample to cancel the leakage signal in the receiver’s directional coupler. The amplifier compensates for the coupling losses and enables cancellation of strong leakage signals.

Conventional RFID readers rarely have that many detectors as were described before. However, at least one is necessary to implement any LCC adjustment routine, but not every detector position or type supports every algorithm. We use the very general setup described in Figure 3.15 to exemplify RFID reader implementations with focus on possible LCC control implementations. Besides the location, we distinguish between scalar power detectors and vector detectors which also capture the phase of the incoming signal. The second type requires a reference signal that is either supplied from the reader’s transmitter part or from the ADC sampling clock. We use this generic RFID reader model through the next sections where we describe different automatic LCC adaption techniques, which aim to find the optimum Inphase- (I) and Quadrature (Q)-component settings for the LCC.

Our generic model is applicable to stationary RFID readers as well as to handheld devices. The latter usually employ integrated antennas which enable a better control of the typical expected leakage values and potentially a simpler LCC design. To save space and costs the LCC may also be included in the antenna which was presented in

[69]. Besides these differences, all LCC circuits need to be adjusted. While it might be desirable for mobile devices to reduce hardware complexity for smaller packages and lower costs, we will see that there is a tradeoff between adjustment speed and necessary hardware complexity for the different adjustment algorithms. Since handheld readers most likely are moved all the time during their use, permanent and fast adjustment routines are beneficial.

Full Search Algorithm

The most primitive way to find the optimum setting for an LCC is by trying all possible LCC settings and picking the one which proved to have the best result. If inphase and quadrature components both have N settings, N^2 measurements have to be performed. So one obvious drawback of this technique is the large amount of measurements and adjustment steps which need to be performed before the final result is gained. Depending on the speed of the given detector hardware, this corresponds to a large overall scanning time of the LCC which might be inadequate even for moderately changing environments. In these cases, this algorithm may completely fail to find an LCC setting, because the slowly moving optimum LCC setting might never be hit during the scanning process. Besides these obvious disadvantages, the full search algorithm has the benefit of accepting any type of power detector as long as it shows a monotone but not necessary linear input output relation. Here, I mean monotone if the output of the detector is increasing (or remains constant) when the input power is increasing. Even if the receiver is completely overloaded by the leakage signal for most LCC settings, the power detector will provide the lowest output signal at the appropriate LCC setting. Therefore, this algorithm may be used in receiver structures, which do not employ a special power detector for LCC adjustment, and it has very limited demands on receiver linearity. For these reasons, some commercial reader chips use this algorithm [71]. An improvement to reduce the scanning time, which is also implemented in [71], is to divide the algorithm into two steps and to scan only a fraction of all N^2 settings in the first step. When this subgrid is properly chosen at least one of the scanned subgrid points is close to the appropriate LCC setting, and therefore the receiver operates in the linear regime and gives useful power detector readings. In the second step only the vicinity of the point with the lowest measured remaining LCC power is scanned.

Gradient Search Algorithm

The gradient search algorithm, which is also called method of the steepest descent [87, Sec.5.3], is an iterative approach to find the optimum LCC setting. For every step n , the algorithm finds the local gradient ∇_n of the power distribution versus the LCC setting. This is done by performing three measurements: First, the power at the actual LCC setting c_n is recorded. Then the LCC setting is changed for some small value δ in the inphase component only, and again the resulting power is recorded. The last measurement records the power after applying a small change in the LCC's quadrature component only. Based on these three power values, the local gradient to the power distribution ∇_n is

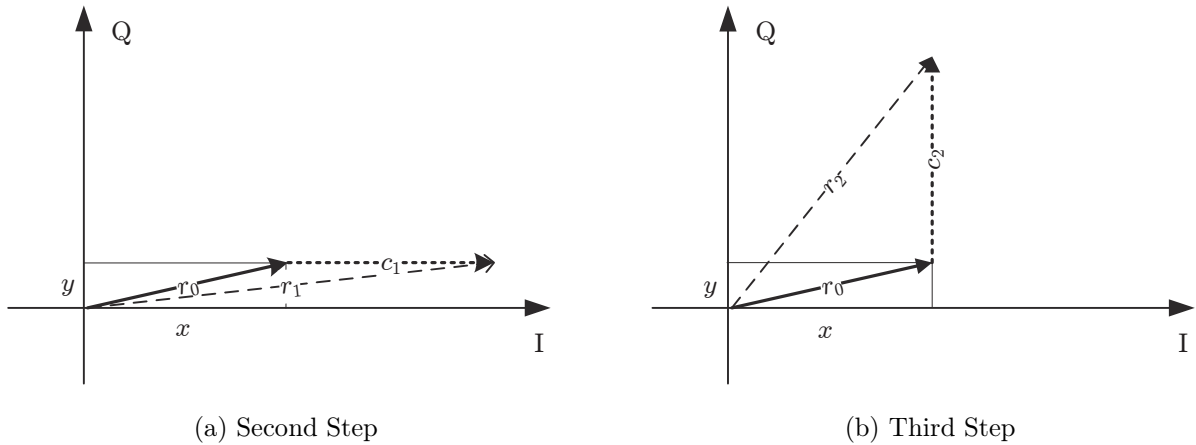


Figure 3.16: Illustration of the leaking signal and the probing signal at the (a) second step; (b) third step of the algorithm.

calculated, and a new LCC setting is found by

$$c_{n+1} = c_n - \mu \nabla_n, \quad (3.17)$$

where μ is a positive, real-valued constant called the step-size parameter. Beginning from a starting point that is usually set to zero ($c_0 = 0$), the gradient search algorithm step by step tries to approach the optimum LCC setting. Setting the step-size parameter μ is critical for this algorithm to work: If it is too small many steps are necessary to obtain the final value. Setting it too high results in oscillations and the algorithm will not converge. A similar problem exists for the deviation value δ that is used to measure the gradient. Choosing δ too large will possibly lead to false gradient measurements when it is applied at close proximity to the optimum value. A small δ implies a small change in power and in the presence of noise an unreliable gradient measure.

Since it is an iterative technique, the gradient search algorithm is well suited for changing environments. Another benefits of this technique are the moderate linearity constraints which it imposes on the reader. As long as the power detector is strictly monotone and the step-width is chosen small enough to ensure stability, the algorithm will converge to the optimum LCC setting point. Few authors explicitly state adjustment algorithms but [69] are using a gradient based approach, as well as [65], who describe a similar approach and use a variable step-width.

Fast Algorithm

The fast algorithm is a new technique which I first published in [84]. In this section we will give a short description of the principle operation, while in later sections a noise analysis, numerical simulations and measurement results are presented.

The algorithm gains the optimum LCC setting by obtaining three amplitude measurements. These measurements are very similar to the ones performed to gain the gradient

in the gradient algorithm, but in contrast to the gradient algorithm do not provide an enhancement in information for the next iteration, but immediately provide the correct LCC setting.

In the first step the plain leakage amplitude without any LCC signal is measured by setting the complex LCC output $c_0 = 0$ and measuring the input amplitude:

$$r_0 = \sqrt{x^2 + y^2}, \quad (3.18)$$

where x and y are the unknown I- and Q-components of the leakage signal.

In the second step we apply a signal of amplitude r_0 with the I-channel of the LCC, as illustrated in Figure 3.16a. Thus the complex output signal of the LCC is $c_1 = r_0 + j0$. The amplitude measurement in this step equals

$$r_1 = \sqrt{(x + r_0)^2 + y^2}. \quad (3.19)$$

In third step we now probe the quadrature component of the leakage by setting the LCC to $c_2 = jr_0$, see Figure 3.16b, and receive:

$$r_2 = \sqrt{x^2 + (y + r_0)^2}. \quad (3.20)$$

With these measurements we find the components of the leaking signal by calculating:

$$\begin{aligned} \hat{x} &= \frac{\frac{1}{2}r_1^2 - r_0^2}{r_0} = x \\ \hat{y} &= \frac{\frac{1}{2}r_2^2 - r_0^2}{r_0} = y \end{aligned} \quad (3.21)$$

So the optimum LCC setting is found to be $c_{\text{opt}} = -x - jy$.

In contrast to the techniques described before, the detector has to be linear in amplitude for this algorithm to perform satisfactorily. The benefit of this approach is that it is very fast and may be used for changing environments as long as the leakage channel remains constant during the three measurement steps, which is the same condition as for the gradient algorithm. However, the fast algorithm requires calibration of the LCC settings, which means that for a pure LCC signal the relation between detector readings and LCC setting has to be known. A practical implementation of this calibration is explained in Section 3.5.3. Based on the calibration it is possible to generate the appropriate probing signal amplitudes and finally the compensation signal c_{opt} based on Equation 3.21.

Direct I/Q Algorithm

This is a straightforward technique which requires a receiver equipped with a vector signal detector. Additionally, the LCC settings have to be calibrated with respect to this detector. Once a leakage signal is received, the inphase and quadrature components of this leakage signal are detected in the vector detector. The only necessary step is to set the LCC I- and Q-values opposite to the leakage signal. The benefit of this approach

Table 3.1: Hardware demand and speed comparison of LCC adjustment techniques.

Algorithm	Detector Type	Lin. Constr.	Number of Steps	LCC Calib.
Full Search	Power	None	N^2	No
Gradient Search	Power	Low	3 to $\frac{3N}{2}$	Minimal
Fast Algorithm	Amplitude	High	3	Yes
Direct I/Q	I/Q Amplitude	High	1	Yes

is extreme speed, when compared to all other techniques. However, it is the technique with the highest hardware demands, both for the detector type and the necessary LCC calibration.

The vector detector may either be implemented in the digital domain as detector C in Figure 3.15, or as separate hardware vector detector in positions A or B. The authors of [63] present a receiver structure which employs a dedicated hardware receiver in position A which is suitable for a direct I/Q detection algorithm.

Comparison of Adjustment Principles

Before we start our description of detector positions and their influence on detector performance, we summarize the descriptions of the described algorithms in Table 3.1. The algorithm name is given in the first column, the second column states the detector type which is employed. While the full search and gradient search algorithms only require power values, the fast algorithm commands for amplitude values, and the direct I/Q-algorithm even demands for a vector amplitude i.e. an I/Q-amplitude detector. The third column lists the linearity constraints of the algorithms and the fourth column states the number of steps which every algorithm requires to find c_{opt} . Here we define step as the process of setting the LCC to a certain value and taking a measurement. The full search algorithm scans the complete I/Q-plane of the LCC, so it takes N^2 steps when N is the number of I- and Q-settings. As the gradient algorithm is iterative, the necessary number of iterations is unknown. Every iteration requires three measurements, therefore the minimum number of steps is equal to three. When the algorithm converges without oscillations, the maximum number of iterations is half of the I- and Q-plane width, corresponding to $\frac{3N}{2}$ steps. The fast algorithm takes three measurements which corresponds to three steps in Table 3.1. As was described before, the full search and the gradient search do not require any LCC calibration, while the fast algorithm and the direct I/Q-method do. However, for picking the proper step-width μ , the maximum change per LCC step needs to be known which corresponds to the “minimal” entry in Table 3.1.

Detector Positions

We now discuss the possible detector positions with respect to our principal RFID reader described in Figure 3.15. Detector A is positioned right at the beginning of the receiver. No active components precede this detector, so only the detector itself is defining its

output linearity. Therefore, this position is well suited for algorithms which require a linear detector behaviour like the fast algorithm or the direct I/Q-method. However, for the second a more complex vector detector needs to be implemented. The other two algorithms will also operate properly with this detector.

Detector position B is positioned at the end of the analogue receiver chain either at a low intermediate frequency or at the baseband. When compared to detector A higher signal levels and lower frequencies are present at position B and therefore the implementation of the detector itself is less demanding. However, the receiver chain which precedes the detector might degrade the linearity of the detector. Therefore this position is well suited for techniques with low linearity constraint, like the full search algorithm or the gradient search approach.

Detector C in general does not require any additional hardware because it is implemented in software. It is relatively easily implemented as a vector power detector. The drawback of this detector is the fact, that the complete receiver chain including amplifiers, mixers and ADCs is passed before the detector. For linear functionality this complete chain has to operate in the linear domain as well. This increases the requirements on the whole receiver, and at the end makes the use of an LCC questionable — if the dynamic range of the receiver is large enough to properly detect signals under leakage carrier conditions, why bother to implement an LCC? It still makes sense to compensate the leakage in this case, because the linearity requirements regarding detecting the leakage or detecting the weak received tag response under the presence of leakage are still diverging, especially when we concern the necessary ADC resolution and TX noise, see Figure 3.3.

3.5.2 Noise Analysis

In this section I will present a detailed noise analysis for the fast algorithm. The estimator's bias and the estimator's error variance will be derived as a function of Carrier to Noise Ratio (CNR). For the other algorithms a short description follows:

As the full search algorithm searches the lattice of N^2 LCC setting points and picks the best one - the final setting error is not only constraint on the CNR at the detector but also on the quantization error due to the finite number of setting points. For high CNR values the correct point will be picked with high probability, and the setting error is dominated by the quantization error which is proportional to $\frac{1}{N^2}$ [88, Chap. 5.6]. For the low CNR regime or when N is very large, noise limits the detection of the minimum power at the optimum LCC setting point when scanning the complete I/Q-plane. Since this null is rather distinct [68, 70], the noise influence is low.

For the gradient search algorithm, the noise influence is uncritical due to its iterative nature. This is of course only true if the step-size is chosen small enough to guarantee convergence under noise influence.

The noise analysis for the direct I/Q-algorithm is straightforward and we will use it as a reference for the fast algorithm. Since the I- and Q-components of the leakage signal are directly measured by an appropriate detector, the detector noise variance and bias are equal to the algorithm's error noise variance and bias.

Analytic analysis

In this section I expand the noise free description of the fast algorithm given in Section 3.5.1 for the case which includes noisy I- and Q-components. In an actual RFID reader implementation, many parts in the transmitter, channel, receiver, detector, and possibly an ADC following the detector contribute to noise which degrades the measurements described in Equation 3.18 to Equation 3.20. Depending on the underlying physics of these noise sources, and their position in the TX–RX-chain, their noise has to be modelled in different ways. In the following section, we will focus on strictly white, statistically independent noise that adds to the I- and Q-components. Further, we focus on the estimation of the inphase component \hat{x} , as these results later may easily be adapted to \hat{y} .

To include the noise, we replace the noise free leakage components x and y with:

$$x_i = x + u_i, \quad y_i = y + v_i, \quad (3.22)$$

where u_i and v_i are the realizations of the statistically independent noise processes U and V . We expand Equation 3.18 and get

$$r_0 = \sqrt{x_0^2 + y_0^2} = \sqrt{(x + u_0)^2 + (y + v_0)^2}, \quad (3.23)$$

which includes the noise realizations u_0 and v_0 of the first step. We apply noise to the second measurement as well and receive:

$$r_1 = \sqrt{(x_1 + r_0)^2 + y_1^2} = \sqrt{(x + u_1 + r_0)^2 + (y + v_1)^2}. \quad (3.24)$$

We proceed to calculate the expectation of the estimated I-component \hat{x} :

$$\begin{aligned} \mathbb{E}\{\hat{x}\} &= \mathbb{E}\left\{\frac{\frac{1}{2}r_1^2 - r_0^2}{r_0}\right\} \\ &= \mathbb{E}\{x\} + \mathbb{E}\{u_1\} + \mathbb{E}\left\{\underbrace{\frac{xu_1 + yv_1 + \frac{u_1^2 + v_1^2}{2}}{r_0}}_{E_1}\right\} - \mathbb{E}\left\{\underbrace{\frac{xu_0 + yv_0 + \frac{u_0^2 + v_0^2}{2}}{r_0}}_{E_2}\right\} \quad (3.25) \\ &= x + \mu_u + \mathbb{E}\{E_1\} - \mathbb{E}\{E_2\}. \end{aligned}$$

This expectation includes x and an additive bias term. To further treat the bias, I now specialize the noise model: The noise of both signal components U and V is white and Gaussian, and has zero mean $\mu_u = \mu_v = 0$. The noise variances are σ_u^2 and σ_v^2 . As stated before, we presume statistical independence of the I- and Q-noise components.

The first bias term E_1 can be divided in the expectation of the numerator and the expectation of $1/r_0$, since numerator and denominator are statistically independent. Therefore

we compute the expectation of E_1 :

$$\begin{aligned}
 E\{E_1\} &= E\left\{xu_1 + yv_1 + \frac{u_1^2 + v_1^2}{2}\right\} E\left\{\frac{1}{r_0}\right\} \\
 &= \frac{\sigma_u^2 + \sigma_v^2}{2} E\left\{\frac{1}{\sqrt{x^2 + y^2 + 2xu_0 + 2yv_0 + u_0^2 + v_0^2}}\right\} \\
 &= \frac{\sigma_u^2 + \sigma_v^2}{2r} E\left\{\frac{1}{\sqrt{1 + \frac{2xu_0 + 2yv_0}{r^2} + \frac{u_0^2 + v_0^2}{r^2}}}\right\} = \frac{\sigma_u^2 + \sigma_v^2}{2r} E\left\{\frac{1}{\sqrt{1 + \varepsilon}}\right\},
 \end{aligned} \tag{3.26}$$

where $r = \sqrt{x^2 + y^2}$ is the noise-free amplitude of the leakage signal. To compute the result of the remaining expectation operator, which acts as a weighting factor for the preceding term including the noise variances, we approximate the root expression by a first order Taylor expansion for ε . This approximation holds when the noise components are small when compared to the carrier power r^2 i.e. the CNR is high.

$$\begin{aligned}
 E\{E_1\} &\approx \frac{\sigma_u^2 + \sigma_v^2}{2r} E\left\{1 - \frac{\varepsilon}{2}\right\} = \frac{\sigma_u^2 + \sigma_v^2}{2r} E\left\{1 - \frac{xu_0 + yv_0}{r^2} - \frac{u_0^2 + v_0^2}{2r^2}\right\} \\
 &= \frac{\sigma_u^2 + \sigma_v^2}{2r} - \frac{\sigma_u^4 + 2\sigma_u^2\sigma_v^2 + \sigma_v^4}{4r^3}
 \end{aligned} \tag{3.27}$$

We treat the second bias term E_2 in a different way, since here the separation of numerator and denominator is not possible. Instead, we reformulate the problem:

$$\begin{aligned}
 E_2 &= \frac{xu_0 + yv_0 + \frac{u_0^2 + v_0^2}{2}}{r\sqrt{1 + \frac{2xu_0 + 2yv_0}{r^2} + \frac{u_0^2 + v_0^2}{r^2}}} = \frac{r\left(-1 + 1 + \frac{2xu_0 + 2yv_0}{r^2} + \frac{u_0^2 + v_0^2}{r^2}\right)}{2\sqrt{1 + \underbrace{\frac{2xu_0 + 2yv_0}{r^2} + \frac{u_0^2 + v_0^2}{r^2}}_{\varepsilon}}} \\
 &= \frac{r}{2} \left(\sqrt{1 + \varepsilon} - \frac{1}{\sqrt{1 + \varepsilon}} \right).
 \end{aligned} \tag{3.28}$$

Similar to the step we used before, we approximate the expression in the brackets by using a second order Taylor expansion. We compute the expectation:

$$\begin{aligned}
 E\{E_2\} &\approx E\left\{\frac{r}{2} \left(1 + \frac{\varepsilon}{2} - \frac{\varepsilon^2}{8} - 1 + \frac{\varepsilon}{2} - \frac{3\varepsilon^2}{8}\right)\right\} = E\left\{\frac{r}{2} \left(\varepsilon - \frac{\varepsilon^2}{2}\right)\right\} \\
 &= r \left(\frac{\sigma_u^2 + \sigma_v^2}{2r^2} - \frac{x^2\sigma_u^2 + y^2\sigma_v^2}{r^4} - \frac{3\sigma_u^4 + 2\sigma_u^2\sigma_v^2 + 3\sigma_v^4}{4r^4} \right),
 \end{aligned} \tag{3.29}$$

using the fact that $E\{u_0^4\} = 3\sigma_u^4$ and $E\{v_0^4\} = 3\sigma_v^4$, since U and V are zero mean Gaussian variables. Finally, we compute $E\{\hat{x}\}$:

$$E\{\hat{x}\} = x + E\{E_1\} - E\{E_2\} \approx x + r \left(\frac{x^2\sigma_u^2 + y^2\sigma_v^2}{r^4} + \frac{\sigma_u^4 + \sigma_v^4}{2r^4} \right). \tag{3.30}$$

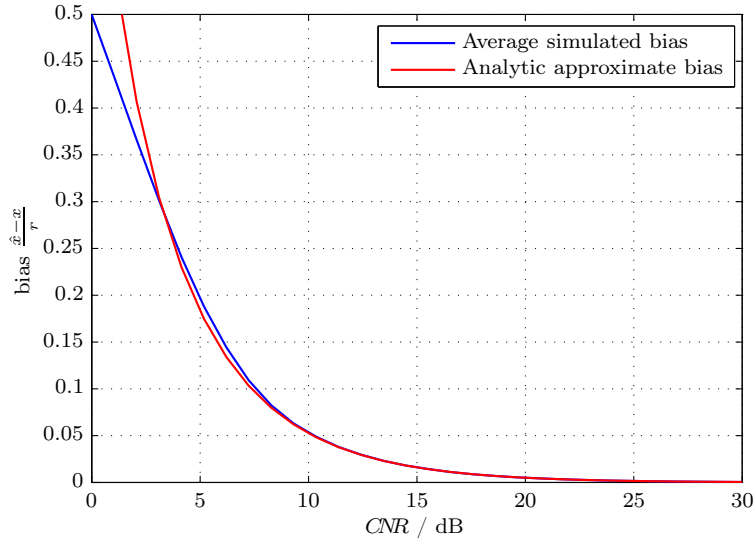


Figure 3.17: Comparison of the relative bias of the I-component estimate for the averaged Monte Carlo simulation results and the approximate analytic results plotted versus the CNR.

For the case of equal noise variances of the I- and Q-components, we further simplify this expression using $\sigma_u^2 = \sigma_v^2 = \sigma^2/2$, where σ^2 denotes the variance of the circularly symmetrical complex Gaussian variable composed of $U + jV$. Using this variance, the CNR is defined as the ratio of the leaking carrier power and the complex noise variance.

$$E\{\hat{x}\} \approx x + r \left(\frac{\sigma^2}{2r^2} + \frac{\sigma^4}{4r^4} \right) = x + r \left(\frac{1}{2CNR} + \frac{1}{4CNR^2} \right), \quad \text{with } CNR = \frac{r^2}{\sigma^2} \quad (3.31)$$

We see, that the proposed fast algorithm acts as a biased estimator. Since the bias is approximately known, it can be compensated if the CNR is known as well. In most RFID applications, leakage carrier compensation is performed to reduce a large leakage signal, so high CNRs are expected. In this case, the bias may be neglected.

Monte Carlo Simulations

I performed a Monte Carlo simulation of the fast algorithm using the same circularly symmetric complex Gaussian noise model as described before. For every CNR value, 4×10^6 simulations were performed. Figure 3.17 shows a comparison between the simulated average bias and the analytic approximate bias of Equation 3.31 derived before. We see that for CNRs larger than 3 dB both curves match very closely and the bias of the estimator is well described in Equation 3.31. For lower CNR values the approximations made in Equation 3.27 and Equation 3.29 do not hold any more and the curves start to diverge. This means that the bias of the estimator can be removed if the CNR is known. However, we will see that there is a good reason not to aim for an unbiased estimator for this particular problem.

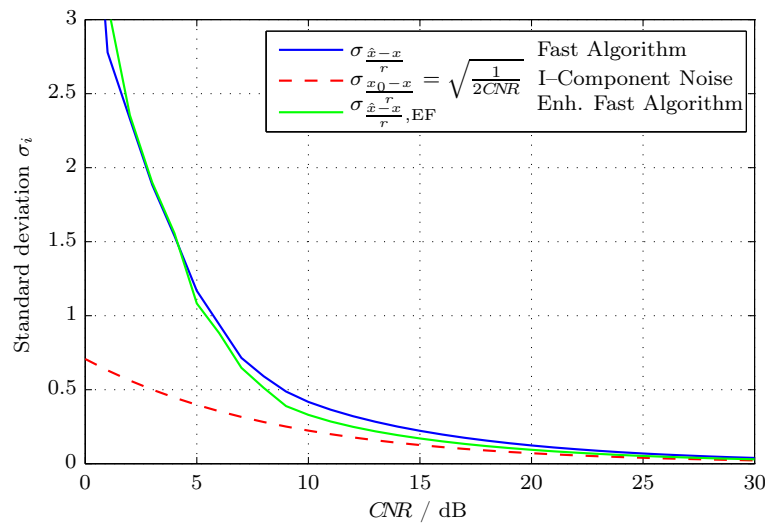


Figure 3.18: Comparison of Standard Deviations σ_i of relative I-Component Errors plotted vs. CNR.

Figure 3.18 shows the standard deviation of the standardized error $\frac{\hat{x}-x}{r}$ of the estimation of the I-component x . This is compared to the standard deviation of the standardized noise on the I-component, which is computed to $\frac{\sigma_u}{r} = \sqrt{\frac{1}{2\text{CNR}}}$. For low CNRs the error variance is severely increased when compared to the noise variance. However, in the higher CNR regime the difference is not so large, and both curves tend to zero. This comparison may also be interpreted as performance comparison between the fast algorithm and the direct I/Q algorithm, since the later algorithm's noise performance is directly given by the noise on each component. So it is evident that the direct vector measurement of the leakage employed by the direct I/Q algorithm does not show the noise enhancement and is superior for low CNRs. The third curve of the enhanced fast algorithm is discussed in Section 3.5.4.

Up to now, we just discussed the moments of the estimator based on the fast algorithm. Based on the Monte Carlo simulations, we now discuss scatter plots and histograms to analyse the statistical distribution of the estimation error. Figure 3.19a illustrates the error distribution for a very low CNR of -5dB by showing 8000 error points from the Monte Carlo simulations. We see that the noise is centred around the origin, but additionally is quite spread in the sector of positive I- and Q-components. The diagram also shows the mean of the error, which was obtained by 4×10^5 simulations and which is at $0.87 + 0.87j$. Applying a bias correction following Equation 3.31 leads to catastrophic over-compensation since the bias is not well captured at low CNRs as we discussed before. Further, from Figure 3.19a we see that there are good reasons not even to try to compensate for the bias and use the slightly biased estimator as it is: The mode of the error, which is the peak of the histogram of the error, is slightly negative ($-0.5 + -0.4j$) and therefore most of the estimates of x and y will be slightly negatively biased. This is also clear from the histogram shown in Figure 3.19b. The distribution has a long tail towards positive values which shifts the mean to this side. The unbiased estimator is found by

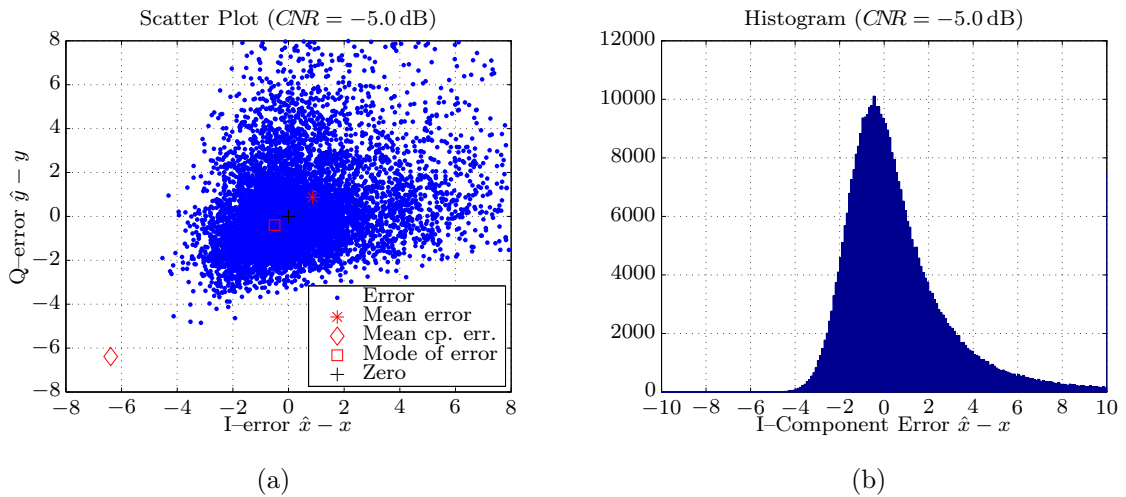


Figure 3.19: Scatterplot (a) and Histogram (b) of Estimation Error at $CNR = -5$ dB.

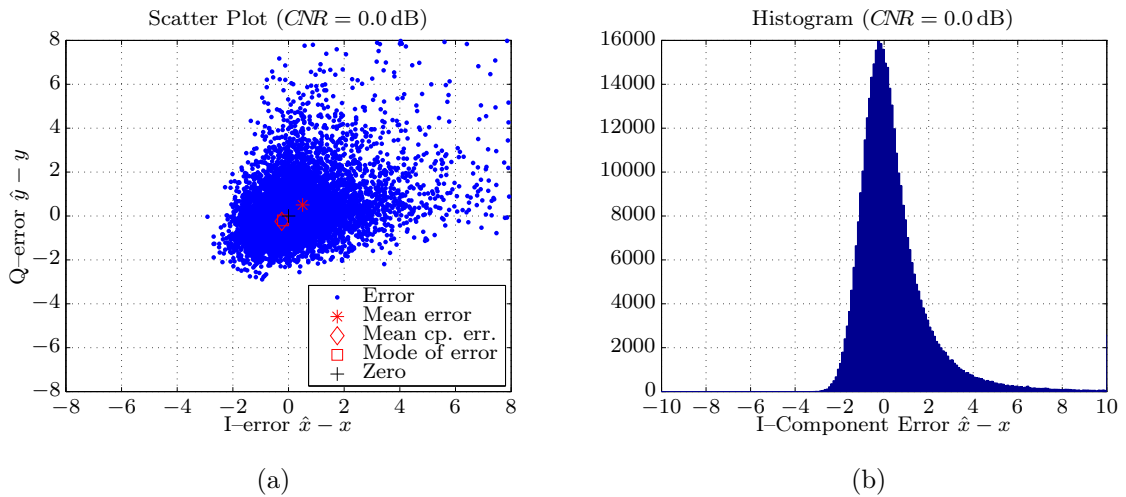


Figure 3.20: Scatterplot (a) and Histogram (b) of Estimation Error at $CNR = 0$ dB.

shifting this distribution to negative values, but this of course will shift the negative mode even further. Therefore, I suggest not to apply any bias correction.

The situation gets less distinct for a CNR of 0 dB as it is used in Figure 3.20. Here the bias compensation still leads to overcompensation, but at least the magnitude of the remaining bias is smaller. Since the mode of the error is still slightly negative for both components, the bias compensation can be omitted in favour of the closer error mode.

We see from the histogram in Figure 3.21b that for medium to high CNRs the error distribution becomes not only more compact, but also the long tail towards positive values is shortening. The same is observed from the scatter plot (Figure 3.21a), and both, mean error and error mode tend to the origin. Since the whole issue of carrier cancellation is tackled to combat strong leakage signals, we expect that most RFID readers will operate

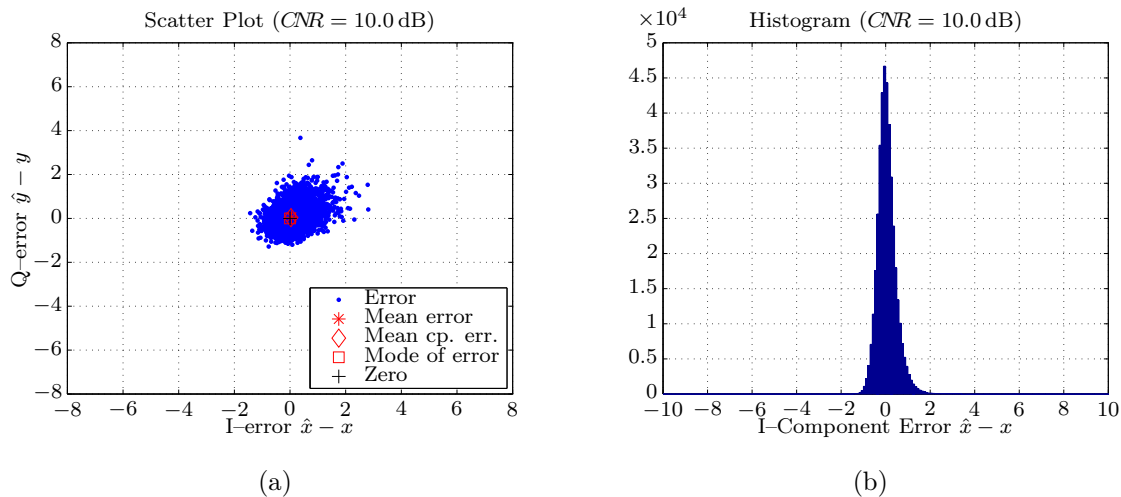


Figure 3.21: Scatterplot (a) and Histogram (b) of Estimation Error at $CNR = 10$ dB.

in high CNR regimes so that the skewness of the fast algorithm's error distribution is not an issue and bias compensation is superfluous.

3.5.3 Measurements

I performed measurements to compare the fast algorithm with the gradient algorithm. These measurements were based on our RFID testbed described in [75], which was controlled via a standard PC. The detailed measurement setup is described in the next section. Further, I will present results of the pure gradient algorithm, the fast algorithm and two enhanced algorithms based on these two.

Setup

Figure 3.22 illustrates the measurement setup used throughout the measurements. A photograph of the measurements setup is shown in Figure 3.23. The algorithms were evaluated for a pure sinewave carrier signal, which was created in the generator shown in the upper left corner. Its output signal is split up into the upper leakage generating path, and the lower cancellation path, which consists of a CCU module (CCU1), as was described in detail in Section 3.1. The upper leakage generating part either consists of one of two antenna scenarios, or is replaced by a second CCU to artificially generate a well defined leakage signal. When using the antennas, I first amplify the signal by 25 dB and then either feed a TX antenna and pick up the signal with a separate RX antenna to mimic a bistatic RFID scenario, or use a monostatic scenario with a single Transceiver (TRX) antenna and a circulator. The antennas have a gain of 8 dBi, and in the bistatic scenario were placed side by side facing the same direction for reasonable TX-RX decoupling.

Both, leakage and compensation signals were routed to the frontend of our RFID receiver [75], where they combine in the first directional coupler. This summed signal is

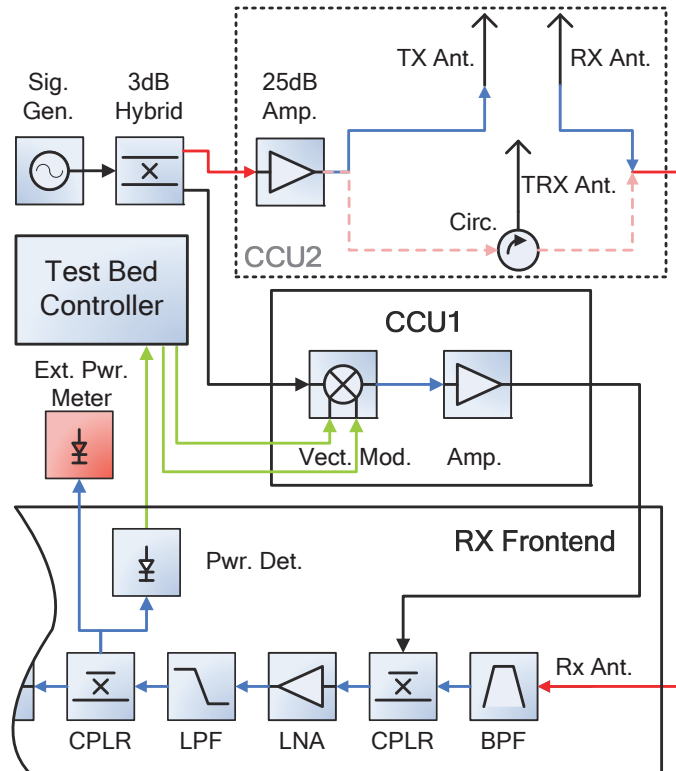


Figure 3.22: Fast algorithm evaluation measurement setup.

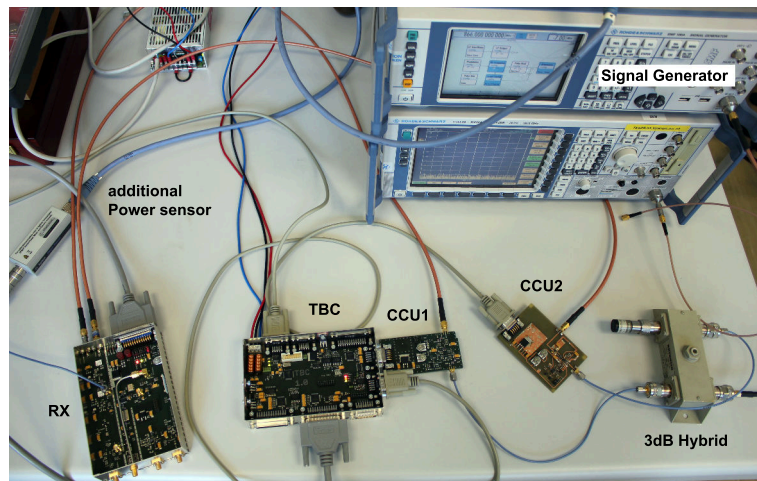


Figure 3.23: Artificial leakage measurement setup.

then fed through an LNA and a Low Pass Filter (LPF) and finally reaches the second directional coupler. Here, a part of the received signal is extracted and fed to the internal power detector and an external power metre. The internal logarithmic power detector output is routed to the Test Bed Controller (TBC) where it is used as a source signal for the tested LCC adjustment routines. Except for the LNA chosen for its highly linear operation, it is not affected by nonlinearity of any receiver hardware component, and therefore is comparable to detector A discussed in Section 3.5.1. The external power metre was used to obtain measurement data only, not for use in the adjustment algorithms. The TBC provides 16-bit ADCs to capture the power metre output signals, and 12-bit Digital to Analogue Converters (DACs) to control the I/Q-channels of CCU1 and CCU2, corresponding to 4096 possible settings for each channel.

The receiver's power detector provides a voltage which is logarithmically dependent on the power detector's input power. Since the fast algorithm demands for a linear amplitude detector, we used a function to convert every voltage measurement from the TBC corresponding to a power measurement from the power detector into a number. This linearizing function consists of an exponential function and additionally a multiplicative constant. This constant was chosen to result in most linear amplitude readings with respect to the output of the function. The LCC composed of CCU1 was calibrated with respect to these amplitude measurements by disconnecting the red antenna input signal in Figure 3.22 and by performing separate sweeps in the I- and Q-domain, always setting the unswept channel to zero. These sweeps were performed with a step-size of 10 corresponding to 410 recorded amplitude measurements per channel. The values obtained in these measurements were stored in a look-up table and aided by interpolation enabled to set the LCC to the correct probing values c_1 and c_2 necessary for steps two and three of the fast algorithm, and finally to c_{opt} found by Equation 3.21.

So in truth the calibration routine does not calibrate the power sensor of the receiver to the actual values of leakage signals, but instead calibrates the LCC settings with respect to power sensor readings. So changes of the antennas or cables will not affect the calibration as long as the connections between the LCC and the reader remain unchanged.

Measurement Results

For a first feasibility test of the hardware and the fast algorithm in a realistic RFID scenario, we conducted measurements using the monostatic and bistatic setups. For three different orientations of the antennas in the laboratory room, called A, B and C, isolation gains of the fast algorithm ranging from 8.1 dB to 27.9 dB were reached. Here we use the TX to RX isolation gain G_I in accordance with (3.16) as the ratio of uncanceled leakage power P_L divided by the remaining power of the cancelled leakage signal P_{CL}

$$G_I = \frac{P_L}{P_{CL}} = \frac{r^2}{|\hat{x} - x|^2 + |\hat{y} - y|^2}. \quad (3.32)$$

According to this definition, the isolation gain directly reveals the improvement of the used cancellation algorithm in comparison to a system without LCC usage. When expressed in

Table 3.2: Comparison of the isolation gains for the fast algorithm and a conventional gradient algorithm for single and dual antenna scenarios.

Scenario	$G_{I_{\text{Fast}}}$	$G_{I_{\text{Grad.}}}$
Dual ant. A	16.4 dB	14.7 dB
Dual ant. B	15.3 dB	16.1 dB
Dual ant. C	27.9 dB	24.6 dB
Single ant. A	8.1 dB	23.9 dB
Single ant. B	18.2 dB	23.7 dB
Single ant. C	18.1 dB	24.7 dB

decibels the isolation gain ranges from small negative values for badly misadjusted LCCs to large positive values for properly adjusted LCCs.

The complete results are summarized in Table 3.2. The second and third columns present the isolation gains G_I for the case of solely using the fast algorithm ($G_{I_{\text{Fast}}}$), and using a gradient algorithm ($G_{I_{\text{Grad.}}}$). Note, that for the dual antenna scenarios A and C the fast algorithm performs even slightly better than the gradient based algorithm. This is a coincidence, maybe caused by people acting as scatterers which were moving in the adjacent rooms while the measurement was running. The single antenna scenario showed less isolation than the dual antenna case, is expected from previous work [11]. The gradient search algorithm used has a gradient finding step-size of $\delta = 10$ in general and $\delta = 2$ for LCC settings close to the optimum LCC setting point. We used a variable step-size μ which was adapted proportional to $\sqrt{\nabla_n}$ according to an empirically chosen factor.

For a more systematic analysis the RFID antenna scenario is replaced with a second CCU module to retrieve systematic leakage cancellation measurements. CCU2 is swept over the I/Q-space in 65 steps per channel producing 4225 points in total. Figure 3.24 shows the resulting isolation gain $G_{I,F}$ of the fast algorithm in a pseudo-colour plot. The figure is plotted with respect to the I/Q-leakage plane i.e. the CCU2 DAC control plane. Since 12-bit DACs are used for both the I- and Q-channels, this plane ranges from -2048 to 2047 . In the centre no isolation gain is obtainable since the input power $P_L = 0$ is equal to zero. For increasing input powers, the isolation gain of the fast algorithm increases as well. Here, the presented gain is also limited by the low end of the power metre's dynamic range, since the absolute power levels at the power metre after the coupler and splitting losses are rather low. We note a decrease in isolation gain in three of the four corners for high input leakage powers. This effect is also visible in Figure 3.25. Here the ratio of the isolation gains of the gradient algorithm and the fast algorithm is plotted. Since I believe the gradient algorithm converges to the optimum LCC setting point under the given hardware constraints, I interpret Figure 3.25 as the fast algorithm's isolation gain deviation from the optimum value. For large areas the performance of the fast algorithm is very good, in 95% of the measured points the error is below 3dB. We again see the degradation at the same three corners.

For further analysis of this behaviour, let's discuss the relative error vector magnitude of

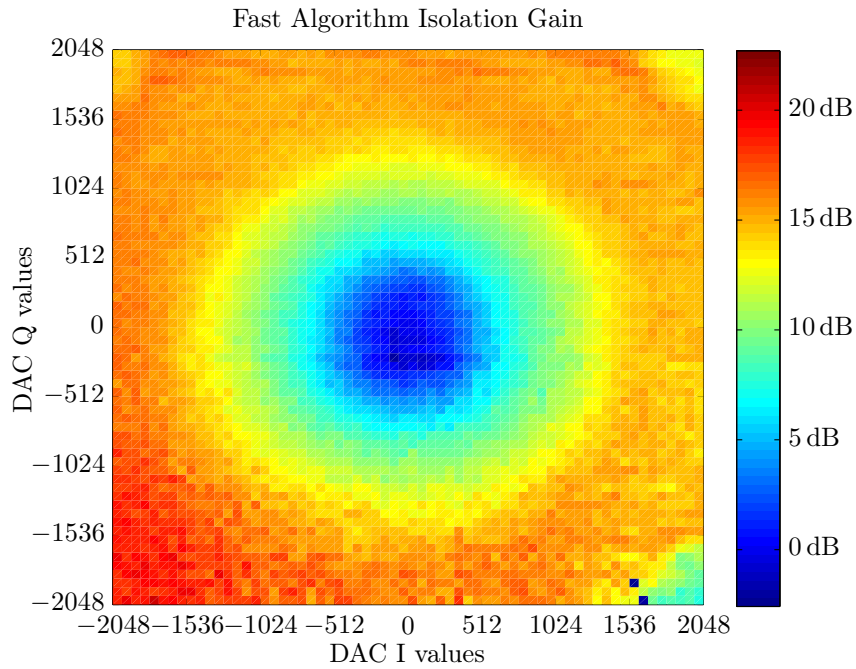


Figure 3.24: Isolation gain $G_{I,F}$ plotted on the I/Q-plane spanned by the leakage generating CCU2.

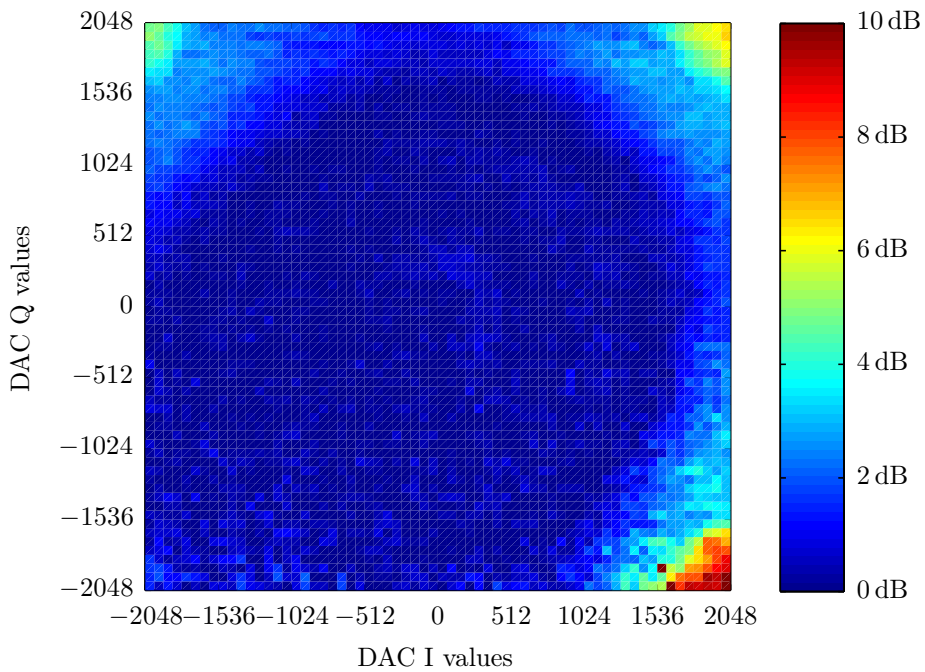


Figure 3.25: Isolation gain ratio $\frac{G_{I,G}}{G_{I,F}}$ of the gradient algorithm and the fast algorithm plotted on the I/Q-plane spanned by the leakage generating CCU2.

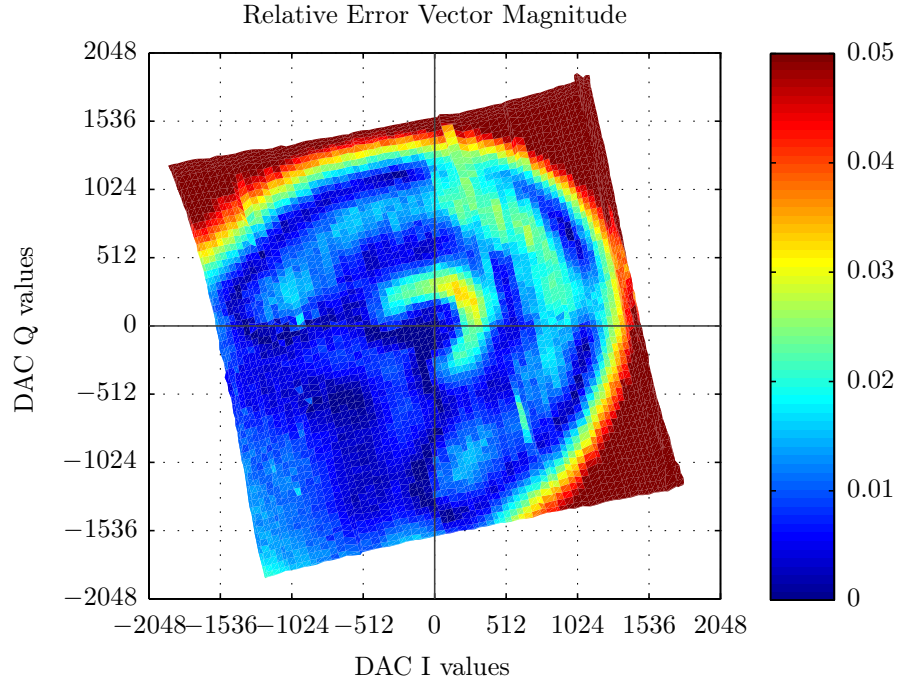


Figure 3.26: Relative magnitude of the setting error of the fast algorithm when compared to the gradient search algorithm $\sqrt{|\hat{x} - \hat{x}_G|^2 + |\hat{y} - \hat{y}_G|^2}/N$, plotted on the I/Q-space of CCU1 on the estimated leakage values \hat{x}_G and \hat{y}_G .

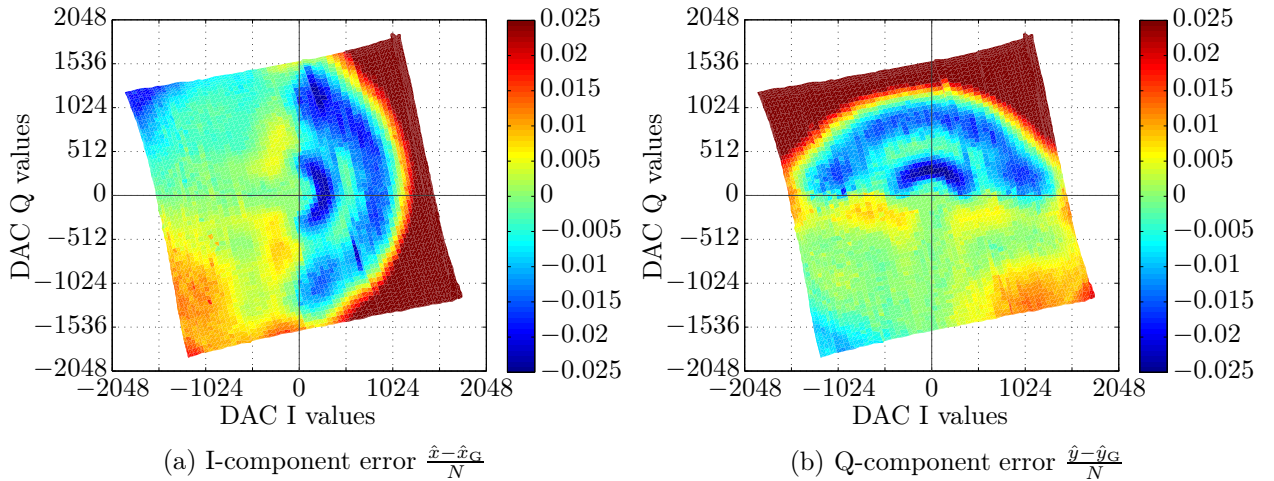


Figure 3.27: Relative setting error of the fast algorithm, plotted on the I/Q-space of CCU1 on the estimated leakage values \hat{x}_G and \hat{y}_G .

the fast algorithm when compared to the gradient algorithm $\sqrt{|\hat{x} - \hat{x}_G|^2 + |\hat{y} - \hat{y}_G|^2}/N$, which is shown in Figure 3.26. In contrast to the plots discussed before, now the plot with respect to the LCC's I/Q-plane is drawn, i.e., the CCU1 DAC values. Each plotted point corresponds to the estimated I- and Q- values \hat{x}_G and \hat{y}_G of the gradient algorithm for this leakage signal. We see that the resulting diagram is a square which is slightly smaller than the LCC's I/Q-space and rotated counterclockwise. The good agreement of the shape of the diagram to a perfect square is a sign that the gradient algorithm captures the true leakage values very closely. The rotation is due to the phase shift between leakage and compensation paths, which is mainly caused by the cabling of the measurement setup. The maximum leakage power was chosen to be slightly smaller than the maximum cancellation power, so that all leakage settings can be compensated. The majority of the measured points, 68%, exhibits an error smaller than 3%.

We see, that the lower left quadrant exhibits very low error magnitudes, typically below 2%. For all other quadrants we notice a behaviour which is primarily dependent on the leakage amplitude which results in concentric circles of higher and lower estimation errors of the fast algorithm. For large amplitudes in these quadrants relative error magnitudes larger than 5% are observed — which corresponds to the degraded performance in the three corners that we noted before. This behaviour is explained by the imperfect amplitude detector. Although the detector is situated almost directly at the receiver input, which is a prerequisite for linear operation under the constraints of reasonable receiver hardware demands (see Section 3.5.1), we see that the estimation error grows for larger amplitudes. This is due to the fact, that we are using a logarithmical power detector which decreases the sensitivity for high input amplitudes, and the conversion to linear values is not perfect. In the lower left quadrant this effect is not observed, since here the probing signals of the fast algorithm have opposite polarity to the leakage signals and therefore result in small signal amplitudes for steps two and three of the fast algorithm according to Equation 3.19 and Equation 3.20. This theory is fortified when we inspect Figure 3.27a and Figure 3.27b, which separately show the relative estimation errors of the I- and Q-components with respect to the gradient algorithm estimate. Figure 3.27a represents the error of the inphase component, which is very small for leakage signals with a negative I-component, and fluctuates for leakage signals with a positive I-component until it rapidly rises for large leakage amplitudes. In this domain the estimator overestimates the I-component. The critical step in the fast algorithm is the second measurement where the probing signal is applied and the resulting sum-amplitude is measured. In the left quadrants of Figure 3.27a this sum-amplitude is ranging from 0 to $\sqrt{2}r$, when r is the amplitude of the leakage signal. In the right quadrants the sum-amplitude ranges from $\sqrt{2}r$ to $2r$. The relatively high sum-amplitude with a small relative change and the use of the logarithmic detector lead to the worse performance of these right quadrants. The same is true for the upper quadrants of the Q-error shown in Figure 3.27b. Combining these two error patterns finally leads to the estimation error we see in Figure 3.26.

3.5.4 Enhanced Procedures

Based on the practical and theoretical findings, we present two enhancements to the set of algorithms described in Section 3.5.1.

Fast Algorithm with Bipolar Probing Signals

We have seen from the measurement results, that for our implemented system the fast algorithm is limited by the nonlinear behaviour of the logarithmical power detector. The quadrant which lies in the negative I- and Q-sectors of the leakage signal is only slightly affected, since here the probing signal and the leakage signal partially cancel each other and result in a low amplitude signal which is measured in the second and third step of the fast algorithm. We extend this beneficial behaviour to all four I/Q-quadrants by using positive and negative probing signals for I- and Q-components. For the negative probing signals, Equation 3.21 becomes

$$\begin{aligned}\hat{x} &= \frac{r_0^2 - \frac{1}{2}r_1^2}{r_0} = x \\ \hat{y} &= \frac{r_0^2 - \frac{1}{2}r_2^2}{r_0} = y.\end{aligned}\tag{3.33}$$

Since the fast algorithm in the first step measures the leakage amplitude r , it is immediately clear after the second step if this step should be repeated with a negative probing signal, because the resulting measured amplitude in the second step is smaller than $\sqrt{2}r$ when the I-component lies in the beneficial region. Using this conditional re-measurement technique, the fast algorithm's step count stated in Table 3.1 is increased from three, to three to five, with an average number of four steps. Of course it is also possible to always perform all five measurements, then even averaging of the two estimates of the same I/Q-component is possible. This makes sense for leakage signals whose signal power is concentrated in the other I/Q-component, so that leakage signal and probing signal are almost orthogonal to each other.

When using this technique of bipolar probing signals, the bias derived in Section 3.5.2 does not change as long as the statistical properties of the noise components U and V are the same, since then Equation 3.31 does not depend on x or y . The variance of the standardized estimation error for medium to high CNR values for this algorithm is smaller than the standard deviation of the regular fast algorithm, as we see from our Monte Carlo simulations in Figure 3.18. Therefore, this improvement which we had considered to overcome limitations due to the linearity of the amplitude detector also improves the estimation in the case of noise limited operation.

Based on the measurements presented in Figure 3.25 we calculate the average isolation gain ratio of the beneficial quadrant shown as the lower left quadrant in Figure 3.26 and get 0.48 dB. So we conclude that using the bipolar probing method for the fast algorithm, we reach the isolation gain of the gradient algorithm with a mean penalty of only 0.48 dB.

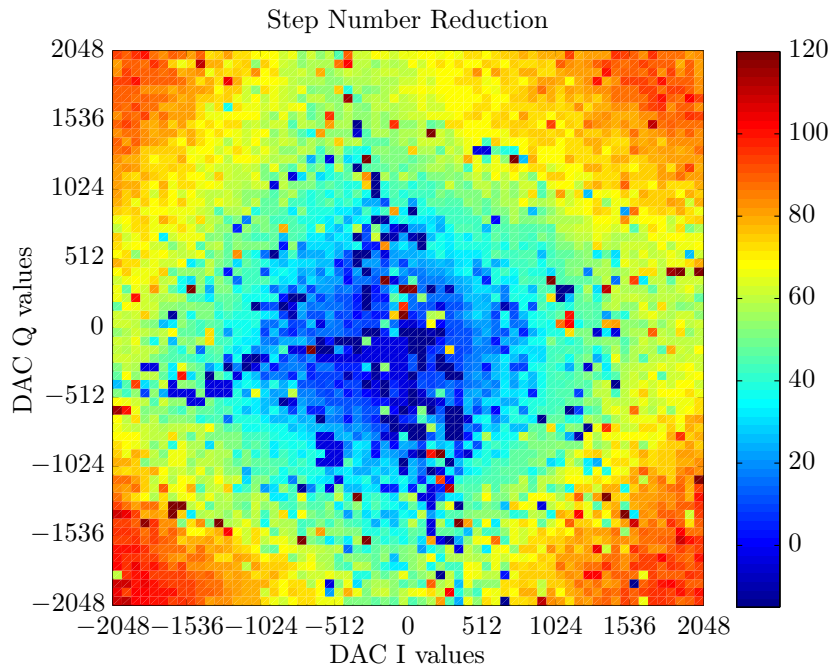


Figure 3.28: Reduction in number of steps required to converge to final value when comparing the pure gradient search algorithm with a gradient search algorithm aided by a fast algorithm starting point.

Fast Algorithm Aided Gradient Algorithm

In practical RFID scenarios many factors limit the performance of the fast algorithm, which are mainly based on nonlinear detector behaviour and imperfect LCC calibration. However, the fast algorithm may be used to aid the gradient algorithm by setting the starting point of the iterative search to the values found by the fast algorithm. We compare this fast algorithm aided gradient algorithm with our standard gradient algorithm using the same measurement setup as described in Section 3.5.3. Using the monostatic and bistatic antenna scenarios we compare the necessary number of steps for the algorithms to converge. If we stick to our step definition as stated in Section 3.5.1, the pure gradient algorithm required 39 to 135 steps, while the aided algorithm for the same scenarios was content with 21 to 60 steps.

We repeated the measurements with the systematic leakage sweep generated by CCU2 to compare the two algorithms on the complete I/Q-plane. A graphical representation of the results is given in Figure 3.28, which shows the reduction in number of steps when compared to the gradient algorithm starting at zero. We see that close to zero no improvement is possible since the starting point of the pure gradient search algorithm is zero anyway. For larger leakage amplitudes, which are practically more relevant, the fast algorithm provides a better starting point and reductions up to 120 steps are possible. On average, the pure gradient algorithm requires 75 steps while the aided algorithm only demands 21 steps, which is a decrease by 72%.

3.6 Summary

In this chapter I have treated the topic of Leakage Cancellation for RFID readers. First, a practical hardware implementation was presented, which is used for all the experiments described in this chapter. Then the issue of broadband cancellation was treated. I demonstrated that broadband cancellation is not only substantial for new RFID standards but also important for classical narrowband RFID where the transmitter noise is an issue. Two models for broadband suppression were derived: A single tap model which treats classical LCCs and leakage channels with a single delay path from transmitter to receiver, and a multi tap model which handles arbitrary leakage channels. I experimentally showed very good agreement of the predicted and measured cancellation bandwidths based on the single tap model using my hardware implementation. The multi tap model and leakage channel measurements, conducted in a realistic RFID scenario, motivated the novel BLC which is an analogue FIR filter and models the leakage channel. In the measured scenario the BLC improved the 15 dB suppression bandwidth by a factor of 11.

In the second part of the chapter, I focused on adjustment procedures for LCCs. Straightforward techniques require specialized reader hardware, which makes the use of an LCC to reduce hardware demands dubious. I gave a classification of adjustment principles and compared their hardware demands. A new technique with low hardware demands, the fast algorithm, was introduced which obtains the necessary LCC setting by three amplitude measurements. I derived an analytic noise analysis for this algorithm and showed Monte Carlo simulation results. The algorithm was found to have a bias, which vanishes for large CNR values. Since the mode of the error is always close to zero, I recommend to use the algorithm without bias compensation. The new fast algorithm was tested experimentally on our RFID testbed, both in a typical RFID scenario, and in a controlled laboratory setup using an artificial leakage generator. A systematic scan of the leakage I/Q-plane demonstrated, that 95% of the measurements show a maximum penalty in isolation gain of 3 dB when compared to the much slower gradient search algorithm. A further enhancement of the fast algorithm using bipolar probing signals reduced this average penalty to 0.5 dB.

In this chapter I have presented all necessary information for broadband leakage cancellation and its fast, and hardware efficient adjustment for changing environments. Proper leakage cancellation for passive RFID is the key for long range, high performance, forward link limited readers, and therefore also essential for RFID-based sensors, especially if they are embedded in a lossy environment.

Chapter 4

Advanced Tyre Monitoring Systems

Classical Tyre Pressure Monitoring Systems (TPMSs) are nowadays in widespread use, primarily because of legal requisites, as the US federal motor vehicle safety standard 138 [89] or its European counterpart the ECE¹ rule 64 [90] require new vehicles to incorporate a TPMS. However, most vehicles are equipped with so called passive systems, which use the existing wheel rotation sensors of the Electronic Stability Control (ESC) to detect tyres not properly inflated. These systems lack the option to exactly display the individual tyre pressure, they just detect the deviation of one of the tyres out of the set of all tyres on the vehicle. Direct systems use dedicated WUs equipped with a pressure sensor in each wheel and therefore provide accurate individual pressure information. For classical direct TPMSs, the WUs are mounted at the rim and communicate with an antenna either using the protruding part of the valve as a monopole, or employing a small loop in the sensor chassis.

While TPMSs provide the driver quasi static information which he might use to leave the road at the next safe stop to inflate his tyres, ATMSs [91] aim to dynamically enhance vehicular safety by providing additional information to dynamic safety systems like Anti-lock Braking System (ABS) and ESC. This is accomplished, by moving the WU from the rim to the tyre, enabling to gather additional sensor data like tyre temperature and acceleration data. The main sources of acceleration are the centrifugal force and the deformation of the tyre from a perfect cylinder when it hits the road surface and leaves it again [92, 93, 23]. An example for this acceleration forces at 20 km/h is documented in [22] and reproduced in Figure 4.1. This acceleration data is then used to calculate the contact area of the thread on the road, by calculating the angular width of the area with negative radial acceleration. The contact area is directly proportional to the maximum force that may be applied to the tyre without wheel spin, which is a valuable information for ESC and related safety systems. The drawback of ATMSs is the technologically difficult mounting position of the WU: From a mechanical standpoint the vibration forces are high and the sensor needs to be very small to not disturb the balanced momentum of the tyre. This effectively prohibits the use of batteries to power the WU. From an electrical standpoint the tyre constitutes a very lossy dielectric because it contains carbon [94, 95], and therefore is a hostile environment for any antenna.

I propose to use RFID technology to communicate with the ATMS WUs. To power the WU electronics and the sensor, RFID technology may be used as well, potentially aided

¹Economic Commission for Europe, a commission of the united nations.

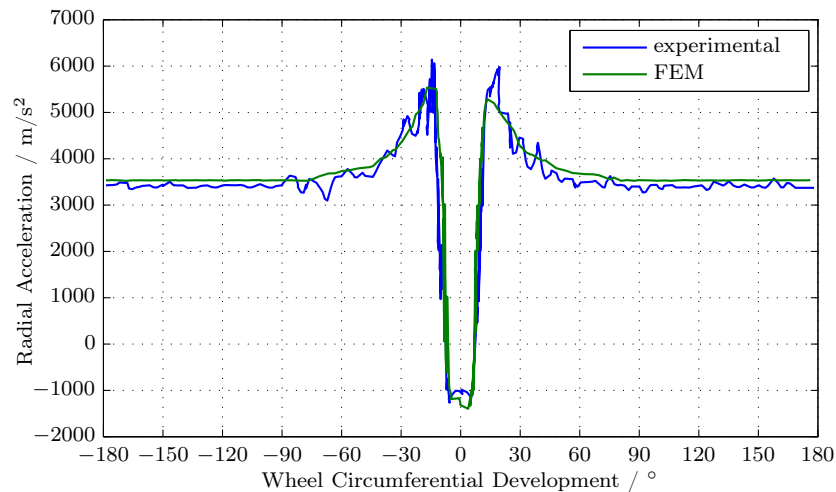


Figure 4.1: Comparison between numerical FEM results and experimental acquisitions for radial accelerations over the tyre circumferential development, reproduced from [22, Figure 6a].

with energy harvesting based on the vibrating environment. This chapter demonstrates that despite the hostile electromagnetic environment, RFID tags mounted at the sidewall of a tyre are read by a UHF reader using a central antenna mounted at the body floor pan with a probability of 75%. First, a channel model is presented and effects like maximum Doppler shift are calculated and discussed. Next, channel simulations based on a simple FEM model are laid out, as well as their spectrally limited channels outcome. Channel measurements carried out in the course of this work are then used as the basis for a statistical analysis and read probability calculations. Finally, this chapter is closed with a summary.

4.1 Channel Modelling

It was already noted in [96], that there is a strong demand for intravehicular channel models that capture “*the propagation and channel impairments to which the technology is sensitive*”. The focus of many publications in the TPMS field is on WU and Onboard Unit (OU) antenna design and simulation techniques [97, 98] and channel loss simulations of conventional TPMS [97, 99, 100]. In [101], a geometry based deterministic model is used to derive the Doppler shift for line of sight situations. In this section, a narrowband radio channel model for TPMSs and ATMSs is elaborated, based on my previous work, originally published in [102]. Further, channel simulations for the UHF RFID band based on FEM field simulations are displayed.

Radio channels generally exhibit time and frequency dispersion. However, if the symbol duration of the data being transmitted over the channel is very long compared to the delay differences of the multipath components, the time dispersion in such a channel is so small

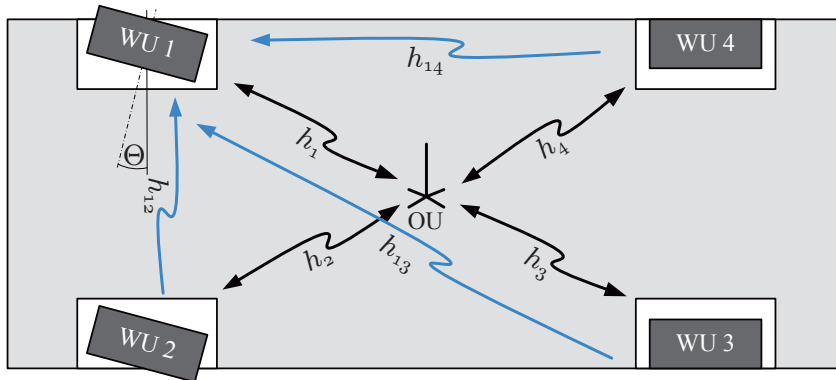


Figure 4.2: Vehicular body seen from below to visualize the relevant channels for WU 1, and the steering angle Θ .

that it can be neglected. In this case, the channel is also uniform in the spectral domain and therefore called flat.

A channel is considered flat, if the maximum delay spread $\Delta\tau$ is much smaller than the symbol duration T_S . For our analysis we choose the highest symbol rate of the popular EPCglobal RFID standard [17, p. 33] of 640 kHz which corresponds to a symbol duration of 1.5625 μs . If we demand the delay spread to be at least ten times smaller, we get a maximum allowed electrical length difference of 46.84 m for the longest and shortest occurring propagation path. Since I consider the magnitudes of scattering components from objects more remote than 23 m as insignificant I claim that the flat fading condition is satisfied for TPMS and RFID-based ATMS channels.

4.1.1 Uplink

The uplink-channel, thus the channel from the WUs to the OU, is modelled as a multiple input, single output channel. In the case of a regular vehicle, there are four tyres, so with the OU as receiver, the channel is represented by the sum of four individual transmission paths from each WU to the OU. The corresponding channels are indicated in Figure 4.2, assuming an OU antenna centred at the body floor pan of the vehicle.

As previously argued, these individual channels are narrowband and therefore their time-varying impulse responses $\hat{h}_i(t, \tau)$ reduce to a delta function multiplied by a complex time-varying factor $\hat{h}_i(t)$ [81, p. 119]. To model the influence of the channel I split $\hat{h}_i(t)$ into a deterministic and a stochastic component, and introduce an additive, white and Gaussian receiver noise component $n(t)$. The deterministic component $h_i(\varphi(t), \Theta(t))$ is dependent on the wheel rotational angle φ and on the steering angle Θ , which are both a function of time. The road surface geometry underneath the vehicle and its motion introduce vibrations to the vehicle and wheels. Changes in the channel coefficients due to these effects are modelled via the stochastic component $\tilde{h}_i(t)$. For the received signal

$r_0(t)$ at the OU we obtain:

$$r_0(t) = \sum_{i=1}^4 \left[h_i(\varphi(t), \Theta(t)) + \tilde{h}_i(t) \right] s_i(t) + n(t), \quad (4.1)$$

where $s_i(t)$ are the transmitted signals from the OUs.

Due to the wheel movement it is clear, that $h_i(\varphi, \Theta)$ is a 2π periodical function in φ and therefore is easily decomposed in a Fourier series:

$$h_i(\varphi, \Theta) = \sum_{m=-\infty}^{\infty} c_{i,m}(\Theta) e^{jm\varphi}, \quad (4.2)$$

with

$$c_{i,m}(\Theta) = \frac{1}{2\pi} \int_0^{2\pi} h_i(\varphi, \Theta) e^{-jm\varphi} d\varphi. \quad (4.3)$$

Note that this Fourier series is not defined in time, but in rotational angle. The reason for choosing this approach is the benefit of time independence and therefore speed independence of the channel model parameters. To analyse at a certain vehicular speed v or tyre angular speed ω , the corresponding channel parameters $h_i(t, \Theta(t))$ are easily calculated by substituting

$$\varphi = \varphi_0 + \omega t = \varphi_0 + \frac{v}{d\pi} t, \quad (4.4)$$

into (4.2) or (4.3), where d is the tyre's diameter and φ_0 is the rotational angle at $t = 0$. The Fourier representation is useful to show the band limitation of the physical ATMS channels and enables artifact free interpolation of point wise measured channels.

4.1.2 Downlink

The downlink channel from the OU to a specified WU is very similar to the uplink channel (4.1). Considering the receiving WU numbered i , the received equivalent baseband signal $r_i(t)$ is expressed by

$$\begin{aligned} r_i(t) = & \left[h_i(\varphi(t), \Theta(t)) + \tilde{h}_i(t) \right] s_0(t) \\ & + \sum_{j=1, j \neq i}^4 \left[h_{i,j}(\varphi_i(t), \varphi_j(t), \Theta(t)) + \tilde{h}_{i,j}(t) \right] s_j(t) \\ & + n_i(t). \end{aligned} \quad (4.5)$$

The first term in (4.5) represents the channel output of the OU's equivalent baseband broadcast signal $s_0(t)$. Interference from other WUs is captured in the second term. The transmitted signals from the other WUs $s_j(t)$ are affected by individual channels between the observed and the other tyres corresponding to the channel coefficients $h_{i,j}(\varphi_i, \varphi_j, \Theta)$ and the associated stochastic parts $\tilde{h}_{i,j}(t)$. Finally, the third term reflects the noise component generated in the WU receiver.

The necessity to analyse the second term depends on the used transmission protocol. For solutions that guarantee that the OUs do not transmit during WU transmissions, like in classical UHF RFID solutions [17], the second term in (4.5) is irrelevant.

4.1.3 Fourier Series Truncation

The two terms in the channel model (4.1), namely, the deterministic component $h_i(\varphi, \Theta)$ and the stochastic component $\tilde{h}_i(t)$ open a possibility of parameter reduction, based on the spectral representation of the deterministic component (4.2). It is limited to significant components only, which for practical channels are grouped around the lower frequencies. So the channel coefficient can be written as a sum over $2M + 1$ components

$$h_i(\varphi, \Theta) = \sum_{m=-M}^M \left[c_{i,m}(\Theta) e^{jm\varphi} \right] + \epsilon_{i,M}(\varphi, \Theta), \quad (4.6)$$

and a remainder term $\epsilon_{i,M}(\varphi, \Theta)$ that contains the higher frequency components. If this term is omitted in favour of a simplified channel representation and M is chosen adequately, a filtered channel model that is comparable to the full channel representation is obtained. Due to the presence of a stochastic channel component, the impact of this parameter reduction on the overall channel $\hat{h}_i(t)$ is negligible if the power of the omitted spectral components is much smaller than the power spectral density of the stochastic component in that region.

This same idea may be applied to the uplink as well as the downlink channel model to simplify both deterministic components $h_i(\varphi(t), \Theta(t))$ and $h_{i,j}(\varphi_i(t), \varphi_j(t), \Theta(t))$.

4.1.4 Doppler Shift

To evaluate the Doppler shift introduced by the moving wheels, it is necessary to substitute (4.4) into (4.2) to explicitly show the time dependency of $h_i(\varphi, \Theta)$:

$$h_i(t, \Theta) = \sum_{m=-\infty}^{\infty} c_{i,m}(\Theta) \left(e^{jm\varphi_0} \cdot e^{jm\frac{v}{d\pi}t} \right). \quad (4.7)$$

To show the Doppler effect, the deterministic channel output $r_D(t)$ is calculated by inserting a sinewave with frequency f_0

$$\begin{aligned} r_D(t) &= h_i(t, \Theta) s(t) = h_i(t, \Theta) e^{j2\pi f_0 t} \\ &= \sum_{m=-\infty}^{\infty} c_{i,m}(\Theta) \left(e^{jm\varphi_0} \cdot e^{j2\pi \left(\frac{mv}{2d\pi^2} + f_0 \right) t} \right). \end{aligned} \quad (4.8)$$

So the output signal is a phase and amplitude weighted sum of sinewaves with frequencies f_m :

$$f_m = m \frac{v}{2d\pi^2} + f_0 = m f_D + f_0, \quad (4.9)$$

where f_D is the Doppler effect's fundamental frequency. For the simplified channel represented by $2M + 1$ Fourier components, as introduced in (4.6), we calculate the Doppler bandwidth

$$B_D = 2M \cdot f_D. \quad (4.10)$$

If a vehicle with tyre dimension 205/55 R16, driving speed of 200 km/h and a channel represented by $M = 16$ frequencies is considered — which is a reasonable value, later explained in Section 4.2.2 — a fundamental Doppler effect frequency f_D of 4.421 Hz and a Doppler bandwidth B_D of 141.5 Hz is obtained.

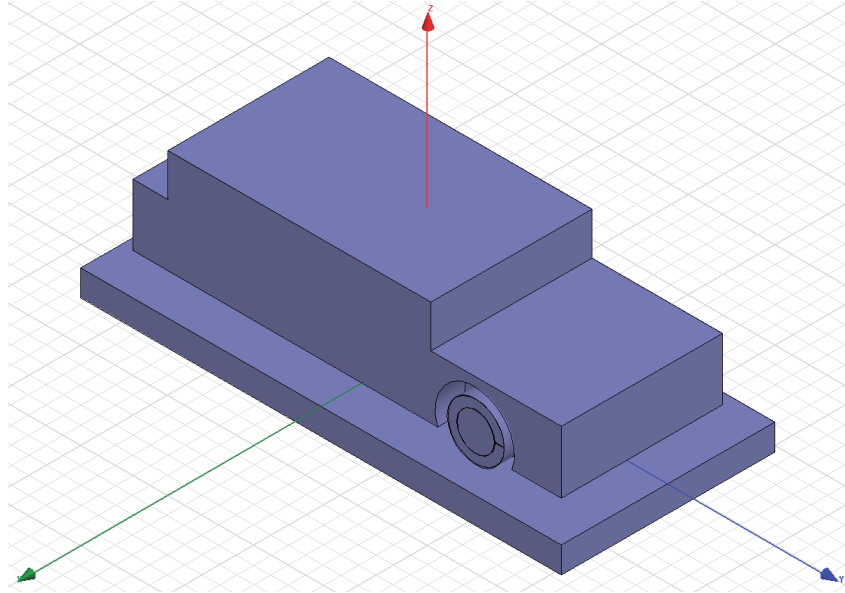


Figure 4.3: Simulation model implemented in HFSS.

4.2 Channel Simulations

To gather numerical results for the deterministic channel component, electromagnetic field simulations in HFSS from Ansoft were carried out. The influence of the changing antenna environment and the relatively small dimensions of the underlying geometry favour the field simulation approach to other propagation channel simulation types, such as ray tracing.

4.2.1 Simulation Setup

Figure 4.3 shows the very simplified model of a vehicle, which was used for electromagnetic field simulations. The vehicle body is represented by a solid block of steel with cut-outs for a single wheelhouse and motor and luggage compartments. Most of the simulations deal with the analysis of the channel coefficient h_1 from the front right wheel to the onboard unit, so only one wheel is modelled for those cases.

To properly capture proximity effects, special care needs to be taken when modelling the antenna environment. Based on the work in [94] and the known negative influence of the steel belt present on the tread, mounting the WU antenna on the tyre's sidewall is considered as the most promising approach. To keep the simulation model simple, the

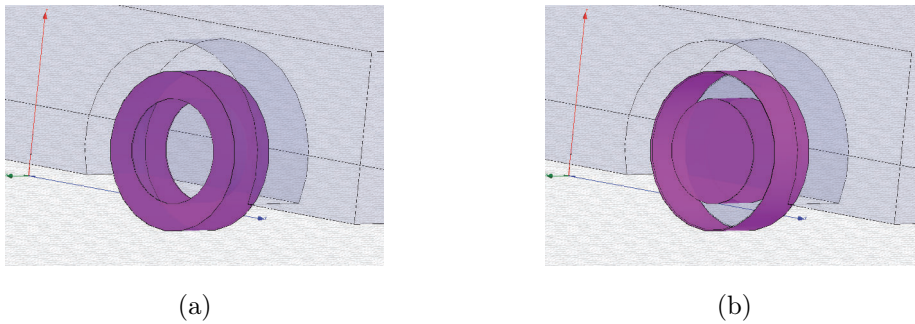


Figure 4.4: Detail of the simulation model implemented in HFSS: tyre rubber parts (a), steel belt and rim (b).

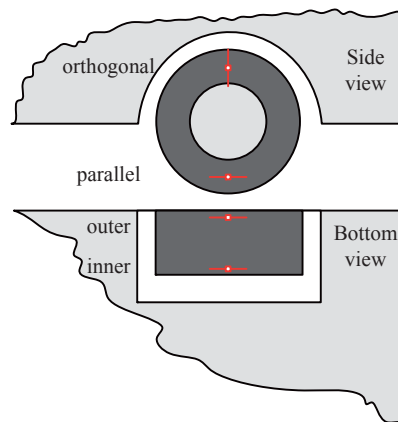


Figure 4.5: Partial view of vehicle body describing WU orientations.

whole tyre was drawn as a homogeneous piece of rubber, where the electrical parameters of the rubber were chosen to match the equivalent of the combined sidewall rubber mixtures. For the chosen tyre these values are $\tan(\delta) = 0.11$ for the dielectric loss tangent and $\epsilon_r = 5.5$ for the relative permittivity [95]. Figure 4.4a depicts a detail of the vehicle model with highlighted tyre rubber. The tyre's steel belt was represented by a thin solid steel band covering the outside of the rubber tyre part explained before. This steel belt equivalent and the rim which was modelled as a steel cylinder are shown in Figure 4.4b.

In the simulation model, a dipole antenna manufactured from copper sheet with dimensions $94\text{mm} \times 10\text{mm}$ is used as WU antenna, which is mounted in the middle of the tyre's inner sidewall. Four different mounting orientations were analysed, where this number results from the combination of two parameters: The orientation of the dipole with respect to the tread (parallel or orthogonal), and the sidewall position as seen from the vehicle centre (inner or outer). See Figure 4.5 for a graphical illustration of these mounting positions.

A monopole is used as OU antenna, whose position was kept fixed at the centre of the vehicle's body floor pan for all simulations. The monopole element of quarter wavelength dimension and the conducting bottom plate of the vehicle form a ground-plane antenna

very similar to the antenna described in Section 2.1.1.

To evaluate the influence of the road surface, two types of simulation models were used. While the first one does not contain any structures to emulate the road, the second type uses a cuboid of 30 cm thickness with constant, homogenous and isotropic material parameters. Based on [103, p. 87] and [104] values of $\tan(\delta) = 0.021$ for the dielectric loss tangent, $\epsilon_r = 5$ for the relative permittivity and 1×10^{-5} S/m for the bulk conductivity were chosen to mimic a tarmac surface.

4.2.2 Model without road surface

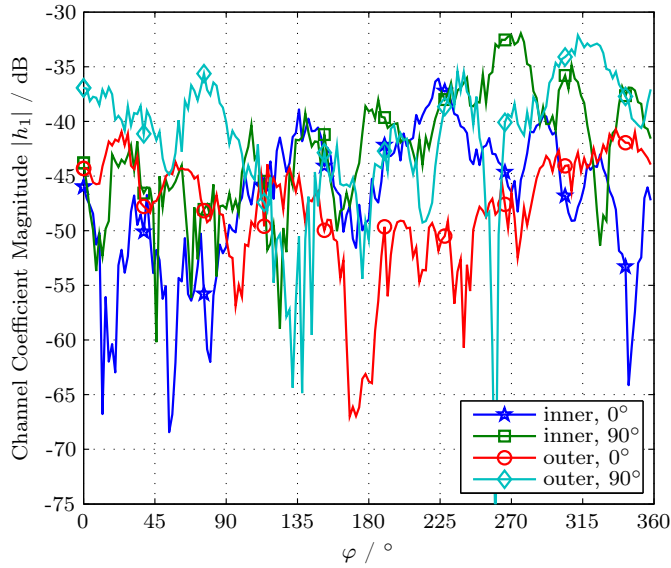


Figure 4.6: Simulated channel coefficient $h_1(\varphi, 0)$ for different antenna positions, without road model.

In Figure 4.6 the absolute value of the channel coefficient $h_1(\varphi, 0)$ is plotted over the rotational angle φ for different antenna positions. Zero degrees correspond to the WU antenna being at the topmost position. The influence of the antenna orientation on the average channel losses is quite small, due to the rich multipath propagation environment formed by the metallic vehicle. For the same reason, a positive effect in the 180° region, which could be considered due to the unobstructed quasi line of sight condition between WU and OU antenna, is not noticed.

There is close electromagnetic coupling between the rotating wheel with its sensor antenna and the vehicle body. To investigate the influence of this coupling the antenna return losses for the different WU mounting positions is plotted in Figure 4.7. For the cases where the WU antenna is oriented parallel to the tyre tread, a ringing clearly identifies a dominant higher spectral frequency component. The expected change in the return loss in a region centred around 180° due to the absence of the wheelhouse is present for the inner parallel and outer orthogonal antennas. For comparison, the return loss of the OU antenna is plotted to see the effect of the numerical simulation errors. These are

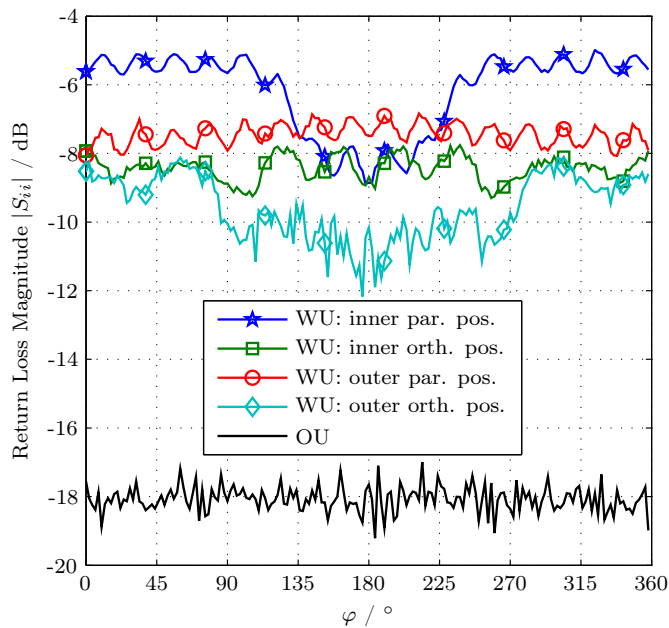


Figure 4.7: Simulated return loss of WU and OU antennas, without road model.

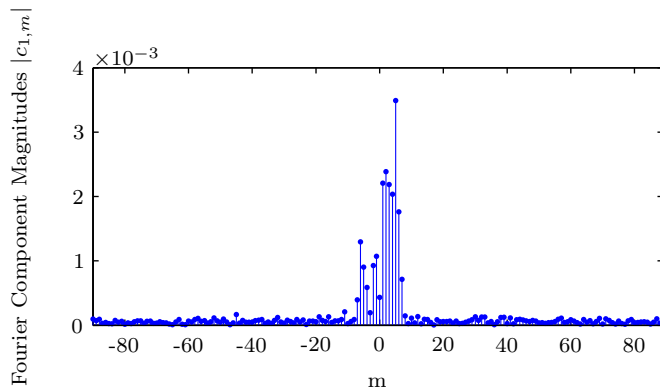


Figure 4.8: Fourier components $c_{1,m}$ for a inner parallel mounted antenna, without road model.

also the dominant source of the noise like spikes on for the outer orthogonal positioned WU antenna, since here the return loss is large.

To investigate the practical feasibility of the parameter reduction introduced in (4.6), the simulated channel is plotted in the Fourier domain. Figure 4.8 shows the magnitudes of the Fourier components for the case of a inner parallel mounted WU antenna. The spectrum of the corresponding antenna return loss is plotted in Figure 4.9. It is obvious that most of the channel power is concentrated in a small band around zero, which indicates that spectral reduction introduced in (4.6) is indeed feasible. As a summation limit $M = 16$ is chosen, which corresponds to the last peaks in the antenna return loss magnitude spectrum, or rather the ringing visible in Figure 4.7. This simplification captures 98.4 % of the channel's transferred power but only uses 18.3 % of the 180 Fourier

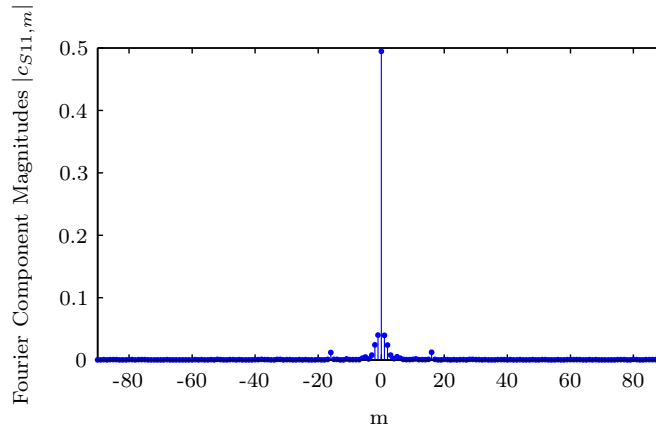


Figure 4.9: Fourier components $c_{S11,m}$ for an inner parallel mounted antenna, without road model.

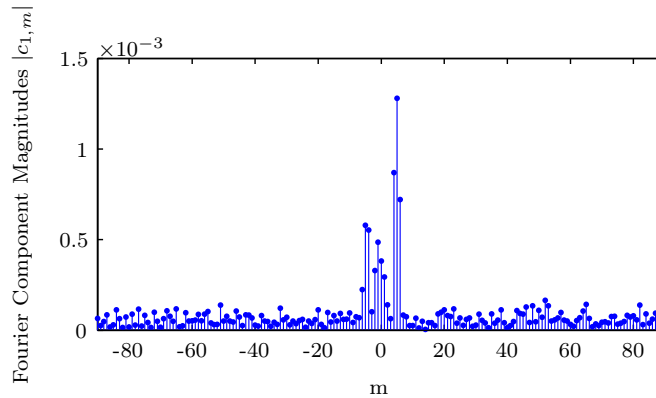


Figure 4.10: Fourier components $c_{1,m}$ for an outer parallel mounted antenna, simulated with road model.

components obtained from the simulation results.

4.2.3 Model with road surface

The addition of a simple road surface element in the simulation model introduces a large scattering object in close vicinity to the antennas. This leads to more scattering and fading effects and more high frequency components in the deterministic channel component. As an example, Figure 4.10 shows the spectrum of an outer mounted antenna oriented parallel to the tread. When compared to Figure 4.8 and the simulations without road surface, the basic structure of few strong components centred around zero remains the same, but the higher frequency components become more dominant. Still, 92% of the channel's transferred power is captured when using a simplified representation with $M = 16$, as before.

For the same sensor antenna orientation, Figure 4.11 compares this filtered channel response to the filtered channel between the front wheel sensors. In this simulation both

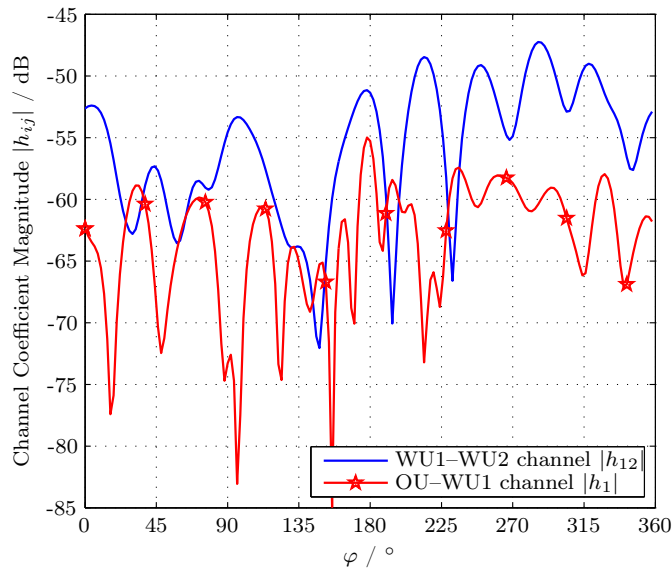


Figure 4.11: Simulated WU–OU and WU–WU channel responses for outer parallel mounted antennas, including a road model.

front wheels were assumed to run completely aligned, so that the abscissa labeling is valid for both front WUs. For this mounting position the channel loss between the front wheel sensors is for many cases approximately 20 dB lower than the loss between one WU and the onboard unit. This is potentially harmful in the downlink, especially to systems that do not employ a strict master-slave scheme.

4.3 Channel Measurements

The simulations presented in Section 4.2 use a radically simplified simulation model of a vehicle to show the principal behaviour of the radio channels encountered in ATMS applications. In this section based on my work previously discussed in [105, 106]. I will present channel measurements carried out in the 865 MHz to 868 MHz band and in the 2.45 GHz range, according to current RFID standards. The knowledge of band limitation of the channel gathered in Section 4.2 enables to reduce the measurement demands to 10° steps in rotational angle φ .

Simulations, especially where complex electromagnetic scenarios like a vehicle body are radically simplified for the simulation model, are error prone. For that reason the aim of the presented simulations was not to obtain quantitative correct results for a specific vehicle model, but gain insight to the general behaviour of ATMS channels instead. To validate these general trends and also obtain results for a specific vehicle, measurements with a Golf V were performed [105].

These experiments are realized in a frequency range from 865 MHz to 868 MHz and in the 2.45 GHz range, according to current RFID standards. The sensor antennas were directly attached to the inner sidewall of a modified standard tyre of a VW Golf V car.

4.3.1 Measurement Setup

The basic principle of the performed measurements is to use a VNA to capture the deterministic channel coefficient for different rotational angles of the front right wheel. A Golf V car is used as vehicle. While the position of the OU antenna is kept fixed during the whole measurement campaign, the WU antennas are mounted at the four different positions at the tyre sidewall shown in Figure 4.5, to evaluate the impact of this mounting. Both, the OU and WU antenna are connected to the VNA using coaxial cables, as indicated in Figure 4.12a. The use of cables in channel measurements is always delicate, because wave guiding effects take place along the cables, and radiation from the cables occurs if unbalanced currents are present. To prevent these negative effects the measurement cables are equipped with ferrite beads which constitute a high impedance for travelling waves. This property is guaranteed for the 865 MHz band where the magnitude of the complex impedance of a single ferrite bead is at least 200Ω . For the measurements at the upper frequency band the impedance of the used ferrite material is unspecified, but due to the longer electrical length between the antennas and the VNA, sufficient damping of sheath currents is assumed.

The front right tyre was modified by a U-shaped cut to enable the swing out of a small part of the tyre sidewall to provide access for WU antenna mounting and routing of the WU feed cable. Naturally, the wheel can not be inflated with this cut out and needs support to remain at the correct height. For this purpose, a steel tube, which is welded to the rim, is slightly lifted by a textile sling which is attached to a gantry crane, as is visible in Figure 4.12b. This method ensures a constant distance between wheel and wheel house and keeps the wheel's suspension in position, which is essential for achieving realistic measurement results. Further, it avoids any objects like jacks or support racks below the vehicle.

OU Antenna

The monopole antenna described in Section 2.1.1 is used as OU antenna. It is mounted to the Golf V car using plastic binders, as indicated in Figure 4.13. It is resonant both, in the 868 MHz UHF and 2.45 GHz ISM bands.

WU Antennas

Dipoles are chosen as WU antennas, because their efficient implementation for this type of application has already been proven [94, 107]. Two different types manufactured of adhesive-coated copper tape are utilized: The long dipole $101 \text{ mm} \times 10 \text{ mm}$, and the short dipole $42 \text{ mm} \times 10 \text{ mm}$. The long dipole is resonant at the UHF band due to the dielectric loading of the tyre rubber. For the orthogonal mounting positions only the short dipoles are used, due to mounting restrictions on the tyre sidewall. All dipole variants are measured at UHF frequencies, but at 2.45 GHz only the short dipole is addressed.

The dipoles are soldered to small PCBs which carry baluns to adapt for the asymmetric coaxial feed line, see Figure 4.12c. For measurements in the low band a wire-wound

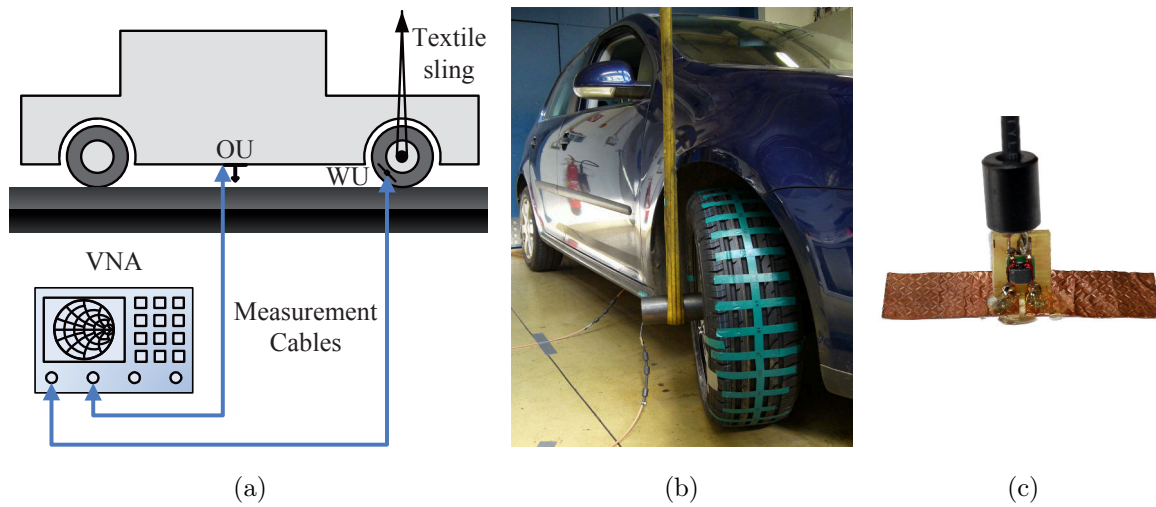


Figure 4.12: Channel measurement setup: (a) Block diagram; (b) picture of measurement setup showing the Golf V car, the modified wheel with the steel tube and the textile sling, and the measurement cables carrying ferrite beads; (c) picture of short dipole, with PCB carrying the UHF balun attached, and the feed cable equipped with a ferrite bead.

transmission line transformer is used. The 2.45 GHz band is covered with a chip hybrid balun.

I characterized the WU antennas in our anechoic chamber, mounted on the same test wheel also taken for the channel measurements. To avoid the influence of a feed cable for the antenna measurements, the technique described in Section A.2 and a small oscillator operating at 864 MHz is applied. The corresponding coordinate system for the pattern measurements is shown in Figure 4.14. Figure 4.15 exhibits gain plots of the obtained antenna measurements for outer mounting positions. As expected the patterns for the same orientations but different dipole lengths are very similar, both for the gain plot corresponding to electric field components in theta direction E_θ and for the gain corresponding to E_φ . The main beam is pointing towards low polar angles, and almost no power is radiated through the opposite tyre sidewall towards high polar angles. The behaviour for the dipole mounted orthogonal to the tread is totally different: If there would not be significant impact of the mounting tyre, the gain pattern of the orthogonal dipole should be similar to the parallel dipole, but shifted 90° in φ . In contrast, most radiation occurs at polar angles close to $\theta = 90^\circ$, and the pattern is very frayed in azimuth. I believe that this is caused by a wave guiding effect in the wheel by a quasi parallel plate line formed by the rim on one side, and the steelbelt on the other side (see Figure 4.14). The steelbelt itself is composed of two crossed layers of steel wires and can also guide (leaking) waves. The measured directivities for the outer mounting positions are 7.2 dB for both parallel mounted dipoles and 6.3 dB for the orthogonal dipole.

The gain plots for the inner mounted dipoles are shown in Figure 4.16. The obtained

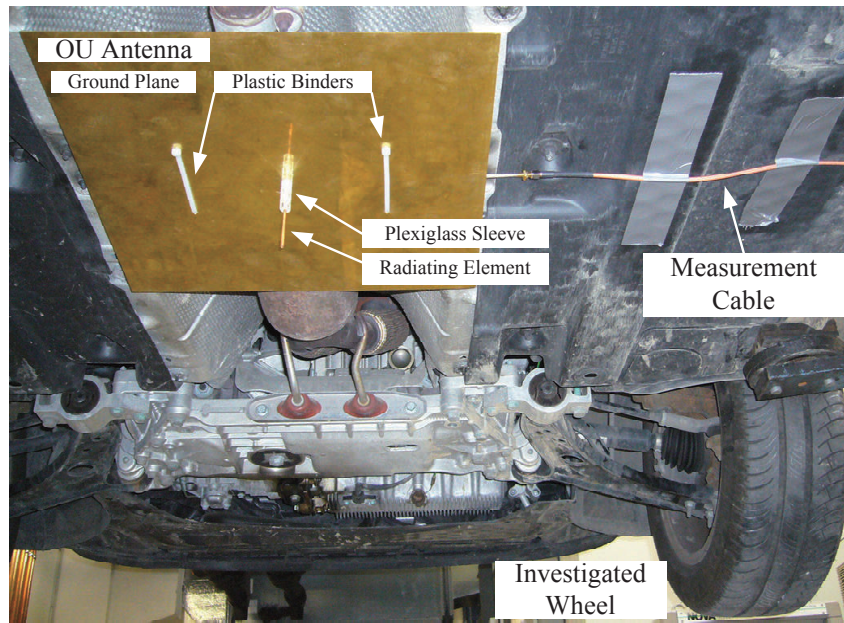


Figure 4.13: Bottom view of measurement vehicle on auto-hoist.

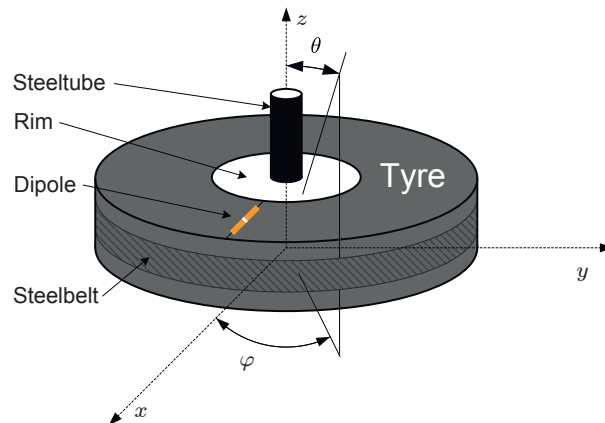


Figure 4.14: Schematic drawing of the tyre in the used coordinate system carrying a dipole mounted in the outer orthogonal position.

plots are very similar to the ones for outer mounting positions if the polar axis is mirrored. Slight differences occur due to the asymmetrical rim, and the additional steel tube at the outer position used for the initial channel measurements [105]. Measured directivities are 7.3 dB for both parallel mounted dipoles and 5.9 dB for the orthogonal dipole.

4.3.2 Calibration and De-embedding

The VNA was calibrated using short, open, load, and through standards at the end of the measurement cables. The OU antenna exhibits an input return loss greater than 10 dB, so no further processing is necessary to obtain accurate results. The situation is different

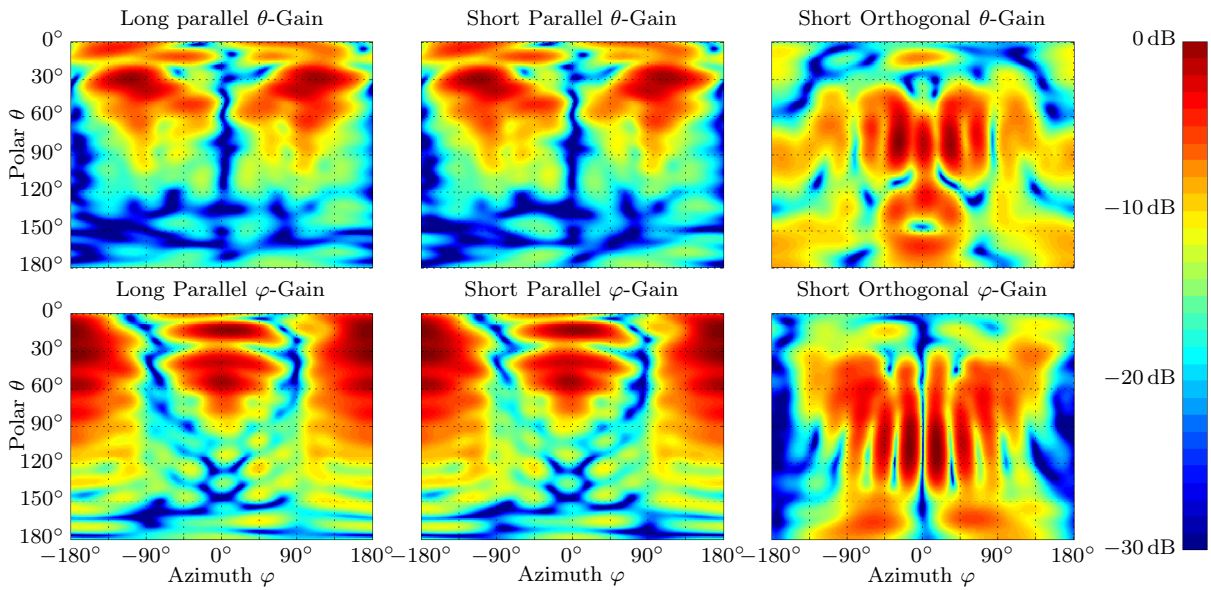


Figure 4.15: Normalized measured gain patterns for WU dipoles mounted on the outer position.

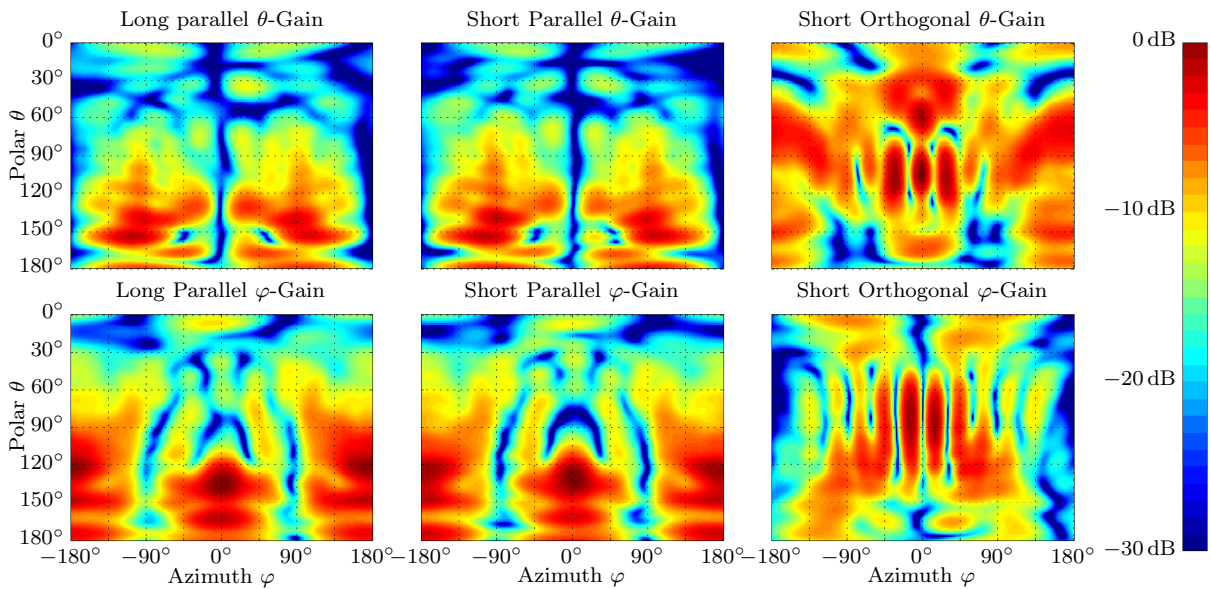


Figure 4.16: Normalized measured gain patterns for WU dipoles mounted on the inner position.

at the WU antenna, which is not properly matched and connected to the VNA by an additional thin lossy cable.

The de-embedding of the WU antenna feed is done in two steps. First the effects of the lossy feed cable are removed in Matlab². The scattering-parameters (S-parameters) of the feed cable were separately measured with a VNA and used to calculate the new

²Matlab is a powerful commercial numeric simulation tool from The MathWorks, Inc.

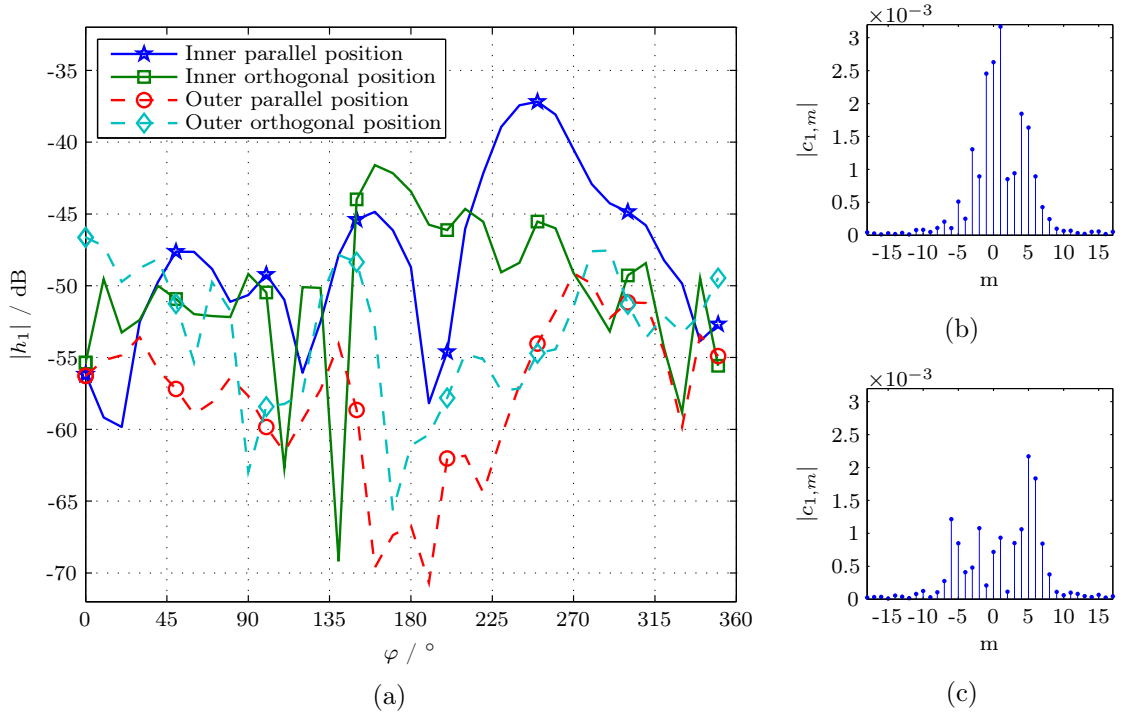


Figure 4.17: Measured magnitude of $h_1(\varphi, 0)$ for the short dipole at 865 MHz: (a) angular representation; (b) spectral components $|c_{1,m}|$ for inner parallel, (c) inner orthogonal oriented antennas.

S-parameter matrix of the channel response with the cable influence removed. In a second step, a virtual lossless tuner is inserted using Matlab postprocessing, to compensate for the matching loss of the WU antenna. The antenna ports were terminated in port 1 of the VNA, so the input reflection coefficient at the WU antenna side equals S_{11} , when S denotes the S-parameter matrix of the channel. The tuner's S-parameter matrix S_T is given by

$$S_T = \begin{pmatrix} -S_{11} & \sqrt{1 - |S_{11}|^2} \\ \sqrt{1 - |S_{11}|^2} & S_{11}^* \end{pmatrix}. \quad (4.11)$$

The tuner is adapted to each measured frequency point for the WU antenna being at the topmost position ($\varphi = 0^\circ$). This tuner setting is then used for all measured rotational steps, to show the consequences of antenna de-tuning caused by proximity effects and produce a fair comparison with a well matched RFID chip.

4.3.3 Measurement Results at the UHF Band

Figure 4.17a presents the de-embedded measurement results for the short dipole and the four mounting positions described before, where $\varphi = 0$ corresponds to the WU antenna being at the uppermost position. The channel coefficients exhibit fading with a dynamic

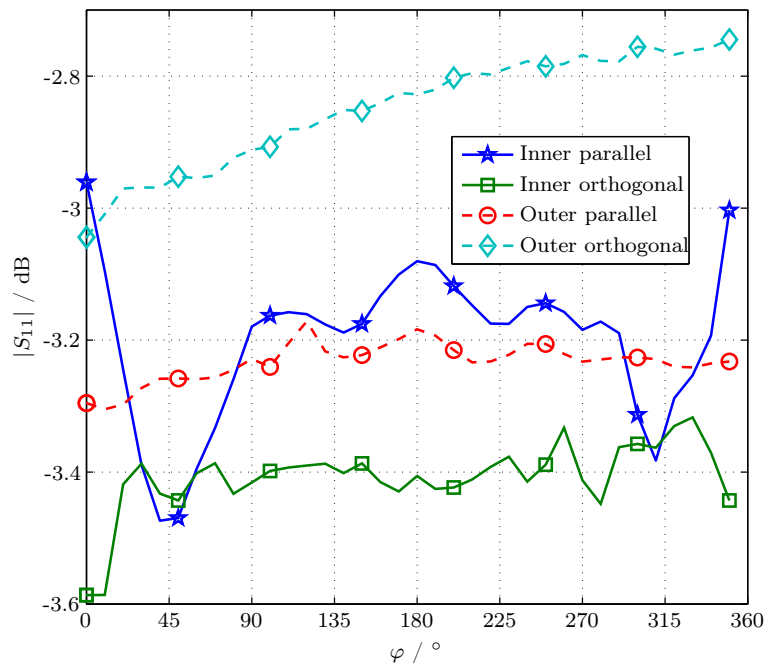


Figure 4.18: Measured WU antenna input return loss prior to de-embedding.

range of approximately 30 dB. This is due to multi path propagation and scattering on the concrete road surface and the wheelhouse. Another indicator of multi path propagation is the missing fundamental change in channel behaviour when the WU is in quasi line of sight conditions close to $\varphi = 180^\circ$. This general behaviour is in very good agreement with the simulation results obtained for the very simple vehicle model presented in Section 4.2.3.

In Section 4.3.2 I stated, that the WU mounted on the tyre is exposed to a changing environment and therefore proximity effects alter the matching of the WU antenna over rotational angle. This effect is the reason for the variation of the WU antenna input return loss plotted in Figure 4.18. The outer orthogonal mounted dipole shows a continuous matching degradation, which is most probably caused by slight unbonding of the copper tape from the rubber during wheel rotation. For an optimal implementation, the WU IC antenna terminal impedance should be close³ to the conjugated complex impedance of the WU antenna. Since this value is not constant for changing φ , a compromise value has to be used.

In Figure 4.17b and Figure 4.17c, the Fourier domain representation introduced in (4.2) is used to show the spectral limitation of the channel. The magnitudes of the Fourier components for the two cases of inner mounted WU antennas are plotted in these diagrams. Visual inspection indicates that the channel is bandlimited and a representation with $M = 9$ Fourier coefficients is possible with little error. Calculating the captured channel power when summing only over these $2M + 1 = 19$ coefficients yields to power capturing ratios of 99.9% for the parallel oriented antenna, and 99.6% for the orthog-

³For RFID choosing the antenna feed point impedance is a tradeoff between minimum tag wake up sensitivity and maximum tag backscatter modulation efficiency. Further, the tag impedance in most RFID tag implementations severely depends on input power. See [9, Chapter 2]

onal one. This means that the measured channels are even more bandlimited than the simulated ones. When comparing the spectral representation of the channels of the parallel and orthogonal mounted WU dipoles shown in Figure 4.17b and Figure 4.17c, it is observable that for the parallel antenna the large Fourier components are centred close to zero, while for the orthogonal antenna the power is spectrally quite evenly distributed up to $M = 9$. This emphasis on lower spectral components for the parallel mounted antenna agrees very well with the obtained gain pattern in Figure 4.16, which is similar to a dipole but concentrated on high polar angles. In contrast, the gain pattern for the orthogonal mounted dipole is very frayed, which causes more simultaneous paths in the channel cluster⁴ close to the WU and therefore less emphasis on the low frequency channel components.

For the four different WU antenna orientations, the channel coefficient's phase over rotational angle is plotted in Figure 4.19. While the channel magnitudes plotted in Figure 4.17a indicate multi path propagation, the almost perfectly linear phase response is a strong evidence for a dominating single cluster component. Especially for the inner mounted WU oriented orthogonal to the tread, the phase curve resolves into three segments: First, for $0^\circ \leq \varphi < 90^\circ$ the phase response exhibits an almost linear track from $\pi/2$ to -2π . The second segment ranges from 90° to 270° and shows a phase rise to more than 3π . In the third part, the slope is negative again. These three segments correspond to the varying differential movements between WU and OU antenna. In the first and third segment the WU–OU distance increases with rising rotational angle, so the slope of the phase response is negative. In the second segment the situation is inverse.

The almost triangular shape of the phase response is used to estimate the resulting Doppler frequency. In the second segment the Doppler angular frequency $\omega_D = \frac{d \arg(h_1)}{dt}$ is approximated by the difference quotient

$$\omega_D \approx \frac{\Delta \arg(h_1)}{\Delta t} = \frac{\Delta \arg(h_1)}{\Delta \varphi} \frac{v}{d\pi}, \quad (4.12)$$

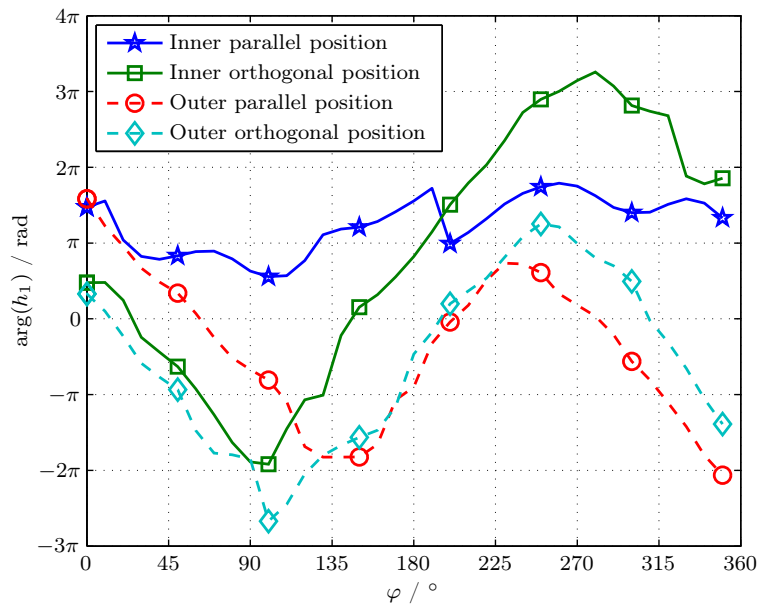
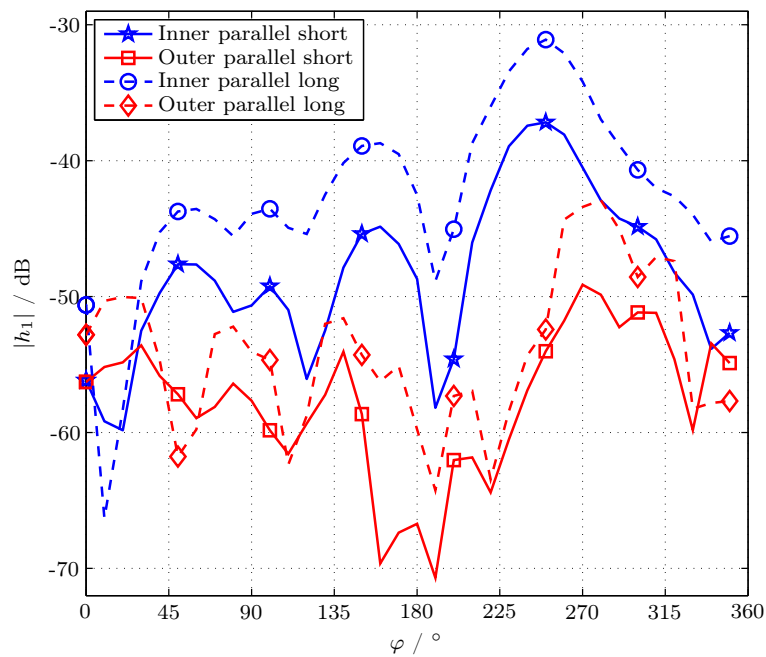
where v denotes the vehicle speed and d the wheel's diameter. This yields to a Doppler frequency of

$$f_D = \frac{\omega_D}{2\pi} \approx \frac{\Delta \arg(h_1)}{\Delta \varphi} \frac{v}{2d\pi^2} \approx \frac{5v}{2d\pi^2}. \quad (4.13)$$

If we neglect the higher Doppler frequency components, and use the linearised phase response with a Doppler shift of $-f_D$ in sections one and three and f_D in section two, we get a total Doppler Bandwidth $B_D = \frac{5v}{d\pi^2}$. This corresponds to (4.10), when $M = 5$ is chosen for the last Fourier component to be included in the sum representation. Figure 4.17c shows that the fifth spectral component $c_{1,5}$ is indeed the largest, but higher frequency components and therefore higher Doppler components exist. This is also indicated by the deviation from a pure triangular shape in Figure 4.19.

A comparison between the the aforementioned short antenna and a resonant $\lambda/2$ dipole is shown in Figure 4.20. This figure compares the magnitudes of the channel coefficient

⁴Clusters are used in channel modelling to express multiple scattering objects which are geometrically grouped in close vicinity, see [81, Chapter 7].

Figure 4.19: Channel phase response $\arg(h_1)$ at 865 MHz.Figure 4.20: Magnitude of $h_1(\varphi, 0)$ for the short and long dipoles at 865 MHz.

for parallel oriented WU antennas. Due to higher efficiency, the resonant dipole in most cases is superior to the shorter version. The shape of the curves is almost the same, especially for the case of inner WU mounting. This is in good agreement to the measured almost identical normalized WU antenna gain patterns for the long and short dipole, as discussed in Section 4.3.1.

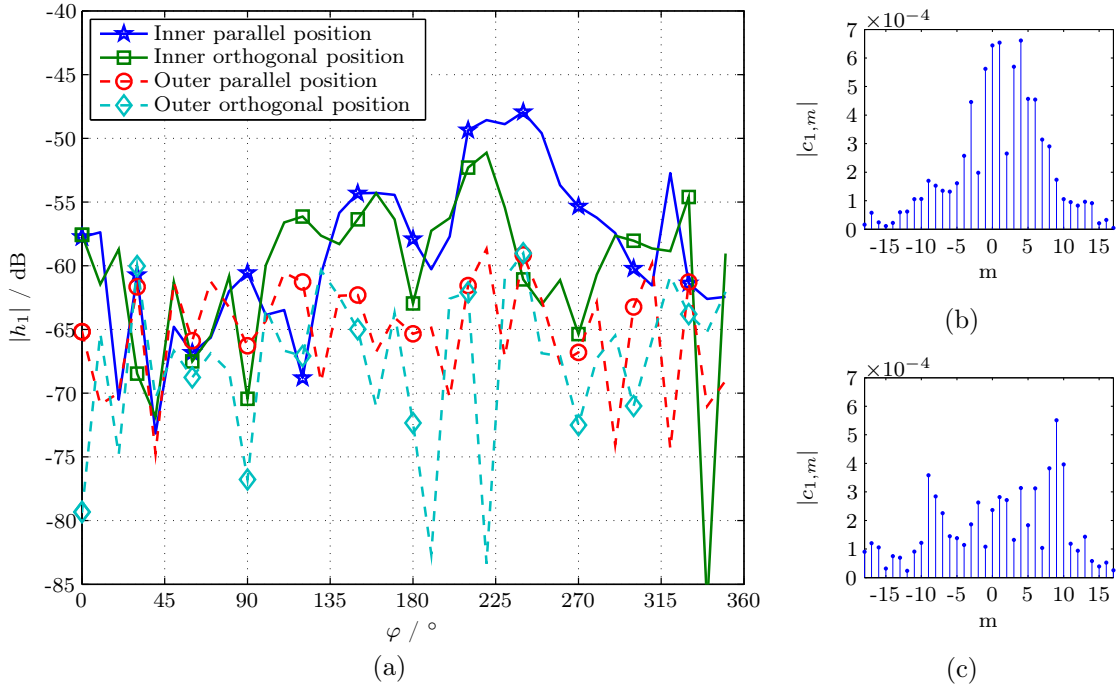


Figure 4.21: Measured magnitude of $h_1(\varphi, 0)$ for the short dipole at 2.45 GHz: (a) angular representation; (b) spectral components $|c_{1,m}|$ for inner parallel, (c) inner orthogonal oriented antennas.

4.3.4 Measurement Results at the ISM Band

At the upper frequency band all measurements were carried out with the short dipole. Figure 4.21a shows the magnitude of the channel coefficient at 2.45 GHz. When compared to the results in the lower frequency band, the average channel losses are approximately 10 dB higher. The channel shows more fluctuations which is also expressed in the Fourier domain, from Figures 4.21b–c. To determine the bandwidth limitation, more frequency points and corresponding finer angular steps are required.

As stated earlier, the channel response is not only measured for different WU antenna orientations, but also for three steering angles Θ : 0° and $\pm 25^\circ$. One full turn of the steering wheel to the left hand side matches the $\Theta = -25^\circ$ measurement curve. As an example of the impact of the steering angle, Figure 4.22 shows a comparison between the magnitudes of the channel coefficients for the three measured angles at 2.45 GHz for an inner, parallel mounted WU antenna. There are some deviations between the curves, but the general trend remains the same.

For the same antenna position, Figure 4.23 depicts a broadband measurement from 2.4 GHz to 2.6 GHz. There is some frequency selective fading, but the amount of deviation in the channel coefficient curve progression between the two frequencies is similar to the deviation between different steering angles.

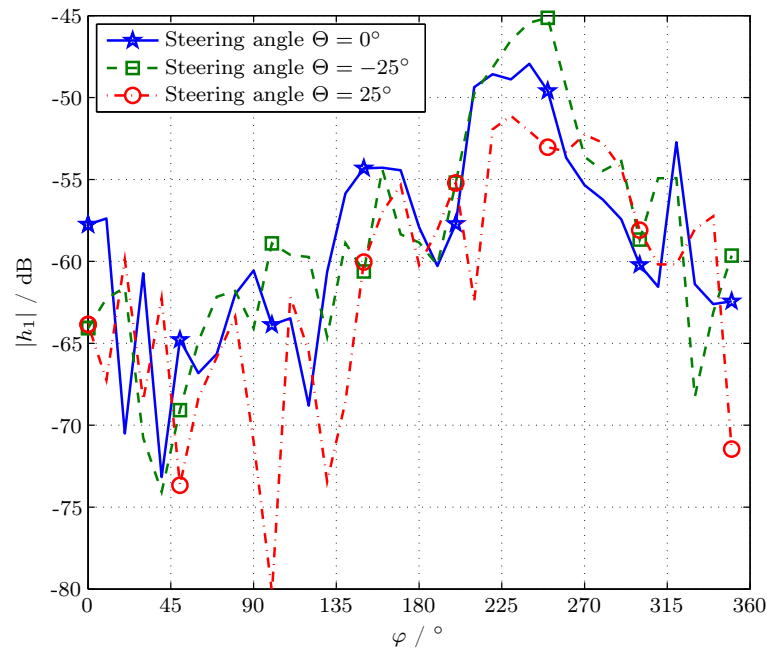


Figure 4.22: Magnitude of $h_1(\varphi, \Theta)$ for the inner, parallel mounted short dipole at 2.45 GHz for different steering angles.

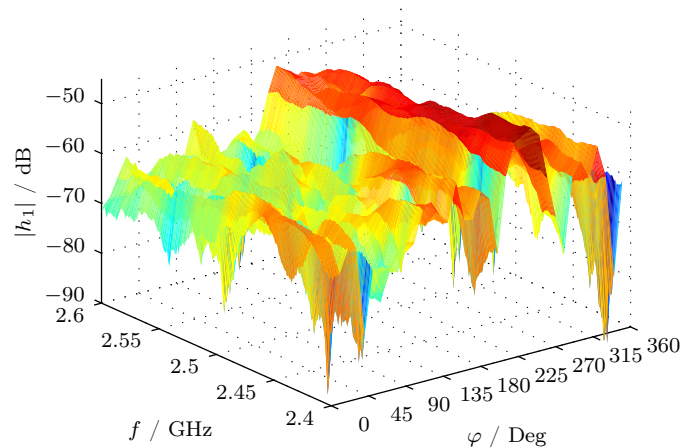


Figure 4.23: Magnitude of $h_1(\varphi, 0, f)$ for the inner, parallel mounted short dipole over frequency f and rotational angle φ .

4.4 Link Budget Evaluation

Based on the channel measurements described before, I now evaluate the read probabilities of RFID-based ATMS sensors. My corresponding original work is published in [108]. Since the channel losses are large for an RFID application, multiple antenna techniques and diversity become the key to enable high read probabilities. The benefits of multi-antenna techniques are well known also for RFID applications, both in theory [109] and in practical validation [110]. In this work, especial focus is given on the received power aspect, since

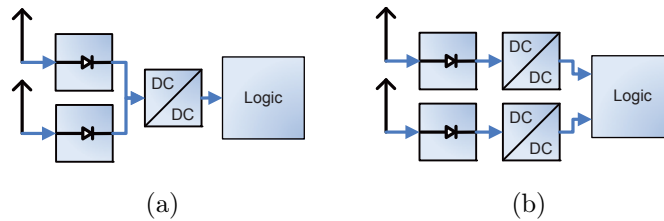


Figure 4.24: Signal combining techniques with respect to received power: (a) Antenna selection; (b) Power combining

the reverse link limitation is handled by appropriate broadband leakage cancellation, as explained in Section 1.1.

4.4.1 Signal Combining Techniques

In the following section the measured channels for a single WU antenna are compared with virtual channels created when using dual-antenna tags. The use of two or more antennas enables diversity and potentially increases forward and backward link quality, as theoretically described in [109]. I will focus on the forward link, as the main concern for ATMS applications is powering the RFID tag, due to the high channel losses. In particular, I focus on the gained DC power if using different antenna and rectifier combination techniques.

Antenna Selection

Antenna selection is a well known low complexity scheme to gain diversity in radio systems [111]. For RFID systems, the implementation is realized even simpler by using one rectifier circuit per antenna and paralleling the outputs, as indicated in Figure 4.24a. In the case of the first antenna receiving a stronger signal than the second, the output voltage of the corresponding rectifier will be larger than the one produced by the second rectifier. In this case, the second antenna does not feed any power in the power conditioning circuits and therefore acts as if being switched off. For the case of almost identical field strengths at the antennas, the paralleled rectifier outputs even produce slightly more power than in classical antenna selection, because both rectifying circuits provide current for the tag's power supply.

Power Combining

In contrast to antenna selection, power combining exploits the sum power simultaneously received at both antennas [112]. A simplified method is described in [113], where both antennas are connected to rectifiers, which are connected in series to implement a summation. Due to differing input powers, the rectifier's output impedances are unequal. Therefore, a compromise is required for the matching to the DC-DC converter when this

simple approach is used. A more general case is shown in Figure 4.24b which exploits the sum of the input powers of both antennas.

Practical Limitations

The efficiency of practical rectifiers and DC–DC converters strongly depends on input power, due to the nature of semiconductor components [114, 115]. For the proposed antenna selection scheme using antenna switching, this dependency has negligible impact on our analysis since our investigation in Section 4.4.3 is based on a tag sensitivity threshold.

The power combining approach operates two rectifiers and DC–DC converters at different input power levels and therefore has to cope with various conversion efficiencies of the mentioned circuits. The further detailed analysis of this approach is restricted to the case of ideal rectifier and converter circuits and therefore constitutes an upper bound for hardware implementations.

4.4.2 Statistical Analysis for Single Antenna Tags

To gain a deeper understanding of the read probability of an RFID sensor node mounted in the tyre, I use a randomization technique of the obtained measurement data. For a given WU antenna mounting position, a random rotational angle and frequency is selected and the magnitude of the channel coefficient is evaluated. For the 866 MHz band, all frequency points between 865 MHz and 868 MHz are evaluated. The broadband measurement results carried out at the 2.45 GHz band are restricted to frequency points from 2.4 GHz to 2.5 GHz. Two subcases are analysed: One, solely for straight driving corresponding to a steering angle of 0° . The other subcase assumes that the three steering angles -25° , 0° and 25° at which measurements were performed, are equally likely.

At the 866 MHz band the channel response primarily depends on rotational angle, and the measured 101 frequency points do not add much variation. Because the channel is bandlimited with respect to the Fourier domain corresponding to the rotational angle, recall Section 4.2.3, interpolation of the measurement points in the angular domain is possible without creating artifacts. This was done by calculating the Fourier series, padding zeros and converting back to angular domain, resulting in an upsample factor of 10. This method corresponds to a $\frac{\sin(x)}{x}$ interpolation of the channel magnitude measurement points to give 1° resolution. These samples were then randomized in the same manner as the original samples in the 2.45 GHz band.

Given a certain transmit power and tag sensitivity, communication is possible if the channel magnitude exceeds a threshold value. This statement is based on the assumption that the channel stays constant throughout the whole communication process, including RFID chip wakeup time, query command and data exchange. When observing the channel measurement results over rotational angle, this is valid for tyre rotations smaller than 10° . So for a tyre radius of 33 cm corresponding to a typical tyre dimension of 205/55R16 and a driving speed of 100 km/h our assumption is satisfied if the communication process is accomplished within 2 ms. For longer communication time the allowed speed has to

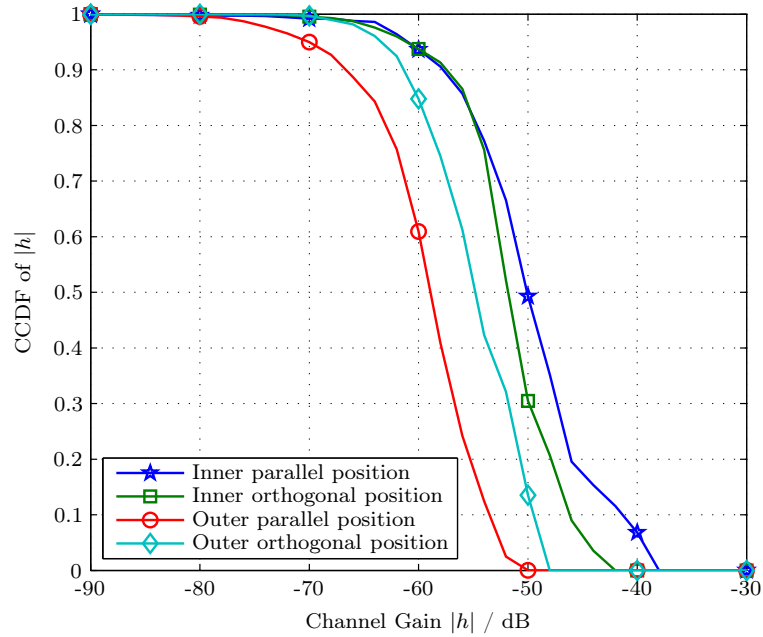


Figure 4.25: CCDFs of channel magnitude for different WU orientations at UHF.

be reduced accordingly, or a more complex analysis technique is necessary where the minimum channel magnitude over a certain time period has to be evaluated.

Results at the UHF Band

Using the randomization technique described before, Complementary Cumulative Distribution Functions (CCDFs) for the four antenna mounting positions are drawn in Figure 4.25, using the short WU antenna. While plotting Cumulative Distribution Functions (CDFs) produces curves that directly relate to the outage probability, the ordinates of the used CCDFs give the probability for the channel magnitude $|h|$ being above a certain value picked on the abscissa. To evaluate the read probability

$$P = P\{|h| > h_{\text{th}}\}$$

we first calculate the maximally allowed channel loss h_{th} . The combination of a state-of-the-art tag sensitivity of -17 dBm [116] and a transmit power of 33 dBm leads to a maximally allowed channel loss of 50 dB⁵. Therefore, the WU tag with an inner parallel mounted antenna has a read probability P of 49% . For inner orthogonal, outer orthogonal and outer parallel mounting the read probabilities are 30% , 14% and 1% , respectively.

A comparison between the short non-resonant WU dipole and the longer resonant version for parallel mounting is depicted in Figure 4.26. Due to the high slope of the

⁵I picked the sensitivity of -17 dBm since it corresponds to the sensitivity of the best dual antenna RFID chip available at the time of writing. There are single antenna chips with lower minimum tag power, as [10] with -21.5 dBm. However, the picked transmit power of 33 dBm is already chosen optimistically, since the used OU antenna has a directivity of 4.3 dB at UHF, see Table 2.5.

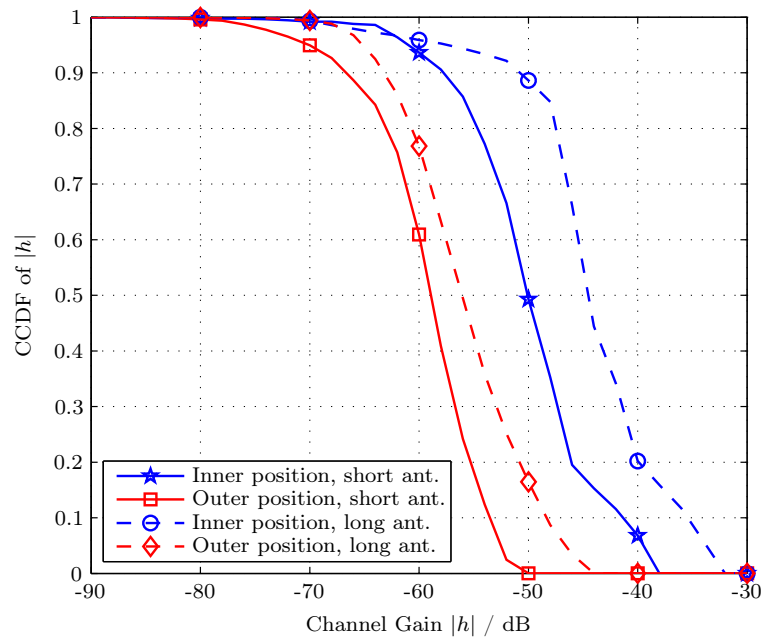


Figure 4.26: CCDFs of channel magnitude for long and short parallel OU antennas at UHF.

CCDFs the efficiency improvement of approximately 5 dB of the long antenna corresponds to reading probabilities of 89% for the inner positioned antenna and 16% for the outer antenna.

Results at the ISM Band

Figure 4.27 compares the CCDFs for different mounting positions of the short WU dipole at the 2.45 GHz microwave band. Compared to the situation at UHF, the channel exhibits approximately 12 dB higher losses. Therefore, achieving approximately the same read probabilities demands an increase in transmit power or tag sensitivity. The legal Equivalent Isotropically Radiated Power (EIRP) for this band for outdoor RFID applications is 27 dBm in Europe [117, Annex C], so in truth the transmit power for this band even needs to be reduced. On the tag side, it seems to be questionable if tags at the microwave ISM band will have higher sensitivities than UHF tags, when current publications are considered [118]. Therefore, I do not calculate any read probabilities as for the UHF case since currently the legal and technological situation does not compensate for the higher channel losses in the ISM band.

To evaluate the effects of steering, the CCDFs for all four WU mounting positions including the equiprobable steering angles -25° , 0° and 25° are plotted in Figure 4.28. Comparing Figure 4.27 and Figure 4.28, only minor changes at high channel gains are noticeable, so in most cases the effects of steering are negligible.

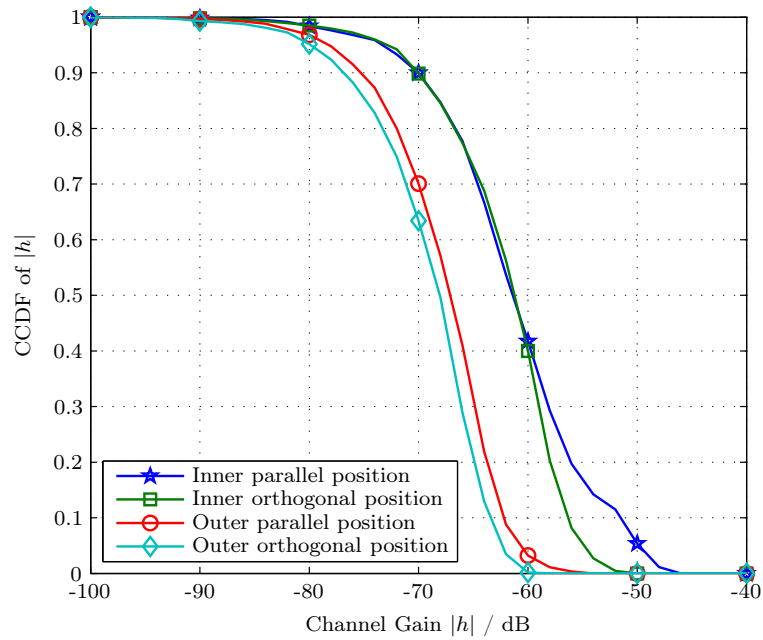


Figure 4.27: CCDFs of channel magnitude for different WU orientations at ISM frequencies, for straight steering only.

4.4.3 Statistical Analysis for Dual Antenna Tags

I now combine two single antenna measurement data curves to form a virtual Single Input Multiple Output (SIMO) channel. In general, this postprocessing is not valid, since antennas in close proximity influence each other. However, when using antennas with a symmetry plane for the electromagnetic field, and placing the first on the symmetry plane of the second (and vice versa), the antennas do not influence each other and separate measurements are feasible.

Since we are joining measurements from dipole antennas which are at the same position but orthogonal to each other, this approach of calculating the SIMO channel from the corresponding Single Input Single Output (SISO) channel is fully equivalent to really measuring the SIMO channels with both WU antennas in place at the same time. The SIMO channels were calculated according to the combining techniques discussed in Section 4.4.1.

Results at the UHF Band

Only the inner WU mounting position is analysed in Figure 4.29, because it exhibits higher channel gains. The use of the simpler antenna selection technique leads to an increased read probability of 58%, the more advanced power combining technique even reaches 75% read probability. But even more important, the diversity gain realized by using two antennas dramatically reduces the requirements on tag sensitivity or transmit power: To reach 100% read probability, the allowed channel loss is reduced from 75 dB to 56 dB for the power combining case.

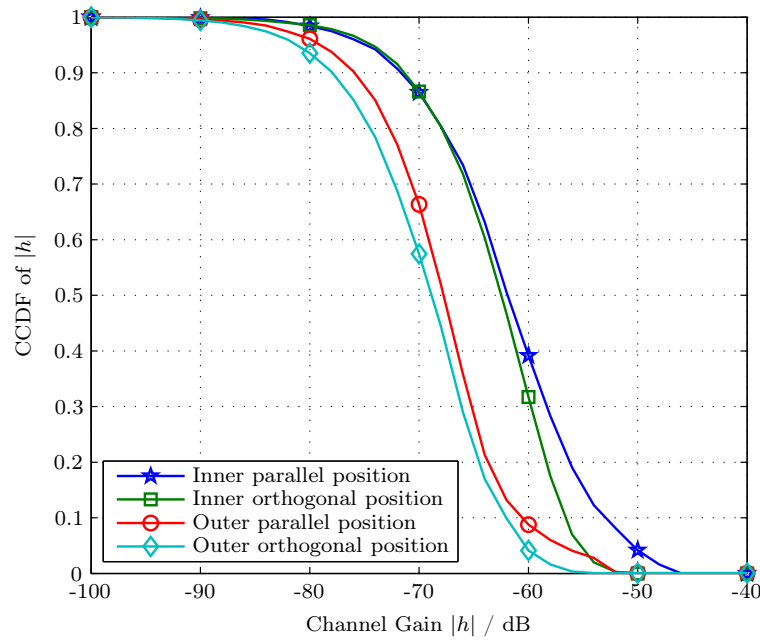


Figure 4.28: CCDFs of channel magnitude for different WU orientations at ISM frequencies, including equiprobable steering angles left and right.

Results at the ISM Band

The improvement due to dual-antenna techniques is also eminent in the microwave band, see Figure 4.30. Since both inner mounted antennas statistically perform almost identical in lower gain regimes, the improvement due to the SIMO approach becomes evident here: The slope of the SIMO CCDFs is steeper than in the SISO case, enabling medium to high read probabilities with less stringent constraints on tag sensitivity or transmit power. The improvement of the more sophisticated power combining technique over the simpler antenna selection is merely 1.5 dB or less. This means that for practical chip design it might be more favourable to use the simpler approach.

4.4.4 Statistical Channel Description

Based on the randomisation technique explained in Section 4.4.2 I use a minimum mean square error approach to fit the magnitude of the channel coefficients to a known distribution. For the 2.45 GHz band, it was found that the gamma distribution with probability density function

$$f_X(x) = \frac{1}{b^a \Gamma(a)} x^{a-1} e^{-x/b} \quad \text{for } x > 0$$

and parameters a and b gives best results. I use the scenario with equiprobable steering angles which maximizes the number of channel measurement points for the statistical fitting. Table 4.1 presents the parameters of the gamma distribution fitting for the four mounting positions. The quality of the fit is assessed by the probability plot, Figure 4.31,

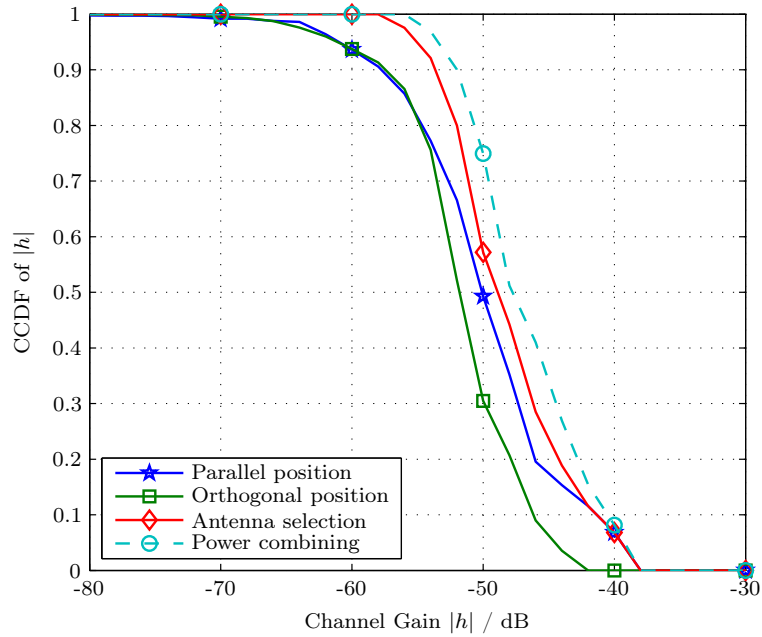


Figure 4.29: CCDFs of channel magnitude at UHF for inner mounted antennas and virtual SIMO channel.

Table 4.1: Parameters of gamma distributions for 2.45 GHz band.

WU Antenna Position	Parameter a	Parameter b
Inner parallel	1.743	7.701×10^{-4}
Inner orthogonal	2.703	3.833×10^{-4}
Outer parallel	2.045	3.152×10^{-4}
Outer orthogonal	2.319	2.255×10^{-4}

which is shown for inner parallel and outer orthogonal mounted WU antennas. The ideal fitted curves of the gamma distribution closely match the actual measured values of the channel magnitude, except for very high channel magnitudes which occur less likely than predicted by the gamma fit.

At the UHF band the distribution of the recorded channel samples significantly departs from a gamma distribution and other more typical distributions for channel coefficients, therefore I waive to give fitted values for this case.

4.5 Summary

In this chapter I addressed the application of RFID to ATMS. This advancement of classical tyre pressure monitoring gathers additional valuable sensor data by positioning a sensor directly in the tyre. This mechanically demanding WU position practically bans batteries due to the induced imbalance of the battery mass. My proposed solution is to

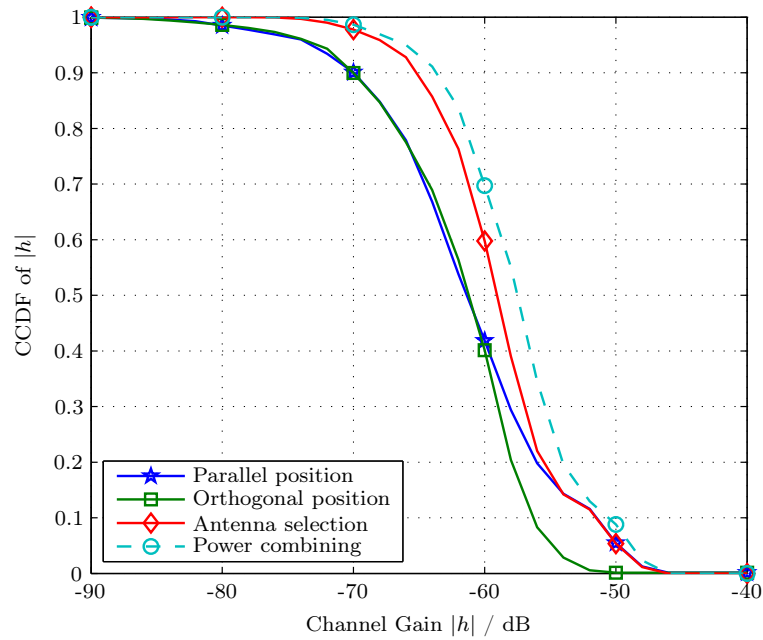


Figure 4.30: CCDFs of channel magnitude at 2.45 GHz for inner mounted antennas and virtual SIMO channel, for straight steering only.

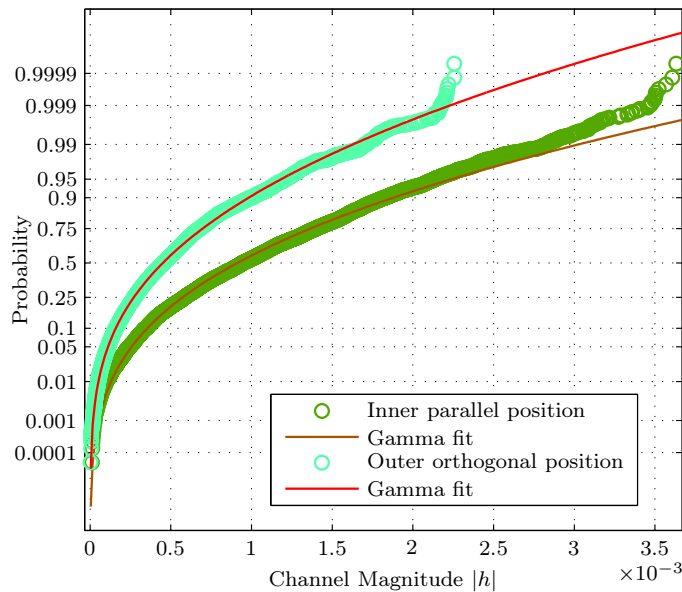


Figure 4.31: Probability plot for gamma distribution fitting of channel magnitudes at 2.45 GHz band.

use RFID technology to power the WU electronics and communicate the sensor data. To evaluate the feasibility of the RFID operated ATMS I investigate the WU–OU channel. First, a frequency-flat channel model is derived and the periodic channel behaviour due to the wheel rotation is exploited for a representation in the Fourier domain. FEM

simulations of a simple vehicle model show a bandlimited behaviour of the channel. This bandwidth limitation is also observed in channel measurements where a Golf V car is equipped with the monopole antenna described in Section 2.1.1 to form the OU antenna, and with dipole antennas manufactured from copper tape to resemble the WU antennas. The measurements reveal large channel losses, especially for the ISM band, and channel magnitude fluctuations during a single rotation up to 30 dB. In contrast, the phase response is smooth and allows for geometrical interpretation according to the changing distance between WU and OU for one revolution. I conclude that the channel is accurately represented by a single dominating channel cluster rotating in close proximity to the WU.

The channel gain of the parallel mounted WUs significantly changes for inner or outer mounting positions, while the orthogonal mounted WU has comparable channel gains for the two remaining mounting options. This is in accord with the pattern measurements of the WU antennas mounted in the vehicle wheel, which show completely different behaviour for orthogonal and parallel mounted dipoles. The reason for this is a guided wave between the anisotropically conducting steel belt in the tread and the metallic rim, which is only excited by the orthogonal mounted WU antenna. Differences for the two mounting orientations are also found in the spectral Fourier representation.

To evaluate the actual read probabilities of an ATMS system based on the proposed antennas and RFID concept, I conduct a statistical analysis of the obtained measurement data. In Section 1.1 I argue that when proper leakage cancellation is applied to a low transmit noise RFID reader, the system is forward link limited. Therefore, the read probabilities directly read from CCDFs given a maximum allowed channel loss, which is calculated for UHF to be 50 dB. While the best SISO case at UHF for a short dipole offers 49 % read probability, the use of power combining enhances the read probability to 75 %. Further, due to the diversity gain the slope in the CCDF is steepened and 100 % read probability is reached with 56 dB of allowed channel loss. This is slightly smaller than the value calculated in Section 1.1.2 for the most current single antenna RFID tag — so a very high read probability is achievable today with the most technologically advanced RFID chips.

For the ISM band channel losses are higher by approximately 12 dB, so given the current European regulations with lower allowed EIRP this band is unsuitable for powering WU using a vertically polarized antenna as used throughout the channel measurements. Statistically, the channel magnitude data is found to closely match a gamma distribution, parameters are tabulated in Table 4.1. The influence of steering effects on the CCDFs are extremely low, meaning that the effects of steering of the front wheels is negligible. Comparing the two SIMO schemes the performance increase from antenna selection to power combining in terms of power is at maximum 1.7 dB, i.e., the simpler technique implies a rather minor penalty.

Chapter 5

Conclusion

Standard far-field Radio Frequency IDentification (RFID) systems are now on the market for several years and are applied in various areas. The application of RFID technology for wireless sensors is not as mature as the application in supply-chain management, logistics, and retail, but still is not considered novel any more. However, in both application fields RFID has failed to become a mainstream technology as the bar code or Wi-Fi. The reasons are manifold, but boil down to lacking reliability, caused by degraded tag antennas due to mounting, lacking advanced signal processing in many RFID readers, insufficient transmit to receive isolations in readers, and limited tag sensitivity. While scenarios with many tags and moderate channel losses are limited by the reader's capabilities to distinguish tags and solve collisions, scenarios with few tags or high channel losses are limited by the link budget. The link budget limitation either occurs at the forward link to power the tag, or at the reverse link, when the received Signal to Noise Ratio (SNR) is insufficient.

In this thesis I focused on two aspects of RFID which, when properly designed, remove the today often dominant reverse link limitation and enable to fully exploit the forward link limit, which is defined by regulatory transmit Equivalent Isotropically Radiated Power (EIRP) bounds and the tag sensitivity. These two aspects are reader antennas and leaking carrier cancellers, which were treated in two separate chapters. The knowledge and preconditions gained from these chapters is then used to analyse the sensor application of an RFID-based Advanced Tyre Monitoring System (ATMS).

The main contributions of this thesis are:

1. I derive the RFID reader receive SNR given the maximum forward link limited Free Space Loss (FSPL). The receiver noise term is often dominated by the leaking transmitter noise. To combat this limitation, a reader antenna with high gain and a broadband Leaking Carrier Canceller (LCC) must be used.
2. I developed a horizontally polarized, compact switched beam antenna, which allows the creation of ten different beams. The antenna exhibits a directivity of 4.7 dB at Ultra High Frequency (UHF) and allows to select an individual Wheel Unit (WU) if mounted at the body floor pan of a car.
3. A solution to the problem of antenna degradation in presence of a metallic object, e.g. a vehicle's body floor pan, is presented: I shield the switched beam antenna using a Frequency Selective Surface (FSS). The shield demands an efficiency penalty of just 0.8 dB at UHF and 0.5 dB at Industrial, Scientific, Medical (ISM) frequencies, when spaced 0.08λ to the antenna. The addition of the FSS shield increases the

directivity of the overall antenna system to 5.7 dB at UHF and 10.2 dB at ISM frequencies, and preserves the fundamental beam shape to allow WU selection.

4. In this thesis I model the broadband performance of LCCs. For single tap leaking channels, the corresponding model accurately predicts the suppression performance and reveals the importance of delay control: Conventional RFID readers without delay adaptation and arbitrary antenna cable lengths are doomed to fail to perform broadband cancellation. They are therefore reverse link limited by their transmit noise. For multi-tap leakage channels, I propose a novel Broadband Leakage Canceller (BLC). In an experiment, the three tap BLC increases the 15 dB isolation bandwidth by a factor larger than 10, when compared to a conventional canceller.
5. I propose the new “fast algorithm” for LCC adjustment, which is based on three amplitude measurements. The algorithm is rigorously analysed regarding noise, bias, and accuracy, both theoretically and experimentally. I recommend to accept the computed bias in favour of a small error mode. On my RFID reader test environment, the optimized fast algorithm’s isolation gain is on average only penalized by 0.5 dB, when compared to the optimum setting.
6. The ATMS channel measurements conducted, reveal large average losses and variations up to 30 dB per wheel revolution, due to the lossy tyre material and multipath propagation. The investigated antenna orientations “parallel” and “orthogonal” show a fundamentally different behaviour regarding spectral components and sensitivity to mounting on the inner or outer sidewall. This is caused by guided waves inside the wheel, which are excited by orthogonal mounted dipoles only.
7. A statistical channel evaluation shows that WU communications based on UHF RFID is feasible. The key to reach high read probabilities is the exploitation of polarization diversity at the WU, which grants 75 % read probability for power combining using the short WU dipole. 100 % are reachable, using tags with state of the art sensitivity and optimized WU antennas, which is shown by the 5 dB higher efficiency of the long antennas when compared to the short ones. For microwave ISM RFID and a vertically polarized Onboard Unit (OU) antenna, I measured on average 12 dB higher channel losses than at UHF. Therefore, under the current legal EIRP limits at this band, the ISM band is not suitable for RFID-based WUs.

Future work for ATMS is proposed in the area of chip design: The integration of low-power pressure and vibration sensors and an RFID chip on a single silicon die requires attention. The sensor electronics might be additionally powered using energy harvesting. The open task of integrating the sensor mounting into the tyre manufacturing process needs to be solved. Possible future research directly extending this thesis could investigate the ATMS channel using a horizontally polarized, FSS shielded OU antenna.

An open question to improve general RFID systems are electrically controllable, variable delay lines for BLCs. Extended BLCs are also important for full-duplex radio systems. I consider leakage cancellation for Multiple Input Multiple Output (MIMO) readers to be of key interest, so that state-of-the-art signal processing techniques are also employable to RFID.

Appendix A

Antenna Measurement System

Performing accurate antenna measurements is an art on its own. Error sources are manifold, and especially problematic areas are Antenna Under Test (AUT) mounting and AUT feeding. Pattern and gain plots are useless, if the used coordinate system including the polarization definition is unknown. Therefore, this chapter treats the used cabled and cable-less measurement hardware, describes the underlying coordinate systems, and presents comparison measurements of the Switched Beam Antenna (SBA) to motivate the use of Mathematical Absorber Reflection Suppression (MARS). The chapter is based on the original publications [106, 119, 120].

A.1 Standard Measurement System

All presented antenna measurements were conducted in our anechoic chamber with outer dimensions of $5\text{ m} \times 5\text{ m} \times 5\text{ m}$ using a commercial Near-Field (NF) measurement system. It is a θ over φ scanner system, so the AUT is mounted on a vertical column connected to the φ -stage. The probe antenna is mounted on a dielectric swing arm and is moved from a place right above the AUT to a place almost directly below the AUT during measurements. With this arrangement an almost full scan of the AUT-enclosing sphere is obtained, except for a cone of $\theta > 160^\circ$, where the φ -stage blocks further movement of the θ -arm. For cabled measurements, the AUT is connected to the measurement hardware using a coaxial cable, which passes the φ -stage using a rotary joint. AUTs that require control signals as the SBA presented in Section 2.2 are additionally connected to a control cable, which is routed parallel to the coaxial feeding cable along the z -axis, and which also passes the φ -stage using a slip-ring assembly.

Antennas which have a defined symmetry plane, an asymmetric coaxial feed, and which are mounted in the chamber so that the cables running along the z -axis lie in this symmetry plane, are measured without additional errors when this feeding method is used. For all other antennas, the feed cable is problematic because it will carry radiating sheath currents which contribute to the measured pattern. These antennas were measured using a cable-less method described in the next section.

The AUT needs to be mounted to the rotation stage. For this purpose the antenna measurement range manufacturer supplied three columns made from glass-fiber reinforced plastic of different lengths (41, 90 and 131 cm), and a plastic disc measuring 2.4 cm in height, which goes on top of the columns and has mounting holes for different AUTs. Due

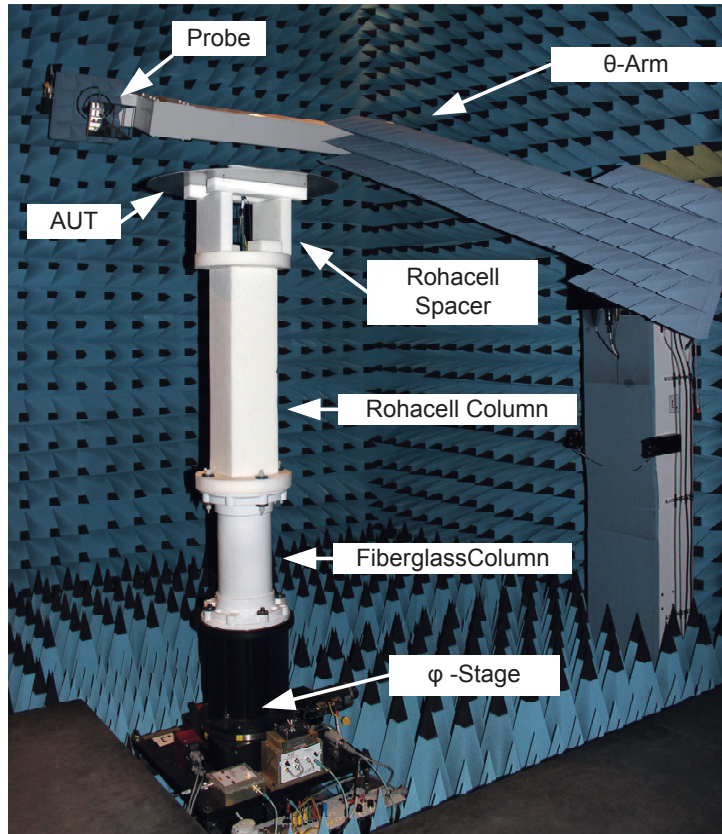


Figure A.1: Measurement setup in the anechoic chamber showing the manufactured Rohacell Column.

to the undefined, but presumably high relative permittivity of the fiberglass columns, I manufactured new additional columns from Rohacell IG31-F where the long one is depicted in Figure A.1. As is visible on this picture, the Rohacell column is directly bolted to the small fiberglass column using nylon screws. The additional Rohacell spacers were used to bring the AUT within 4 cm of the scan centre for NF measurements. The relative permittivity of Rohacell IG31-F is $\epsilon_r = 1.05$, and its loss tangent at 2.5 GHz is $\tan \delta = 0.0003$ [121].

The standard Far-Field (FF) patterns of the AUTs were generated using near-field scans of the AUT and performing a near-field to far-field transform using a commercial software. For these measurements the Maximum Radial Extend (MRE) or radius of the minimum sphere enclosing the AUT as defined in [122], was set to the minimum necessary value to reduce scan time and exploit only the spherical modes necessary to represent the AUT.

A.2 Cable-Less Measurement System

As described before, the standard measurement procedure requires a cable to be connected to the antenna, which then is routed through a rotary joint at the bottom of the azimuth-stage and connects to a Vector Network Analyser (VNA). This method is prone to measurement errors if electrically small low gain antennas or symmetric antennas without proper baluns are measured, mostly because radiating sheath currents on the feed cable cannot be avoided. The measurement system described here was originally published in [106].

Similar to [123, 124] I use a small battery driven oscillator directly attached to the AUT to eliminate the feed cable, see Figure A.2a. The oscillator assembly has dimensions of $18\text{ mm} \times 9\text{ mm} \times 3\text{ mm}$. It operates crystal controlled at 864 MHz and is further described in [124, 9]. In contrast to [123, 124] I perform NF measurements on my AUTs. The benefits of NF scans of small AUTs when compared to conventional FF scans are faster scanning times for the same resolution and lower AUT positioning accuracy demands. Since phase information is essential for all NF measurements [122], a phase reference locked to the oscillator must be provided. For this purpose I use a pickup antenna mounted directly on top of the φ -stage, see Figure A.2b. It is connected to the measurement VNA using the rotary joint of the φ -stage. Since the pickup antenna is almost level with the metallic flange of the φ -stage, I do not expect any measurable influence of the pickup antenna on the pattern of the AUT.

The assembly of the AUT and the oscillator is mounted on the azimuth-stage using dielectric spacers. Therefore, the AUT rotates on the azimuth-stage in full mechanical synchronization with the pickup antenna and the channel between AUT and pickup antenna remains unchanged throughout the measurement. The NF data is measured using a VNA with the pickup antenna directly connected to the input of receiver $R1$, and the scanner probe antenna connected to the receiver A input. The complex ratio $A/R1$ is recorded and used to calculate the FF patterns using a commercial unmodified software.

A.3 Used Coordinate Systems

Throughout this thesis, for all gain and pattern plots, a classical spherical coordinate system with Ludwig 2 polarization coordinates is used [125], as shown in Figure A.3. The vectorial FF is completely parameterized by the azimuth angle φ and the polar angle θ . For every point P the electrical field components are decomposed in an azimuth component E_φ and a polar component E_θ .

The vertically polarized antennas presented in Section 2.1, namely the monopole and the Low-Profile Dual-band Loop (LPDL), are measured with their radiator parallel to the z -axis, as indicated in the corresponding drawing Figure 2.1a. In this orientation, and using Ludwig 2 coordinates, the E_θ components corresponds to the co-polarization, and E_φ is the cross-polarization, ideally being zero. Therefore in Section 2.1 all pattern and gain plots correspond to E_θ .

For the horizontally polarized SBA oriented as indicated in Figure 2.12, neither the E_φ

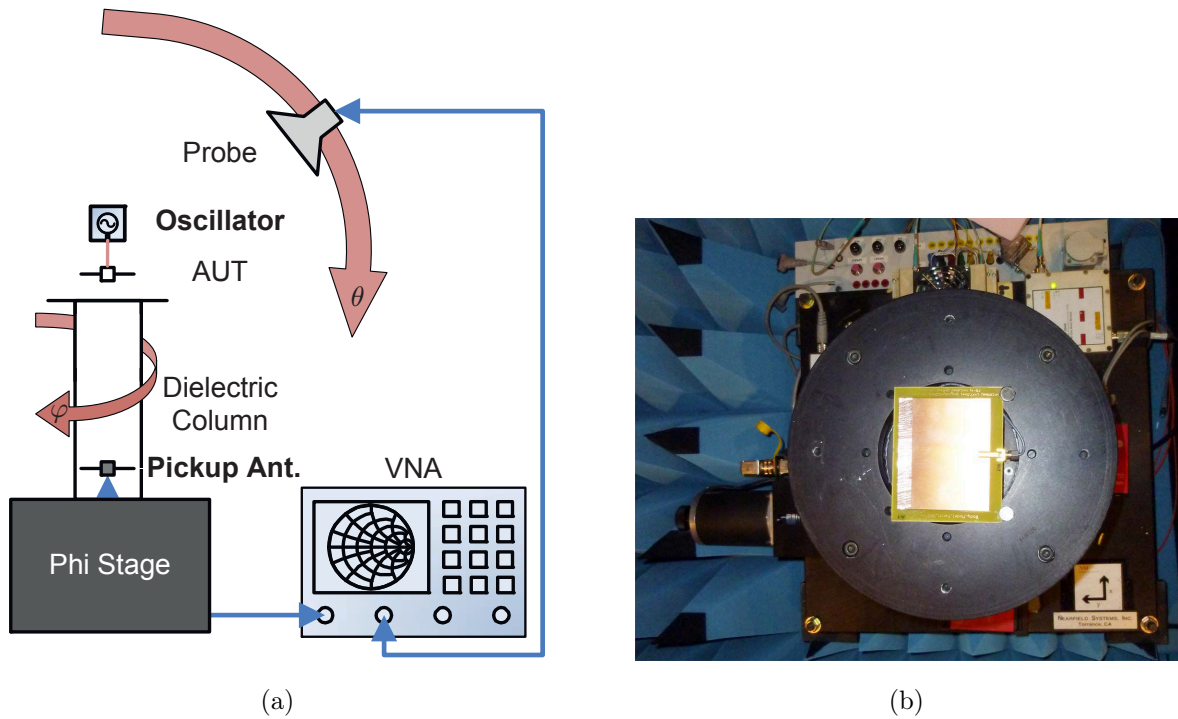


Figure A.2: Cable-less NF antenna measurement system: (a) Block diagram , (b) picture of the pickup antenna mounted on the azimuth-stage.

nor the E_θ component directly relate to a co- or cross-polarization, i.e. both components contain significant power. Since I am interested in the horizontal polarization, all gain and radiation plots in Section 2.2 and Section 2.3 correspond to E_φ . Further, this coordinate systems allows for direct comparison of the different beam settings. For gain plots in both polarizations and representations in different coordinate systems, see Figure A.9.

The gain plots of the WU antennas in Section 4.3.1 were obtained in the coordinate system shown in Figure 4.14. Here both polarizations are drawn, since these antennas, especially in the orthogonal mounting position, have a very irregular pattern.

A.4 Analysis of Measurement Impairments

In this section I describe distortions in measured antenna patterns of low gain AUTs in our chamber. I encountered problems when attempting to measure the UHF SBA described in Section 2.2.1. These comparison measurements described here motivated the use of MARS, described in Section A.5.

When I first noticed, the significant impact of the mounting parameters of the SBA on its measurement result, I started to conduct a measurement series to evaluate the influences of different parameters in the measurement setup. I was especially hoping to find a minimum required foam spacer height for the SBA to operate without detuning effects due to the dielectric column. The results of these measurements are summarized

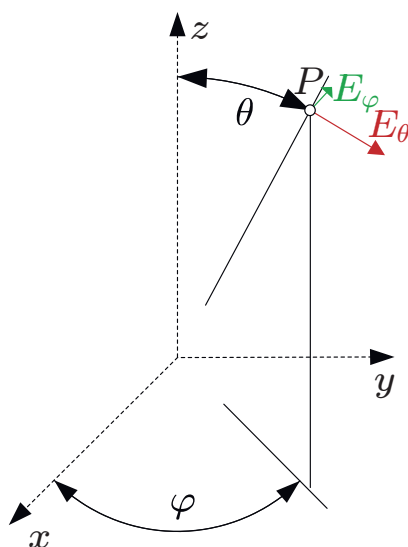


Figure A.3: Spherical coordinate system used for antenna measurements.

Table A.1: Comparison of performed evaluation measurement data: The column, absorber, and foam spacer heights, and the MRE and antenna z offset are given in cm.

Index	Column	Absorber	Spacer	MRE	z offset	Directivity	θ Peak
1	90	0	52	small	7,4	5.3 dB	111°
2	131	0	12	small	8,4	6.1 dB	43°
3	131	0	26,5	small	22,9	5.7 dB	92°
4	131	0	14,5	small	10,9	6.4 dB	57°
5	131	0	4	small	-0,4	7.1 dB	176°
6	41	0	89	small	-4	4.9 dB	90°
7	41	0	111	small	18	5.4 dB	136°
8	41	0	52	small	-41,6	5.6 dB	122°
9	41	0	52	95	-41,6	8.8 dB	14°
10	41	10,2	45	95	-38,4	9.7 dB	13°
11	41	10,2	45	44	-38,4	5.8 dB	104°
12	41	10,2	69,5	26	-13,9	5.9 dB	127°
13	41	10,2	69,5	95	-13,9	6.7 dB	62°
14	41	10,2	69,5	115	-13,9	7.2 dB	136°

in Table A.1. The columns “Column”, “Absorber” and “Spacer” state the length of the used support elements in cm: “Column” corresponds to the fiberglass column, “Spacer” represents foam spacers from styrofoam and Rohacell.

For the first scans the MRE was chosen to be as small as possible, based on the physical size of the antenna and the mounting height with respect to the intersection of the two rotation axes φ and θ which is given in the next column labelled “ z offset”.

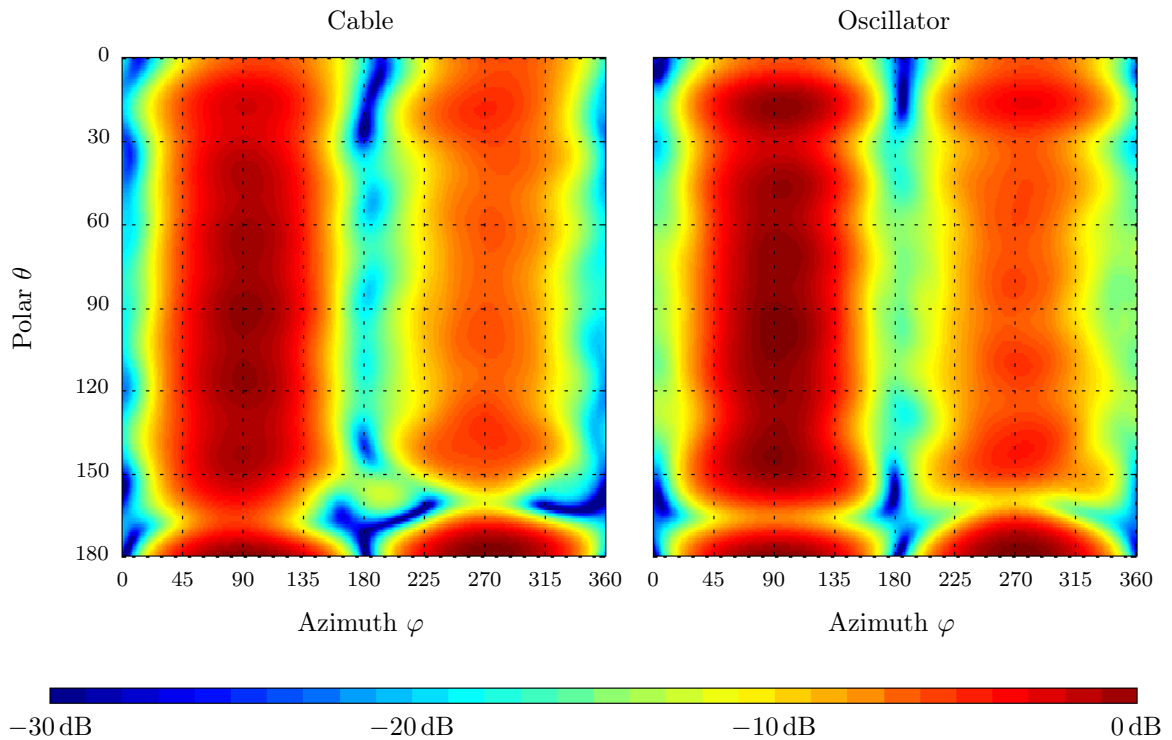


Figure A.4: SBA measurement gain plot comparison for the E_φ component: Cable feed versus oscillator.

Additionally, for each measurement the evaluated directivity values and the polar peak position are given. It is evident that the different values vary considerably for the different measurement setups. Further, most obtained gain patterns carry significant ripple in the polar domain. I suspected multipath propagation in the chamber, especially reflections from the plastic disc, which was used as an interface between the columns and the foam spacers. To rule out this effect, for measurements 10 to 14 two layers of flat foam absorbers (Eccosorb FS-50-NRL) with a total height of 10.2 cm were placed between the plastic disc terminating the column and the foam spacer. This also did not significantly reduce the polar ripple, or stabilize the directivity measurement,

The polar ripple remained, as well as the varying directivity and θ -peak values, so I conclude that scattering from the plastic disc is not the reason for the observed measurement impairments.

A.4.1 Feed Cable Issues

To rule out sheath currents on the coaxial feed of the SBA, which could explain the behaviour explained before, the cable-less measurement method described in Section A.2 is applied. A modified version of the SBA where the pin diodes are replaced with wire jumpers (for deactivated dipole elements) or left unconnected (for the activated element) was manufactured so no Direct Current (DC) supply cables for this modified antenna are

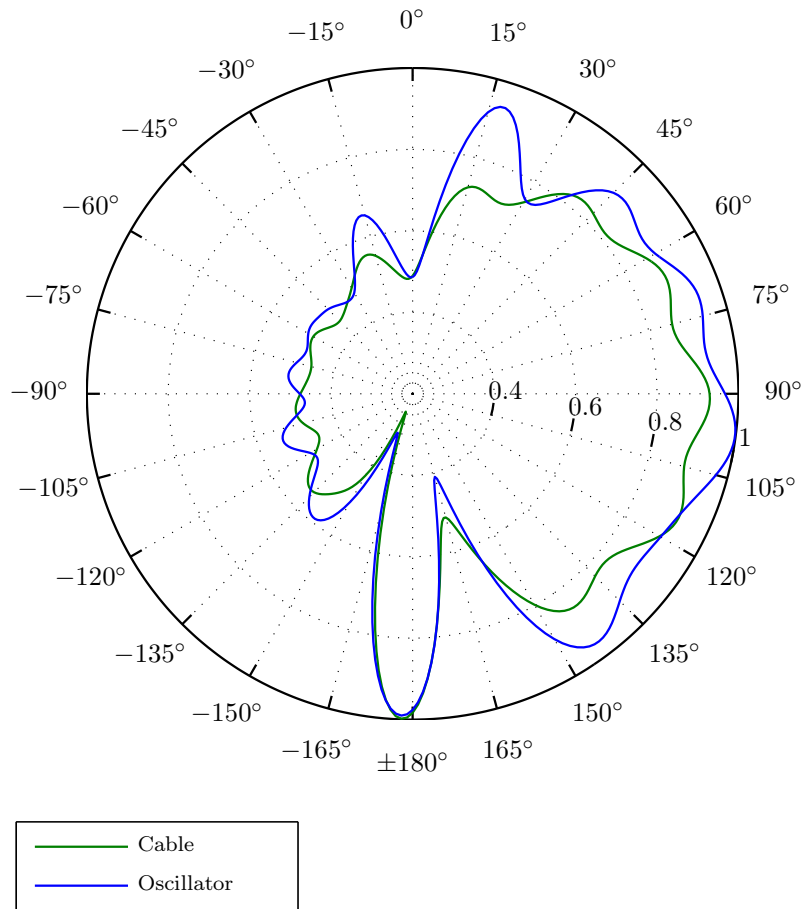


Figure A.5: SBA measurement pattern comparison for the E_φ component: Cable feed versus oscillator.

required. The battery equipped oscillator feeding the antenna is directly mounted on the AUT Printed Circuit Board (PCB). The AUT plus oscillator assembly is then placed on top of the Rohacell spacers which are mounted on the azimuth-stage.

I performed comparison measurements to see the influence of the feed cable when all other parameters remain unchanged. Figure A.4 presents the comparison of the two gain plots corresponding to E_φ . In both cases the antenna PCB was mounted parallel to the X/Y plane according to Figure 2.12. Both plots show some ringing in the theta direction, the ringing at very low and very high theta values is even more pronounced in the oscillator driven measurements. Figure A.5 presents a theta cut based on this data. Interestingly, the peak of both plots is at approximately $\theta = 180^\circ$, which is an unphysical artifact partially explained by sphere truncation. The next section discusses the effect of sphere truncation in more detail. The measured directivities for these two cases are 5.5 dB for the cabled measurements and 4.8 dB for the oscillator version.

Based on this comparison, it seems hard to decide, which measurement technique pro-

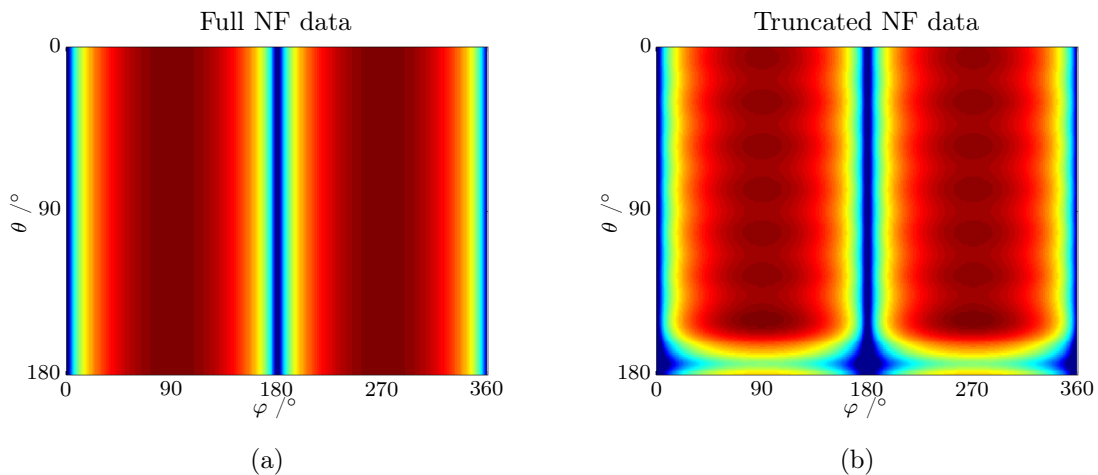


Figure A.6: FF gain plot of the E_φ component of an ideal Hertzian dipole (a) based on a complete NF data set (b) based on truncated NF data [120].

duces more accurate results. However, this comparison rules out sheath currents as a source of the measurement inaccuracies.

For the measurements discussed in the following sections I used the oscillator driven method because we compare measurements of the antenna mounted in orientations which would be hard to feed with coaxial cable without interfering with the AUT reactive near field.

A.4.2 Sphere Truncation

Remember that the measurement hardware only captures data up to theta angles of $\theta = 160^\circ$, and the missing data points in the NF are replaced by zeros in the NF to FF transform software. To demonstrate the effects of measurement sphere truncation in our chamber, I present a comparison of numerically calculated FF patterns of a Hertzian dipole being collinear with the x-axis, centred at the origin, see Figure A.6.

Both plots are created in two steps: First, the NF of a Hertzian dipole in the mentioned orientation is calculated. Then either the complete NF is transformed to the FF, or the NF is first modified by setting the amplitude and phase values for polar angles $\theta > 160^\circ$ to zero. The second case shown in Figure A.6b corresponds to the truncation applied in the measurement chamber due to the limited probe scan range.

The FF pattern calculated from the truncated NF data shown in Figure A.7 exhibits a ripple in the polar domain, as we saw on the measurement of the SBA in Figure A.5. Note that this ripple occurs in areas where the NF was not truncated. Further, there is a small peak at $\theta = 180^\circ$. The maximum deviation from the untruncated data occurs at $\theta = 150^\circ$ with an amplitude of 1.1.

The conversion from NF data to FF data is processed by performing a multipole expansion of the NF data in spherical modes, and then performing an inverse transform at

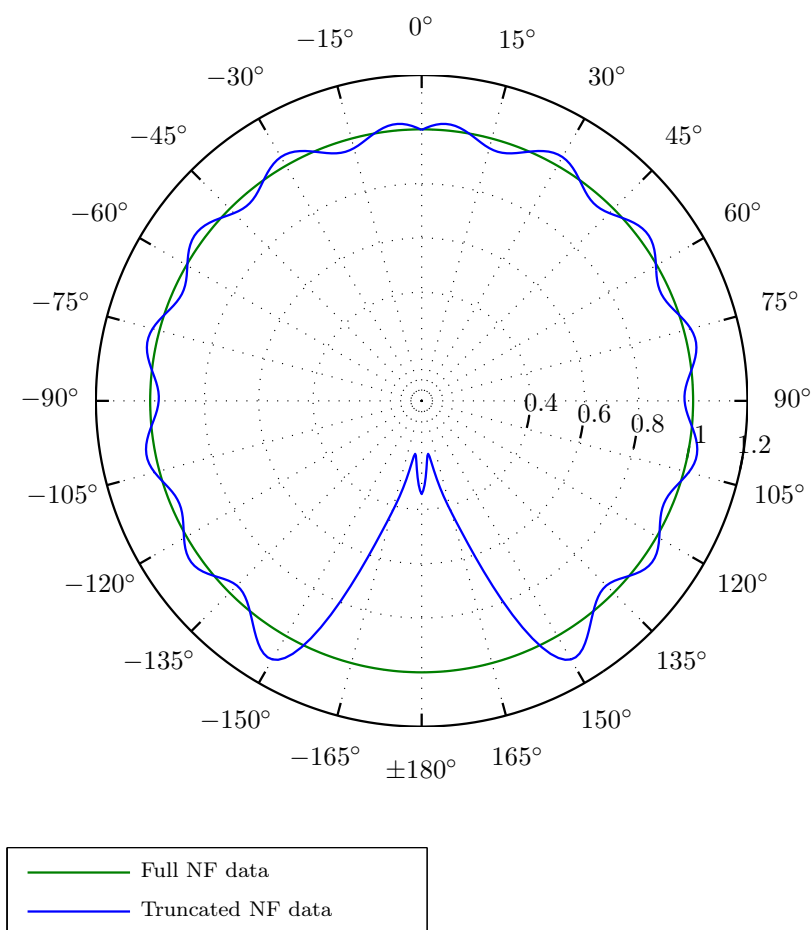


Figure A.7: Demonstration of truncation effects on NF data: Theta cut comparison [120].

radius infinity, corresponding to the FF [59]. A finite number of spherical modes is used, based on the MRE. Here, spherical mode coefficients up to order 15 were used, which is the same value as in the comparison measurements of the SBA described in Section A.4.1. The ripple effect is explained by the abrupt change in the NF data due to truncation, which creates a Gibbs phenomenon in the spherical modes. A higher order of spherical coefficients will result in a higher frequency theta ripple.

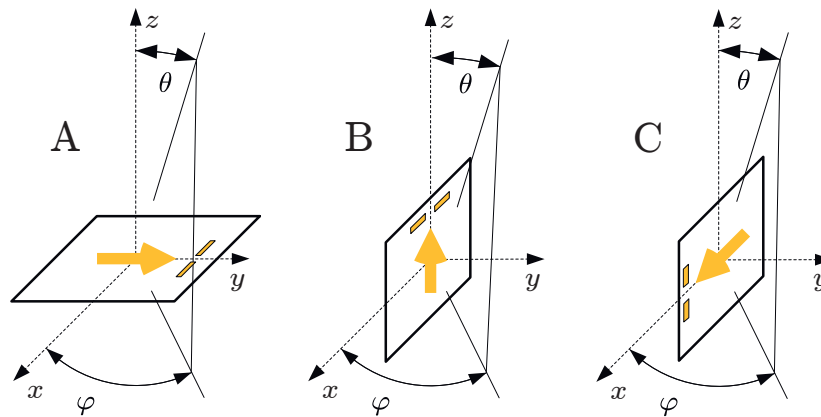


Figure A.8: Graphical representation of the three measured antenna directions. The arrows indicate the expected direction of the main beam.

A.4.3 Orientation Comparison

We already have seen that different mounting positions give quite different pattern measurement results. Further, due to the effects of probe truncation, the AUT should be mounted in such a way, that the expected minimum in the radiation pattern points downwards — so the truncated energy is minimized. I compare three different orientations, which I will refer to as A, B, and C, and which are illustrated in Figure A.8. Geometry A is the one used up to now, also represented in Figure 2.12. Orientation B ensures that most power is radiated towards the ceiling of the anechoic chamber, and orientation C and its coordinate system constitute the most natural form of representation for a dipole like antenna in Ludwig 2 coordinates. Note that the axis names in Ludwig’s paper [125] are exchanged. The measurements are performed using the cable-less measurement setup, since orientations B and especially C cause problems when using a feed cable running parallel to the z axis.

Plain SBA

Figure A.9 shows the gain plots of the three obtained measurements in both polarizations. The FF data of the untrustworthy area of theta angles $\theta > 150^\circ$ is replaced by alternating 0 dB and -80 dB values to indicate this area of sphere truncation. This method is chosen to clearly identify these areas also in the transformed data, which is presented in Figure A.10. These gain plots are created by transforming the FF vector data for measurements B and C into the θ/φ -coordinate system of orientation A.¹ The marked area of untrustworthy theta angles is now compressed into an ellipsis. For both plots the top row represents gain plots corresponding to the E_θ -component, and the bottom shows gain plots corresponding to the E_φ -component

¹The transformation is performed by converting the spherical coordinates into cartesian coordinates, performing the vector rotation of both polarizations, and converting back to spherical. Finally, the now unevenly spaced data points are interpolated and remeshed to the same resolution as the initial data set.

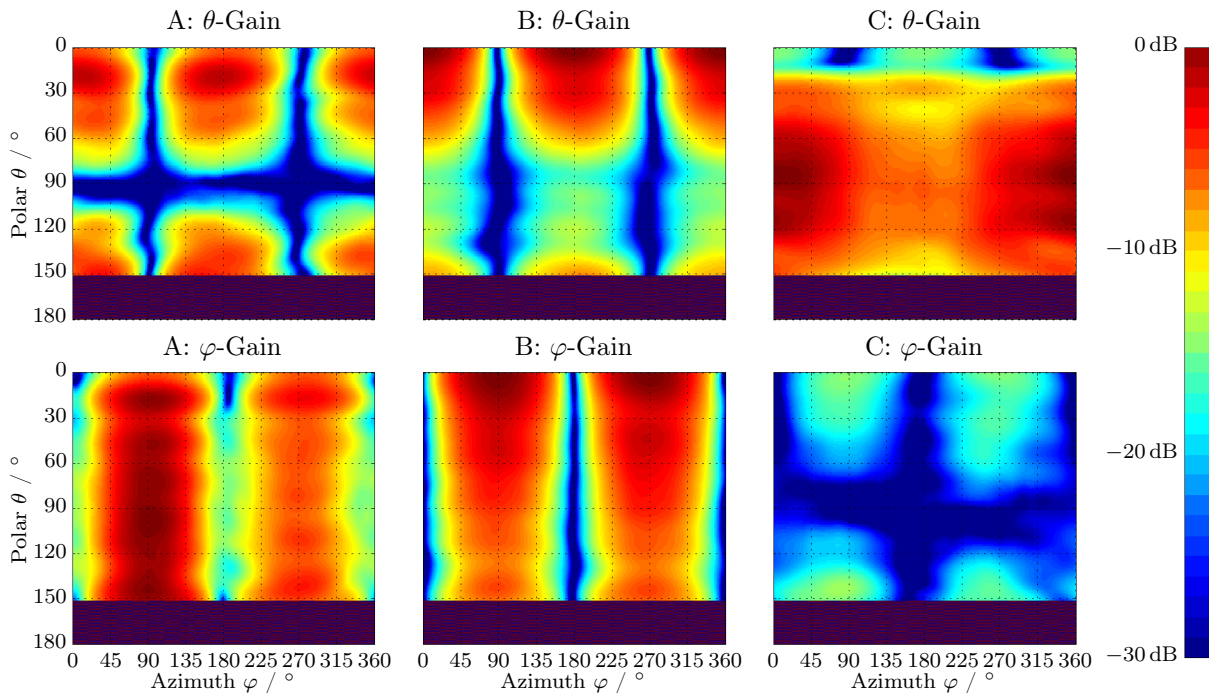


Figure A.9: Comparison of gain plots in three mounting configurations in their native coordinate system. Note that the range $\theta > 150^\circ$ is marked by alternating power levels.

Visual inspection of the three plots indicates that orientation B creates plots with least ripple. This can be argued by the fact that pointing the antenna towards the ceiling will put its symmetry axis colinear with the symmetry axis of the scanner system. Therefore, all truncation effects of the measurement hardware will cause symmetric truncation with respect to the obtained NF data. Additionally, the cropping is applied to the regime with minimum radiation which results in less truncation ripple. For the transformed gain plot for orientation C in Figure A.10 no ripple in θ -direction is observed, but some asymmetric ripple in φ -direction. Again, this is an effect of truncation in the polar domain when performing the measurement, which is asymmetric regarding the NF pattern. The coordinate transform converts it to an azimuth ripple. The different patterns of course also correspond to different measured directivities: For orientations A, B, C these are 7.8 dB, 6.2 dB, and 5.1 dB, respectively.

The ripple in the θ -domain is best compared in the θ -cut presented in Figure A.11. Measurement C obviously gives the smoothest curve because it is based on an untruncated φ -measurement in the original measurement coordinate system. The zigzag of measurements A and B centred at $\theta = 180^\circ$ and $\theta = 90^\circ$ follows from the marking method of the untrustworthy angular regions in the original FF data.

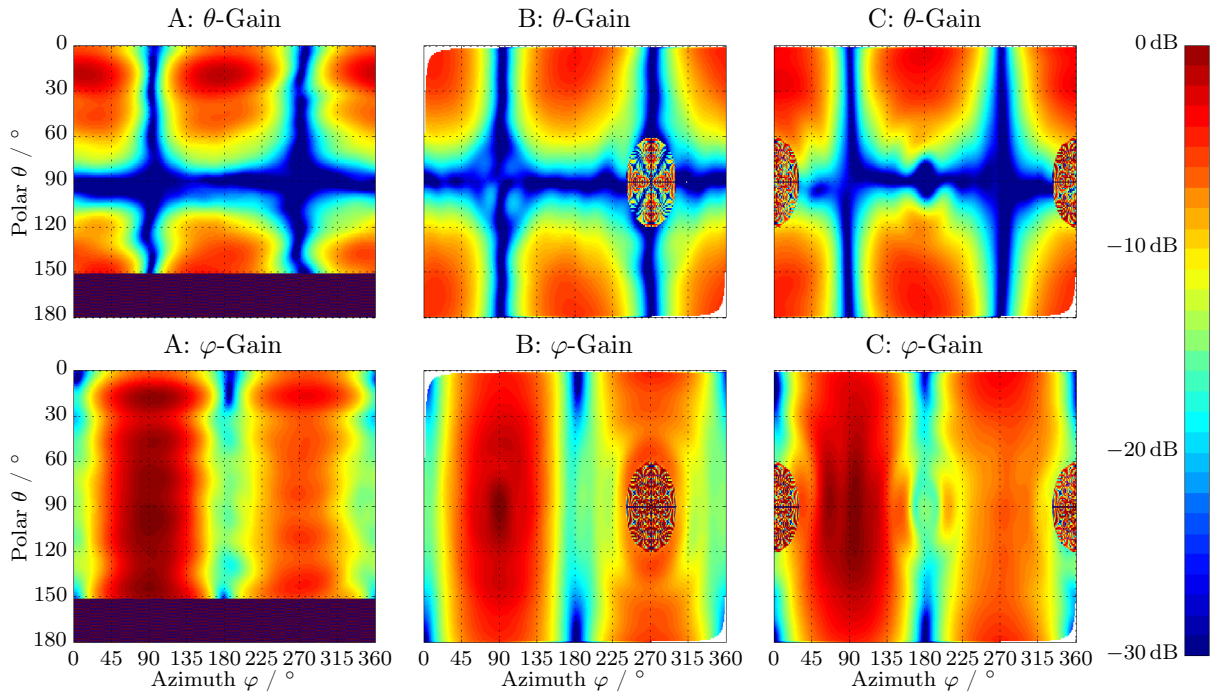


Figure A.10: Comparison of gain plots in three mounting configurations, transformed to coordinate system A. Note that the previously marked area now appears as colourful ellipse.

SBA over Groundplane

The original aim of this investigation of measurement errors in of low gain AUTs was basis work for measurements of the SBA with an FSS, as presented in Section 2.3.2. To evaluate the significance of these measurements I did comparison measurements of an SBA plus Ground-Plane (GP) assembly in the mounting positions A and B for three differed GP-SBA separations (28 mm, 46 mm, 74 mm) according to setups 2 to 4 in Table 2.4. The results are presented in Figure A.12 which represents gain plots in coordinate system A corresponding to the E_φ -component. When the two orientations are compared, we see that the differences between A and B are much smaller than in Figure A.10. Further, the ripple which is only seen in measurement A is also smaller than for the measurements without GP. This is caused by the effect of the GP on the radiation pattern: The power towards the lower hemisphere of the measurement system is reduced, so sphere truncation effects play a less prominent role. Further, the floor of our chamber is less ideal regarding absorber layout than the ceiling, due to walkway absorbers and measurement hardware. Less radiation towards the floor also means less scattering from this imperfect absorber area.

I conclude that for all measurements of the SBA plus GP or SBA plus FSS assemblies the standard cabled measurement method in orientation A performs satisfactory. For the measurements of the plain SBA MARS is used, see next section.

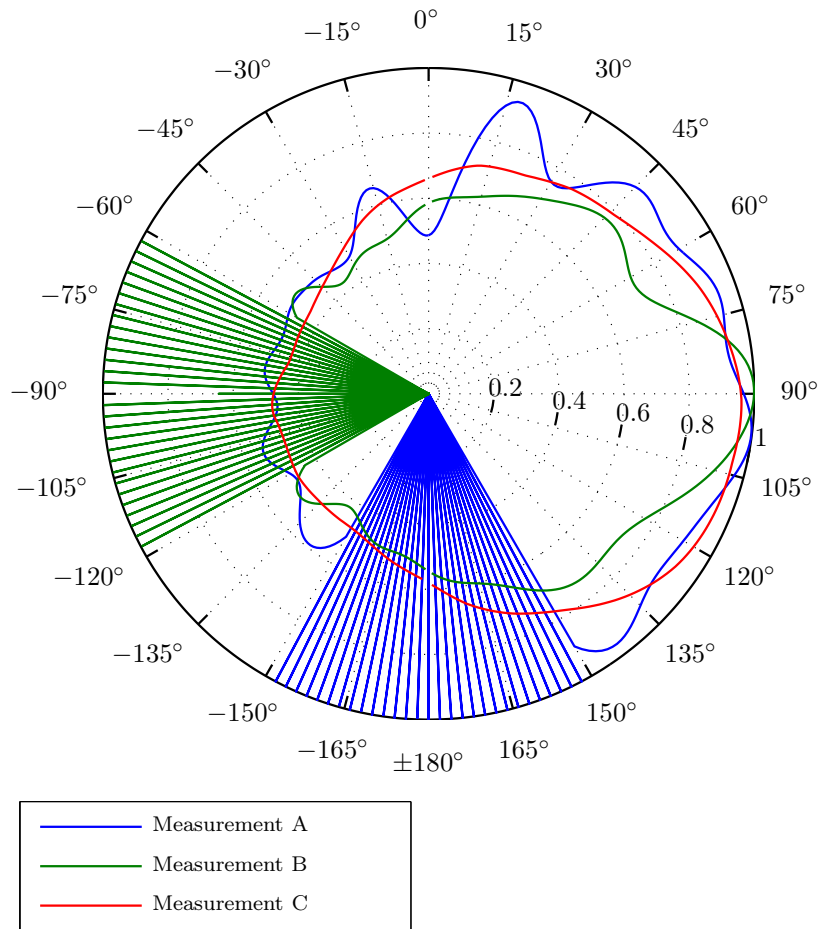


Figure A.11: Comparison of transformed measurements of the SBA for different orientations: Theta cut comparison.

A.5 MARS

MARS is a technique first proposed by [126]. It aims on the separation of spherical modes caused by reflections in the chamber, and modes actually corresponding to the AUT. As mentioned before, the number of spherical modes required to capture the AUT pattern with negligible errors depends on the MRE, which is the radius of the smallest sphere centred at the scanner coordinate system which encloses the AUT. The idea behind MARS is to artificially increase the MRE and therefore the number of modes by offsetting the AUT from the scanner origin. Then the AUT is mathematically shifted back to the coordinate system centre which also exchanges spherical modes of lower order to modes of higher order. Since now the MRE of the “new” shifted AUT is smaller, the cropping of higher order spherical modes does not alter the pattern of the mathematically shifted AUT. Instead, the cropped modes contain most of the scattering components due to the imperfect chamber. Therefore, the FF pattern calculated from the cropped spherical modes of the shifted AUT is purified. This is paid by longer scanning times based on the

Appendix A Antenna Measurement System

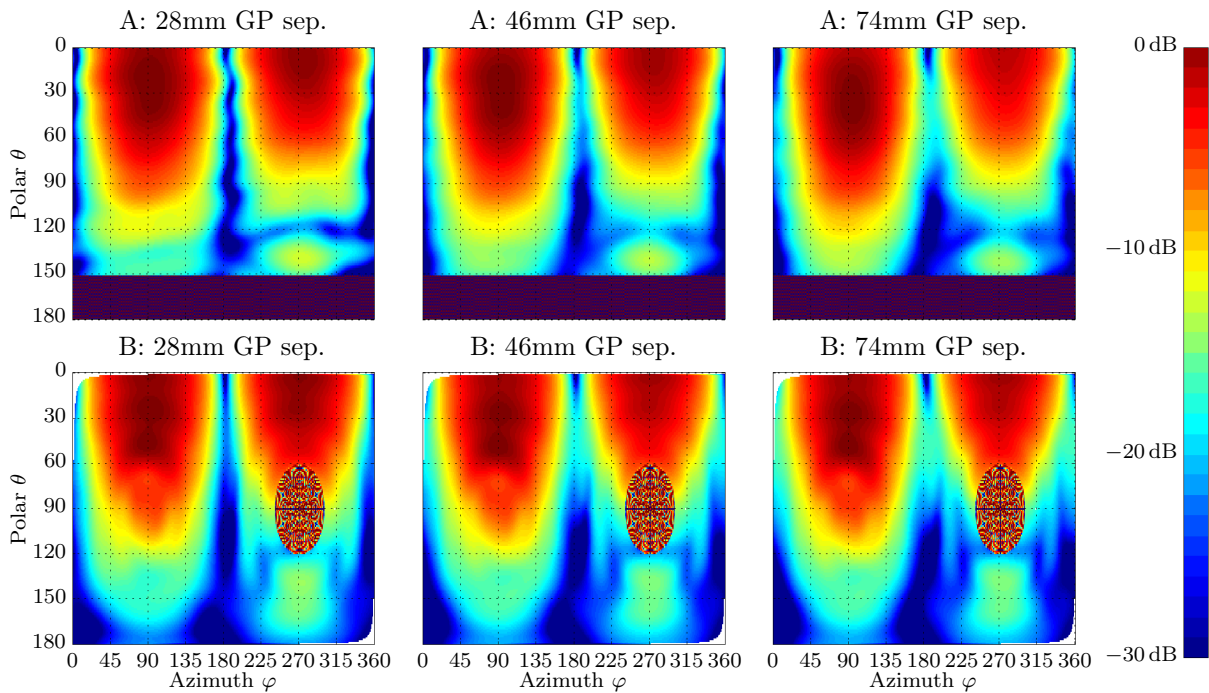


Figure A.12: Comparison of gain plots corresponding to the E_φ -component of coordinate system A of the SBA mounted atop a GP with different separations, for mounting positions A (cabled measurements) and B (transformed oscillator measurements).

extended MRE and the spacial sampling theorem.

Our MARS implementation at Vienna University of Technology uses the processed FF data from the our commercial NF to FF software including probe compensation. The AUT is then shifted by applying a phase correction to the FF data, based on the initial offset of the AUT from the origin and the wavelength. The FF is then converted to spherical modes and the expansion is performed up to the mode index specified by the physical size of the AUT. The data is converted back to FF and the purification is complete.

This method is applied to all SBA measurements presented in Section 2.2. Both, the UHF and the ISM-SBA were offset in z -direction by 39.5 cm. A positive offset is chosen, because it additionally reduces the effect of sphere truncation: The upper hemisphere of the scanner due to the offset covers more than the upper hemisphere of the AUT. Due to the offset position, the probe compensation is important to obtain an accurate FF data set. As mentioned before, this step was conducted in the commercial software. The FF data is then moved and processed with a maximum mode index of 10, to obtain the purified FF data. Figure A.13 shows the FF data obtained for the ISM-SBA directly after the measurement without MARS application. Compared to Figure 2.22, where the same data is shown with MARS applied, the increased ripple becomes obvious. The higher ripple frequency is due to the large MRE to obtain the offset measurement.

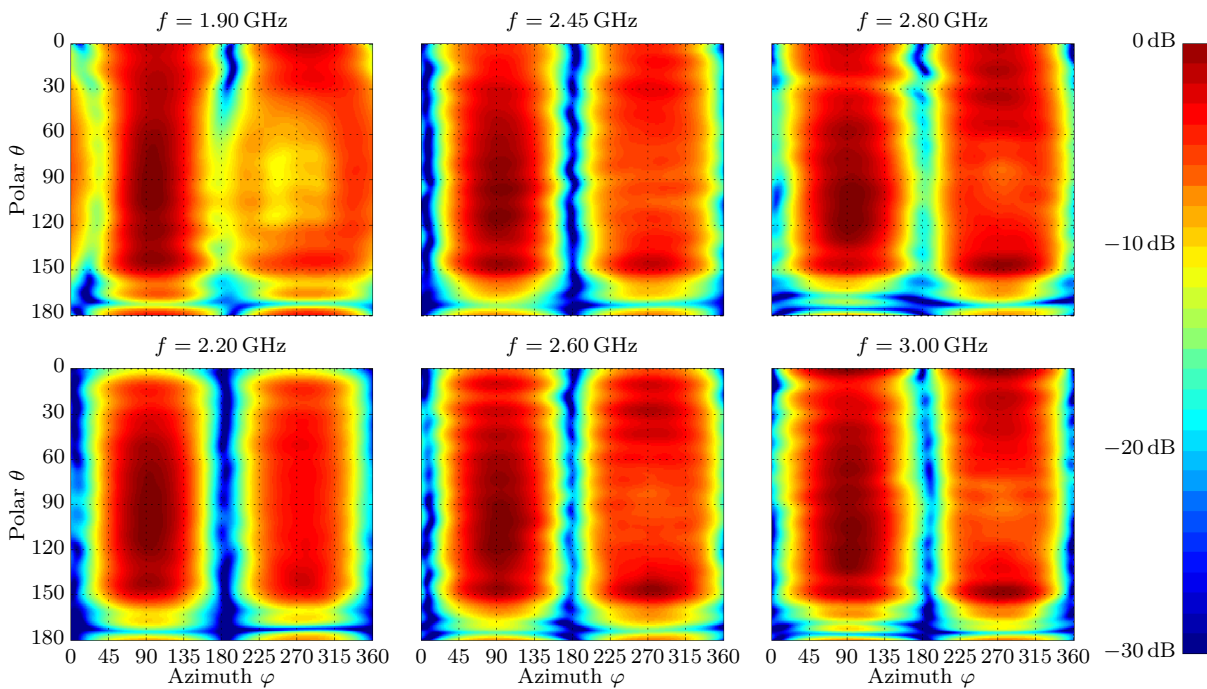


Figure A.13: Comparison of normalized gain plots for the ISM-SBA in free space for different frequencies f ; plotted for beam I pointing in y -direction, prior to MARS processing. Compare to Figure 2.22.

A.6 Summary

Not only the design of antennas but also their proper measurement is an art, even if sophisticated commercial measurement equipment is available. In this chapter I described the measurement setups and methods used for the antenna pattern and gain plots presented in this thesis. Besides the standard NF measurement method, a cable-less measurement method is presented, which is essential to obtain accurate antenna measurements from small or symmetrically fed antennas. Further, I presented a critical review of measurements conducted to evaluate the accuracy of the measurement system for low gain AUTs as the SBA. While the feed cable and reflections from the dielectric support structure were ruled out as sources of errors, the sphere truncation and the imperfect absorber layout of the anechoic chamber floor were identified as error sources. A comparison measurement of the UHF SBA in three different orientations within the chamber emphasized the effects of sphere truncation. The same comparison with the SBA plus GP assembly revealed that all combination measurements of the antenna plus the FSS are accurately conducted using the standard cabled measurement setup in orientation A. Here, the concentration of the radiation towards the upper hemisphere reduces the negative effects of sphere truncation and floor absorbers.

For the plain SBA measurements the key to acquire accurate measurements is MARS. The AUT is measured offset to the coordinate centre. This artificially increases the MRE and enables a mathematical purification of the measured antenna pattern and removal

Appendix A Antenna Measurement System

of chamber scattering without blurring features of the underlying AUT pattern. An offset towards the chamber ceiling additionally practically reduces the effect of sphere truncation.

Appendix B

Scale Drawings of the FSS Unit Cells

See next page

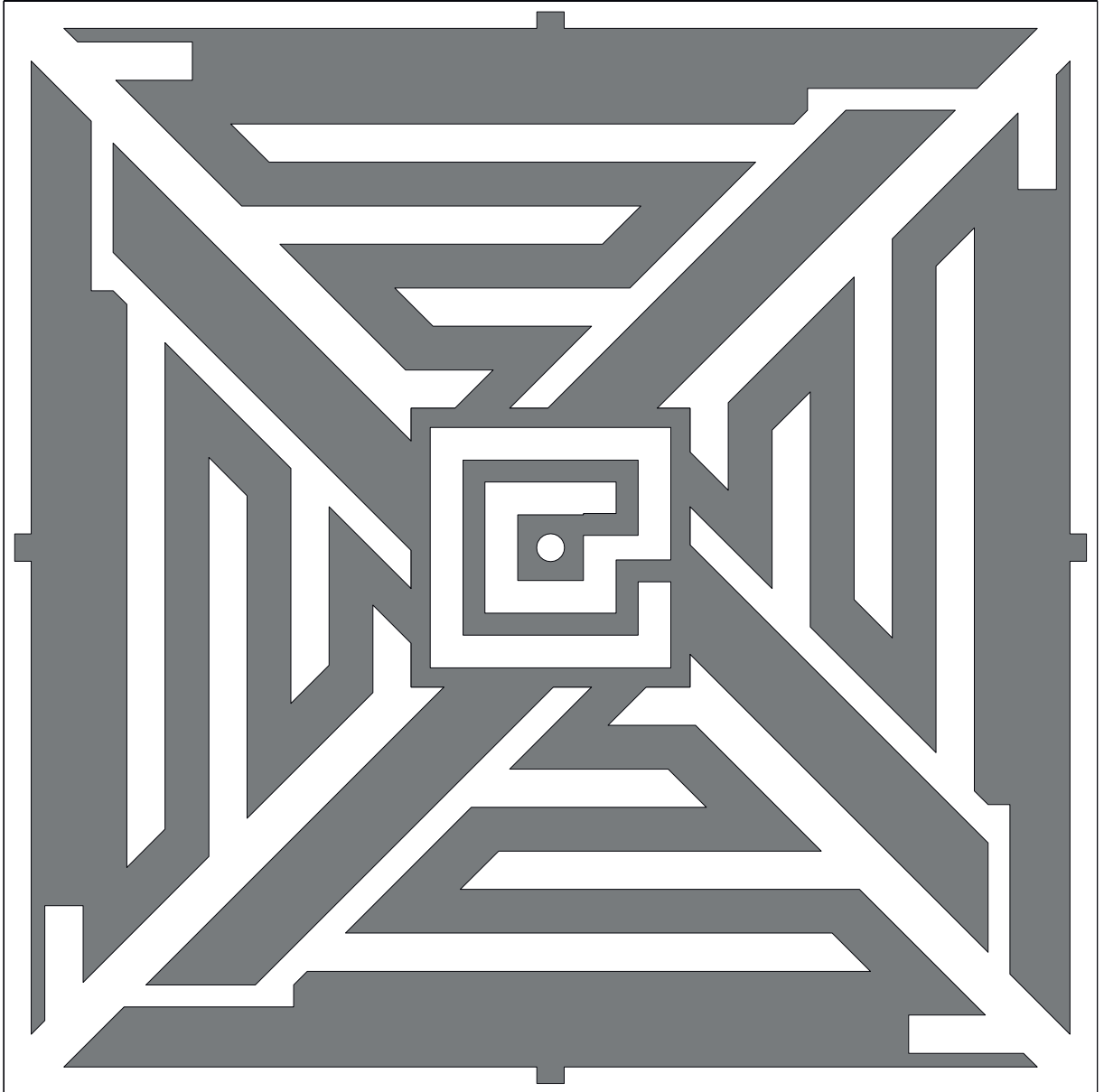


Figure B.1: Drawing of a unit cell of FSS FSS1 in scale 8:1. The thin boarder line corresponds to the 20 mm unit cell boundary.



Figure B.2: Drawing of a unit cell of FSS FSS2 in scale 8:1. The thin boarder line corresponds to the 20 mm unit cell boundary.

Bibliography

- [1] R. Want, “An introduction to RFID technology,” *IEEE Pervasive Computing*, vol. 5, no. 1, pp. 25–33, jan.-march 2006.
- [2] D. M. Dobkin, *The RF in RFID*, 1st ed. Burlington, MA, USA: Newnes by Elsevier, 2008.
- [3] K. Finkenzeller, *RFID Handbook*, second edition ed. Wiley, 2003.
- [4] G. Lasser, “Development of a UHF frontend for a comprehensive RFID rapid prototyping system,” Master’s thesis, Vienna University of Technology, Oct. 2008.
- [5] H. Stockman, “Communication by means of reflected power,” *Proceedings of the IRE*, vol. 36, no. 10, pp. 1196–1204, Oct.
- [6] P. V. Nikitin, K. Rao, and R. Martinez, “Differential RCS of RFID tag,” *Electronics Letters*, vol. 43, no. 8, pp. 431–432, Apr. 2007.
- [7] P. V. Nikitin and K. V. S. Rao, “Theory and measurement of backscattering from RFID tags,” *IEEE Antennas and Propagation Magazine*, vol. 48, no. 6, Dec. 2006.
- [8] J.-P. Curty, M. Declercq, C. Dehollain, and N. Joehl, *Design and Optimization of Passive UHF RFID Systems*, 1st ed. Springer, 2007.
- [9] L. W. Mayer, “Antenna design for future multi-standard and multi-frequency RFID systems,” Ph.D. dissertation, Technische Universität Wien, 2009.
- [10] NXP Semiconductors, *SL3S1204 UCODE7*, rev. 3.3 ed., Dec. 2013.
- [11] R. Langwieser, G. Lasser, A. L. Scholtz, and M. Rupp, “Comparison of multi-antenna configurations of an RFID reader with active carrier compensation,” in *2011 IEEE International Conference on RFID-Technologies and Applications (RFID-TA)*, Sitges, Spain, Sep. 2011, pp. 109–114.
- [12] R. Want, “Enabling ubiquitous sensing with RFID,” *IEEE Computer*, vol. 37, no. 4, pp. 84–86, Apr. 2004.
- [13] M. Philipose, J. R. Smith, B. Jiang, A. Mamishev, S. Roy, and K. Sundara-Rajan, “Battery-free wireless identification and sensing,” *IEEE Pervasive Computing*, vol. 4, no. 1, pp. 37–45, Jan. 2005.
- [14] L. Catarinucci, R. Colella, and L. Tarricone, “A cost-effective UHF RFID tag for transmission of generic sensor data in wireless sensor networks,” *IEEE Transactions on Microwave Theory and Techniques*, vol. 57, no. 5, pp. 1291–1296, May 2009.
- [15] J. R. Smith, B. Jiang, S. Roy, M. Philipose, K. Sundara-Rajan, and A. Mamishev, “Id modulation: Embedding sensor data in an rfid timeseries,” in *Information Hiding*. Springer, 2005, pp. 234–246.
- [16] A. P. Sample, D. J. Yeager, P. S. Powledge, A. V. Mamishev, and J. R. Smith, “Design of an rfid-based battery-free programmable sensing platform,” *Instrumentation and Measurement, IEEE Transactions on*, vol. 57, no. 11, pp. 2608–2615, 2008.

Bibliography

- [17] EPCglobal, “EPC radio-frequency identity protocols class-1 generation-2 UHF RFID protocol for communications at 860 MHz – 960 MHz version 1.2.0,” Mar. 2007.
- [18] A. van Zanten, M. Nimmo, M. Stams, J. Pineau, and P. Gauthier, “Optimization of a vehicle dynamics control using tire information,” Patent, May 17, 2007.
- [19] J. Grosinger, “Backscatter radio frequency systems and devices for novel wireless sensing applications,” Ph.D. dissertation, Technische Universität Wien, Aug. 2012.
- [20] M. D. Brzeska, “RF modelling and characterization of tyre pressure sensors and vehicle access systems,” Ph.D. dissertation, Karlsruher Institut für Technologie, 2013.
- [21] S. Goparaju, “Low power tire pressure monitoring system,” Master’s thesis, University of Akron, Dec. 2008.
- [22] F. Braghin, M. Brusarosco, F. Cheli, A. Cigada, S. Manzoni, and F. Mancosu, “Measurement of contact forces and patch features by means of accelerometers fixed inside the tire to improve future car active control,” *Vehicle System Dynamics*, vol. 44, no. sup1, pp. 3–13, 2006.
- [23] M. J. Matilainen and A. J. Tuononen, “Intelligent tire to measure contact length in dry asphalt and wet concrete conditions,” *Seoul: AVEC*, vol. 12, pp. 1–6, 2012.
- [24] G. Vietti, D. Dassano, and M. Orefice, “ISM and UWB channel characterization and measurement in an intelligent tire sensor system,” in *Antennas and Propagation (APSURSI), 2011 IEEE International Symposium on*, Jul. 2011, pp. 472–475.
- [25] J. Hidalgo, F. G. Zurbriggen, M. Orefice, and G. C. Vietti, “Wireless link measurement at UWB in a tire sensor system,” in *Applied Electromagnetics and Communications (ICECom), 2013 21st International Conference on*, Oct. 2013, pp. 1–5.
- [26] G. Lasser and C. F. Mecklenbräuker, “Vehicular low-profile dual-band antenna for advanced tyre monitoring systems,” in *2012 IEEE 23rd International Symposium on Personal, Indoor and Mobile Radio Communications - (PIMRC)*, Sydney, Australia, Sep. 2012.
- [27] K. Kark, *Antennen und Strahlungsfelder*, 1st ed., ser. Informationstechnik. Wiesbaden: Vieweg, Mar. 2004.
- [28] B. Riddle, J. Baker-Jarvis, and J. Krupka, “Complex permittivity measurements of common plastics over variable temperatures,” *IEEE Transactions on Microwave Theory and Techniques*, vol. 51, no. 3, pp. 727–733, Mar. 2003.
- [29] J. M. Boyer, “Open ring antenna,” U.S. Patent, Sep. 29, 1964.
- [30] R. D. Wanselow and D. W. Milligan, “A compact, low profile, transmission line antenna — tuneable over greater than octave bandwidth,” *IEEE Transactions on Antennas and Propagation*, vol. AP-14, no. 6, pp. 701–707, Nov. 1966.
- [31] A. M. Smith, “Vandalism-resistant UHF antenna,” U.S. Patent, Apr. 28, 1987.
- [32] R. King, C. Harrison, Jr., and D. Denton, Jr., “Transmission-line missile antennas,” *IRE Transactions on Antennas and Propagation*, vol. 8, no. 1, pp. 88–90, 1960.
- [33] O. Garay and Q. Balzano, “An antenna for a portable data terminal,” in *Vehicular Technology Conference, 1984. 34th IEEE*, vol. 34. IEEE, 1984, pp. 54–56.

- [34] K. Kobayashi, S. Nishiki, T. Taga, and A. Sasaki, "Detachable mobile radio units for the 800 MHz land mobile radio system," in *Vehicular Technology Conference, 1984. 34th IEEE*, vol. 34, May 1984, pp. 6–11.
- [35] O. Zinke and H. Brunswig, *Lehrbuch der Hochfrequenztechnik*, 1st ed. Berlin, Göttingen, Heidelberg: Springer, 1965.
- [36] K. Sundaresan and R. Sivakumar, "A unified MAC layer framework for ad-hoc networks with smart antennas," in *Proceedings of the 5th ACM international symposium on Mobile ad hoc networking and computing*. ACM, 2004, pp. 244–255.
- [37] J. Kaitovic and M. Rupp, "Improved physical layer collision recovery receivers for RFID readers," in *IEEE International Conference on RFID*, Orlando, Apr. 2014, pp. 103–109.
- [38] J. Sahaya Kulandai Raj, J. Bonney, P. Herrero, and J. Schoebel, "A reconfigurable antenna for MIMO application," in *Antennas Propagation Conference, 2009. LAPC 2009. Loughborough*, Nov. 2009, pp. 269–272.
- [39] V. A. Nguyen and P. S. Ook, "Compact switched and reconfigurable 4-ports beam antenna array for MIMO applications," in *Intelligent Radio for Future Personal Terminals (IMWS-IRFPT), 2011 IEEE MTT-S International Microwave Workshop Series on*, Aug. 2011, pp. 1–3.
- [40] J. Sahaya Kulandai Raj, J. Fahlbusch, and J. Schoebel, "A beam switching three layer reconfigurable antenna," in *Microwave Conference (GeMiC), 2012 The 7th German*, Mar. 2012, pp. 1–4.
- [41] P. Deo, A. Mehta, D. Mirshekar-Syahkal, P. J. Massey, and H. Nakano, "Thickness reduction and performance enhancement of steerable square loop antenna using hybrid high impedance surface," *IEEE Transactions on Antennas and Propagation*, vol. 58, no. 5, pp. 1477–1485, May 2010.
- [42] G. Lasser, L. W. Mayer, and C. F. Mecklenbräuer, "Compact low profile UHF switched-beam antenna for advanced tyre monitoring systems," in *2012 IEEE-APS Topical Conference on Antennas and Propagation in Wireless Communications*, Kapstadt, Sep. 2012.
- [43] I. Ackerl and W. Kleindel, *Die Chronik Österreichs*. Chronik Verlag im Bertelsmann Verlag, 1994.
- [44] C.-H. Tsao and R. Mittra, "Spectral-domain analysis of frequency selective surfaces comprised of periodic arrays of cross dipoles and jerusalem crosses," *IEEE Transactions on Antennas and Propagation*, vol. 32, no. 5, pp. 478–486, 1984.
- [45] M. Hosseini and M. Hakkak, "Characteristics estimation for jerusalem cross-based artificial magnetic conductors," *IEEE Antennas and Wireless Propagation Letters*, vol. 7, pp. 58–61, 2008.
- [46] S. Gregson, A. Newell, and G. Hindman, "Reflection suppression in cylindrical near-field antenna measurement systems—cylindrical MARS," in *AMTA 31st Annual Meeting & Symposium, Salt Lake City, UT*, 2009.
- [47] D. Sevenpiper, L. Zhang, R. F. Jimenez Broas, N. G. Alexopolous, and E. Yablonovitch, "High-impedance electromagnetic surfaces with a forbidden fre-

Bibliography

- quency band,” *IEEE Transactions on Microwave Theory and Techniques*, vol. 47, no. 11, pp. 2059–2074, Nov. 1999.
- [48] A. P. Feresidis, G. Goussetis, S. Wang, and J. Y. C. Vardaxoglou, “Artificial magnetic conductor surfaces and their application to low-profile high-gain planar antennas,” *IEEE Transactions on Antennas and Propagation*, vol. 53, no. 1, pp. 209–215, Jan. 2005.
- [49] G. Lasser, L. W. Mayer, Z. Popović, and C. F. Mecklenbräuker, “Dual-band FSS shield for a switched beam antenna,” 2014, planned submission to *IEEE Transactions on Antennas and Propagation*.
- [50] J. Pendry, L. Martin-Moreno, and F. J. Garcia-Vidal, “Mimicking surface plasmons with structured surfaces,” *Science*, vol. 305, no. 5685, pp. 847–848, Aug. 2004.
- [51] M. J. Lockyear, A. P. Hibbins, and J. R. Sambles, “Microwave surface-plasmon-like modes on thin metamaterials,” *Physical review letters*, vol. 102, no. 7, p. 073901, Feb. 2009.
- [52] A. Byers, I. Rumsey, Z. Popović, and M. Piket-May, “Surface-wave guiding using periodic structures,” in *Antennas and Propagation Society International Symposium, 2000. IEEE*, vol. 1. IEEE, 2000, pp. 342–345.
- [53] M. F. Abedin, M. Z. Azad, and M. Ali, “Wideband smaller unit-cell planar ebg structures and their application,” *IEEE Transactions on Antennas and Propagation*, vol. 56, no. 3, pp. 903–908, Mar. 2008.
- [54] D. J. Kern, D. H. Werner, A. Monorchio, L. Lanuzza, and M. J. Wilhelm, “The design synthesis of multiband artificial magnetic conductors using high impedance frequency selective surfaces,” *IEEE Transactions on Antennas and Propagation*, vol. 53, no. 1, pp. 8–17, Jan. 2005.
- [55] M. Bray and D. Werner, “A novel design approach for an independently tunable dual-band EBG AMC surface,” in *Antennas and Propagation Society International Symposium, 2004. IEEE*, vol. 1, Jun. 2004, pp. 289–292 Vol.1.
- [56] D. F. Sievenpiper, J. H. Schaffner, H. J. Song, R. Y. .Loo, and G. Tangonan, “Two-dimensional beam steering using an electrically tunable impedance surface,” *IEEE Transactions on Antennas and Propagation*, vol. 51, no. 10, pp. 2713–2722, 2003.
- [57] S. G. Johnson and J. Joannopoulos, “Introduction to photonic crystals: Bloch’s theorem, band diagrams, and gaps,” MIT Website, Feb. 2003.
- [58] M. Tsuji, H. Shigesawa, and K. Takiyama, “On the complex resonant frequency of open dielectric resonators,” *IEEE Transactions on Microwave Theory and Techniques*, vol. 31, no. 5, pp. 392–396, 1983.
- [59] R. C. Hansen, “Relationships between antennas as scatterers and as radiators,” *Proceedings of the IEEE*, vol. 77, no. 5, pp. 659–662, May 1989.
- [60] K. Penttilä, L. Sydänheimo, and M. Kivikoski, “Implementation of tx/rx isolation in an rfid reader,” *International Journal of Radio Frequency Identification Technology and Applications*, vol. 1, no. 1, pp. 74–89, 2006.
- [61] Y. Liu, Q. Zhang, and M. Zheng, “Signal analysis and design criteria for UHF RFID reader,” *ITS Telecommunications Proceedings*, pp. 233–236, Jun. 2006.

- [62] T. I. Al-Mahdawi, “Adaptive coherent RFID reader carrier cancellation,” U.S. patent application, Apr. 4, 2005.
- [63] D. P. Villame and J. S. Marciano, Jr., “Carrier suppression locked loop mechanism for UHF RFID readers,” in *IEEE Int. Conf. on RFID*, Apr. 2010, pp. 141–145.
- [64] R. Langwieser, G. Lasser, C. Angerer, M. Fischer, and A. L. Scholtz, “Active carrier compensation for a multi-antenna RFID reader frontend,” in *2010 IEEE MTT-S International Microwave Symposium Digest*, Anaheim, CA, May 2010, pp. 1532–1535.
- [65] I. Mayordomo and J. Bernhard, “Implementation of an adaptive leakage cancellation control for passive UHF RFID readers,” in *IEEE Int. Conf. on RFID*, Apr. 2011, pp. 121–127.
- [66] G. Lasser, R. Langwieser, and A. L. Scholtz, “Broadband suppression properties of active leaking carrier cancellers,” in *IEEE Int. Conf. on RFID*, Orlando, USA, April 2009.
- [67] P. Pursula, M. Kiviranta, and H. Seppä, “UHF RFID reader with reflected power canceller,” *IEEE Microwave and Wireless Components Letters*, vol. 19, no. 1, pp. 48–50, Jan. 2009.
- [68] T. Xiong, X. Tan, J. tian Xi, and H. Min, “High tx-to-rx isolation in UHF RFID using narrowband leaking carrier canceller,” *IEEE Microwave and Wireless Components Letters*, vol. 20, no. 2, pp. 124–126, Feb. 2010.
- [69] L. W. Mayer and A. L. Scholtz, “Circularly polarized patch antenna with high tx / rx-separation,” in *IEEE International Conference on RFID*, Orlando, USA, Apr. 2009, pp. 213–216.
- [70] J. Y. Wang, B. Lv, W. Z. Cui, W. Ma, J. T. Huangfu, and L. X. Ran, “Isolation enhancement based on adaptive leakage cancellation,” in *Progress In Electromagnetics Research Symposium*, Xi’an, China, Mar. 2010, pp. 1059–1063.
- [71] Impinj, Inc., *Indy® R2000 Reader Chip (IPJ-R2000)*, rev. 1.3 ed., Jul. 2012.
- [72] J. Lee, J. Choi, K. H. Lee, B. Kim, M. Jeong, Y. Cho, H. Yoo, K. Yang, S. Kim, S.-M. Moon, J.-Y. Lee, S. Park, W. Kong, J. Kim, T.-J. Lee, B.-E. Kim, and B.-K. Ko, “A UHF mobile RFID reader IC with self-leakage canceller,” in *IEEE Radio Frequency Integrated Circuits (RFIC) Symposium*, Honolulu, Hawaii, Jun. 2007, pp. 273–276.
- [73] P. Beasley, A. Stove, B. Reits, and B. As, “Solving the problems of a single antenna frequency modulated CW radar,” *Record of the IEEE 1990 International Radar Conference*, pp. 391–395, May 1990.
- [74] K. Lin, Y. E. Wang, C.-K. Pao, and Y.-C. Shih, “A ka-band FMCW radar front-end with adaptive leakage cancellation,” *IEEE Transactions on Microwave Theory and Techniques*, vol. 54, no. 12, pp. 4041–4048, Dec. 2006.
- [75] R. Langwieser, G. Lasser, C. Angerer, M. Rupp, and A. L. Scholtz, “A modular UHF reader frontend for a flexible RFID testbed,” in *The 2nd Int. EURASIP Workshop on RFID Technology*, Budapest, Hungary, Jul. 2008.
- [76] A. T. Blischak and M. Manteghi, “Embedded singularity chipless RFID tags,” *IEEE*

Bibliography

- Transactions on Antennas and Propagation*, vol. 59, no. 11, pp. 3961–3968, Nov. 2011.
- [77] D. Arnitz, K. Witrissal, and U. Muehlmann, “Multifrequency continuous-wave radar approach to ranging in passive UHF RFID,” *IEEE Transactions on Microwave Theory and Techniques*, vol. 57, no. 5, pp. 1398–1405, May 2009.
- [78] H. Deng, “Performance enhancement of radio frequency identification (RFID) using spread spectrum technology,” *Antennas and Propagation Society International Symposium*, pp. 1205–1208, Jun. 2007.
- [79] D. Arnitz, “Tag localization in passive UHF RFID,” Ph.D. dissertation, Graz University of Technology, Austria, May 2011.
- [80] G. Lasser, R. Langwieser, R. Dallinger, and C. F. Mecklenbräuker, “Broadband leaking carrier cancellation for RFID systems,” in *IEEE MTT-S International Microwave Symposium*. Montreal: IEEE, Jun. 2012.
- [81] A. F. Molisch, *Wireless communications*, 1st ed. John Wiley & Sons, LTD, 2005.
- [82] A. L. Ballestrín, “Development of a delay line based leaking carrier canceller for an RFID testbed,” Master’s thesis, Vienna University of Technology, Austria, Sep. 2011.
- [83] F. J. Harris, “On the use of windows for harmonic analysis with the discrete fourier transform,” *Proceedings of the IEEE*, vol. 66, no. 1, pp. 51–83, Jan. 1978.
- [84] G. Lasser, W. Gartner, R. Langwieser, and C. F. Mecklenbräuker, “Fast algorithm for leaking carrier canceller adjustment,” in *Fourth International EURASIP Workshop on RFID Technology*, Torino, Italy, Sep. 2012.
- [85] G. Lasser, R. Langwieser, and C. F. Mecklenbräuker, “Automatic leaking carrier canceller adjustment techniques,” *EURASIP Journal on Embedded Systems*, vol. 2013, no. 1, 2013. [Online]. Available: <http://dx.doi.org/10.1186/1687-3963-2013-8>
- [86] R. Langwieser and G. Lasser, “Measurement and simulation of crosstalk and crosstalk compensation in UHF RFID,” in *Fourth International EURASIP Workshop on RFID Technology*, Torino, Italy, Sep. 2012.
- [87] S. Haykin, *Adaptive Filter Theory*, 1st ed. Upper Saddle River (NJ), USA: Prentice-Hall, 1986.
- [88] I. A. Glover and P. M. Grant, *Digital Communications*, 2nd ed. Edingburgh Gate, Harlow, Essex: Pearson Education Limited, 2004.
- [89] US National Highway Traffic and Safety Administration, “§571.138 standard no. 138; tire pressure monitoring systems.” Code of Federal Regulations, Apr. 2005, 70 FR 18187, Apr. 8, 2005, as amended at 70 FR 53100, Sept. 7, 2005; 72 FR 38025, July 12, 2007.
- [90] “Regelung nr. 64 der wirtschaftskommission für europa der vereinten nationen (UN/ECE) — einheitliche bedingungen für die genehmigung von fahrzeugen hinsichtlich ihrer ausstattung mit einem komplettnotrad, notlaufreifen und/oder einem notlaufsystem und/oder einem reifendrucküberwachungssystem,” Amtsblatt der Europäischen Union.
- [91] S. C. Ergen, A. Sangiovanni-Vincentelli, X. Sun, R. Tebano, S. Alalusi, G. Audisio, and M. Sabatini, “The tire as an intelligent sensor,” *IEEE Transactions on*

- Computer-Aided Design of Integrated Circuits and Systems*, vol. 28, pp. 941–955, Jul. 2009.
- [92] R. Matsuzaki and A. Todoroki, “Intelligent tires based on measurement of tire deformation,” *Journal of Solid Mechanics and Material Engineering*, vol. 2, no. 2, pp. 269–280, 2008.
- [93] G. Audisio, F. Cheli, S. Melzi, and M. Velardocchia, “Cyber tyre for vehicle active safety,” *Proc. XIX AIMETA*, pp. 14–17, 2009.
- [94] J. Grosinger, L. W. Mayer, C. F. Mecklenbräuker, and A. L. Scholtz, “Input impedance measurement of a dipole antenna mounted on a car tire,” in *Proc. 2009 International Symposium on Antennas and Propagation*, Bangkok, Thailand, Oct. 2009, pp. 1175–1178.
- [95] —, “Determining the dielectric properties of a car tire for an advanced tire monitoring system,” *Vehicular Technology Conference. VTC 2009-Fall. IEEE 70th*, Sep. 2009.
- [96] D. G. Michelson, J. Chuang, and M. Kicherer, “Requirements for standard radiowave propagation models for vehicular environments,” *Vehicular Technology Conference, 2006. VTC 2006-Spring. IEEE 63rd*, vol. 6, pp. 2777–2781, May 2006.
- [97] M. Brzeska and G.-A. Chakam, “RF modelling and characterization of a tyre pressure monitoring system,” *The Second European Conference on Antennas and Propagation, 2007. EuCAP*, pp. 1–6, Nov. 2007.
- [98] S. Genovesi, A. Monorchio, and S. Saponara, “Double-loop antenna for wireless tyre pressure monitoring,” *Electronics Letters*, vol. 44, no. 24, pp. 1385–1387, 2008.
- [99] H. J. Song, H. P. Hsu, R. Wiese, and T. Talty, “Modeling signal strength range of TPMS in automobiles,” *Antennas and Propagation Society International Symposium, 2004. IEEE*, vol. 3, pp. 3167–3170, Jun. 2004.
- [100] H. J. Song, J. S. Colburn, H. P. Hsu, and R. W. Wiese, “Development of reduced order model for modeling performance of tire pressure monitoring system,” *Vehicular Technology Conference, 2006. VTC-2006 Fall. IEEE 64th*, pp. 1–5, Sep. 2006.
- [101] Y. Leng, Y. Pan, Q. Li, and S. Liu, “Analysis of electromagnetic wave propagation characteristics in rotating environments,” *International Conference on Electronic Packaging Technology & High Density Packaging*, pp. 1–7, Jul. 2008.
- [102] G. Lasser and C. F. Mecklenbräuker, “Channel model for tyre pressure monitoring systems (TPMS),” in *Proc. EuCAP’2010 The 4th European Conference on Antennas and Propagation*, Barcelona, Spain, Apr. 2010.
- [103] J. Hunter and M. Cox, *Forensic archaeology*, new ed. Taylor & Francis, 2005.
- [104] K. Burnley, “High-voltage stator insulation assessment by measurement of loss tangent and capacitance,” *IEE Proceedings*, vol. 136, no. 5, pp. 229–236, Sep. 1989.
- [105] G. Lasser and C. F. Mecklenbräuker, “Dual-band channel measurements for an advanced tyre monitoring system,” *Vehicular Technology Conference. VTC 2010-Spring. IEEE 71th*, pp. 1–5, May 2010.
- [106] G. Lasser, D. Löschenbrand, and C. F. Mecklenbräuker, “Near field scans of tyre mounted dipoles using a separate phase reference antenna,” in *2014 IEEE-APS*

Bibliography

- Topical Conference on Antennas und Propagation in Wireless Communications*, Palm Beach, Aruba, Aug. 2014.
- [107] J. Grosinger, G. Lasser, C. F. Mecklenbräuker, and A. L. Scholtz, “Gain and efficiency measurement of antennas for an advanced tire monitoring system,” in *Antennas and Propagation Society International Symposium (APSURSI), 2010 IEEE*, Jul. 2010, pp. 1–4.
- [108] G. Lasser, R. Langwieser, F. Xaver, and C. F. Mecklenbräuker, “Dual-band channel gain statistics for dual-antenna tyre pressure monitoring RFID tags,” in *Proceedings of the 2011 IEEE International Conference on RFID*. Orlando, FL: IEEE, Apr. 2011, pp. 57–61.
- [109] J. D. Griffin and G. D. Durgin, “Gains for RF tags using multiple antennas,” *IEEE Transactions on Antennas and Propagation*, vol. 56, no. 2, pp. 563–570, Feb. 2008.
- [110] P. V. Nikitin and K. Rao, “Performance of RFID tags with multiple RF ports,” in *Antennas and Propagation Society International Symposium, 2007 IEEE*, Jun. 2007, pp. 5459–5462.
- [111] S. Sanayei and A. Nosratinia, “Antenna selection in MIMO systems,” *IEEE Communications Magazine*, vol. 42, no. 10, pp. 68–73, Oct. 2004.
- [112] J. D. Hyde, O. Onen, and R. A. Oliver, “RFID tags combining signals received from multiple RF ports,” U.S. patent application, Aug. 26, 2005.
- [113] D. W. Duan and D. J. Friedman, “Cascaded DC voltages of multiple antenna RF tag front-end circuits,” U.S. Patent, Jun. 5, 2001.
- [114] J.-P. Curty, N. Joehl, F. Krummenacher, C. Dehollain, and M. J. Declercq, “A model for μ -power rectifier analysis and design,” *IEEE Transactions on Circuits and Systems—Part I: Regular Papers*, vol. 52, no. 12, pp. 2771–2779, Dec. 2005.
- [115] K. Seemann, G. Hofer, F. Cilek, and R. Weigel, “Single-ended ultra-low-power multistage rectifiers for passive RFID tags at UHF and microwave frequencies,” in *Radio and Wireless Symposium, 2006 IEEE*, Jan. 2006, pp. 479–482.
- [116] Impinj, Inc., *Monza® 4 Tag Chip Datasheet*, rev. 5.3 ed., Sep. 2014.
- [117] ETSI, *EN 300 440-1*, v1.5.1 ed., European Telecommunications Standards Institute, Sophia Antipolis Cedex - FRANCE, Mar. 2009, electromagnetic compatibility and Radio spectrum Matters (ERM); Short range devices; Radio equipment to be used in the 1 GHz to 40 GHz frequency range; Part 1: Technical characteristics and test methods.
- [118] V. Pillai, H. Heinrich, D. Dieska, P. V. Nikitin, R. Martinez, and K. S. Rao, “An ultra-low-power long range battery/passive RFID tag for UHF and microwave bands with a current consumption of 700 na at 1.5 v,” *IEEE Transactions on Circuits and Systems—Part I: Regular Papers*, vol. 54, no. 7, pp. 1500–1512, 2007.
- [119] G. Lasser and C. F. Mecklenbräuker, “Distortions of measured antenna patterns caused by dielectric support structures,” in *COST IC1004 9th MC & Scientific Meeting*, no. TD(14)09048, 2014.
- [120] G. Lasser, D. Löschenbrand, and C. F. Mecklenbräuker, “Update on distorted measured antenna patterns,” in *COST IC1004 10th MC & Scientific Meeting*, no. TD(14)10033, 2014.

- [121] Evonik Industries, *Rohacell Dielectric Properties*, 64293 Darmstadt, Deutschland, 2011.
- [122] J. Hansen, Ed., *Spherical Near-Field Antenna Measurements*, ser. IET Electromagnetic Wave Series 26. London, UK: The Institution of Engineering and Technology, 2008.
- [123] A. K. Skrivervik and J.-F. Zürcher, “Recent advances in pcs antenna design and measurement,” *AUTOMATIKA – Journal for Control, Measurement, Electronics, Computing and Communications*, vol. 43, no. 1-2, pp. 55–61, Oct. 2002.
- [124] L. W. Mayer and A. L. Scholtz, “Gain and input impedance measurement for UHF transponder antennas,” *2008 International Symposium on Antennas and Propagation*, p. 4, 2008.
- [125] A. C. Ludwig, “The definition of cross polarization,” *IEEE Transactions on Antennas and Propagation*, vol. 21, no. 1, pp. 116–119, Jan. 1973.
- [126] G. Hindman and A. C. Newell, “Reflection suppression in a large spherical near-field range,” in *AMTA 27th Annual Meeting & Symposium, Newport, RI*, 2005.

List of Abbreviations

- ABS** Anti-lock Braking System.
ADC Analogue to Digital Converter.
AGC Automatic Gain Control.
AMC Artificial Magnetic Conductor.
ATMS Advanced Tyre Monitoring System.
AUT Antenna Under Test.
- BLC** Broadband Leakage Canceller.
BPF Band Pass Filter.
- CCDF** Complementary Cumulative Distribution Function.
CCU Carrier Compensation Unit.
CDF Cumulative Distribution Function.
CNR Carrier to Noise Ratio.
CPLR directional coupler.
CW Continuous Wave.
- DAC** Digital to Analogue Converter.
DC Direct Current.
DDRR Directly Driven Resonant Radiator.
- EIRP** Equivalent Isotropically Radiated Power.
ERP Equivalent Radiated Power.
ESC Electronic Stability Control.
- FEM** Finite Element Method.
FF Far-Field.
FIR Finite Impulse Response.
FSPL Free Space Loss.
FSS Frequency Selective Surface.
- GP** Ground-Plane.
- IC** Integrated Circuit.
ISM Industrial, Scientific, Medical.

List of Abbreviations

- LCC** Leaking Carrier Canceller.
LNA Low Noise Amplifier.
LPDL Low-Profile Dual-band Loop.
LPF Low Pass Filter.
- MAC** Medium Access Control.
MARS Mathematical Absorber Reflection Suppression.
MIMO Multiple Input Multiple Output.
MRE Maximum Radial Extend.
- NF** Near-Field.
- OU** Onboard Unit.
- PA** Power Amplifier.
PCB Printed Circuit Board.
PEC Perfect Electric Conductor.
PMMA polymethylmethacrylate.
- RF** Radio Frequency.
RFID Radio Frequency IDentification.
RX Receiver.
- SBA** Switched Beam Antenna.
SIMO Single Input Multiple Output.
SISO Single Input Single Output.
SNR Signal to Noise Ratio.
SOLT Short Open Load Thru.
- TBC** Test Bed Controller.
TE Transversal Electric.
TM Transversal Magnetic.
TPMS Tyre Pressure Monitoring System.
TRX Transceiver.
TX Transmitter.
- UHF** Ultra High Frequency.
- VGA** Variable Gain Amplifier.
VNA Vector Network Analyser.
- WU** Wheel Unit.

List of Figures

2.1	Illustration of the modified monopole.	8
2.2	Logarithmically scaled pseudo-color plot of the gain pattern of the modified monopole antenna corresponding to E_θ at 866 MHz.	10
2.3	Radiation pattern of the modified monopole antenna.	11
2.4	Logarithmically scaled pseudo-color plot of the gain pattern of the modified monopole antenna at 2.45 GHz for vertical polarisation.	12
2.5	Radiation pattern of the modified monopole antenna in polar angle at 2.45 GHz.	12
2.6	Image showing the LPDL antenna.	13
2.7	Dimensional drawing of the LPDL antenna PCB on a scale of 1:1.	13
2.8	Comparison of antenna return losses of both antennas, both measured and simulated.	14
2.9	Logarithmically scaled pseudo-color plot of the gain pattern of the LPDL antenna at 866 MHz for vertical polarisation.	15
2.10	Radiation pattern of the LPDL antenna.	16
2.11	Logarithmically scaled pseudo-color plot of the gain pattern of the LPDL antenna at 2.45 GHz for vertical polarisation.	17
2.12	Antenna geometry of the UHF-SBA for simulation showing feeding side in red and dipole side in blue.	18
2.13	Feeding network of the UHF-SBA including discrete components.	19
2.14	Simulated surface currents on bottom side of the dipole layer at 866 MHz for the UHF-SBA to illustrate the principle of directivity. Strong surface currents appear in red, weak currents in blue.	20
2.15	Picture of the manufactured UHF-SBA showing radiating elements and PIN-diode control circuitry.	21
2.16	Measured SBA return loss for different beam settings.	22
2.17	Comparison of normalized gainplots for the UHF-SBA in free space for different frequencies f ; plotted for beam I pointing in y -direction.	23
2.18	Comparison of normalized gainplots for the UHF-SBA at 866 MHz in free space for different activated beams.	23
2.19	Azimuth radiation pattern of the UHF-SBA at $f = 865$ MHz.	24
2.20	Polar radiation pattern for beam I at different frequencies f	25
2.21	Picture of the manufactured ISM-SBA looking at the feed side printed up to scale.	25
2.22	Comparison of normalized gain plots for the ISM-SBA in free space for different frequencies f ; plotted for beam I pointing in y -direction.	26

List of Figures

2.23	Artificial Magnetic Conductor (AMC) principle.	27
2.24	Unit cell geometry of the designed AMC FSS1.	28
2.25	Equivalent circuit model for the developed AMC structures.	30
2.26	AMC phase response measurement.	31
2.27	Schematic representation of the different performed measurement configurations.	32
2.28	Simulated band structure diagram of FSS1.	33
2.29	Simulated band structure diagram of FSS2.	34
2.30	Surface Wave Measurement.	35
2.31	Return Loss of UHF-SBA mounted atop either a ground-plane or FSS2 in different heights. The thicker line without markers shows a free space measurement of the SBA. The design frequency band is 865 MHz to 868 MHz.	36
2.32	Relative efficiency of the SBA mounted atop different substrates in four different heights when compared to the SBA in free space. The different setups correspond to different SBA–FSS-spacings according to Table 2.4 and GP denotes a ground-plane.	38
2.33	Comparison of normalized gain plots in setup 2 (28 mm separation): ground-plane, FSS2, and FSS2 plus large ground-plane at 850 MHz and 866 MHz.	39
2.34	Comparison of normalized gain plots in setup 2 (28 mm separation): ground-plane, FSS2, and FSS2 plus large ground-plane at 910 MHz and 930 MHz.	39
2.35	Polar peak position of the SBA mounted atop different substrates in four different heights when compared to the SBA in free space. The different setups correspond to different SBA–FSS-spacings according to Table 2.4 and GP denotes a ground-plane.	40
2.36	Thetacut for SBA at 865 MHz over different substrates in setup 2 (28 mm separation) and beam II except where noted otherwise.	41
2.37	Thetacut for SBA at 930 MHz over different substrates in setup 2 (28 mm separation) and beam II except where noted otherwise.	42
2.38	Comparison of normalized gain plots in setup 2 (28 mm separation) for the ISM-SBA assembly over FSS2 plus large ground-plane for different frequencies f	43
2.39	Comparison of normalized gain plots in setup 2 (28 mm separation) for the ISM-SBA assembly over FSS1 plus large ground-plane for different frequencies f	43
3.1	Block diagram of an RFID reader using an LCC: (a) monostatic; (b) bistatic scenario.	48
3.2	Picture of the Carrier Compensation Unit (CCU) module.	48
3.3	RFID link budget chart focusing on carrier cancellation and transmit noise.	49
3.4	Monostatic RFID system with LCC illustrating the single tap model.	50
3.5	Transfer function of the modelled suppression system with $\Delta\tau = 1.06$ ns and $\alpha = 29.02^\circ$, creating 40 dB of suppression in the European RFID band.	52
3.6	Isolation gain G_I plotted over the electrical offset length Δl_e for two fixed bandwidth values.	52

3.7	Measurement setup for broadband suppression properties of the CCU as leaking carrier canceller	53
3.8	Magnitude response of the LCC measurement test setup.	54
3.9	Block diagram of the proposed three tap BLC.	56
3.10	Photo (a) and principal drawing (b) of the measurement setup.	56
3.11	Leakage transfer function magnitude $ H_L $ for different tag positions.	57
3.12	Impulse responses h_L and h_{BLC} for the leakage and BLC channel.	58
3.13	Magnitudes of the transfer functions of the leakage channel H_L , the Tukey windowed H_L , and the channels of the cancellers H_{BLC} , and H_{LCC}	59
3.14	Isolation gain $G_I = \frac{ H_L(f) }{ H(f) }$ for BLC and LCC.	60
3.15	Block diagram of a simplified RFID reader showing possible detector positions for LCC adjustment routines.	62
3.16	Illustration of the leaking signal and the probing signal.	64
3.17	Comparison of the relative bias of the I-component estimate for the averaged Monte Carlo simulation results and the approximate analytic results plotted versus the Carrier to Noise Ratio (CNR).	70
3.18	Comparison of Standard Deviations σ_i of relative I-Component Errors plotted vs. CNR.	71
3.19	Scatterplot (a) and Histogram (b) of Estimation Error at $CNR = -5$ dB.	72
3.20	Scatterplot (a) and Histogram (b) of Estimation Error at $CNR = 0$ dB.	72
3.21	Scatterplot (a) and Histogram (b) of Estimation Error at $CNR = 10$ dB.	73
3.22	Fast algorithm evaluation measurement setup.	74
3.23	Artificial leakage measurement setup.	74
3.24	Fast Algorithm Isolation Gain.	77
3.25	Isolation gain ratio.	77
3.26	Relative error vector magnitude.	78
3.27	Relative component setting errors.	78
3.28	Step number reduction.	81
4.1	Comparison between numerical Finite Element Method (FEM) results and experimental acquisitions for radial accelerations over the tyre circumferential development, reproduced from [22, Figure 6a].	84
4.2	Vehicular body seen from below to visualize the relevant channels for WU 1, and the steering angle Θ	85
4.3	Simulation model implemented in HFSS.	88
4.4	Detail of the simulation model implemented in HFSS: tyre rubber parts (a), steel belt and rim (b).	89
4.5	Partial view of vehicle body describing WU orientations.	89
4.6	Simulated channel coefficient $h_1(\varphi, 0)$ for different antenna positions, without road model.	90
4.7	Simulated return loss of WU and OU antennas, without road model.	91
4.8	Fourier components $c_{1,m}$ for a inner parallel mounted antenna, without road model.	91

List of Figures

4.9	Fourier components $c_{S11,m}$ for a inner parallel mounted antenna, without road model.	92
4.10	Fourier components $c_{1,m}$ for an outer parallel mounted antenna, simulated with road model.	92
4.11	Simulated WU–OU and WU–WU channel responses for outer parallel mounted antennas, including a road model.	93
4.12	Channel measurement setup.	95
4.13	Bottom view of measurement vehicle on auto-hoist.	96
4.14	Schematic drawing of the tyre in the used coordinate system carrying a dipole mounted in the outer orthogonal position.	96
4.15	Normalized measured gain patterns for WU dipoles mounted on the outer position.	97
4.16	Normalized measured gain patterns for WU dipoles mounted on the inner position.	97
4.17	Measured magnitude of $h_1(\varphi, 0)$ for the short dipole at 865 MHz.	98
4.18	Measured WU antenna input return loss prior to de-embedding.	99
4.19	Channel phase response $\arg(h_1)$ at 865 MHz.	101
4.20	Magnitude of $h_1(\varphi, 0)$ for the short and long dipoles at 865 MHz.	101
4.21	Measured magnitude of $h_1(\varphi, 0)$ for the short dipole at 2.45 GHz.	102
4.22	Magnitude of $h_1(\varphi, \Theta)$ for the inner, parallel mounted short dipole at 2.45 GHz for different steering angles.	103
4.23	Magnitude of $h_1(\varphi, 0, f)$ for the inner, parallel mounted short dipole over frequency f and rotational angle φ	103
4.24	Signal combining techniques.	104
4.25	CCDFs of channel magnitude for different WU orientations at UHF.	106
4.26	CCDFs of channel magnitude for long and short parallel OU antennas at UHF.	107
4.27	CCDFs of channel magnitude for different WU orientations at ISM frequencies, for straight steering only.	108
4.28	CCDFs of channel magnitude for different WU orientations at ISM frequencies, including equiprobable steering angles left and right.	109
4.29	CCDFs of channel magnitude at UHF for inner mounted antennas and virtual SIMO channel.	110
4.30	CCDFs of channel magnitude at 2.45 GHz for inner mounted antennas and virtual SIMO channel, for straight steering only.	111
4.31	Probability plot for gamma distribution fitting of channel magnitudes at 2.45 GHz band.	111
A.1	Measurement setup in the anechoic chamber showing the manufactured Rohacell Column.	116
A.2	Cable-less NF antenna measurement system.	118
A.3	Spherical coordinate system used for antenna measurements.	119
A.4	SBA measurement gain plot comparison for the E_φ component: Cable feed versus oscillator.	120

A.5	SBA measurement pattern comparison for the E_φ component: Cable feed versus oscillator.	121
A.6	FF gain plot comparison for NF truncation effects.	122
A.7	Demonstration of truncation effects on NF data: Theta cut comparison. . .	123
A.8	Graphical representation of the three measured antenna directions. The arrows indicate the expected direction of the main beam.	124
A.9	Comparison of gain plots in three mounting configurations in their native coordinate system. Note that the range $\theta > 150^\circ$ is marked by alternating power levels.	125
A.10	Comparison of gain plots in three mounting configurations, transformed to coordinate system A. Note that the previously marked area now appears as colourful ellipse.	126
A.11	Comparison of transformed measurements of the SBA for different orientations: Theta cut comparison.	127
A.12	Comparison of gain plots corresponding to the E_φ -component of coordinate system A of the SBA mounted atop a GP with different separations, for mounting positions A (cabled measurements) and B (transformed oscillator measurements).	128
A.13	Comparison of normalized gain plots for the ISM-SBA in free space for different frequencies f ; plotted for beam I pointing in y -direction, prior to MARS processing. Compare to Figure 2.22.	129
B.1	Drawing of a unit cell of FSS FSS1 in scale 8:1. The thin boarder line corresponds to the 20 mm unit cell boundary.	132
B.2	Drawing of a unit cell of FSS FSS2 in scale 8:1. The thin boarder line corresponds to the 20 mm unit cell boundary.	133

List of Tables

2.1	Mechanical parameters of the modified monopole antenna.	9
2.2	Mechanical parameters of LPDL antenna.	14
2.3	Values of equivalent circuit model for FSS1.	31
2.4	Used measurement setups.	36
2.5	Data summary of the designed antennas.	45
3.1	Comparison of LCC adjustment techniques.	66
3.2	Comparison of the isolation gains for the fast algorithm and a conventional gradient algorithm for single and dual antenna scenarios.	76
4.1	Parameters of gamma distributions for 2.45 GHz band.	110
A.1	Comparison of performed evaluation measurement data.	119